ABSTRACT

Title of dissertation: OPTICAL PROPERTIES OF STRONGLY CORRELATED TRANSITION METAL OXIDES

Jeffrey R. Simpson, Doctor of Philosophy, 2004

Dissertation directed by: Professor H. Dennis Drew
Department of Physics

The strong electron interactions in transition metal oxides offer wide-ranging phenomena of interest to condensed matter physics and potential applications in novel electronic devices. This thesis focuses on optical studies performed on three such systems: colossal magnetoresistant (CMR) manganites, multiferroic $LuMnO_3$, and dilute magnetic oxide (DMO) cobalt-doped TiO_2. Optical measurements, using a variety of techniques, of thin film and bulk samples extend over a range of frequencies ($0.002 - 5$ eV) and temperatures ($4 - 350$ K) and determine the optical constants. Optical properties provide important insights into the electronic structure of these exciting systems and illustrate the value of optical measurements as a probe of novel materials.

The pseudocubic manganites exhibit a rich phase diagram that includes, in addition to CMR, various types of magnetic, charge, and orbitally ordered phases. For the CMR manganites, the optical spectra and oscillator strength changes compare with models that require both double exchange and the dynamic Jahn-Teller effect

in the description of the electronic structure. In the ferromagnetic state, results on the electronic scattering rate and mass enhancement refute the claims of an anomalously small Drude weight in these materials.

Smaller rare-earth ions in the manganites (*e.g.*, Lu) result in crystallization into a hexagonal structure and a multiferroic ground state, in which ferroelectricity and antiferromagnetism occur simultaneously. A symmetry-allowed on-site Mn $d-d$ optical transition blueshifts in the antiferromagnetic state resulting from Mn-Mn superexchange. TO phonon frequencies exhibit similar temperature dependent shifts arising from spin-phonon interactions. Further, these phonons dominantly contribute to the known anomaly below T_N of the quasi-static ϵ.

Cobalt-doped TiO_2 has received recent attention as a new DMO displaying room temperature ferromagnetism. Optical conductivity of low-doped samples reveals an absence of absorption below an onset of interband transitions at 3.6 eV and a blue shift of the band edge with doping. The absence of below band gap absorption remains inconsistent with band calculations and suggests that strong on-site Coulomb interactions shift the optical transitions to energies above the gap.

Optical Properties of Strongly Correlated Transition Metal Oxides

by

Jeffrey Ray Simpson

Dissertation submitted to the Faculty of the Graduate School of the
University of Maryland, College Park in partial fulfillment
of the requirements for the degree of
Doctor of Philosophy
2004

Advisory Committee:
Professor H. Dennis Drew, Chair/Advisor
Professor Richard L. Greene
Professor Satishchandra B. Ogale
Professor Lourdes Salamanca-Riba
Professor Victor M. Yakovenko

Dedication

To my parents

Raymond M. Simpson, Jr.

and

Linda E. Simpson

Acknowledgments

First and foremost I am indebted to my advisor, Prof. H. Dennis Drew whose keen scientific interests, kind mentoring, and positive encouragement have guided my research. Truly, his patience knows no bounds. Under Dennis's tutelage, I have grown as researcher and as a person.

The work presented in this thesis represents, in part, a collaborative effort involving researchers at the University of Maryland (UM) and other institutions affiliated with the Materials Research Science and Engineering Center. Without their helpful advice and collaborative efforts, this work would not have been possible.

I gratefully acknowledge the members of Prof. Drew's Magneto-Optics group with whom I have shared many fruitful discussions over the years. In particular, Greg Jenkins with whom I shared many a late night in the lab discussing physics among other wide ranging topics. Additionally, I wish to express my gratitude to Manuel Quijada and Andrei Sushkov for offering their expertise and assistance measuring the optical properties of transition metal oxides. To John Cerne, Matt Grayson, and Don Schmadel, I offer the sincerest thanks for many informative conversations.

The high-quality thin film samples studied herein were prepared and characterized in the pulsed laser deposition at UM. I especially acknowledge the beneficial

collaboration with Sanjay Shinde, Satish Ogale, and M. Rajeswari. Professor Sang-W Cheong and his group at Rutger's University prepared and characterized the high-quality single crystals of $LuMnO_3$. For his acute theoretical insight, I acknowledge Andy Millis at Columbia University.

I wish to thank the committee members Prof. Richard L. Greene, Prof. Satishchandra B. Ogale, Prof. Victor M. Yakovenko, and Prof. Lourdes G. Salamanca-Riba for their constructive feedback and stimulating questions. Additionally, I appreciate the support and insightful comments of friends and colleagues who attended the oral defense.

Finally, I wish to thank my family and friends for providing support throughout my graduate school tenure. Especially, I offer profound gratitude to my girlfriend Sara for her patience, understanding, and encouragement. To my parents, I am eternally grateful for their support and encouragement throughout my academic career.

Table of Contents

List of Figures

List of Tables

Chapter 1

Introduction

1.1 Transition Metal Oxides

The discovery[1] of high-temperature superconductivity in the cuprates renewed interest in the study of transition metal oxides (TMO). This fascinating class of inorganic solids exhibits a wide variety of exotic and imperfectly understood structures, properties, and phenomena.[2,3] The material properties result from strong interactions and depend on external parameters such as temperature, mechanical pressure, chemical composition, oxygen concentration, applied magnetic field, and applied electric field. Exploiting these properties in novel electronic devices remains an active area of research. Given these considerations, transition metal oxides represent a veritable playground for condensed matter physicists and materials scientists.

The outer d electrons of the transition metal ions are largely responsible for the interesting electronic and magnetic properties. Hund's rules for the partially filled d-levels provide for the large magnetic moments. The coupling of these moments through both direct and indirect exchange mechanisms produce various long-range magnetic order (depending on the sign of the exchange and the details of the coupling) including ferromagnetic, antiferromagnetic, and ferrimagnetic. In addition to magnetic ordering, TMOs exhibit various other ordering: charge, orbital, and ferroelectric. The small electronic bandwidth W relative to the electron-electron interaction energy U in these materials leads to strong correlation effects, which often exceed

the capabilities of band theory.

1.1.1 Practical applications

Transition metal oxides offer promising applications in the emerging field of magnetoelectronics or “spintronics”, which exploits the quantum-mechanical spin of electrons in addition to the conventional utilization of charge. Possible device applications include[4] (i) spin valves, (ii) nonvolatile memory, (iii) spin-based field-effect transistors (FET), (iv) spin-based light emitting diodes (LED), and (v) Spin resonant tunnelling diodes (RTD). The success of these devices depends on understanding spin interactions in solid state systems, including the role of dimensionality, defects, and band structure.[4]

“Spintronic” devices offer the possibility of combining information processing with non-volatile information storage. Typically, information processing is implemented using semiconducting technology and information storage is implemented using high-density magnetic storage. The proliferation of personal computers (PC) stimulates advances in materials with applications to information technology. Specifically, semiconducting chip density progresses exponentially, doubling every approximately eighteen months according to Moore’s law.[5] Such advances in information processing capabilities drive similar developments in non-volatile storage. Magnetic storage capacity follows a power law analogous to Moore’s law for semiconducting chip density. Figure 1.1 shows a plot of the storage capacity (in megabytes) of 5.25 in. hard disk drives (HDD) as a function of time over several decades.[6] An exponential fit reveals a doubling of HDD storage capacity roughly every two years. For typical hard drive platter dimensions, the current hard drive capacity corresponds to a storage density of approximately 40 bits/μm^2 (8 bits $= 1$ byte). A hypothetical limiting density of approximately 1 bit/nm^2 results from consideration of a single magnetic moment located in a unit cell. Comparing this

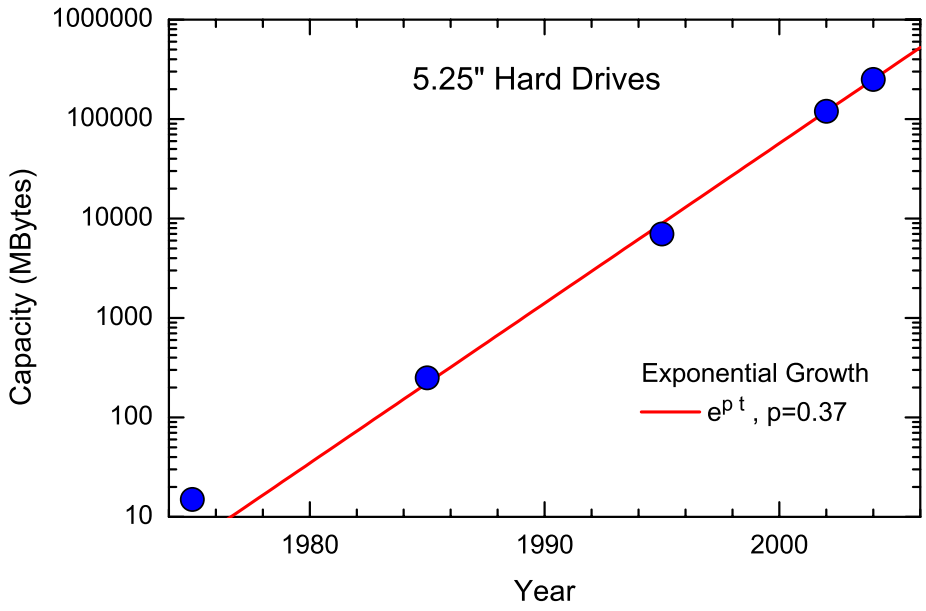

Figure 1.1: Storage capacity (megabytes) of 5.25 in. personal computer hard drives from the 1970's until the present. Data prior to 2000 from Ref. 7. Straight line represents an exponential fit to the data.

limit with the presently realized storage density suggests a potential improvement of $\sim 10^7$. At the current rate of increase, this represents nearly a half century of continued development.

The rapid transition from discovery to product[8] of the spin-polarized transport employed in giant magnetoresistance (GMR) materials significantly advanced magnetic storage capacity. GMR materials consist of alternating layers between magnetic and nonmagnetic thin films. An external field polarizes spins in the magnetic layers and minimizes spin-dependent scattering. As a result, large resistive changes occur for small changes in applied field, making GMR materials sensitive magnetic read heads. The GMR effect, initially reported[9] in 1988, first found commercial application[8] in magnetic field sensors in 1994 and in HDD read heads in 1997. The successful application of the GMR effect fuels interest in related materials with even larger magnetoresistance. These aptly-named "colossal magnetoresistance" (CMR)

materials have attracted a great deal of attention and generated a wealth of unexpected condensed matter phenomena. However, the CMR materials have not yet enjoyed the applied success of their merely giant cousins.

The application of GMR materials in magnetic read heads produced immediate benefits to information technology. A broader goal involves integration of both spin and charge functionality not currently existing in either ferromagnets or semiconductors alone.[10] Such functionality includes demonstrating control of the magnetic ordering by the application of an electric field and vice versa. Several groups have demonstrated this extra degree of freedom in TMO systems. Ohno *et al.*[11] have demonstrated electric field control of ferromagnetism in (In,Mn)As heterostructures. Cheong *et al.* have demonstrated[12] similar effects in the multiferroic $TbMn_2O_5$.

1.1.2 Strong correlation effects on condensed matter systems

Two limiting descriptions of the outer atomic electrons in solids consist of the localized or ligand-field, appropriate for insulators, and the delocalized band theory, appropriate for metals. The localized description applies whenever electrons are tightly bound to the ions and interatomic interactions are weak. This corresponds to a small electron bandwidth W relative to the electron-electron Coulomb energy U, *i.e.*, $W \ll U$. On the other hand, band theory applies for appreciable overlap of neighboring orbitals, in which case $W \gg U$. Typically, the d electrons in transition metal oxides exhibit narrow bands overlapping with relatively broad $s-p$ bands and neither limit applies. In this intermediate case, $W \sim U$ and the behavior lies between local and band theory. Theoretical models describing this strong correlation regime attempt to explain the interactions responsible for the tendency of electrons to localize more than predicted from noninteracting pictures. Examples of the these interactions include those between electrons (el-el), between electrons and the lattice (el-phonon), and between spins and the lattice (spin-phonon). The strong correlation

regime leads to both localized and itinerant electron behavior.

Localized models describe ions fixed in the crystal lattice with little overlap of the atomic orbitals. Crystal or ligand field theory describes the perturbation of atomic levels due to the local coordination environment of additional atoms in the lattice. Intra-atomic exchange (Hund's rule splitting) and electron-phonon interactions favor localized electrons.[2] At finite temperatures el-el and el-ph interactions become important. For el-ph interactions, Frohlich's coupling constant λ characterizes the strength of the interaction. The self-trapping of an electron due to lattice interactions is called a polaron. The size of λ determines the transport properties of the polaron. Weak coupling gives rise to large polarons with itinerant transport, while strong coupling produces small polarons that tend to localize and display activated hopping transport.

Perhaps one of the best studied and simplest models including strong correlation effects is that due to Hubbard.[13] The Hubbard model parameterizes the Hamiltonian of a single orbital per site in terms of the nearest-neighbor hopping parameter t and the on-site electron-electron interaction term U. This single band model describes the splitting of bands into upper and lower Hubbard bands. As W increases the upper and lower bands come together and the energy gap disappears. The Hubbard model is given[13] by

$$H_{Hub} = -\sum_{i,\boldsymbol{\delta}} t_{\boldsymbol{\delta}} \left(d^{\dagger}_{i\alpha} d_{i+\boldsymbol{\delta}\,\alpha} + H.c. \right) + U \sum_{i} n_{i\uparrow}\, n_{i\downarrow}\,, \tag{1.1}$$

where i denotes a lattice site, $\boldsymbol{\delta}$ is the displacement vector between sites, α is the spin, and $n_{i\uparrow}$ ($n_{i\downarrow}$) denotes the electron density on site i with spin up (down). For $n = 1$ electron per site and finite U, the ground state is insulating, known as a Mott insulator. With increased hole-doping, $x = 1 - n$, the electron-electron interaction tendency decreases. This results in a metal-insulator transition (Mott transition) at some critical doping concentration. For $t \ll U$, the kinetic energy $K \sim t^2/U$. Hence,

an increase in hopping increases the kinetic energy. The Mott-Hubbard model is appropriate for magnetic insulators, *e.g.*, $3d$ TMOs with a small electronic bandwidth W.[2] A single band model, the Hubbard model is relevant only for t and U small compared to the energy gap between other bands and may not apply for transitions to other levels, for example O $2p$ to Mn $3d$.

In addition to interacting with each other, outer electrons interact with the core spins localized on the transition metal ions. Coupling of the itinerant carriers with the core spins are important for magnetic TMO (*e.g.*, the hole-doped orthorhombic manganites). The Kondo lattice model adds a term to the Hamiltonian that includes carrier interactions with the core spins

$$H_{Hund} = -J_H \sum_{\substack{i,a \\ \alpha\beta}} \boldsymbol{S}_i \cdot \boldsymbol{\sigma}_{\alpha\beta}\, d^{\dagger}_{i\alpha} d_{i\beta}\,, \tag{1.2}$$

where J_H denotes the Hund's coupling, S_i denotes the core spin on site i, and $\sigma_{\alpha\beta}$ denotes the carrier spin. In the limit where the coupling energy $J_H S_c$ is large compared to W, the carrier spins align with the core spins.

For the relatively narrow bands of the transition metal oxides, the tight binding model plus interactions well-describes the calculated band structure. The tight-binding Hamiltonian has the form

$$H = -\sum_{\substack{i\boldsymbol{\delta} \\ ab}} t^{ab}_{\boldsymbol{\delta}} \left(e^{i\frac{e}{c}\boldsymbol{A}\cdot\boldsymbol{\delta}} d^{\dagger}_{ia\alpha} d_{i+\boldsymbol{\delta}b\alpha} + H.c. \right) + H_{INT}\,, \tag{1.3}$$

where i represents lattice sites, δ denotes a displacement connecting two lattice sites, a and b represent electron orbitals on a given site, and H_{int} represents additional interaction effects. Interactions may take the form of Hund's exchange coupling, el-el interactions, el-ph interactions, etc. Hopping matrix elements $t^{ab}_{\boldsymbol{\delta}}$ are estimated from fits to band structure calculations. The introduction of the Peierls phase term $e^{i\frac{e}{c}\boldsymbol{A}\cdot\boldsymbol{\delta}}$ affords consideration of the interaction with electromagnetic radiation relevant to

optical conductivity studies. The tight binding parameterization, valid only for nearest neighbor hopping, facilitates calculations over the full Hamiltonian approach.

1.1.3 Specific TMO compounds

There exists a vast number of transition metal oxides to study, at least enough to engage the condensed matter and materials science community for quite some time. Knowing which materials to study requires experienced insight. This thesis focuses on several such systems displaying magnetic and strong correlation effects, including the manganites and Co-doped titanium dioxide.

Next to the high-T_c cuprates, the manganites represent possibly the next well-known TMO system owing to the discovery of colossal magnetoresistance. Manganites $R\mathrm{MnO_3}$ form different crystal structures depending on the size of the rare-earth ion R. Figure 1.2 presents Shannon ionic radii[14] for the lanthanide series (circles). The horizontal line represents the approximate boundary between orthorhombic and

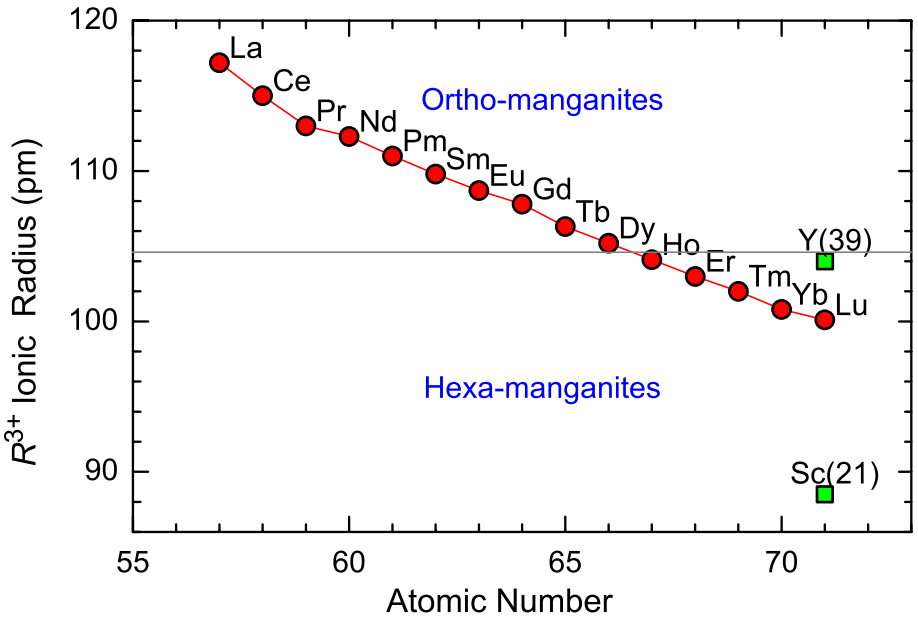

Figure 1.2: Ionic radii of R^{3+} ions. Smaller ionic radii form a hexagonal crystal structure.

hexagonal crystal structures. For ionic radius larger than approximately $105\,\text{pm}$, the manganites crystallize in the orthorhombic phase. For smaller radii, the hexagonal crystal is realized. In addition to the lanthanides, yttrium and scandium also crystalize in the hexagonal lattice. Ions near the separatrix between the two phases (*e.g.*, Y or Ho), may exhibit either phase depending on the growth conditions or the application of mechanical stress.

The remainder of this chapter will be dedicated to introducing the structural, magnetic, and electronic properties of the orthorhombic manganites, the hexagonal manganites, and diluted magnetic semiconductors/oxides.

1.2 Ortho-manganites and Colossal Magnetoresistance

The discovery of colossal magnetoresistance (CMR) in hole-doped manganites of the form $R_{1-x}A_x\text{MnO}_3$, where R is a rare-earth lanthanide (La, Ce, Pr, Nd, Pm, Sm, Eu, Gd, Tb, Dy), A is an alkaline-earth (*e.g.*, Sr or Ca) element, and x is the hole-doping concentration, renewed interest in this complex magnetic system.[15–19] Changing doping x results in a rich phase diagram characterized by the interplay of magnetic, charge ordering, and orbital ordering tendencies. Strong electron-lattice coupling effects lead to a variety of interesting physical phenomena.[3] Figure 1.3 shows the phase diagram in temperature and doping x for the prototypical CMR compound $\text{La}_{1-x}\text{Ca}_x\text{MnO}_3$. At low doping ($x \leq 0.2$), material is insulating and paramagnetic at high temperatures and antiferromagnetic below the Néel temperature $T_N \approx 140\,\text{K}$. The parent compound LaMnO_3 exhibits A-type antiferromagnetic order below T_N and C-type orbital order below $T_{OO} \approx 780\,\text{K}$ (Ref. 21). In the CMR doping range, $0.2 \leq x \leq 0.5$, the ground state exhibits metallic behavior commensurate with ferromagnetism. Above the ferromagnetic transition temperature T_c the material is paramagnetic and insulating. Charge-ordered and additional AFM states exists above $x > 0.5$.

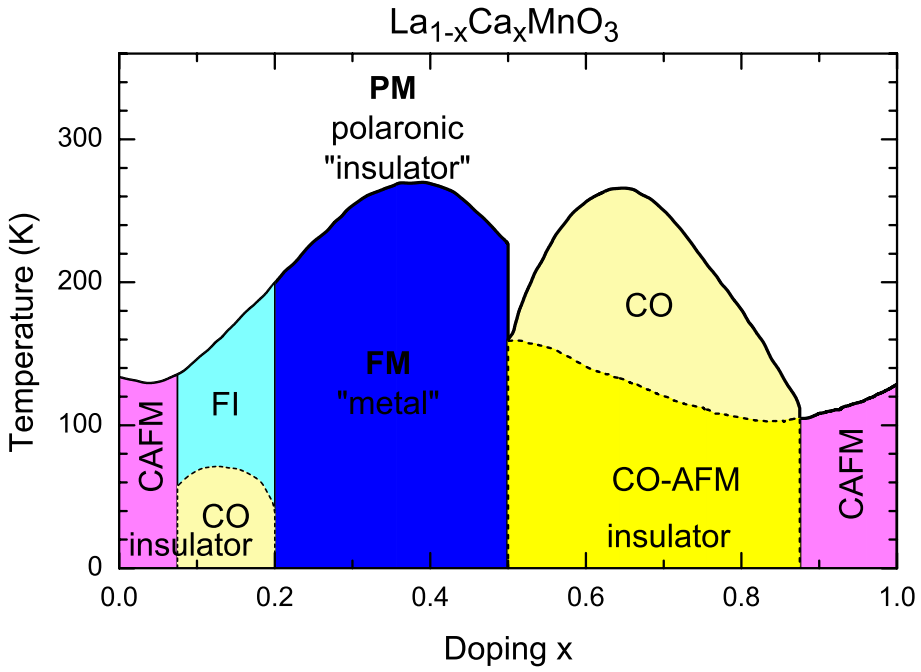

Figure 1.3: $La_{1-x}Ca_xMnO_3$ phase diagram after Ref. 20.

1.2.1 Crystal structure

The ortho-manganites crystallize in the pseudo-cubic perovskite structure shown schematically in Fig. 1.4 In the unit cell representation shown here, the trivalent rare-earth R^{3+} or divalent alkaline-earth A^{2+} occupies the body-center position and Mn ions occupy the vertices. Corner-sharing oxygen octahedra surround the Mn ions. The octahedral oxygen coordination introduces a crystal field splitting in the Mn d-levels discussed below.

Structural distortions, including cation disorder and the Jahn-Teller (JT) distortion, reduce the symmetry of the perovskite lattice from cubic to tetragonal. Cation disorder results in rotations of the oxygen octahedra and subsequent buckling of the Mn-O-Mn bonds. The resulting crystallographic space group is $Pbnm$. Figure 1.4(b) schematically represents the octahedral tilts (not to scale) for $Pbnm$ after Glazer.[22]

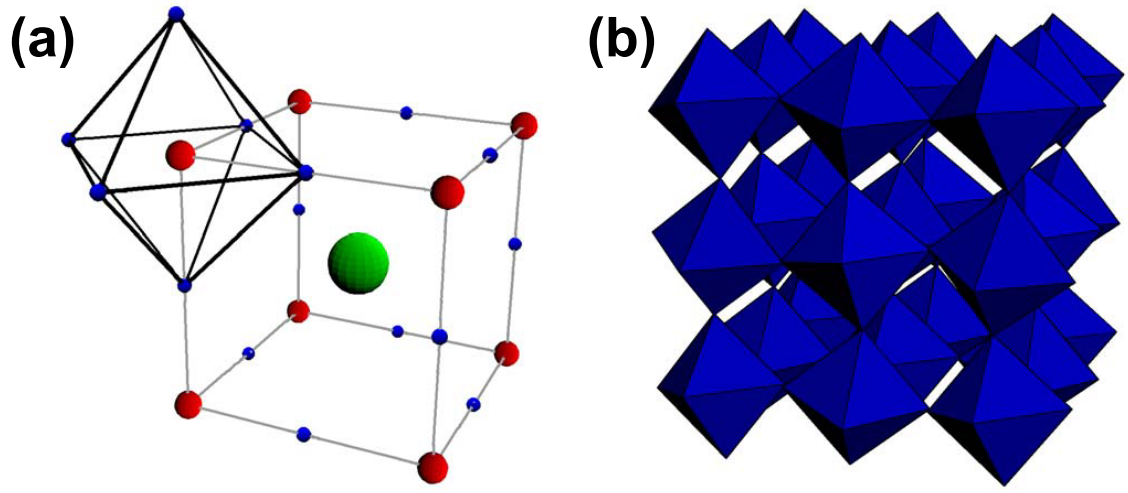

Figure 1.4: (a) Perovskite crystal structure. Mn, La, and O ions are represented (not to scale) by red, green, and blue spheres, respectively. (b) Schematic representation of tilting of the oxygen octahedra in the orthorhombic distortion.

The tolerance factor f quantifies[23] the deviations from pure cubic

$$f = \frac{r_{Mn} + r_O}{\sqrt{2}(r_{RE} + r_O)}, \tag{1.4}$$

where the r_i denote the ionic radii for Mn, O, and the average radius of the rare-earth and alkaline-earth in the bcc twelve-fold coordinated oxygen environment. $f \approx 1$ is a cubic lattice, $0.96 < f < 1$ is rhombohedral, and $f < 0.96$ is so-called $GdFeO_3$-type orthorhombic.[23] For the orthorhombic case, the Mn-O-Mn bond angle varies continuously with f. This bond-buckling plays a critical role in the hopping matrix elements important to transport properties discussed below. Hwang *et al*. studied changes in hopping as a function of R/A.

1.2.2 Magnetoresistance

In the doping region $0.2 < x < 0.5$, the ground state of $La_{0.7}Ca_{0.3}MnO_3$ is a ferromagnetic metal where $d\rho/dT > 0$. Above T_c, the material displays an activated temperature dependent resistivity. Evidently a metal-insulator transition is commensurate with the ferromagnetic to paramagnetic transition. The resistivity in the manganites

shows similarities with the magnetization in terms of a correlation in their temperature dependence. The remarkable phenomenon from which the hole-doped manganites derive their name is the observed magnetoresistance. Figure 1.5(a) shows the resistivity as a function of temperature for several different externally applied magnetic fields.[20] As the applied field increases, the resistivity drops dramatically and the re-

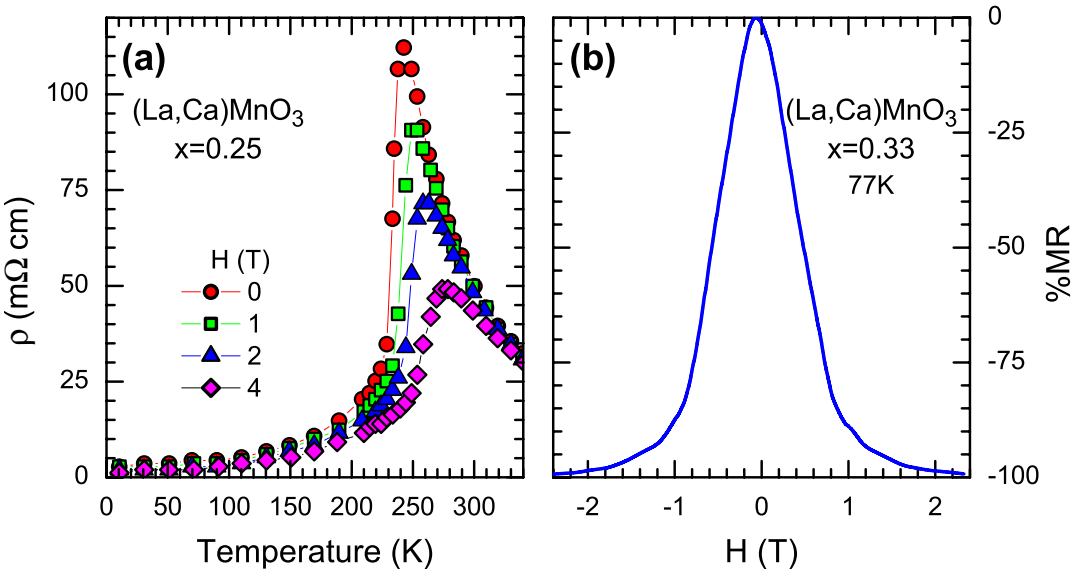

Figure 1.5: Magnetic-field dependent resistivity in (La,Ca)MnO_3 for $x \approx 0.3$. (a) Resistivity versus temperature for $x = 0.25$ at different applied magnetic field after Ref. 20. (b) Magnetoresistance as function of applied magnetic field for $x = 0.33$ after Ref. 18.

sistivity peak shifts to higher temperatures. Magnetoresistance is defined as

$$\mathrm{MR}(H) = \frac{\rho(H) - \rho(0)}{\rho(0)}, \tag{1.5}$$

where the decrease in resistivity in field [$\rho(H) < \rho(0)$] leads to a negative magnetoresistance. Figure 1.5(b) shows %MR as a function of applied field. The magnetoresistance exceeds 99 % for modest applied fields around a few Tesla. Large magnetoresistance effects may not be surprising.[3] Obviously ferromagnetic transitions are sensitive to the applied magnetic field. As the metal-insulator transition appears

commensurate with the magnetic phase transition, then it also displays a sensitivity to the applied magnetic field. Especially surprising is the localization mechanism for $T > T_c$. Understanding the origin of the insulating localization in the paramagnetic state proves to be an interesting problem.

1.2.3 Electronic structure

Mn d-electrons comprise the key players determining the electronic properties of the manganites. The number of electrons per Mn is $4 - x$. Hund's rule coupling implies that 3 electrons are localized on the t_{2g} orbitals forming a core spin of $S_c = 3/2$, while the remaining $1 - x$ electrons go into a band derived from the e_g orbitals. Each e_g electron contributes $S = 1/2$. A strong Hund's coupling constrains the spin of an occupied e_g orbital to align with the core spin, producing a total spin on a Mn^{3+} site of $S = 2$.

Qualitatively, ligand field theory provides the crystal field splitting of the Mn d-levels resulting from consideration of the surrounding oxygen ions as point charges. Figure 1.6(a) shows an energy diagram of crystal field splitting of the Mn d-levels. The

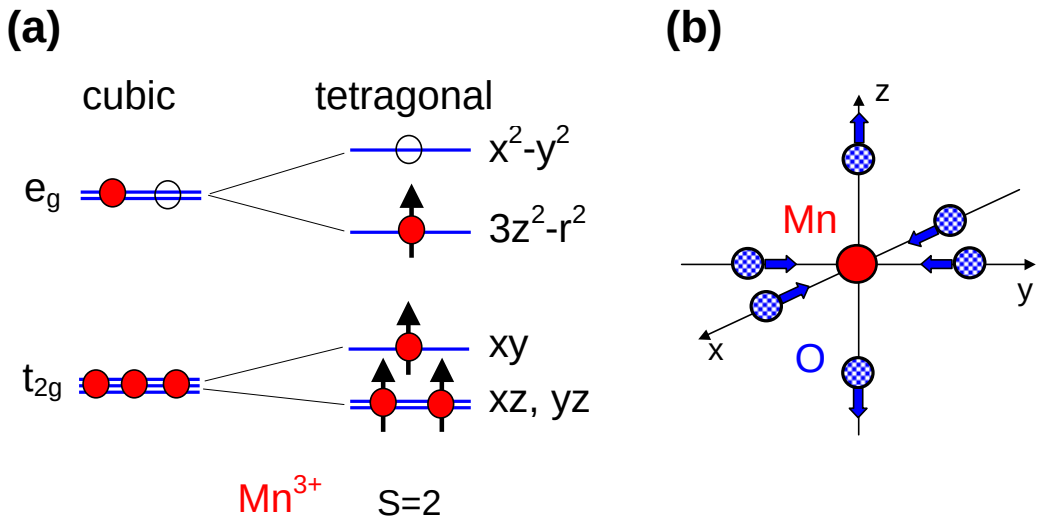

Figure 1.6: (a) Crystal field splitting of Mn d-levels resulting from cubic and tetragonal crystal fields. (b) Normal mode Q_3 of the Jahn-Teller distortion. Arrows represent displacements of the O ions.

quintuply degenerate Mn d-levels split in the cubic crystal environment into a lower t_{2g} triplet and an upper e_g doublet. The lobes of maximal probability of the lower-energy t_{2g} orbitals (d_{xz}, d_{yz}, d_{xy}) point away from both the apical and the equatorial oxygen ions. For the e_g orbitals ($d_{3z^2-r^2}$ and $d_{x^2-y^2}$), the lobes direct towards oxygens and hence these levels reside higher in energy. Tetragonal distortions, arising from cation disorder and the Jahn-Teller effect, introduce additional crystal field splitting of the degenerate e_g orbitals by an energy E_{JT} and partially lift the degeneracy of the t_{2g} orbitals. Figure 1.6(b) shows the Q_3 mode[24] of the Jahn-Teller distortion in $LaMnO_3$. In the hole-doped system, degenerate e_g levels on Mn^{4+} sites equally shift higher in energy by the breathing mode distortion E_B. Transitions to the unoccupied e_g orbital will be of prime importance to the observed optical spectrum presented in Chap. 3.

The double-exchange model (DE) first proposed by Zener[25] explains the metal-insulator phase transition in terms of the Mn d-electrons, namely, the strong Hund's coupling between the three electrons localized in the t_{2g} orbitals and the $1-x$ electrons in the e_g orbitals. The e_g electrons hop from Mn to Mn site providing alignment of the core spins. In this model, parallel alignment of the core spins maximizes the hopping probability between Mn sites for the electrons residing on the e_g orbitals, producing metallic conduction for $T < T_c$. Thus, ferromagnetic order favors hopping in the double-exchange picture.[26] The effective hopping interaction (neglecting the Berry phase of Anderson-Hasegawa[26]) is given by

$$t_{ij} = t_{ij}^0 \cos(\theta_{ij}/2)\,, \tag{1.6}$$

where t_{ij}^0 is the spin-independent hopping matrix element and θ_{ij} is the angle between neighboring spins. The hopping parameter given by Eq. (1.6) qualitatively describes the observed transport behavior. The increase of electron vacancies with hole doping affords hopping of the e_g electrons from Mn^{3+} to Mn^{4+} sites. At low temperatures, ferromagnetic alignment of the Mn spins maximizes the kinetic energy of the carriers

and stabilizes the ferromagnetic state.[23] As temperature increases above T_c, the spins order randomly and the effective hoping is reduced.

1.2.4 Jahn-Teller small polaron

While DE qualitatively describes the metal-insulator transition at T_c, recent experimental[27–29] and theoretical[30–33] work indicates the importance of coupling between charge carriers and the lattice, specifically the dynamic Jahn-Teller effect,[3,31,32] in explaining the high temperature insulating phase. The splitting of the e_g levels by the JT distortion is static for $0 < x < 0.2$ and dynamic for $x > 0.2$. Since the JT distortion is associated with the Mn^{3+} ions it can localize the e_g electrons in the paramagnetic phase of the alloys leading to insulating behavior, whereas the increased e_g band width in the ferromagnetic state quenches the JT effect and produces metallic conduction.

Localization of the e_g electron on the Mn^{3+} ions in the paramagnetic state of the doped manganites due to Jahn-Teller distortions is a self-trapping effect, *i.e.*, a small polaron.[32] Accompanying a localized small polaron resulting from electron-phonon coupling should be an optical signature associated with photo-induced hopping of the carriers, as has been reported in systems such as TiO_2.[34,35] Indeed early optical studies on $Nd_{0.7}Sr_{0.3}MnO_3$ report[28] evidence of a small polaron signature in the optical conductivity. Other experimental results also support the presence of strong electron-lattice interaction effects in these materials: (i) shifts in the IR phonon frequencies[36] related to the Mn−O bonds in $La_{0.7}Ca_{0.3}MnO_3$ near T_c, (ii) anomalies in the local structure of the MnO_6 octahedron near T_c obtained from neutron scattering studies[29] of $La_{1-x}Ca_xMnO_3$, (iii) magnetic-field driven structural phase transformation[37] in $La_{0.83}Sr_{0.17}MnO_3$, and (iv) disappearance of small polaronic behavior below the insulator-metal transition observed in thermopower measurements[38] of $La_{0.7}Ca_{0.3}MnO_3$.

Optical absorption studies[39,40] of the stoichiometric parent compound $LaMnO_3$ give evidence for static JT distortions. Analysis of the optical conductivity of $LaMnO_3$ within the local-spin-density approximation suggests that the observed gap in the optical conductivity of about $1.0\,\text{eV}$ corresponds to the optical process of promoting a hole between the JT split e_g bands on the Mn^{3+} ions.[41] Optical measurements have also been reported for the series of compounds $La_{1-x}Sr_xMnO_3$.[42–44] The results from optical reflectivity studies of metallic samples ($x > 0.2$) show large transfers of spectral weight from high frequencies to low frequencies as the samples cool from the paramagnetic state through T_c into the ferromagnetic metallic state.[42,43] These studies conclude that a simple DE picture does not explain the observed changes in the optical spectral weight over such a large energy scale compared to k_BT for all doping concentrations.[42,43]

1.3 Hexa-manganites and Multiferroic Behavior

Another class of manganite materials with a rare-earth ionic radius R^{3+} smaller than the orthomanganites (R=Ho, Er, Tm, Yb, Lu, Y, Sc, and In) crystallize in the hexagonal lattice. The hexagonal manganites generate interest as examples of multiferroic systems (or ferroelectromagnets),[45] which simultaneously display both magnetic and ferroelectric order parameters. In the case of the $LuMnO_3$, ferroelectricity occurs below the critical temperature[46] $T_c \gtrsim 900\,\text{K}$ and strongly frustrated antiferromagnetic order occurs below $T_N \approx 90\,\text{K}$. The coupling between ferroelectric and magnetic order parameters provides the prospect of manipulating electrical properties through magnetic fields and vice versa.[12,47] The capability of such manipulation in these compounds affords potential applications in novel “spintronic” devices.[4]

There exists several studies on the crystallographic structure[48–50] and on the magnetic structure[48,50–52] in hexa-manganites. Figure 1.7 illustrates a schematic view of the crystallographic structure of $LuMnO_3$.[49] The high-temperature paraelectric

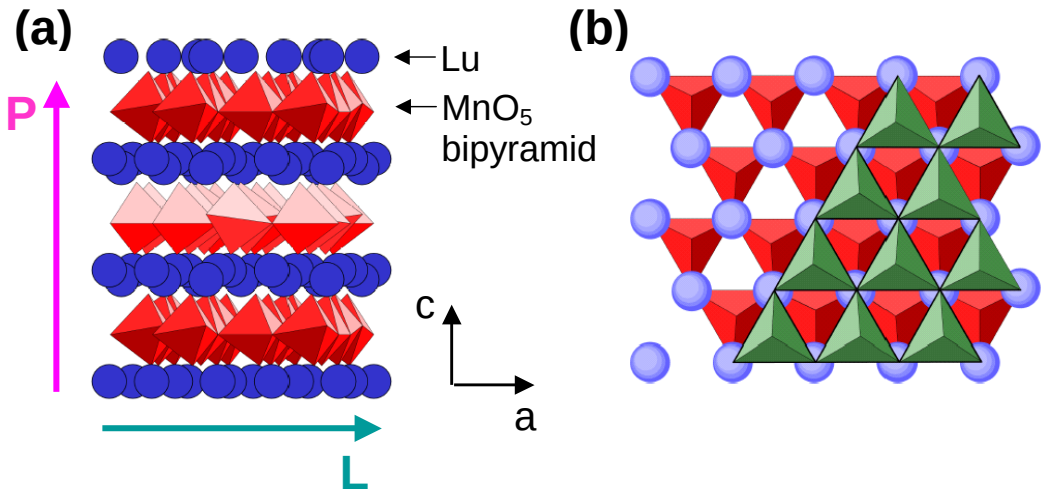

Figure 1.7: Schematic view of the $LuMnO_3$ crystallographic structure adopted from van Aken *et al.* (Ref. 49). Spheres represent Lu^{+3} ions and trigonal bipyramids represent MnO_5 clusters. (a) View along the basal plane. $\boldsymbol{P}$ and $\boldsymbol{L}$ indicate the c-axis ferroelectric order parameter and the in-plane antiferromagnetic order parameter, respectively. (b) View along the c-axis of two layers illustrating the alternate stacking of MnO_5 bipyramids.

phase in the hexagonal manganites consists of layers of corner-sharing MnO_5 triangular bipyramids separated by a layer of Lu-ions. The bipyramids alternate stacking between layers, as shown in Fig. 1.7(b). In the ferroelectric phase below T_c, R-ions alternate their c-axis coordinates, producing a net electric moment $\boldsymbol{P}$ of the unit cell, and the MnO_5 pyramids tilt away from the c-axis, as shown in Fig. 1.7(a). Bertaut *et al.*[48] report $P \approx 3\,\mu\text{C cm}^{-2}$.

Below T_N, the Mn spins order antiferromagnetically in the basal plane.[50–52] The in-plane antiferromagnetic order parameter given by $\boldsymbol{L}$ [Fig.1.7(a)] characterizes this ordering. Spin frustration in the triangular planar lattice and a weak inter-plane exchange interaction result in a Néel temperature $6 - 10$ times smaller than the Curie-Weiss temperature θ_{CW}. Neutron powder diffraction[50,51] finds the spins order in a $120°$ structure. Nonlinear optics, specifically second harmonic generation (SHG), provides additional information regarding the sign of the inter-plane coupling and the spin orientation angle ϕ. A schematic view of the magnetic structure is illustrated in

Fig. 1.8(a). Filled and hatched circles represent the Mn spins in the $z = 0$ and $z = c/2$

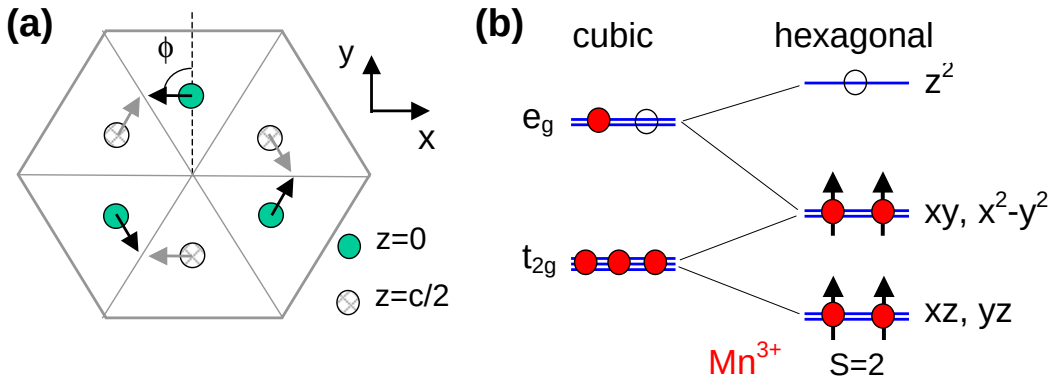

Figure 1.8: Magnetic structure and crystal-field splitting. (a) Mn spin projections in the ab-plane. Filled (hatched) circles represent Mn ions in the $z = 0$ ($z = c/2$) plane. The angle ϕ specifies spin orientations relative to the hexagonal face normal. (b) Splitting of the Mn^{3+} d-levels in cubic and hexagonal crystal-fields.

planes, respectively. The $\phi = 90°$ and inter-plane ferromagnetic spin configuration is shown, consistent with SHG observations.[52]

The trigonal bipyramid of five O^{2-} ions surrounding the Mn^{3+} produces a hexagonal crystal-field splitting of the quintuply-degenerate Mn d-orbitals into three groups in order of increasing energy: $d_{xz,yz}$, $d_{xy,\,x^2-y^2}$, and $d_{3z^2-r^2}$. Figure 1.8(b) illustrates this crystal-field splitting from cubic to hexagonal for the trivalent Mn ion. The out-of-plane orbitals $d_{xy,yz}$ directed away from the apical oxygens have the lowest energy, owing to their small overlap with O orbitals. Next highest in energy, the in-plane $d_{xy,\,x^2-y^2}$ orbitals strongly hybridize with oxygen p-orbitals. Finally, the $d_{3z^2-r^2}$-orbital has the highest energy resulting from the shorter Mn to apical-O bond lengths. In the ground state of the Mn^{3+} ion, four electrons occupy the four lowest orbitals giving $\langle L \rangle = 0$ and $S = 2$. The $d_{3z^2-r^2}$ orbital remains empty in the ground state. Transitions to this unoccupied orbital will be of prime importance to the observed optical spectrum presented in Chap. 4.

Several groups report anomalous behavior in transport and magnetic suscepti-

bility at temperatures correlated with T_N. Of particular interest is the observation[53–56] of a temperature anomaly of the quasi-static dielectric constant ϵ_0 below T_N. Figure 1.9 shows the quasi-static dielectric constant of Katsufuji *et al.*[53] taken at 100 kHz. The anomaly occurs around T_N for the in-plane response only. These anomalies are

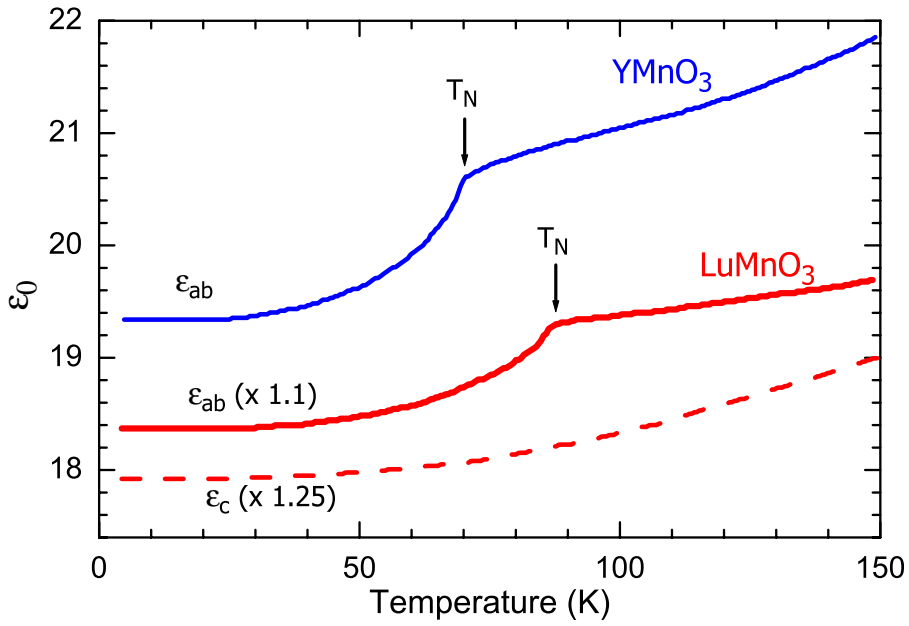

Figure 1.9: Anomaly in the temperature dependence of the quasi-static dielectric constant of hexagonal manganites $LuMnO_3$ and $YMnO_3$ after Ref. 53. Anomaly appears around T_N for the in-plane response only.

cited[45,53,54,57] as evidence of the coupling between the ferroelectric and magnetic order parameters. Theoretically, an expansion of the Landau free energy F in terms of the FE and AFM order parameters P and l, respectively, predicts[45] the anomaly. Performing this expansion results in a generic coupling term of the form $\delta F \propto \gamma P^2 l^2$, where the coefficient γ depends on symmetry and the microscopic physics. From both theoretical and applied prospectives, the manifestations of order parameter coupling are of great interest. However, the appearance of the ϵ anomaly is a necessary but not sufficient condition for order parameter coupling.[45] The dynamical response measured in optics offers a powerful tool to identify contributions to the static dielec-

tric constant and to further understand the realization of order parameter coupling in this multiferroic manganite.

1.4 Ferromagnetism in Dilute Semiconductors/Oxides

1.4.1 Dilute magnetic semiconductors

Dilute magnetic semiconductors (DMS) offer a possible system to realize control of the charge transport by using the spin degrees of freedom.[4,58] The integration of a "spintronic" material with existing semiconducting architecture opens possibilities of linking nonvolatile magnetic storage and processing in a single device. DMS consist of magnetic impurities doped in a semiconducting host (e.g., Mn-doped GaAs). Figure 1.10 illustrates a schematic for DMS. Panel (a) shows a nonmagnetic semi-

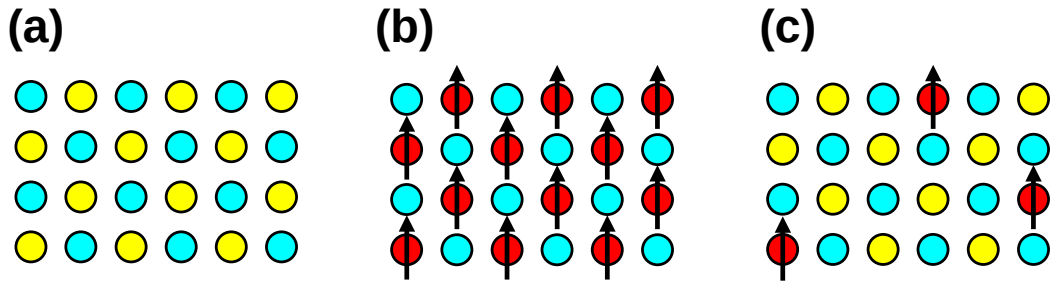

Figure 1.10: Schematic representation of doping semiconductors with magnetic impurities after Ref. 58. (a) A diatomic (*e.g.*, GaAs) semiconductor with no magnetic impurities. (b) A magnetic semiconductor with a periodic array of magnetic elements. (c) A diluted magnetic semiconductor doped with a small concentration of magnetic impurities.

conducting (diatomic) host background. Traditional magnetic semiconductors (*e.g.*, europium chalcogenides) consist of a regular array of magnetic ions incorporated in the lattice represented in panel (b). On the other hand, diluted magnetic semiconductors consist of only a small concentration, typically $\lesssim 0.1$, of magnetic impurities doped in the semiconducting background as illustrated in panel (c). Such materials undergo a ferromagnetic phase transition below the Curie temperature, where for

Mn-doped GaAs $T_c \lesssim 150\,\mathrm{K}$.

Various theoretical models have been posited to explain the presence of magnetic order in these dilute systems including: (i) Ruderman-Kittel-Kasuya-Yoshida[59] (RKKY), (ii) mean field theory,[60] (iii) spin wave,[61] (iv) double-exchange,[62] and (v) double resonance.[63] A summary description of several of the models follows.

In the RKKY[59] picture, itinerant carriers provide an indirect exchange mechanism between localized spins on the dilute magnetic ions. The local impurities polarize nearby itinerant carriers. Adjacent localized impurities experience this polarization and effectively align. RKKY is a second order perturbation theory applicable only when the magnetic ions produce a small perturbations of the itinerant carrier dynamics, *i.e.*, a small exchange coupling relative to the carrier kinetic energy. This condition is not satisfied in DMS.[61] Moreover, RKKY neglects the dynamics of free carriers.

The mean-field theory (MFT) considers the local moments sitting in an effective external field generated by the mean polarization of the itinerant charge carriers. This effective field represents an Ising limit of exchange coupling. A minimization of the Ginzburg-Landau free energy[64] determines the critical temperature. MFT finds an increase of T_c with narrowing free carrier bands, increasing hole density, or moving E_f to peaks in the density of states. Dietl *et al.*[64] predict T_c for various DMS systems using the mean-field method. MFT neglects correlations between local-moment spins and the free carrier response and therefore cannot predict long-wavelength spin excitations.

Neither RKKY nor mean-field approximation to kinetic-exchange model adequately describe the ferromagnetism.[61] The spin-wave model describes the elementary spin-wave excitations and accounts both for itinerant-carrier spin splitting and dynamical correlations. Spin-splitting vanishes at the transition temperature, so both RKKY and MFT work well at estimating T_c.

No single theory appears capable of explaining the range of Curie temperatures for the various carrier densities in DMS systems. At present, theoretical understanding of the exact nature of ferromagnetism in DMS materials remains uncertain.

1.4.2 Co-doped TiO_2

While the initial possibilities of DMS appear promising, practical applications demand a T_c above room temperature. Therefore, the recent discovery of ferromagnetism with $T_c > 300\,\mathrm{K}$ in cobalt-doped TiO_2 has generated considerable interest in this system and similar dilute magnetic oxides.[65] Co-doped TiO_2 offers a particularly interesting system owing to its high Curie temperature, *n*-type carriers (as opposed to hole carriers in typical DMS), and large optical gap conducive for opto-electronic devices.

High-temperature magnetization measurements using vibrating sample magnetometry[66] find a $T_c \gtrsim 1180\,\mathrm{K}$ for $x = 0.07$ doped $Ti_{1-x}Co_xO_{2-\delta}$, nearly that of bulk Co ($T_c = 1404\,\mathrm{K}$). Such a large T_c suggests that cobalt appears in clusters and that the magnetism results from this clustering rather than a new dilute magnetic oxide. Indeed several groups report additional evidence of cobalt clustering.[66–68] A careful doping-dependent study of films grown by pulsed laser deposition (PLD) reports[66] a limited solubility of cobalt in $Ti_{1-x}Co_xO_{2-\delta}$ above a concentration of $x \sim 0.02$, with Co clustering beginning thereafter. Post-growth annealing in an O_2 environment or high-temperature deposition increases the Co solubility[66] and suggests the importance of growth conditions to clustering. Co-doped systems showing no evidence[66] for clustering exhibit a $T_c \approx 700\,\mathrm{K}$. The existence of such a high T_c for a dilute magnetic system without Co clustering remains puzzling. Thus, further measurements to elucidate the electronic structure and resolve the nature of the magnetism are warranted.

Shinde *et al.*[66] report high-temperature magnetization measurements using

vibrating sample magnetometry (VSM). Figure 1.11 shows the magnetization versus temperature data. The as-grown $x = 0.07$ sample (squares in Fig. 1.11) exhibits a

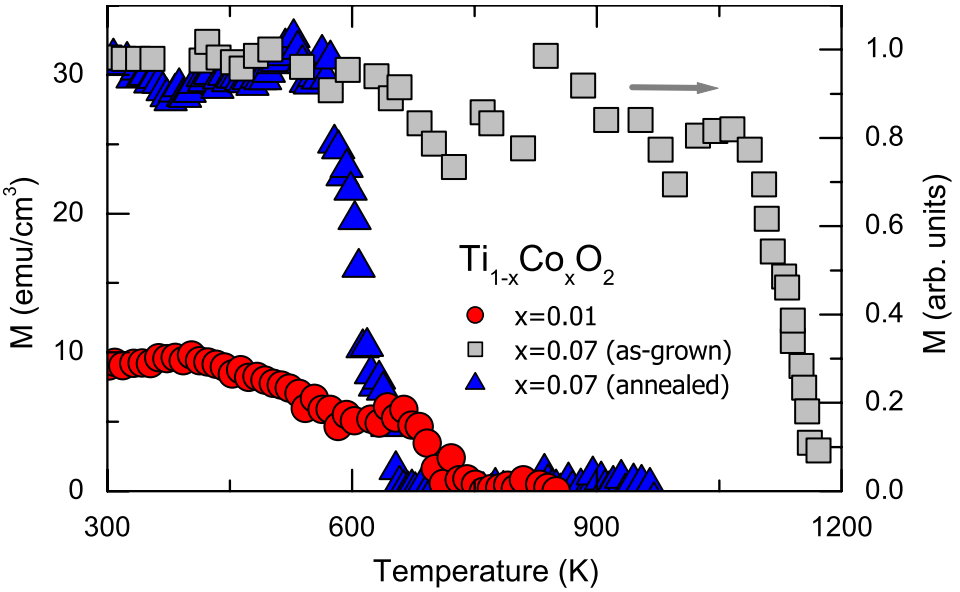

Figure 1.11: Magnetization as a function of temperature obtained from vibrating sample magnetometry measurements for $Ti_{1-x}Co_xO_{2-\delta}$ $x = 0.01$ and 0.07 as-grown and annealed.

clear transition around 1200 K, approaching the T_c of Co metal (1388 K). Such a high T_c suggests the presence of metallic Co clusters.[66] In addition to a T_c near bulk Co, this as-grown sample exhibits a precursive dip beginning around 650 K. A subsequent measurement of the $x = 0.07$ sample after the initial high-T VSM treatment (triangles) displays a lower T_c, near the precursive onset and similar to the T_c of the low-doped material. This behavior suggests the high-temperature measurement anneals the sample and that this treatment may reduce Co clusters. Figure. 1.11 also shows magnetization for a $x = 0.01$ sample (circles). This low-doped sample exhibits a $T_c \approx 700$ K similar to that of the precursive dip and much lower than either the $x = 0.07$ sample or bulk Co metal. Moreover, the T_c for low-doped samples, though well above room-T, is much lower than T_c of bulk Co.

High-resolution transmission electron microscopy (TEM) provides direct evi-

dence for cobalt clusters. Figure 1.12 shows a cross-sectional dark field TEM image of $Ti_{0.93}Co_{0.07}O_{2-\delta}$ after Ref. 66. Five clusters with diameters $\approx 20 - 50$ nm are easily

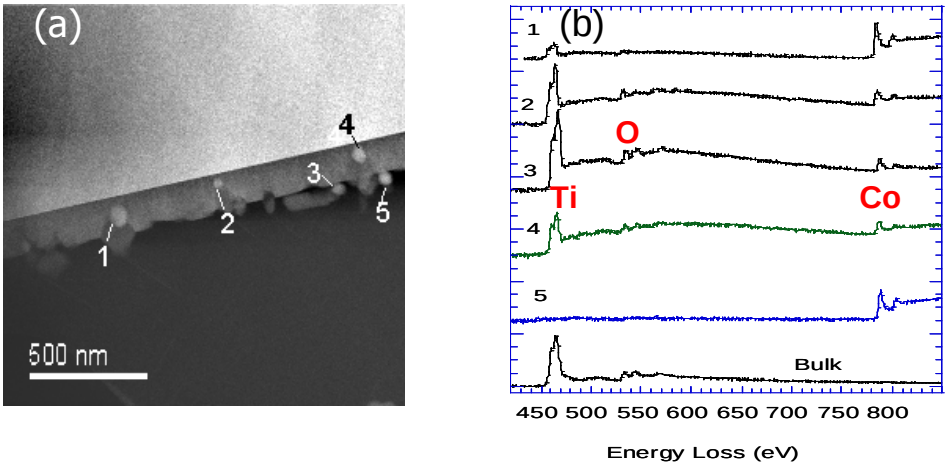

Figure 1.12: $Ti_{0.93}Co_{0.07}O_{2-\delta}$(a) Cross-section TEM dark field image with five clusters identified. (b) EELS data in the corresponding numbered regions reveals the clusters consist of cobalt.

visible in the micrograph. Electron-energy-loss spectra (EELS) of the corresponding clustered regions confirm a large concentration of Co in these clusters,[66] which is not present in the bulk. Several of the clusters also show the presence of Ti and O. However, Cluster #5, located near the surface, lacks the Ti or O signature, which suggests the presence of Ti and O in the other clusters originates from proximity to the bulk TiO_2.

The experimental evidence of Co clustering in $Ti_{1-x}Co_xO_{2-\delta}$ and the sensitivity to growth conditions raise concerns regarding the intrinsic nature of magnetism. However, the observation[66] of ferromagnetism with a high T_c in well-studied systems showing no evidence of Co clustering offers promise for this dilute magnetic oxide. Clearly further studies are warranted to explain the large T_c in these systems.

1.5 Outline of Forthcoming Chapters

The forthcoming chapters present the results of optical studies on the magnetic transition metal oxides introduced above. Chapter 2 discusses experimental details

of the optical measurements, including newly developed techniques for the extraction of optical constants from thin films and bulk samples. Chapter 3 presents optical measurements on the orthorhombic phase manganites $R_{1-x}A_x\mathrm{MnO}_3$, beginning with the lanthanum manganite parent compound ($x = 0$). Alloys around optimal CMR doping ($x = 0.3$) are studied in detail both in the spectral region of electronic transitions and in the far-infrared region of Drude-like conduction. Changing rare-earth ion to Lu affords investigation of manganites in the hexagonal phase. Chapter 4 presents optical studies on the multiferroic hexa-manganite LuMnO_3. These studies address spin-phonon coupling and exchange interaction effects on the electronic properties. Diverging from the manganites to the diluted magnetic oxides, Chap. 5 presents the first optical conductivity results on cobalt-doped titanium dioxide. Finally, Chapter 6 offers concluding remarks and suggests future optical studies on these strongly correlated transition metal oxides.

Chapter 2

Experimental Methods

Extraction of the commonly named “optical constants” comprises the main goal of the experimental techniques described in this chapter. For typical material systems, these quantities are not really constant, but rather exhibit dependence on frequency, temperature, magnetic field, and perhaps other experimental parameters. Hence, the term optical coefficients more appropriately describes these intrinsic material properties. Identifying changes with various controllable experimental parameters provides important insight into the electronic, magnetic, and structural properties of these materials via comparison with the predictions of theoretical models, *e.g.*, band structure calculations. While measuring the optical constants directly often proves difficult, they may be extracted from other measurements, *e.g.*, transmittance and reflectance of thick film or bulk samples. Fourier transform infrared (FTIR) spectroscopy offers the capability of determining the frequency response of the optical coefficients over a wide spectral range.

The following sections introduce the basic principles of FTIR spectroscopy and their implementation in a specific instrument design. Other experimental apparatus and methods required for temperature dependent optical studies are discussed. In addition, relations between the optical coefficients and optical sum rules are addressed. Finally, this chapter presents methods for extracting the optical coefficients from experimental measurements on specific sample configurations.

2.1 Principles of FTIR Spectroscopy

Many different types of available spectrometers and spectroscopic techniques exist, which provide spectral measurements over a range of frequencies covering the infrared (IR) to ultraviolet (UV). Two of the more popular instruments are Fourier transform infrared (FTIR) spectrometers and grating monochromators. FTIR offers advantages in multiplexing[69] and throughput,[70] particularly important at long wavelengths. Among FTIR spectrometers, several instrument designs are available.[71] This section addresses the popular Michelson[72] interferometer design.

Figure 2.1 illustrates a schematic of the Twyman-Green version of the classic Michelson interferometer. Collimated light (represented with rays) emitted from a

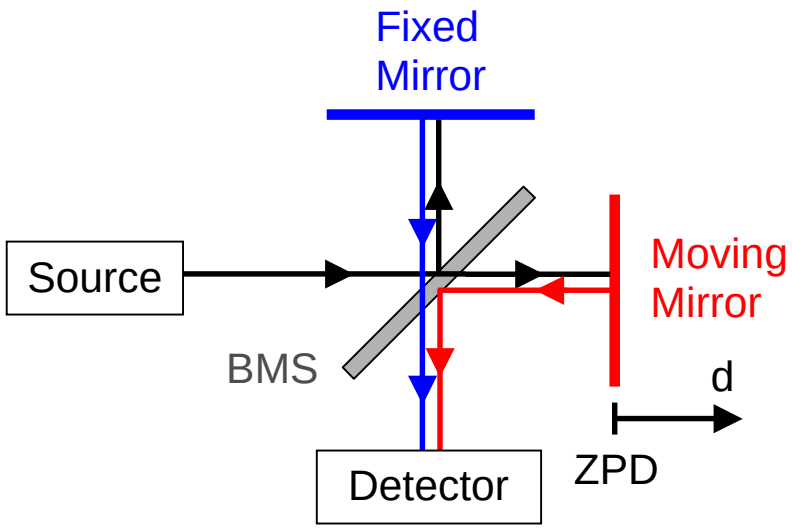

Figure 2.1: Schematic of a Michelson interferometer.

broad-band optical source impinges upon a half-silvered beamsplitter (BMS), which ideally transmits $50\,\%$ and reflects $50\,\%$ of the incident light intensity. The transmitted and reflected beams travel to a moveable and a fixed mirror, respectively. The moving mirror travels a distance d from zero path difference (ZPD) and the corresponding optical path length is $x = 2\,d$. These two beams then interfere upon recombination. The recombined beam is then focused onto the detector. The optical

paths reflected/transmitted back to the source have been omitted from Fig. 2.1 for simplicity. The detector signal varies as the optical path length or relative phase of the two detector beams changes. A maximum signal results for the constructive interference at ZPD. As the moving mirror translates the relative phase of the two beams changes and the detector records a signal that varies in time. The time-varying signal represents the Fourier transform of the original source intensity and is termed an interferogram.

The phase difference $\Delta\theta$ of the recombined beams is given by

$$\Delta\theta = 2\pi\,\nu\,x\,, \tag{2.1}$$

where x is the optical path distance from ZPD and ν is the frequency of the source in inverse length units or wavenumbers ($8.066\,\mathrm{cm}^{-1} = 1\,\mathrm{meV} = 1.240\,\mathrm{mm}$). The amplitudes of the electric fields for the two different paths may be represented by E_1 and $E_2\,\mathrm{e}^{-\mathrm{i}\,\Delta\theta}$ where the amplitude for the second beam (moving mirror) has the additional phase factor $\Delta\theta$ included. Beamsplitters consisting of a half-silvered film on a supporting substrate require an identical substrate be placed as a compensator (not shown in Fig. 2.1) such that both beams undergo equal paths through the BMS. Beam one consists of a reflection r and transmission t from the BMS giving $r\,t$, while beam two interacts with the BMS in reverse order $t\,r$. Even for an imperfect BMS, $t \neq r$ and/or finite absorption, the two recombined beams have equal amplitudes, *i.e.*, $E_1 = E_2 = r\,t\,E_0$, where E_0 is the amplitude of the incident light. A sum of the two separate beam amplitudes gives the total amplitude at the detector

$$E_{det}(x,\nu) = E_1(\nu) + E_2(\nu)\,\mathrm{e}^{\mathrm{i}\,\Delta\theta(x,\nu)} = r\,t\,E_0(\nu)\,(1 + \mathrm{e}^{\mathrm{i}\,2\pi\,\nu\,x})\,. \tag{2.2}$$

The detectors measure the light intensity, which for a given wavelength ν is given by

$$I(x,\nu) = \frac{c}{4\pi}\,|E_{det}(x,\nu)|^2 = 2|r\,t|^2 S(\nu)[1 + \cos(2\pi\,\nu\,x)]\,. \tag{2.3}$$

Here $S(\nu) = |E_0(\nu)|^2$ represents the power spectrum or spectral density function of the incident source. By superposition, the total signal at the detector for a broadband source results from an integration over all frequencies

$$I_{det}(x) = \frac{2|r\,t|^2}{\bar{\nu}} \left[\int_0^\infty S(\nu)\,\mathrm{d}\nu + \int_0^\infty S(\nu)\cos(2\pi\,\nu\,x)\,\mathrm{d}\nu \right]$$
$$\equiv \frac{1}{2}\,I(0) + I_{int}(x)\,, \tag{2.4}$$

where $\bar{\nu}$ represents an average frequency from the integration and $I_{int}(x)$ is the interferogram. The total signal intensity on the detector consists of a cosine Fourier transform of the incident light and varies with the position of the moving mirror x. Translation of the moveable mirror transforms the frequency spectrum of the source into a positional or temporal spectrum ($t = x/v$, where v is the mirror speed).

Recovering the original power spectrum requires only an inverse fourier cosine transform of the interferogram signal. The original source power spectrum is given by

$$S(\nu) = \frac{\bar{\nu}}{\pi|r\,t|^2} \int_0^\infty I_{int}(x)\,\cos(2\pi\,\nu\,x)\,\mathrm{d}x\,. \tag{2.5}$$

Modern computers utilizing fast-fourier transform (FFT) algorithms[73] calculate the inverse transform in nearly real time.

Fourier transform spectrometers offer advantages over grating or slit spectrometers in terms of multiplexing (Fellgett[69] advantage) and throughput (Jacquinot[70] advantage). The multiplexing advantage results from the FTIR spectrometer *simultaneously* modulating the entire spectrum. For comparison, consider a grating spectrometer requiring m frequency intervals to cover a spectral range with frequency resolution $\Delta\nu$. If each frequency interval requires a time τ to measure with a specified signal-to-noise ratio (S/N), then $T = m\,\tau$ represents the total scan time. A FTIR spectrometer with similar throughput produces the entire spectrum in time τ with equal S/N. Thus, the same total time T affords m repetitions of the FTIR spectrum, for a statistical improvement in S/N of $\sqrt{m}$. For $\Delta\nu = 1\,\mathrm{cm}^{-1}$ and $\nu_{max} = 10000\,\mathrm{cm}^{-1}$,

the advantage is a factor of 100. Note the multiplex advantage exists only whenever the noise is independent of the intensity of the source, *i.e.*, detector limited noise. Such conditions occur in the IR frequency range, but tend to diminish in the visible where the photon counting noise is proportional to the square root of power.

FTIR provides an additional advantage over grating spectrometers in terms of throughput. Étendue, $\mathcal{E} = \Omega A$, describes the spectrometer throughput, where Ω is the solid angle of the light beam and A is the cross-sectional area of the collimating optic. A finite source aperture size results in divergence of the collimated beam. The maximum half angle α that preserves phase information between the on-axis and edge beams is given by $\alpha^2 \approx 2\Delta\nu/\nu$ and the resulting solid angle $\Omega \approx \pi\alpha^2$. So the étendue for a FTIR spectrometer is $\mathcal{E} = 2\pi\Delta\nu/\nu A$. For a grating spectrometer, the solid angle is given by $\Omega_s = L w/f^2$ where L and w are the slit length and width, respectively, and f is the focal length. The ratio of the slit width to the focal length determines the frequency resolution, $w/f \approx \Delta\nu/\nu$. For equal area collimating optics and frequency resolution, the étendue ratio of the grating to FTIR spectrometer is $L/(2\pi f)$. A typical grating spectrometer with $L \approx 0.1\,\text{cm}$ and $f \approx 30\,\text{cm}$ gives a throughput advantage to the FTIR spectrometer of about 1800.

Although FTIR inteferometers offers several advantages over grating instruments, spectroscopists must be careful to avoid errors associated with asymmetrical interferograms, apodization, and aliasing. The inverse cosine transform produces the correct power spectrum for symmetrical interferograms. For an ideal interferometer, beamsplitters provide no dispersion and finite sampling of the interferogram exactly includes ZPD. In practice the occurrence of both types of errors results in asymmetrical interferograms. Such asymmetrical interferograms require a phase correction to yield the correct spectrum. The phase function Θ is given by

$$\Theta(\nu) = \tan^{-1}\left(\frac{\Im m\{\mathscr{F}(\nu)\}}{\Re e\{\mathscr{F}(\nu)\}}\right), \tag{2.6}$$

where $\mathscr{F}(\nu)$ is the Fourier transform of the interferogram. The acquisition of Θ allows symmetrization of the interferogram prior to performing FFT to recover the power spectrum.

In addition to phase errors, real spectrometers scan only over a finite distance, truncating the acquired interferogram. Abrupt truncation in the moving mirror position introduces spurious side lobes near sharp features. Such features may be diminished by applying, at the expense of spectral resolution, tapering or apodizing functions. Table 2.1 lists several of the more common apodizing functions, where $\tilde{x} = x/x_{max}$

Name	Function	W/W_0	h/h_0
Boxcar	1	1.00	1.000
Bartlett	1-$\tilde{x}$	1.47	0.217
Hamming	$0.53856 + 0.46144\ \cos(\pi\,\tilde{x})$	1.51	0.032
Blackman-Harris	$0.42323 + 0.49755\ \cos(\pi\,\tilde{x}) + 0.0792\ \cos(2\,\pi\,\tilde{x})$	1.88	0.001
Weak	$0.548 - 0.0833(1-\tilde{x}^2) + 0.5353(1-\tilde{x}^2)^2$	1.20	0.267
Medium	$0.261 - 0.154838(1-\tilde{x}^2) + 0.894838(1-\tilde{x}^2)^2$	1.40	0.065
Strong	$0.09 + 0.5875(1-\tilde{x}^2)^2 + 0.3225(1-\tilde{x}^2)^4$	1.60	0.017

$\tilde{x} = x/x_{max}$ is the normalized optical path difference.

Table 2.1: Apodizing functions available in the Bomem DA3 PCDA software.

represents the path length difference between the two Michelson arms and x_{max} is the maximum path length difference. In addition to the functional form of the apodizing functions, Table 2.1 includes the half-width W and height of the largest secondary (not necessarily first) maximum h normalized to the respective values W_0 and h_0 of the sinc function, $\mathrm{sinc}(\nu) \equiv \sin(\nu)/\nu$. For sinc, W_0 corresponds to $0.3017/x_{max}$ and h_0 corresponds to 0.1284. Whenever the width of the measured spectral features exceeds several cm^{-1}, relevant for most of the broad band spectroscopy performed in this work, smoothing apodization functions such as Hamming or Strong[74] suite well. For étalon experiments or resolving narrow phonon modes, no apodization (Boxcar) or Weak[74] apodizing functions are more appropriate. Figure 2.2 shows the apodizing functions listed in Table 2.1. Panel (a) shows the functional form of the

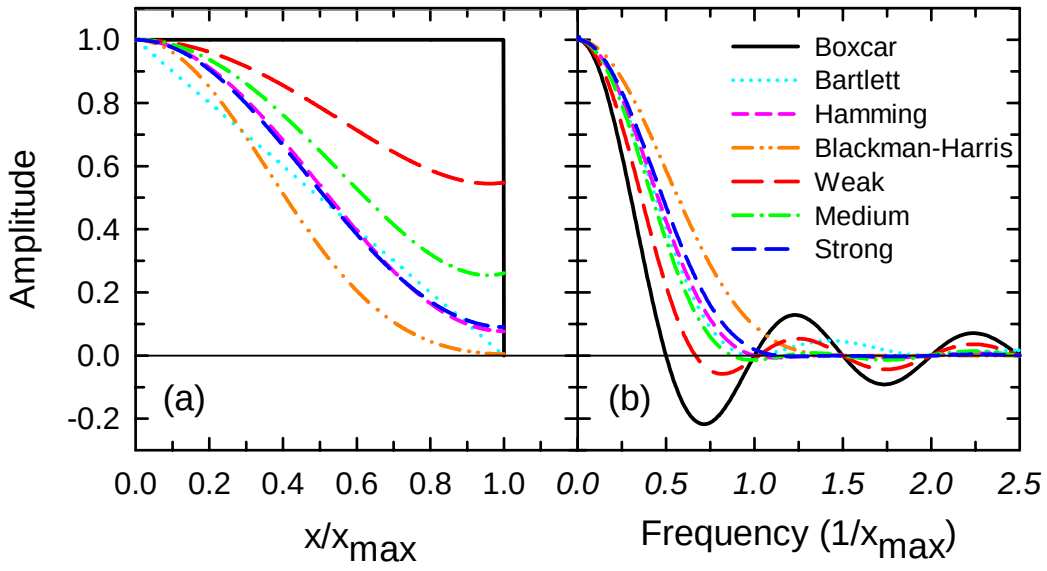

Figure 2.2: Apodization (a) functions and (b) resulting instrument line-shapes.

apodization functions and panel (b) shows the resulting instrument line shapes (ILS) for a theoretical monochromatic source. Note that boxcar apodization produces a sinc function ILS. Other apodizing functions have reduced secondary maxima at the expense of wider widths, as evidenced in the figure. Norton and Beer[74] generated the Weak, Medium, and Strong apodizing functions to produce the optimal h/h_0 for a given W/W_0 (see Filler diagram plotted in Fig. 1 of Ref 74).

In addition to errors introduced by apodization, care must be taken to avoid aliasing associated with a finite sampling of the interferogram. Data points in the interferogram are sampled at equal intervals of phase difference Δx up to the maximum path difference x. The sampling theorem of Nyquist[75] specifies the minimum Δx for a given maximum frequency in the power spectrum ν_{max}. For a power spectrum limited in frequency to $\nu \leq \nu_{max}$, the optimum sample spacing is given by $\Delta x = 1/(2\,\nu_{max})$. The replacement of the continuous Fourier transform of Eq. (2.5) with a discrete Fourier series results in a transformed spectrum with both mirror and translational symmetry[75] about a "folding" frequency $1/(2\,\Delta x)$. Thus, any real intensity in the power spec-

trum above ν_{max} folds back into the transformed spectrum and introduces errors in the interferogram signal. In practice, filtering of undesired frequencies avoids these aliasing problems. Suitable filtering techniques include numerical, electrical, or optical filtering. Numerical filtering, though easiest to employ, tends to introduce spurious effects at the frequency cutoffs. Electrical filtering of the detector signal proves difficult due to complications designing programmable, sharp bandwidth electrical filters. Physically truncating the spectrum with optical filters or the intrinsic frequency bandwidth of the various optical elements provides the safest means to avoid aliasing errors.

2.2 Apparatus

2.2.1 FTIR spectrometer

Several companies produce laboratory grade FTIR spectrometers based on the Twyman-Green implementation of the Michelson inferometer, including ABB-Bomem and Bruker Optics. ABB-Bomem (Québec, Canada) manufactures the DA3.02 FTIR spectrometer (referred to hereafter as the DA3) utilized in the optical measurements presented herein. The DA3 offers spectral resolution from 64-$0.04\,\mathrm{cm}^{-1}$ over a frequency range from approximately 10-$50000\,\mathrm{cm}^{-1}$ using a variety of sources, beamsplitters, and detectors (described below). This spectrometer design employs a continuous scanning motor (as compared to a stepper motor) capable of mirror speeds from 0.01-$4.6\,\mathrm{cm/s}$ $\pm 0.5\%$. Scan times for a single trace range between seconds to minutes depending on the required frequency resolution, mirror velocity, and detector response time. A novel dynamical alignment (described below) of the “fixed mirror” provides accurate, $\leq 1\,\mu$radian, RMS tilt over the full scanning mirror displacement. The DA3 spectrometer system manual[76] provides additional specifications and operation details. In addition to the spectrometer, a vector processor performs fast Fourier transform (FFT) of the measured interferogram and provides an interface be-

tween the DA3 and a controlling personal computer (pc). The pc affords instrument control and data acquisition via the software program PCDA. Details of the software program are provided in the PCDA users manual.[77]

Figure 2.3 shows a schematic of the optical beam path for the DA3 spectrometer. Starting from the top of Fig. 2.3, an off-axis ellipsoidal Al mirror focuses light

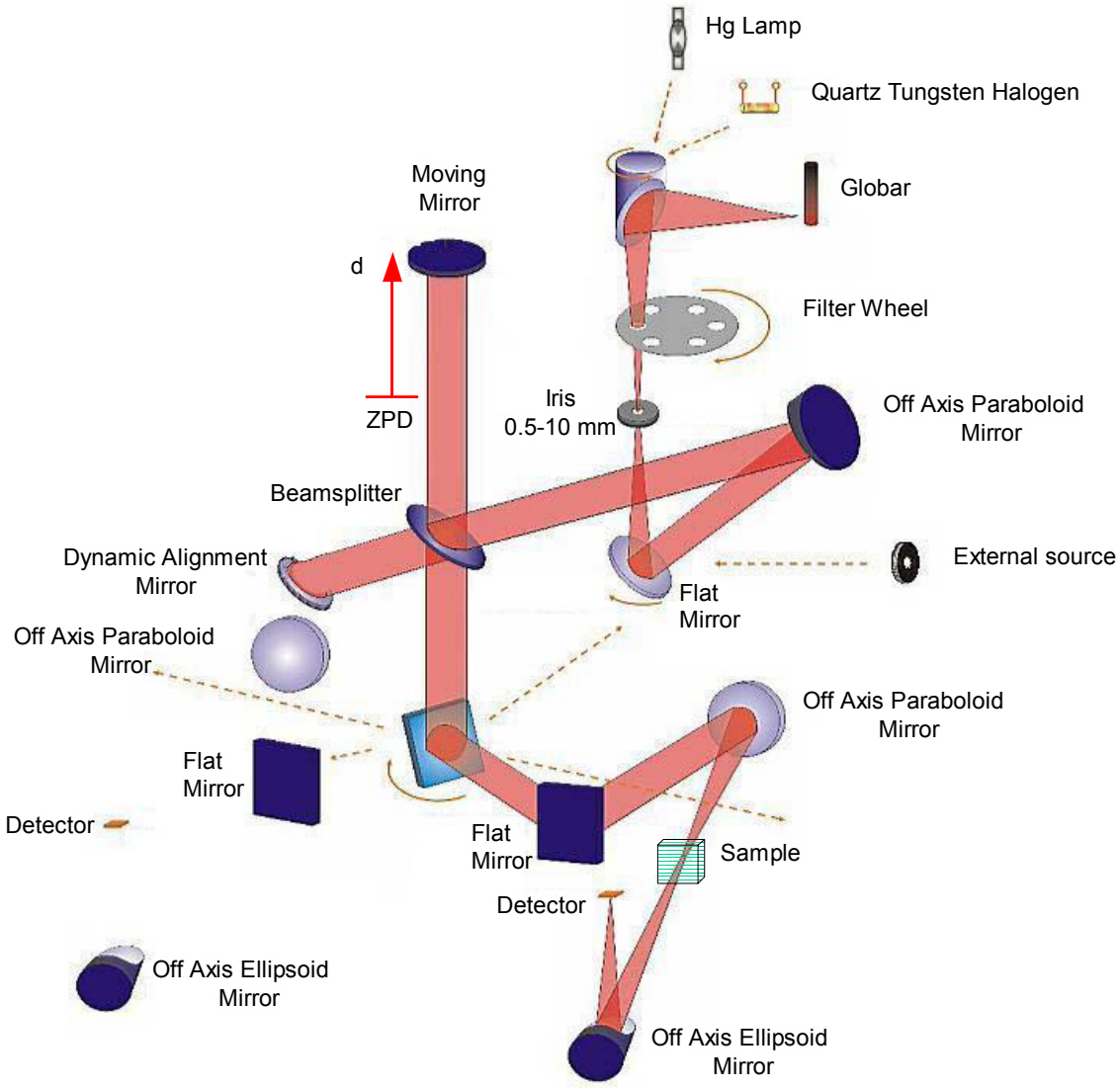

Figure 2.3: Optical beam path for the DA3 spectrometer. Figure adapted with permission from ABB-Bomem

from one of three internal sources onto a mechanical iris of diameter adjustable from 0.5-10 mm. The aperture size determines the throughput of the spectrometer and

the size of the source image to be focused on the sample. Below the aperture, light passes through one of six optional optical filters. A flat mirror (manually moveable to accommodate light from either the three internal sources or an external source) diverts the diverging beam to an off-axis paraboloid Al mirror. The off-axis paraboloid collimates the light for processing in the Michelson arms. This collimated light impinges upon the BMS with roughly half transmitting to the dynamically aligned fixed mirror and half reflecting to the moving (scan) mirror. Upon reflection from their respective mirrors, the two beams recombine and proceed towards the sample selection mirror. This mirror rotates to direct the output beam to one of five sample locations. An off-axis paraboloid refocuses the collimated light onto the sample. After either transmitting or reflecting (not shown) from the sample, another off-axis paraboloid focuses the diverging beam onto the detector element. The entire optical configuration shown in Fig. 2.3 may be evacuated or purged with dry nitrogen to alleviate water absorption lines, which are particularly strong in the far-IR to IR spectral range.

The sample measurement geometry shown in Fig. 2.3 illustrates the transmission configuration. Often, extracting optical coefficients requires measurement of the reflection from the sample surface. Figure 2.4 shows the rig for measuring sample reflectance. The reflectance rig consists of two flat mirrors and two spherical mirrors. The initial flat mirror redirects the focused sample beam to a spot at the focal length of the first spherical mirror. This mirror refocuses the source image on the sample. Upon reflecting from the sample, the second spherical mirror again focuses the beam before being directed into the detector ellipsoid by the final flat mirror.

Acquiring accurate spectra with a Michelson-based FTIR spectrometer requires precise determination of the scanning mirror location. The DA3 utilizes both a white light source (WLS) and a helium-neon laser (HeNe) for location of the moving mirror. The WLS and HeNe enter the DA3 from the rear of the instrument (not shown in

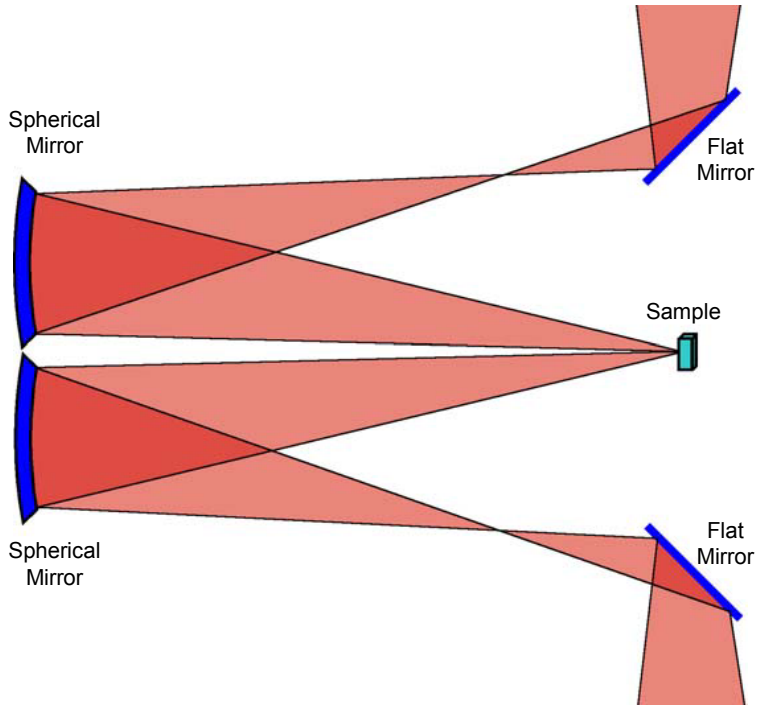

Figure 2.4: Reflectance rig for Bomem DA3 FTIR spectrometer.

Fig. 2.3) and impinge upon the central portion of the Michelson optics along with the source light. The WLS produces an interferogram peaked at ZPD. The HeNe laser produces a sinusoidal interferogram that, although not useful for locating ZPD, provides a very accurate determination of the change in the optical path length Δx. Specifically, a change from bright to dark in the HeNe interference fringe pattern corresponds to $\Delta x = \lambda_{HeNe}/2$. The repetitive nature of the HeNe interferogram allows positioning to even greater accuracy. In addition to determining Δx, the HeNe source provides information crucial for dynamical alignment of the "fixed mirror". The "fixed mirror" or dynamic alignment mirror (Fig. 2.3) tilts slightly to account for wobble in the moving mirror during translation. This dynamical alignment procedure maintains coherence across the collimated beams and reduces phase errors.

Rather impressively, Bomem achieves nearly five orders of magnitude in frequency range by offering a variety of optical elements for the DA3. Figure 2.5 (reprinted with permission from ABB-Bomem) plots the operational range of the

various sources, beamsplitters, and detectors. The abscissa represents increasing wavelength (μm) from UV to far-IR (left to right) on a quasi-logarithmic scale. Frequency in cm^{-1} is also included for comparison. The top panel plots the relative sensitivity (arb. units) for the various available detectors. Colored bands represent approximate detector sensitivity requirements for different experiments. The middle and bottom panels plot the relative throughput and intensity (arb. units) of the beamsplitters and sources, respectively.

The DA3 offers three broadband blackbody radiation sources located internally: mercury vapor discharge (Hg) lamp, globar, and quartz tungsten halogen (QTH). Additionally, a deuterium lamp extends the visible into the UV range. The Hg lamp emits best in the far-IR below approximately ($200\,\mathrm{cm}^{-1}$). Additionally, the Hg exhibits a UV spectrum rich in features owing to the atomic emission lines of Hg. The globar, named for the red-orange glow produced, consists of a ceramic material through which a large current passes. The globar operates best from the upper far-IR to mid-IR spectral range ($200\text{-}5000\,\mathrm{cm}^{-1}$). Above this range, the QTH lamp provides a bright white light source covering through the visible spectral range to approximately $25000\,\mathrm{cm}^{-1}$. For measurement into the UV, the deuterium lamp extends the spectral range to $50000\,\mathrm{cm}^{-1}$. UV emissions from either the Hg or deuterium lamp necessitate protective eyeware for visual alignment with these sources. With the exception of the external deuterium lamp, the ellipsoidal source mirror easily selects the sources *in situ* without breaking vacuum in the DA3.

Various available beamsplitters provide coverage over the entire spectral range. The large size of the collimated beams in the Michelson arms, necessary to maintain phase coherence across the beam, require similarly large beamsplitters. As a result, BMS exchange requires manual substitution and the breaking of vacuum. Most of the beamsplitters consist of a half-silvered film on an essentially non-absorbing substrate material with an appropriate compensator of the the same material as the substrate.

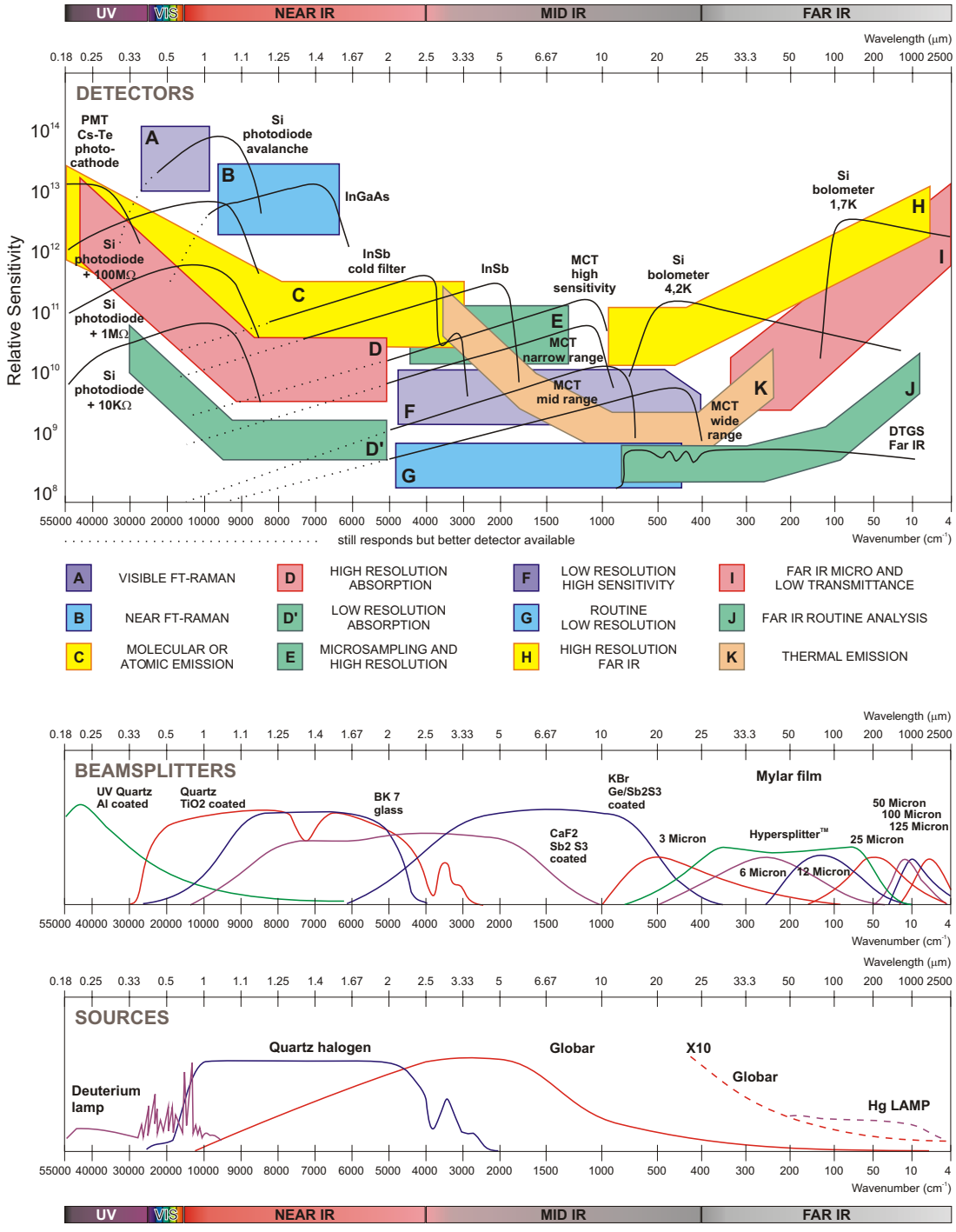

Figure 2.5: Spectral range for the DA3 optical elements (sources, beamsplitters, and detectors). Figure reprinted with permission from ABB-Bomem.

Frequency dependence of both the substrate material and the corresponding films limits the operational spectral bandwidth. Care must be exercised in the handling of beamsplitters in the spectrometer. Additionally, the potassium bromide (KBr) substrate material is extremely hygroscopic, requiring storage in a low humidity dry box to prevent water absorption and accompanying clouding. The far-IR BMS design differs slightly from the others. These beamsplitters consist of various thicknesses (3-$100\,\mu$m) of freestanding Mylar pellicles. The different thicknesses of Mylar optimize spectrometer throughput in a narrow spectral range (see Fig. 2.5) about the interference (étalon) maxima in the Mylar pellicle. The interchangeable pellicles require careful alignment with the central island (WLS and HeNe) to maximize signal output at the shortest operational wavelength. Substituting the multitude of Mylar beamsplitters necessary to cover the entire far-IR proves tedious. A novel BMS design[78] for the far-IR consists of substituting a thick (2 mm) silicon wafer for the Mylar pellicles. Silicon exhibits essentially zero absorption up to $1000\,\mathrm{cm}^{-1}$ (excepting a weak phonon feature around $600\,\mathrm{cm}^{-1}$) and nearly perfect reflection and transmission coefficients ($|r|^2 \approx 0.46$ and $|t|^2 \approx 0.54$). As a result, a single Si BMS outperforms all of the Mylar pellicles across the entire far-IR range.

Available detectors fall into one of three categories: (i) photo-voltaic, (ii) photoconductive, and (iii) thermal. The first class comprises the Si, InSb, and HgCdTe (MCT) detectors. Thermal detectors include the deuterated triglycine sulfate (DTGS) pyroelectric detector and the resistive far-IR bolometric detectors. Several properties characterize detectors: sensitivity, linearity, frequency response, and response time. Ideal detectors provide high sensitivity and high linearity over the operational range. Photometric accuracy demands linearity, but linearity may be sacrificed for sensitivity. The DTGS and Si detectors offer the highest linearity, while the MCT and InSb provide the highest sensitivity. The DA3 detector modules consist of an ellipsoidal focusing mirror, detector element, and electrical preamplifier. Detectors come paired

with a preamplifier specially matched to the detector's impedance and frequency roll-off. Preamps increase the relatively weak detector signals to levels appropriate for analog to digital conversion (ADC). Detector preamps offer both manual gain settings, selected by dip switches, and software controlled gain in increments of 1, 4, 16, and 64. Additionally, for high resolution scans an option positional gain increases the interferogram signal away from ZPD. Detector response time related to the 3 dB frequency roll-off of the detector/preamplifier pair together with the maximum spectral frequency to be measured determine the optimum operational scanning mirror speed.

Figure 2.6 shows the DA3 spectrometer in conjunction with additional equipment and apparatus for measuring temperature dependence. These various apparatus will be addressed below.

2.2.2 Optical cryostat

The Supertran-B ST-4 optical cryostat manufactured by Janis Research Company, Inc. (Wilmington, MA) affords the acquisition of temperature dependent (4.2 – 475 K) optical spectral. Figure 2.7 (top panel) shows the Janis cryostat and an exploded view of the radiation shield and cold finger. The bottom panel expands the view of the copper sample mount or optical head. The cryostat cools the sample via a continuous flow of liquid helium (LHe). A needle valve regulates the flow of LHe from a dewar through a flexible transfer line to the cryostat. A combination of LHe flow control and current control of a $25\,\Omega$ bifilar-wound heater allow precise temperature control of the sample. By pumping on the gas vent port, temperatures below 4.2 K may be achieved. Inside the outer vacuum jacket of the cryostat sits a radiation "cold" shield designed to filter room temperature blackbody radiation. The transferred liquid cools a cold finger at the end of which is attached the sample mount. Four orthogonal windows in the vacuum tailpiece of the cryostat provide optical access to

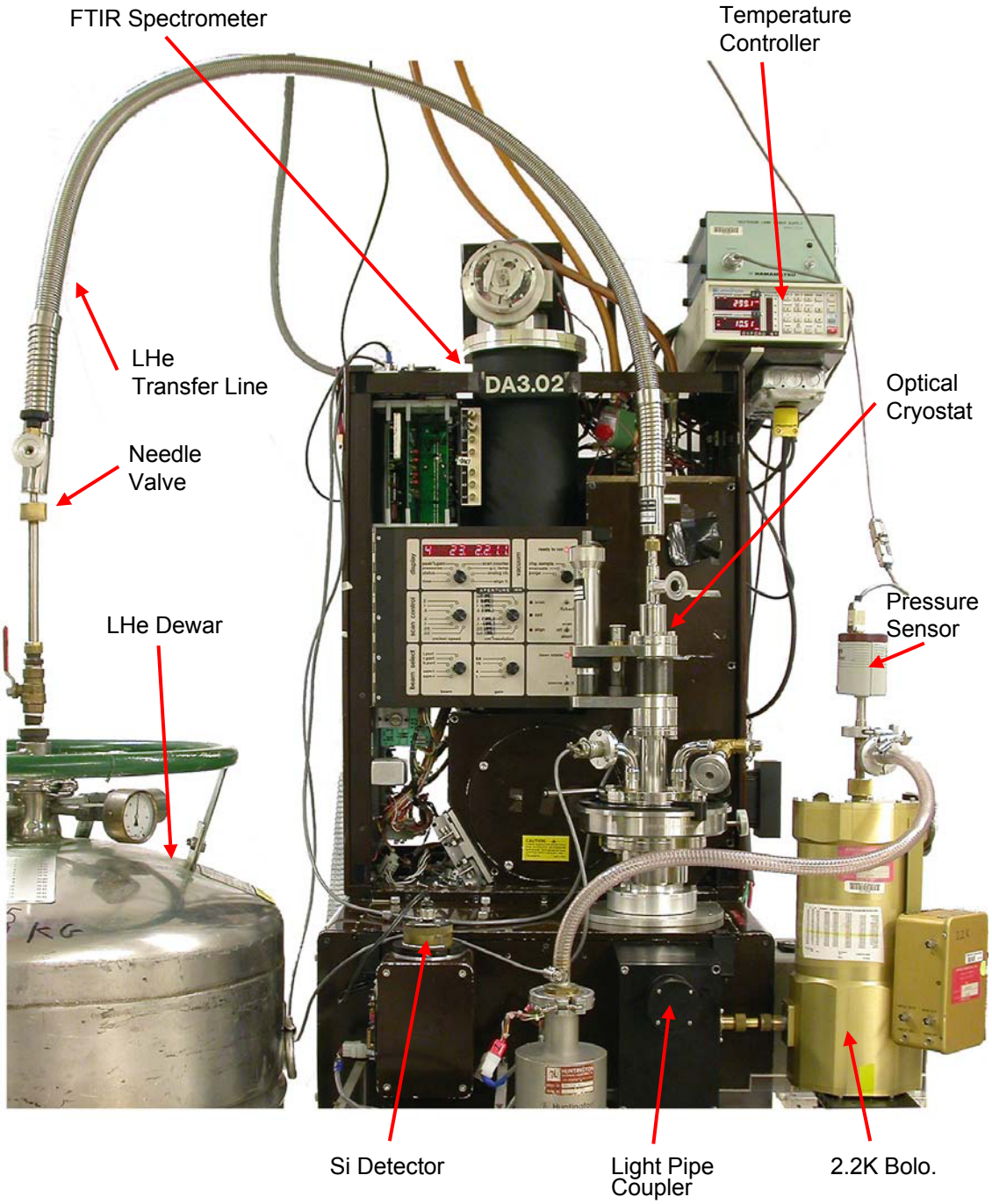

Figure 2.6: Experimental apparatus, including the DA3 FTIR spectrometer, for measuring temperature dependent optical spectra.

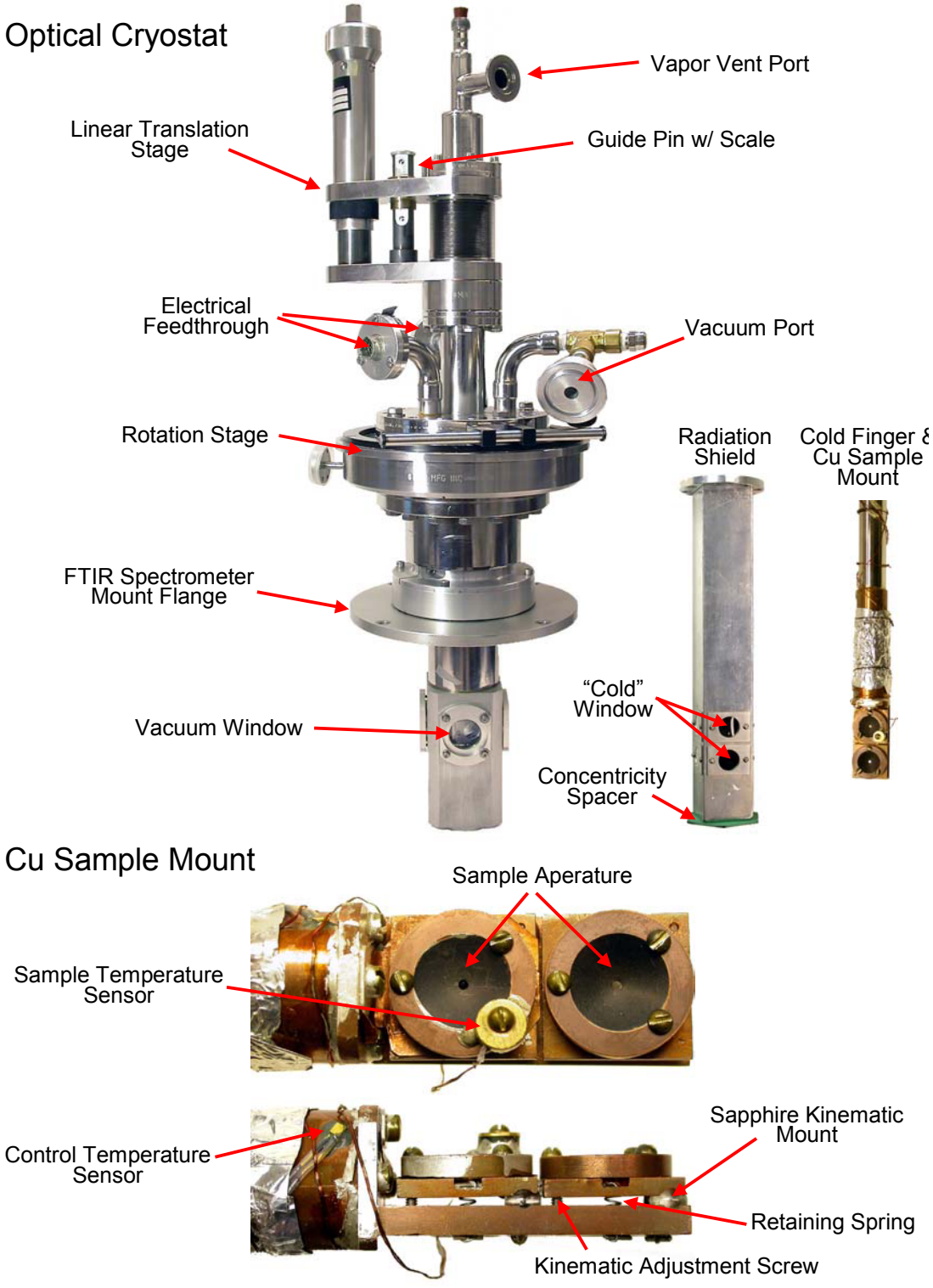

Figure 2.7: Optical cryostat.

the sample mount. A translation stage and a rotation stage provide linear (z-motion) and rotational positioning, respectively, of the sample.

Several modifications to this early model cryostat significantly improved the performance and reproducibility of measured spectra. Reproducibility of the measured sample spectra requires precise linear translation (z-motion) of the sample rod between sample and reference positions. The original linear translation design, which included a "thimble" type drive screw, developed unacceptable lateral leeway and proved difficult to translate. Improving the performance involved retrofitting the cryostat with a linear translation stage LMT-152-SP manufactured by MDC Vacuum Products. This stage provides an $18:1$ translation ratio (18 turns per inch of linear travel) or 0.055 inches per revolution. A large guide pin ensures lateral stability. The addition of both linear and angular scales allows precise sample positioning to better than ± 0.0025 inches. In addition to the retrofitting the translation stage, a redesigned cold shield concentricity spacer improved preformance. This spacer originally consisted of a triangular section of teflon. Shrinkage of the teflon spacer upon cooling (teflon has a large thermal expansion coefficient $\alpha \approx 10^{-4}\,\mathrm{K}^{-1}$) resulted in decreased lateral stability of the sample rod. A modified spacer (see bottom of radiation shield in Fig. 2.7) consists of a six point hexagonal contact design fabricated from FR4 ($\alpha \approx 10^{-5}\,\mathrm{K}^{-1}$), an epoxy-bonded glass material used for printed circuit boards. The improved spacer, with an order of magnitude smaller α and twice the number of contact points, significantly increases reproducibility at lower temperatures.

Overall, the popular continuous-flow cryostat design used by Janis suffers several inherent deficiencies that limit precise optical measurements. First, exchange gas from the cold finger fails to effectively cool the "cold" shield below approximately $100\,\mathrm{K}$. An effective radiation shield should cool to around or below liquid nitrogen temperatures ($77\,\mathrm{K}$), serving both to shield the sample from blackbody radiation and cryopump. Failing to effectively cryopump, the shield allows particulate accumulation

on sample surfaces and results in spurious signals, particular noticeable in the visible to UV reflectance. Moreover, the long sample rod undergoes significant thermal contraction during cooling. The large length L of the rod results in large contraction even for modest temperature changes, $\Delta L = \alpha \Delta T L$. The appreciable ΔL necessitates constant realignment and decreases experimental reproducibility. Finally, the rather bulky LHe transfer line tends to apply force on the cold finger, which introduces additional lateral displacement errors in the sample positioning.

2.2.3 Far-IR transmission dewar

The far-IR blackbody sources available in the DA3 (*e.g.*, Hg and globar) exhibit a spatially dependent intensity pattern. As a result, accurate measurement of the far-IR transmittance requires precise positioning of the sample and reference in the optical beam to ensure reproducible imaging of the source on the sample apertures. Such precision exceeds the capabilities of the Janis cryostat. A transmission dewar together with a carefully machined sample position stage match the required specifications. Figure 2.8 shows the far-IR transmission dewar manufactured by Infrared Laboratories, Inc. (IRLabs Tucson, AZ). The dewar consists of a liquid Helium (LHe) reservoir surrounded by a radiation shield cooled by a liquid nitrogen (LN) reservoir. Figure 2.8 indicates the fill tubes for the cryogenic reservoirs. A copper stage thermally contacts to the base of the LHe reservoir. The sample mount assembly (bottom panel of Figure 2.8) attaches to this stage. A 10 mm diameter light pipe couples light from the DA3 spectrometer output to the transmission dewar. White polyethylene windows at the light pipe access maintain vacuum in the dewar. Wedging the outer vacuum windows and optional LN cold filter windows remove étalon interference. Temperature dependence is achieved via control of a resistive heater attached to the sample stage in combination with adjustment of the cooling power of the sample stage via a “heat” clamp. The clamp varies the thermal contact between the LHe

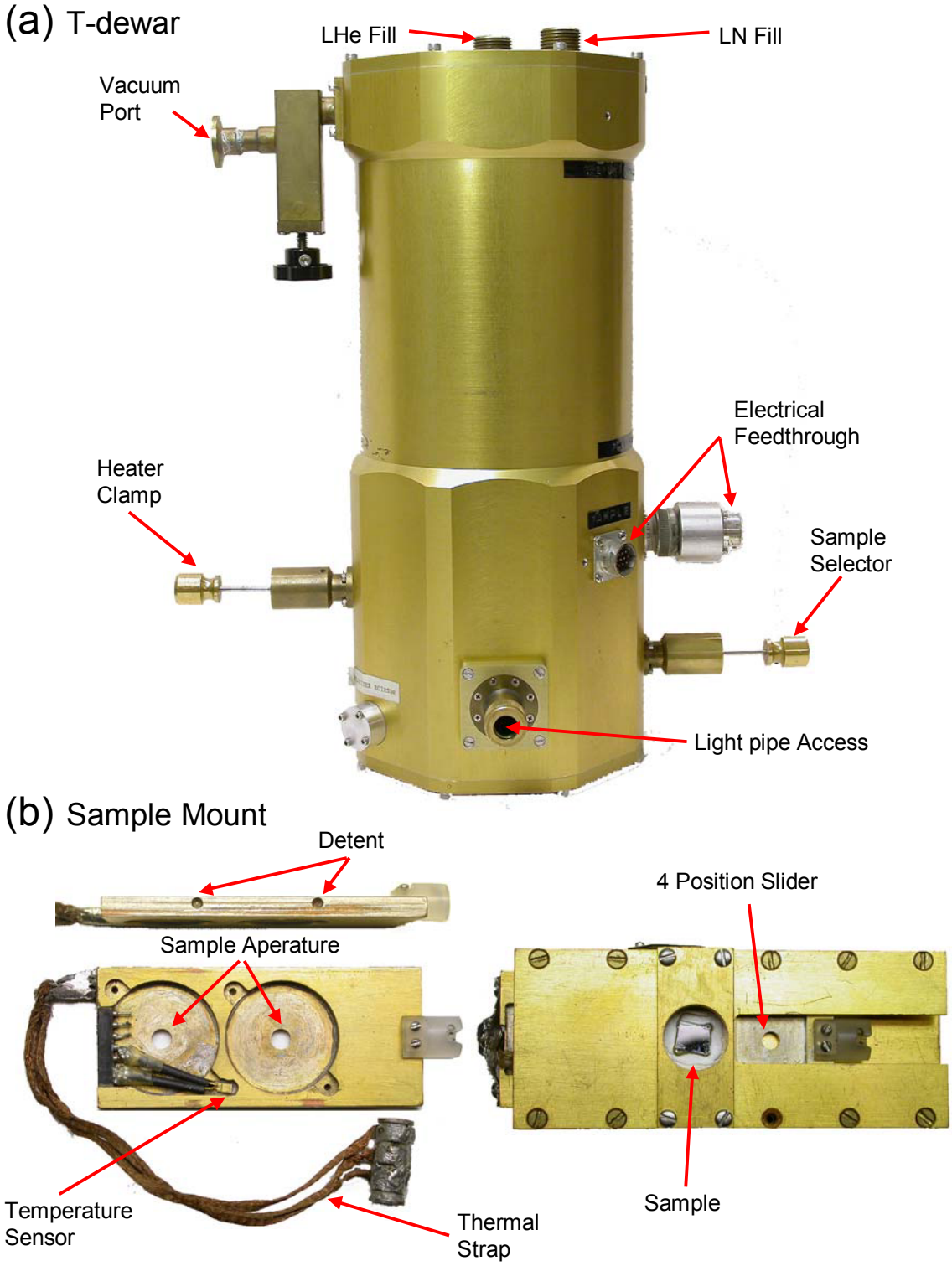

Figure 2.8: Far-infrared transmission dewar and sample mount.

reservoir and the sample stage. Electrical feedthroughs allow for measurement and control of temperature and additional measurements, *e.g.*, dc resistance.

The sample selector rod translates the sample slider (left bottom panel of Fig. 2.8) between positions. Sample sliders with both two and four positions have been machined from copper and plated for increased thermal conduction with the slider housing. Detents machined on the plated beryllium-copper edges of the sample slider ensure accurate and reproducible alignment of the slider mechanism to better than 0.001 in. resolution. To achieve low temperatures, $T \approx 4$ K, a thermal strap has been hard-soldered to the slider. The edge of the slider consists of a teflon mount to engage with the sample selector rod. The thermally insulating teflon prevents excessive heat leak from the outside. In addition to the heater and temperature sensor on the sample stage, Si diode temperature sensors have been added to the sample sliders as indicated in Fig. 2.8. Wood's metal, a low temperature solder, provides excellent thermal contact and attaches the sensor to the slider without damaging the diode.

2.2.4 Temperature sensing and control

A model 330 autotuning temperature controller manufactured by Lake Shore Cryotronics, Inc. (LSCI) provides temperature sensing and control to better than ± 1 K. The 330 determines temperature by measuring the change in resistance of a silicon diode sensor. A standard 4-probe technique measures the voltage drop across a silicon diode sensor upon applying a constant current ($10\,\mu$A $\pm 0.1\,\%$). The diodes follow the standard LSCI curve 10, which exhibit a resistance versus temperature characteristic of activated semiconducting transport. This activated responses increases at low temperatures displaying a steep $\mathrm{d}R/\mathrm{d}T$ and subsequently provide an increase in sensitivity. For the calibrated Si diode sensor DT-470-C0, the typical measurement resolution ranges from 1.3 mK at 4.2 K to around 20 mK at room tem-

perature. For controlling the sample temperature, the LSCI 330 provides temperature stability of ± 2.5 mK at 4.2 K to ± 25 mK at 300 K.

2.2.5 Sample mounting and preparation

The samples studied in this work range in size from $\lesssim 1 \times 1\,\mathrm{mm}^2$ (typical of single crystals) to $\gtrsim 5 \times 5\,\mathrm{mm}^2$ (typical of thin films). A range of sample apertures is required to accommodate the various sample sizes. Apertures should be small enough to prevent leakage of stray light from around the sample yet large enough to alleviate alignment issues and provide the maximum throughput. Sample apertures are machined from a 1" OD copper rod. Sets of apertures are drilled with identically centered holes (± 0.001 in.) of varying diameter. Concentrically surrounding the hole is a conical surface designed to scatter any light impinging on the aperture area surrounding the sample. Additionally, matte black paint has been applied to this conical surface to further reduce scattered light.

The bottom panel of Fig. 2.7 shows top and side views of the sample apertures mounted on the copper optical head. Kinematic positioning is achieved with sapphire spheres and two orthogonal alignment screws. Two steel springs hold the alignment. In addition to providing a fixed pivot for positioning, the sapphire balls allow thermal conduction between the cold finger on the sample rod and the sample apertures. A LSCI Si diode temperature sensor mounts directly on the sample aperture for precise measurement of sample temperature. An electrical conducting adhesive (Eccobond solder 59C manufactured by Emerson and Cuming, Inc.) provides both excellent thermal conduction and a relatively strain free mounting of the samples to the apertures.

A Minimet automatic polisher manufactured by Buehler provides optically flat sample surfaces. Together with a range of Metadi diamond pastes of 3, 1, and $1/4$ μm grain size and ultrapad polishing cloths, the Minimet polishes the front surface

of bulk samples and the back side of substrates for use in thin film measurements. The automatic polisher affords control over the applied load and polishing time. A steel polishing rig assures parallel surfaces and helps reduce rounding on the corners, although some rounding at the edges generally occurs. Limiting the polishing time decreases the probability of contamination from the outside or chipping of the sample, both of which tend to scratch the sample.

2.3 Optical Coefficients

2.3.1 Definitions

Perhaps most well known of the optical coefficients is the index of refraction n. The index of refraction relates the ratio of the velocity of propagation of an electromagnetic wave in vacuum c to the velocity in a medium v

$$n = \frac{c}{v}\,. \tag{2.7}$$

Whenever the index depends on the frequency of the incident light $n = n(\omega)$, the medium is said to be dispersive. In addition to a decrease in the propagation velocity, light in a medium may undergo absorption. The intensity a distance x in the medium from the boundary is given by

$$I(x) = I_0\,\mathrm{e}^{-\alpha x}\,, \tag{2.8}$$

where I_0 is the incident intensity and the absorption coefficient α is the fraction of power absorbed in the medium per unit length. The absorption coefficient is given by

$$\alpha = 4\pi\kappa\nu\,, \tag{2.9}$$

where κ is the extinction coefficient.

The index of refraction n and the extinction coefficient κ represent the real and imaginary parts, respectively, of a single complex quantity, namely the complex index of refraction

$$\tilde{n}(\omega) = n(\omega) + \mathrm{i}\,\kappa(\omega)\,. \tag{2.10}$$

Knowledge of $\tilde{n}$ allows derivation of additional optical coefficients more useful in comparing with predictions from theoretical models, *e.g.*, the complex dielectric constant $\tilde{\epsilon}$ or the complex optical conductivity $\tilde{\sigma}$. The complex dielectric constant obtained

from Maxwell's equations (see App. A) is related to $\tilde{n}$ by

$$\begin{aligned}\tilde{\epsilon} &= \epsilon_1 + \mathrm{i}\,\epsilon_2 = \tilde{n}^2 \\ &= (n + \mathrm{i}\,\kappa)^2 = n^2 - \kappa^2 + \mathrm{i}\,2\,n\,\kappa\,. \end{aligned} \tag{2.11}$$

The complex optical conductivity $\tilde{\sigma} = \sigma_1 + \mathrm{i}\,\sigma_2$ relates to $\tilde{\epsilon}$ (see App. A) giving

$$\tilde{\epsilon}(\omega) = \tilde{\epsilon}_b(\omega) + \frac{4\pi\,\mathrm{i}\,\tilde{\sigma}(\omega)}{\omega}\,. \tag{2.12}$$

Here ϵ_b is defined by the relation of the electric displacement to the electric field, $\boldsymbol{D} = \epsilon_b\,\boldsymbol{E}$. Conventionally ϵ_b represents the response of bound charges,[79] though may in principle be redefined providing that Eq. (2.12) is maintained. Rearranging Eq. (2.12) gives the real σ_1 and imaginary σ_2 parts of the complex optical conductivity

$$\sigma_1 = \frac{\omega}{4\pi}\,\epsilon_2 = \frac{\omega}{4\pi}\,2\,n\,\kappa \tag{2.13}$$

$$\sigma_2 = \frac{\omega}{4\pi}\,(\epsilon_b - \epsilon_1) = \frac{\omega}{4\pi}\,(\epsilon_b - n^2 + \kappa^2) \tag{2.14}$$

Equations (2.11), (2.13), and (2.14) provide relations between the complex index of refraction, optical conductivity and dielectric constant: $\sigma_1 \propto \epsilon_2$ (absorption) and $\sigma_2 \propto \epsilon_1$ (screening).

2.3.2 Kramers-Kronig dispersion relations

The interaction of light with matter obeys causality, which simply states no effect precedes its cause. Light cannot be reflected or absorbed from a medium prior to arriving.[80] A response functions F describe the response $\mathcal{R}$ of a medium to some applied stimulus S. In general, for a linear response function F, $R(\omega) = F(\omega)\,S(\omega)$. For example the electric polarization $\boldsymbol{P}$ resulting from an applied electric field $\boldsymbol{E}$ is given by $\boldsymbol{P} = \tilde{\chi}\,\boldsymbol{E}$. In this example, the electric susceptibility $\tilde{\chi}$ is the linear response function. As long as the response function converges in the upper half of the complex

frequency plane, the real and imaginary part are related to one another by

$$F_1(\omega) \equiv \Re e\{F(\omega)\} = \frac{1}{\pi} \fint_{-\infty}^{\infty} \frac{\Im m\{F(\omega')\}}{\omega' - \omega} \, \mathrm{d}\omega'$$
$$F_2(\omega) \equiv \Im m\{F(\omega)\} = -\frac{1}{\pi} \fint_{-\infty}^{\infty} \frac{\Re e\{F(\omega')\}}{\omega' - \omega} \, \mathrm{d}\omega' \,, \tag{2.15}$$

where $\fint$ is the Cauchy principal value integral operator. Eq. (2.15) illustrates that the real and imaginary parts of the response functions are not independent, but rather are intimately connected via the dispersion relations. Dispersion relations relate dispersive processes (*e.g.*, the index of refraction) to absorptive processes (*e.g.*, the extinction coefficient) through integral formulas. This property may be exploited for determining one of these quantities when the other is known completely. In particular, these relations will prove invaluable for determining the phase in bulk reflectance measurements and selecting the physical roots from $\mathcal{T}$ and $\mathcal{R}$ measurements on thin films.

Equation (2.15) may be applied to optical coefficients such as the complex index of refraction or the complex dielectric constant. Exploiting symmetry properties of the response functions further simplifies Eq. (2.15). Specifically, for the dielectric constant $\tilde{\epsilon}(-\omega) = \tilde{\epsilon}^*(\omega)$. Note that $\tilde{\chi} \propto \tilde{\epsilon} - 1$ is the actual response function. Including the symmetry relation into Eq. (2.15) gives the dispersion relations for the complex dielectric constant

$$\epsilon_1(\omega) - 1 = \frac{2}{\pi} \fint_0^{\infty} \frac{\omega' \epsilon_2(\omega')}{\omega'^2 - \omega^2} \, \mathrm{d}\omega'$$
$$\epsilon_2(\omega) = -\frac{2\,\omega}{\pi} \fint_0^{\infty} \frac{\epsilon_1(\omega') - 1}{\omega'^2 - \omega^2} \, \mathrm{d}\omega' \,. \tag{2.16}$$

Eq. (2.16) is referred to as the Kramers-Kronig dispersion relation for $\tilde{\epsilon}$. Similar relations for the optical conductivity may be derived. A later section of this chapter illustrates the application of the K-K dispersion relations to the complex reflectance amplitude and phase.

2.3.3 Sum Rules

The distribution of optical spectral weight provides important information regarding the underlying physics of an electronic medium.[81] The spectral weight or integrated conductivity will prove invaluable in this discussion. The following illustrates the relation of this integrated conductivity to the optical sum rules.

To arrive at a derivation of the sum rules for solids, first consider an extension of the interaction of light with atoms to the more general case of a solid. For a solid consisting of N noninteracting atoms per unit volume, the static dielectric constant is written as a sum over the optical transitions

$$\tilde{\epsilon}(\omega) = 1 + \frac{4\pi N e^2}{m} \sum_m \frac{f_{mn}}{\omega_{mn}^2 - \omega^2 - \mathrm{i}\,\gamma\,\omega}\,, \tag{2.17}$$

where ω_{mn} and f_{mn} represents the frequency difference and oscillator strength, respectively, from the initial state n to the final state m. The oscillator strength is given by the quantum mechanical transition probability

$$f_{mn} = \frac{2m}{\hbar^2}\hbar\omega\,|x_{mn}|^2\,, \tag{2.18}$$

where $x_{mn} = \langle\psi_m|x|\psi_n\rangle$ is the dipole matrix element of the electron between states ψ_m and ψ_n. The Thomas-Reiche-Kuhn (TRK) sum rule[82] for generalized transitions in an atom with Z electrons[80] gives

$$\sum_m f_{mn} = Z\,. \tag{2.19}$$

Interactions in solids generally modify the form of the TRK sum rule,[80] $\sum_m f_{mn} = 1 - m/m_n^*$.

The application of the dispersion relations[80,83] given by Eq. (2.16) provides a more general f-sum rule for solids than Eq. (2.17). Consider a cutoff frequency ω_c, above which no absorption occurs. For $\omega > \omega_c$, $\epsilon_2 = 0$ and $\epsilon_1(\omega) = 1 - \omega_p^2/\omega^2$, the Drude form. Substituting into Eq. (2.16) results in the general f-sum rule for solids

$$\frac{2}{\pi}\int_0^\infty \omega\,\epsilon_2(\omega)\,\mathrm{d}\omega = \omega_p^2 = \frac{4\pi N e^2}{m} \tag{2.20}$$

or, using Eq. (2.12), in terms of σ_1

$$\frac{2}{\pi}\int_0^\infty \sigma_1(\omega)\,\mathrm{d}\omega = \frac{N\,e^2}{m}\,. \tag{2.21}$$

Here N is the total number density of electrons in the medium, ω_p is the plasma frequency, and m is the free electron mass. The f-sum rule is independent of details in the microscopic physics.[81] If information regarding the static dielectric function, $\epsilon_0 \equiv \epsilon_1(\omega = 0)$, is required then Eq. (2.16) gives

$$\epsilon_0 = 1 + \frac{2}{\pi}\int_0^\infty \frac{\epsilon_2(\omega)}{\omega}\,\mathrm{d}\omega\,. \tag{2.22}$$

Eq. (2.22) shows that the static dielectric constant results from contributions of oscillators at all frequencies.

Often information regarding the low-lying electronic states contributes important insight towards understanding the electronic properties. The partial or restricted spectral weight $S(\omega)$ is defined by

$$S(\omega) = \frac{2}{\pi}\int_0^\omega \sigma_1(\omega')\,\mathrm{d}\omega'. \tag{2.23}$$

In general, the restricted spectral weight given by Eq. (2.23) will depend on temperature and interaction strength as well as carrier density.[13] Note the difference with the full f-sum rule in Eqs. (2.20) and (2.21), which depends solely on carrier density. The integrated conductivity over a finite frequency range will be proportional to an effective number of electrons per unit cell N_{eff} given by

$$N_{eff}(\omega) = \frac{V_{cell}\,m}{e^2}\,S(\omega)\,, \tag{2.24}$$

where V_{cell} is the unit cell volume. Carrying out the integral to $\omega = \infty$ in Eq. (2.23), recovers the familiar sum rule $N_{eff}(\omega = \infty) = N\,V_{cell}$ where N is the total number density of electrons (core plus valence) in the unit cell. Care must be exercised in applying Eq. (2.24) to ensure states not under consideration are well-separated in energy.[80]

The restricted sum rule given by Eqs. (2.23) and (2.24) relate oscillator strength to the expectation value of the hopping amplitude in the tight binding model.[13] The kinetic energy K is given by

$$K(\omega) = \frac{a_0}{e^2}\,\hbar^2 S(\omega) = \frac{a_0\,\hbar^2}{e^2}\frac{2}{\pi}\int_0^{\omega}\sigma_1(\omega')\,d\omega' = \frac{\hbar^2}{m\,a_0^2}\,N_{eff}(\omega) = 2\,Ry\left(\frac{a_B}{a_0}\right)^2 N_{eff}(\omega)\,, \tag{2.25}$$

where $a_0 = V_{cell}^{1/3}$ is the lattice constant and in the last line Ry and a_B represent the Rydberg energy and Bohr radius, respectively. The kinetic energy given by Eq. (2.25) offers an important quantity for a comparison of the experimentally determined optical properties with the predictions from theoretical models.

2.4 Extracting Optical Coefficients from Measurements

Several main optical processes describe the interaction of light with matter: transmission, reflection, absorption, scattering, and luminescence. This section discusses transmission and reflection in the linear response regime and derives expression for the measured experimental quantities in terms of the optical coefficients. The Fresnel coefficients (App. A) describe the transmission and reflection from the boundary between two optical media. The results for a single boundary are extended to include the multiple boundaries of a particular sample geometry. In each specific sample configuration expressions for the transmittance $\mathcal{T}$ and reflectance $\mathcal{R}$ intensity are derived, where $\mathcal{T}$ ($\mathcal{R}$) represent the ratio of the transmitted (reflected) power to the incident power. In the absence of lossy processes, *e.g.*, absorption or scattering, $\mathcal{T} + \mathcal{R} = 1$.

Figure 2.9 shows the typical sample configurations considered in this work: bulk, slab, and film on a substrate. Bulk samples are either single crystal or polycrystalline samples. These samples are sufficiently thick such that the incident light does not reach the back surface. For substrates or thin bulk samples in trans-

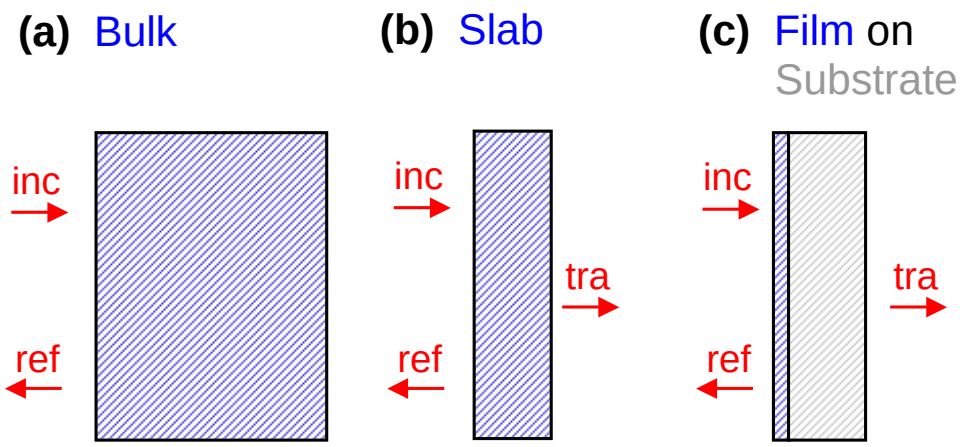

Figure 2.9: Measurement configureations for (a) bulk, (b) slab, and (c) thin film on substrate samples. Arrows indicate the propagation direction of incident (inc), reflected (ref), and transmitted (tra) light.

parency regions, light reaches the back surface and may be either transmitted or reflected. Finally, thin films (typical thickness approximately 100 nm) are deposited on ideally non-absorbing substrates. In this case both transmission and reflection occurs. Knowledge of the complex index of refraction and thickness of the substrate is also required.

2.4.1 Reflection measurements

All of the sample configurations illustrated in Fig. 2.9 experience reflection from the front surface. Additionally, transmission occurs in the slab and thin film cases. Several complications arise in performing reflection measurements not present in transmission: surface quality, surface alignment, and suitable reflection reference. Reflection measurements require surfaces producing specular rather than diffuse reflection. The polishing procedure outlined above generally provides surfaces of sufficient quality. Annealing after polishing is recommended to restore any damage. In addition to surface preparation, coincident alignment of the sample and reference is required. A HeNe laser facilitates the alignment procedure of the kinematic mounts discussed above. Finally, aluminum mirrors provide a suitable reference material.

Ideally a reference reflects perfectly over a wide frequency range and exhibits little temperature dependence. A thermal vapor technique deposits Al films onto glass slides to thicknesses of 200 nm. Figure 2.10 shows the frequency dependence of the aluminum mirrors over the entire spectral range of the DA3. The room temperature

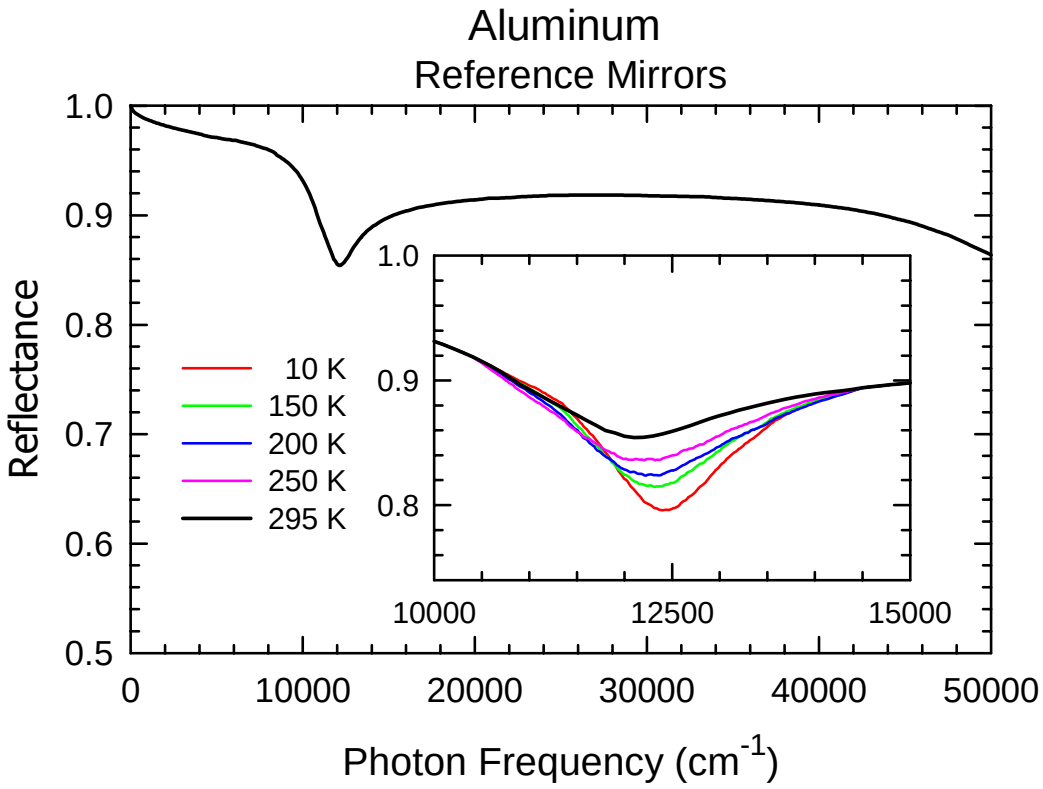

Figure 2.10: Aluminum reference mirror reflectance spectra. Inset shows temperature dependence of interband feature.

curve shown in Fig. 2.10 was produced by Manuel Quijada in an absolute reflectance setup at NASA, Greenbelt. Despite the appearance of pinholes, the mirrors reflect comparably to bulk Al. The inset highlights the slight temperature dependence of the interband feature around $12500\,\mathrm{cm}^{-1}$. Temperature dependent studies were achieved with a gold reference mirror using the DA3. Gold mirrors provide a better reflectance reference in the IR and remains relatively flat until around $18000\,\mathrm{cm}^{-1}$.

2.4.2 Bulk sample reflectance

The reflectance amplitude measured in bulk reflectance provides only one experimental quantity. Additional information is required to fully describe the complex optical coefficients. A Kramers-Kronig (KK) analysis of the bulk reflectance amplitude provides the reflectance phase θ. The KK analysis requires knowledge of the bulk reflectance over an infinite spectral range $0 - \infty$. Necessarily finite range measurements therefore require extrapolations to low and high frequencies. At low frequencies ($\omega < 10\,\mathrm{cm}^{-1}$), the extrapolation to zero depends on the dc conductivity of the material. For insulators, at frequencies well below any phonons or other low-frequency electronic transitions, the reflectance extrapolates to zero frequency as a constant. For metallic samples, the reflectance extrapolates to zero following the Hagen-Rubens form $R(\omega) = 1 - \xi\sqrt{\omega}$, where ξ is determined by the reflectance value at the low-frequency experimental cutoff. At high frequencies ($\omega > 45000\,\mathrm{cm}^{-1}$), reflectance extrapolations split into two regions, the interband and the free-electron. For interband frequencies ($45000 < \omega < \omega_{FE}$), $\mathcal{R} \sim \omega^{-\beta}$, where β represents the frequency dependence of the interband spectral range and ω_{FE} represents the frequency onset of free-electron behavior. In the free-electron region, $\mathcal{R}$ falls off with frequency as ω^{-4}.

Taking these extrapolations together with the measured reflectance determines the phase θ of the complex reflection coefficient

$$\theta(\omega) = \frac{\omega}{\pi}\int_0^\infty \frac{\ln[\mathcal{R}(\omega')/\mathcal{R}(\omega)]}{\omega^2 - \omega'^2}\,\mathrm{d}\omega' \,. \tag{2.26}$$

$\mathcal{R}(\omega)$ and $\theta(\omega)$ from Eq. (2.26) provide the frequency-dependent complex index of refraction $\tilde{n}$

$$n = \frac{1 - \mathcal{R}}{1 - 2\sqrt{\mathcal{R}}\cos(\theta) + \mathcal{R}} \tag{2.27}$$

$$\kappa = \frac{2\sqrt{\mathcal{R}}\sin(\theta)}{1 - 2\sqrt{\mathcal{R}}\cos(\theta) + \mathcal{R}} \,. \tag{2.28}$$

In the far-IR of insulators, where phonon absorption dominates, Kramers-Kronig analysis again allows extraction of optical coefficients. However, additional phonon characterization results from fitting the bulk reflectance with an appropriately modeled dielectric constant. The bulk reflectance written in terms of $\tilde{\epsilon}$ is given by

$$\mathcal{R} = \left| \frac{1 - \sqrt{\tilde{\epsilon}}}{1 + \sqrt{\tilde{\epsilon}}} \right|^2 = \frac{(n-1)^2 + \kappa^2}{(n+1)^2 + \kappa^2}. \tag{2.29}$$

All that remains is a suitable model for $\tilde{\epsilon}$ in the phonon region.

The classical dielectric constant consists of a sum of Lorentz oscillators

$$\tilde{\epsilon}(\omega) = \epsilon_\infty + \sum_{j=1}^{N_{osc}} \frac{A_j^2}{\omega_{\mathrm{TO},j}^2 - \omega^2 - \mathrm{i}\,\gamma_j\,\omega}, \tag{2.30}$$

where N_{osc} is the total number of phonon oscillators, ϵ_∞ is the static dielectric constant at frequencies much larger than the phonons, and $\omega_{\mathrm{TO},j}$, γ_j, and A_j are the transverse optical (TO) frequency, width, and spectral weight, respectively, of the j^{th}-phonon. This classical form for the dielectric function given by Eq. (2.30) suites crystals with a small number of uncoupled modes.

However, for crystals having a larger number of phonons with wide reflectivity bands, a model $\tilde{\epsilon}$ parameterized by the frequencies and damping of the TO and longitudinal optical (LO) phonon modes better fits the reflectance.[84,85] In this four-parameter semi-quantum (FPSQ) model,[85] $\tilde{\epsilon}$ is given by

$$\tilde{\epsilon}(\omega) = \epsilon_\infty \prod_{j=1}^{N_{osc}} \frac{\omega_{\mathrm{LO},j}^2 - \omega^2 - \mathrm{i}\,\gamma_{\mathrm{LO},j}\,\omega}{\omega_{\mathrm{TO},j}^2 - \omega^2 - \mathrm{i}\,\gamma_{\mathrm{TO},j}\,\omega}, \tag{2.31}$$

where $\omega_{\mathrm{LO},j}$ and $\gamma_{\mathrm{LO},j}$ represent the frequency and the width, respectively, of the j^{th} longitudinal optical (LO) phonon mode. In general the LO and TO damping of Eq. (2.31) need not be the same. However, conditions on their relative magnitudes and ratio compared to the LO and TO frequency ratio preserve the physical meaning of damping.[85] Additionally, the Lydanne-Sachs-Teller relation may be generalized to accommodate multiple phonons.[84]

Dielectric constant values resulting from least squares fits of $\mathcal{R}$ given by Eq. (2.29) agree well with results from KK analysis. The fitting procedure has the advantages of producing the characteristic phonon parameters and providing well-behaved functions for the dielectric constant.

2.4.3 A single layer bounded by air: Substrate

A single layer bounded by air on either sides models a bulk sample, whenever the absorption becomes negligible enough such that the incident light experiences the back surface. This "slab" geometry model is an appropriate description of a substrate material or a thin bulk sample in transparency regions. In this case, the total resultant transmission and reflection coefficients consist of a sum of the Fresnel coefficients at both boundaries over multiple passes (see Fig. A.2 in App. A). The resulting expressions for the transmittance $\mathcal{T}_s$ and reflectance $\mathcal{R}_s$ intensities are given by

$$\mathcal{T}_s = \left| \frac{t_1 t_2 \, \mathrm{e}^{\mathrm{i}\,\phi_1}}{1 + r_1 r_2 \, \mathrm{e}^{\mathrm{i}\,2\phi_1}} \right|^2 \tag{2.32}$$

$$\mathcal{R}_s = \left| r_1 + \frac{t_1 t_1' r_2 \, \mathrm{e}^{\mathrm{i}\,2\phi_1}}{1 + r_1 r_2 \, \mathrm{e}^{\mathrm{i}\,2\phi_1}} \right|^2 = \left| \frac{r_1 + r_2 \, \mathrm{e}^{\mathrm{i}\,2\phi_1}}{1 + r_1 r_2 \, \mathrm{e}^{\mathrm{i}\,2\phi_1}} \right|^2 , \tag{2.33}$$

where the Fresnel coefficients for $t_j \equiv t_{j-1,j}$ and $r_j \equiv r_{j-1,j}$ are given by Eqs. (A.9) and (A.10) and the phase ϕ_1 is given by Eq. (A.13). The right side of Eq. (2.33) results from conservation of energy, $t_1 t_1' + r_1^2 = 1$. Typical substrate values, $d_s \approx 0.05$ cm and $n_s \approx 2$ in the IR to UV range, lead to étalon effects occurring approximately every $5\,\mathrm{cm}^{-1}$, a frequency scale generally smaller than features of interest. A simplified formula for $\mathcal{T}$ and $\mathcal{R}$ results from considering the average or incoherent addition of multiple passes in the substrate. Here the multiple passes are treated as a sum of the *intensities* of the Fresnel coefficients ($\mathcal{T}_j = |t_j|^2$ and $\mathcal{R}_j = |r_j|^2$)

at the boundaries. For incoherent addition, $\mathcal{T}_s$ and $\mathcal{R}_s$ are given by

$$\mathcal{T}_s = \frac{\mathcal{T}_1 \mathcal{T}_2 \, \mathrm{e}^{-\alpha_1 d_1}}{1 - \mathcal{R}_1 \mathcal{R}_2 \, \mathrm{e}^{-2\alpha_1 d_1}} \tag{2.34}$$

$$\mathcal{R}_s = \mathcal{R}_1 + \frac{\mathcal{T}_1 \mathcal{T}_1' \mathcal{R}_2 \, \mathrm{e}^{-2\alpha_1 d_1}}{1 - \mathcal{R}_1 \mathcal{R}_2 \, \mathrm{e}^{-2\alpha_1 d_1}} \,, \tag{2.35}$$

where α_1 is the slab absorption coefficient given by Eq. (2.9), d_1 is the slab thickness, and $\mathcal{T}_1' \equiv \mathcal{T}_{10}$. Numerically inverting[86] the equations for $\mathcal{T}_s$ and $\mathcal{R}_s$ of a finite thickness slab determines n_s and κ_s.

For non-absorbing materials (where $\kappa \approx 0$), the slab acts as a Fabry-Pérot resonant cavity. The resulting $\mathcal{T}_s$ and $\mathcal{R}_s$ given by Eqs. (2.32) and (2.33) will display interference (étalon) maxima and minima in high-resolution scans. Peak fits to the transmittance maxima (or reflectance minima) determine the index of refraction. For a given $\mathcal{T}$ peak, n is given by

$$n = \frac{m}{2\,\nu\, d} \,, \tag{2.36}$$

where m is the order of the peak, ν is the peak frequency, and d is the thickness of the slab. Using étalon in determining the material index of refraction takes full advantage of the spectral resolution of the instrument (better than $1 : 10000$ in the IR). The accuracy in determining n is limited only by the ability to accurately determine m and the thickness, which typically is $\approx 500 \pm 1\,\mu$m. Identifying the peak order becomes difficult with increasing frequency. Thus, this method works best in the far-IR to IR region. The index of refraction for several substrates determined in the far-IR using Eq. 2.36 are shown in Fig. A.4 of App. B.

2.4.4 Two layers bounded by air: film on a substrate

For a thin film on a substrate (both potentially absorbing) and bounded by air on either side, the coherent transmission and reflection intensity are given by

$$\mathcal{T}_f = |t|^2 = \left| \frac{t_1\, t_2\, t_3\, \mathrm{e}^{\mathrm{i}(\phi_1+\phi_2)}}{1 + r_1\, r_2\, \mathrm{e}^{2\mathrm{i}\,\phi_1} + r_1\, r_3\, \mathrm{e}^{2\mathrm{i}(\phi_1+\phi_2)} + r_2\, r_3\, \mathrm{e}^{2\mathrm{i}\,\phi_2}} \right|^2 \tag{2.37}$$

$$\mathcal{R}_f = |r|^2 = \left| \frac{r_1 + r_2\, \mathrm{e}^{2\mathrm{i}\,\phi_1} + r_3\, \mathrm{e}^{2\mathrm{i}(\phi_1+\phi_2)} + r_1\, r_2\, r_3\, \mathrm{e}^{2\mathrm{i}\,\phi_2}}{1 + r_1\, r_2\, \mathrm{e}^{2\mathrm{i}\,\phi_1} + r_1\, r_3\, \mathrm{e}^{2\mathrm{i}(\phi_1+\phi_2)} + r_2\, r_3\, \mathrm{e}^{2\mathrm{i}\,\phi_2}} \right|^2 . \tag{2.38}$$

Although Eqs. (2.37) and (2.38) represents the complete solution for $\mathcal{T}_f$ and $\mathcal{R}_f$, extracting $\tilde{n}$ from these equations proves difficult. As discussed above, simplified formula for $\mathcal{T}_f$ and $\mathcal{R}_f$ once again result from considering incoherent addition in the substrate (coherent addition in the film is maintained). The resulting film on substrate $\mathcal{T}_f$ and $\mathcal{R}_f$ with incoherent substrate addition are given by

$$\mathcal{T}_f = \frac{\mathcal{T}'\,\mathcal{T}_3\, \mathrm{e}^{-\alpha_2\, d_2}}{1 - \mathcal{R}''\,\mathcal{R}_3\, \mathrm{e}^{-\alpha_2\, d_2}} \tag{2.39}$$

$$\mathcal{R}_f = \mathcal{R}' + \frac{\mathcal{T}'\,\mathcal{T}''\, \mathrm{e}^{-2\alpha_2\, d_2}}{1 - \mathcal{R}''\,\mathcal{R}_3\, \mathrm{e}^{-\alpha_2\, d_2}} . \tag{2.40}$$

These equations then provide for $\mathcal{T}_f$ and $\mathcal{R}_f$ in terms of the index n, extinction coefficient κ, thickness of the film, frequency, and substrate parameters. Moreover, these equations may be used to produce contours of constant $\mathcal{T}$ and $\mathcal{R}$ for various values of the complex index of the film. Figure 2.11 shows such contours for typical substrate parameters ($n_s = 2$, $k_s = 0$, and $d_s = 0.05\,\mathrm{cm}$) in the IR to visible range for a film of thickness $d_f = 10^{-5}\,\mathrm{cm}$. Contour plots for frequencies of 5000, 10000, 15000, and $20000\,\mathrm{cm}^{-1}$ are shown. Starting in the infrared ($\nu = 5000\,\mathrm{cm}^{-1}$), Fig. 2.11 illustrates that for a given value of transmittance and reflectance, multiple pairs of n and k simultaneously solve Eqs. (2.39) and (2.40). As frequency increases, additional roots appear. Determining the correct root requires appealing to the physical constraints imposed on n and k. Specifically, the K-K relations will ensure selection of the physically relevant root. Particular care in following the correct solution must be exercised

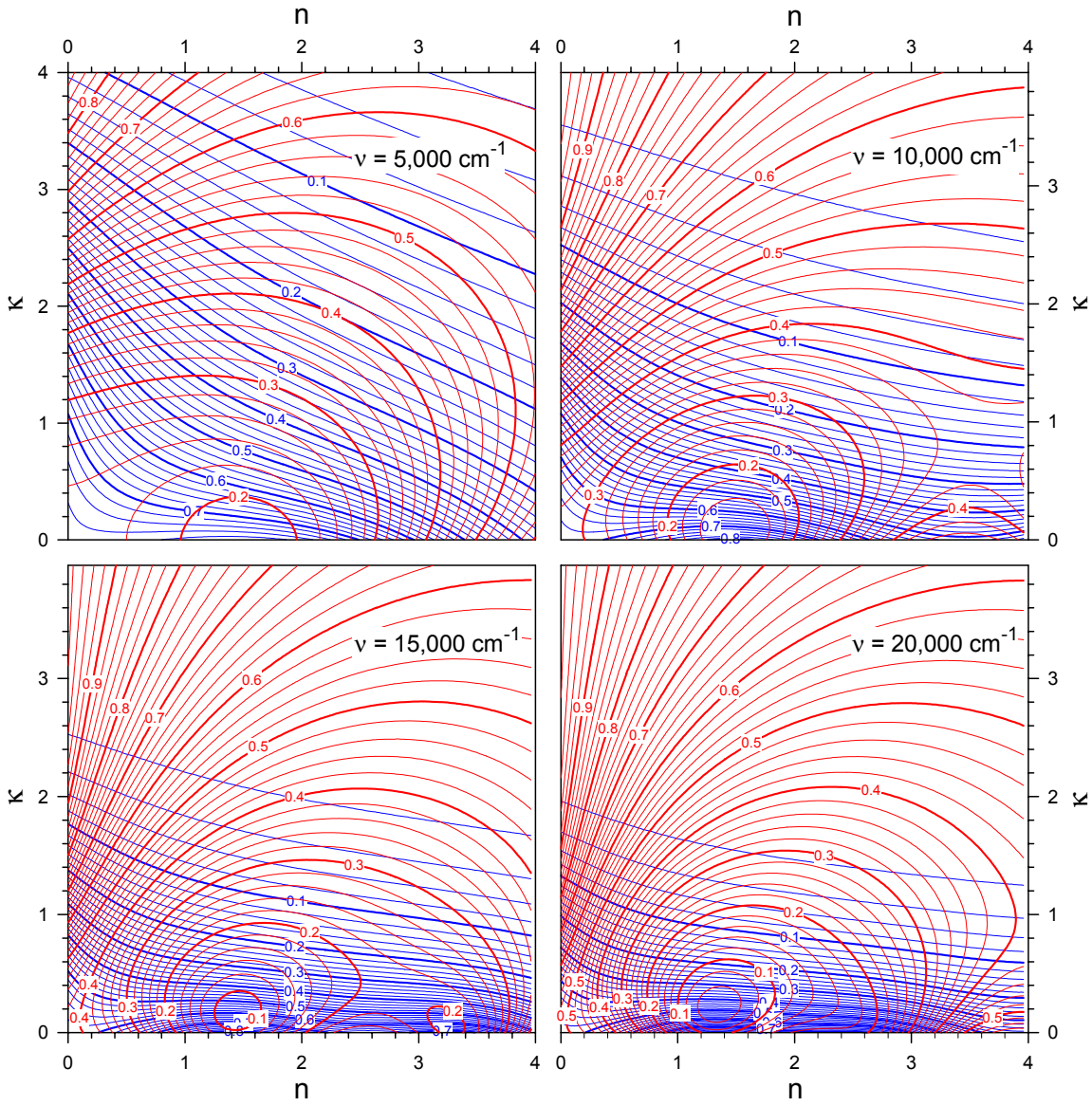

Figure 2.11: Transmittance (blue) and reflectance (red) contours for a film on a non-absorbing substrate as a function of the index of refraction n and extinction coefficient κ for a thin film on a substrate. Parameter values for the substrate are $n_s = 2$, $k_s = 0$, and $d_s = 0.05\,\text{cm}$. The film thickness is $100\,\text{nm}$.

whenever a multiple root becomes degenerate (root crossing). In practice, this requires appropriately selecting initial conditions in the least-squares fit employed to extract n and k from Eqs. (2.39) and (2.40) Further complications arise in film transparency regions, where the small value of k results in additional roots. The n values are particularly sensitive to these roots, while k remains roughly constant. These

complications lessen with increasing film absorption.

Numerical inversion of the $\mathcal{T}_f$ and $\mathcal{R}_f$ formulae for a thin film on a weakly absorbing substrate yield the optical properties of the thin films. This procedure yields the index of refraction and extinction coefficient of the thin-film material, n and κ, respectively, using n_s and κ_s for the substrate. The results of n and κ are then used to derive the other optical coefficients, *e.g.*, the complex dielectric function, $\tilde{\epsilon}(\omega)$ or the complex optical conductivity $\tilde{\sigma}(\omega)$.[80] This technique avoids extrapolation errors associated with Kramers-Kronig analysis and permits reliable measurement of the optical conductivity up to the high frequency cutoff of the spectrometer ($5\,\mathrm{eV}$).

Chapter 3

Colossal Magnetoresistance in the Ortho-Manganites

3.1 Introduction

Optical studies provide great promise for understanding the underlying physical principles govern the colossal magnetoresistance (CMR) manganites. Measurements of the optical conductivity afford comparison with the predictions of band theory models, which describe the relevant electronic states. The double exchange model proposed by Zener[25] (and discussed in more detail in Chap. 1) provides an explanation of the observed dc and ac transport properties in the doped ferromagnetic manganites. While DE qualitatively describes the metal-insulator transition at T_c, recent experimental[27–29] and theoretical[30–33] work indicates the importance of coupling, specifically the dynamic Jahn-Teller (JT) effect, between charge and the lattice in explaining the high temperature insulating phase. Optical absorption studies of the stoichiometric parent compound $LaMnO_3$ give evidence for static JT distortions. Moreover, analysis of the optical conductivity of $LaMnO_3$ within the local-spin-density approximation suggests that the observed gap in the optical conductivity of about 1.0 eV corresponds to the optical process of promoting a hole between the JT split e_g bands on the Mn^{3+} ions.[41]

Optical measurements have also been reported for the series of compounds $(La,Sr)MnO_3$.[42,43] The results from optical reflectivity studies of metallic samples ($x > 0.2$) show large transfers of spectral weight from high frequencies to low fre-

quencies as the samples cool from the paramagnetic state through T_c into the ferromagnetic metallic state.[42,43] These studies conclude that a simple DE picture does not explain the observed changes in the optical spectral weight over such a large energy scale compared to $k_B T$ for all doping concentrations.[42,43] The observed spectral weight transfers suggest the important influence of Jahn-Teller lattice distortions on the electronic states. The localization of e_g electrons on the Mn^{3+} ions in the paramagnetic state of the doped manganites results in a self-trapping effect, *i.e.*, a small polaron.[32] An optical signature associated with the photo-induced hopping of the carriers accompanies a small polaron. In addition to the importance of coupling with the lattice and ferromagnetic order, other types of order have been reported in the manganites. Charge and orbital ordering have been observed at certain dopings; suggesting the ground state of the doped manganites may result from a competition of various types of order. The observance of anomalously small Drude weights in the metallic manganites has been cited as evidence for the existence of charge ordering.

The remainder of this chapter presents a detailed optical study of the orthorhombic manganites, including the parent compound and alloys doped in the range exhibiting CMR effects. The first section discusses the optical properties of $LaMnO_3$, focusing on the relevant low-lying electronic excitations. In addition, this section presents the phonon spectra. The next section addresses changes in the optical properties upon doping with divalent cations. This analysis includes identifying the relevant optical transitions and spectral weights characteristic of several alloys doped at $x = 0.3$. The final section addresses the observation of anomalously small Drude weights, including the effects of charge ordering on the mass enhancement. The low-frequency behavior of the Drude-like conduction in the far-IR at low temperatures will be examined. An extension of the Drude model above the far-IR includes a frequency-dependent scattering rate relevant for strong electron-phonon interactions and necessary for restoring the observed infrared

spectral weight.

3.2 $LaMnO_3$

3.2.1 Parent compound of the CMR manganites

The rich phase diagram of the doped manganite $La_{0.7}Ca_{0.3}MnO_3$ shown in Fig. 1.3 motivates research interest in understanding of the stoichiometric parent compound $LaMnO_3$. Room temperature optical measurements[39] report evidence of static Jahn-Teller (JT) effects in $LaMnO_3$. In the doped alloys, JT interactions are believed to be dynamic and play a pivotal role on phase transitions, particularly the "colossal" magnetoresistance (CMR) effect.[3,30] Below the antiferromagnetic Néel temperature, $T_N \approx 140\,\mathrm{K}$, Mn spins align ferromagnetically in the ab-plane and antiferromagnetically along the c-axis (A-type antiferromagnetic order). In addition to spin order, $LaMnO_3$ displays orbital ordering. In-plane occupied Mn e_g orbitals alternate between $d_{3x^2-r^2}$ and $d_{3y^2-r^2}$ in the C-type orbital order below the orbital ordering temperature $T_{OO} \approx 780\,\mathrm{K}$ (Ref. 21).

Optical spectroscopy studies of $LaMnO_3$ provide insight into the physics governing both the doped and undoped manganites. Jung *et al.*[39] identify the low energy electronic transitions in a room temperature optical conductivity study. However, no temperature dependence was reported. Various interpretations of the assignment of the optical transitions remain uncertain. Clearly, a more complete understanding of the optical transitions including temperature dependence is required.

This section presents optical conductivity studies of $LaMnO_3$, including the temperature dependence of the phonon and electronic spectral regions. Kramers-Kronig analysis provides $\tilde{\sigma}(\omega)$ from bulk reflectance measurements over a wide spectral range ($20 - 50,000\,\mathrm{cm}^{-1}$) at temperatures from $300 - 10\,\mathrm{K}$. In the spectral range of electronic transitions, absorption features at approximately $2\,\mathrm{eV}$ and $4\,\mathrm{eV}$ characterize the conductivity spectra. The stronger $4\,\mathrm{eV}$ feature is attributed to the O $2p$ -

Mn $3d$ charge transfer transition ubiquitous in the perovskite transition metal oxides.[44] Remarkably, the 2 eV feature grows in oscillator strength as temperature lowers. This strong temperature dependence of the spectral weight agrees with models considering this feature as a Mn-Mn *inter-site* transition, contrary to the predictions of Allen and Perebeinos.[87] At lower frequencies, phonons dominate the optical conductivity of this insulating material. Several phonons exhibit temperature dependent shifts of the transverse optical frequencies that correlate with T_N. These shifts provide evidence of spin-phonon coupling.

3.2.2 Measurement details

Samples

The floating-zone technique prepares single crystals of stoichiometric $LaMnO_3$. Dispersive x-ray, microwave absorption, and neutron-scattering experiments characterize the quality of the samples. Neutron scattering results[40] show the temperature dependence of the (003) antiferromagnetic Bragg peak intensity. Fig. 1 of Ref. 27 shows a sharp onset of scattering intensity at the antiferromagnetic Néel temperature $T_N = 139\,\mathrm{K}$ and hence confirms the A-type antiferromagnetic ordering of Mn spins in $LaMnO_3$.

Additional x-ray diffraction and neutron diffraction studies find the crystals to be heavily twinned. Near-field scanning microscopy (NSOM) measurements,[40] display a variation of reflectance intensity corresponding to the anisotropic optical response of randomly oriented twinned domains. The NSMO data indicate domains with a typical dimension of $\approx 0.2\,\mu$m.

Optical techniques

Polishing with a $0.3\,\mu$m diamond paste prepares the optical surfaces. Takenaka *et al.*[88] reported large changes in reflectance for $(La,Sr)MnO_3$ after polishing. Polishing reduced the infrared reflectance and subsequently the spectral weight.

While a post-polish annealing restored some of the damage, even annealed samples showed losses relative to cleaved samples. For the undoped parent compound, polished surfaces exhibited little change versus cleaved surfaces.[88] Therefore, polishing should not have introduced spurious reflectance effects in the $LaMnO_3$ sample studied here and no post-polish annealing was performed.

Fourier-transform spectroscopy provides bulk reflectance $\mathcal{R}$ measurements of the $LaMnO_3$ sample in the usual way.[89] Frequency extrapolations of $\mathcal{R}$ spectra to 0 and ∞ necessary for Kramers-Kronig (K-K) analysis are performed as follows. Low-frequency $\mathcal{R}$ extrapolates to dc as a constant, consistent with the insulating dc resistivity behavior. For frequencies above the measurement range, merging $\mathcal{R}$ with the room temperature data of Jung *et al.*[39] extends the spectra to $30\,\text{eV}$. Beyond $30\,\text{eV}$, the usual free electron behavior, $\mathcal{R} \sim \omega^{-4}$, power law serves to extrapolate the data. As seen in the results section below, the measured $\mathcal{R}$ exhibits temperature dependence at the upper limit ($\approx 5\,\text{eV}$) of the measurements and hence the extrapolations should be temperature dependent as well. In order to satisfy the reflectance sum rule,

$$\int_0^\infty \ln\left[\frac{\mathcal{R}(T_1,\omega)}{\mathcal{R}(T_2,\omega)}\right] \mathrm{d}\omega = 0\,, \tag{3.1}$$

where T_1 and T_2 are two different temperatures, the temperature-dependent trend in $\mathcal{R}$ must be reversed at higher frequency. For the purposes of the K-K analysis, the addition of temperature dependence in $\mathcal{R}$ between $5 - 10\,\text{eV}$ ensures all temperatures merge by $12\,\text{eV}$. Reference 40 presents further details of this temperature dependent extrapolation technique. This extrapolation procedure satisfies the sum rule of Eq. (3.1) with little affect on the measured spectra below $\approx 4.5\,\text{eV}$.

Reflectance spectra

Figure 3.1 displays the temperature dependence of the bulk reflectance over the measured spectral range at temperatures from $10 - 300\,\text{K}$. The dashed black

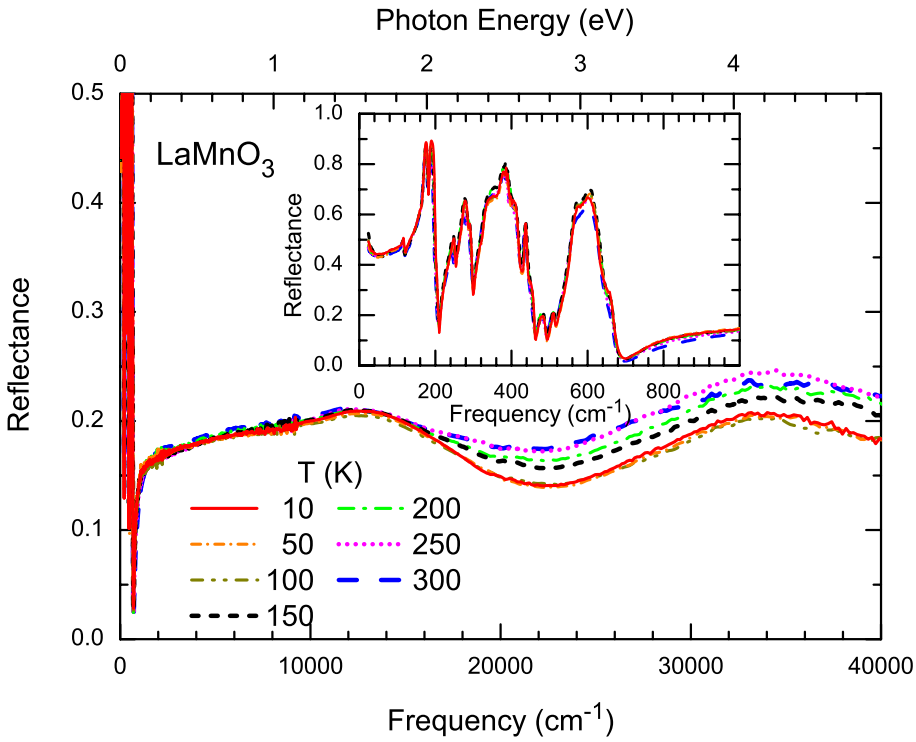

Figure 3.1: Temperature dependence of reflectance spectra for $LaMnO_3$. Inset highlights phonons in the far-infrared region.

curve represents $\mathcal{R}$ at $T = 150\,\text{K}$, near the Néel temperature T_N. In the visible region, $\mathcal{R}$ decreases with decreasing temperature. The largest reduction in $\mathcal{R}$ occurs between $300 - 150\,\text{K}$, with saturation below $T \approx 100\,\text{K}$. Temperature dependence in $\mathcal{R}$ above $\approx 2\,\text{eV}$ persists to the experimental cutoff frequency ($\approx 5\,\text{eV}$). Although the measurement errors increase as the frequency approaches the instrumentation limits, the observed temperature dependence exceeds the measurement uncertainty. However, such temperature dependence at the cutoff complicates the K-K analysis, as mentioned earlier.

In the far-infrared (far-IR), optically active phonons appear clearly in the reflectance spectra, typical for an insulator. The inset of Fig. 3.1 highlights phonons in the spectral region below $0.125\,\text{eV}$. Randomly oriented twinned domains in this sample provide an average response of the three crystallographic directions and

preclude polarization dependent studies. As a result, the measured spectra contain all symmetry-allowed IR phonons. The Lorentz sum model given by Eq. (2.30) fits the reflectance spectra. The resulting fit parameters describe the phonon parameters, transverse optical (TO) frequency, scattering rate, and oscillator strength. In general, the observed phonons show a shift towards higher frequency (harden) and narrow in width with decreasing temperature. Shifts of the TO phonon frequencies are addressed below.

3.2.3 Results

Electronic conductivity spectra

The K-K analysis of the bulk reflectivity shown in Fig. 3.1 provides the complex optical conductivity $\tilde{\sigma}$. Figure 3.2 displays the real part of the optical conductivity σ_1 in the electronic spectral range for the measured temperatures. Two main absorp-

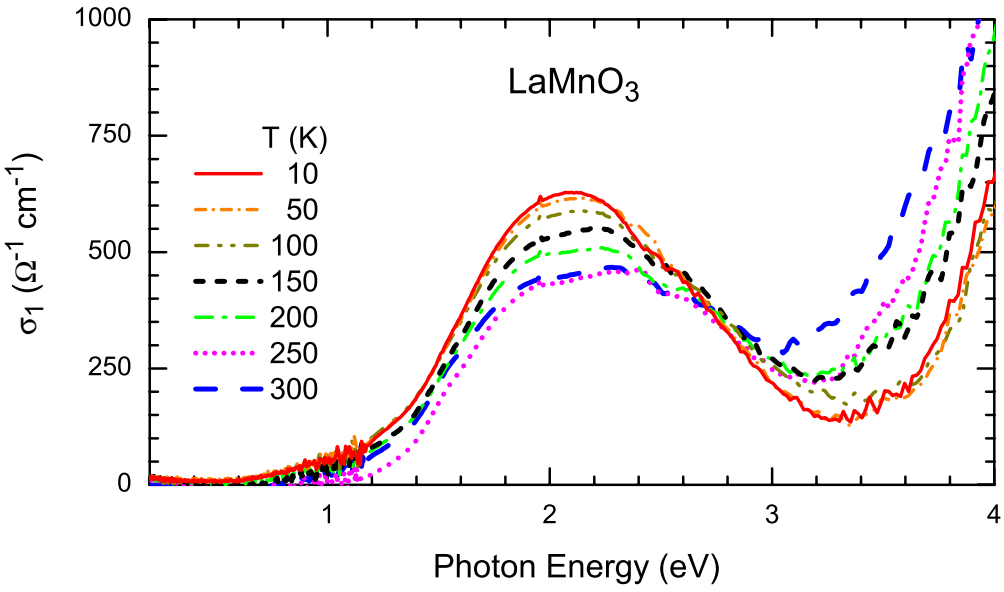

Figure 3.2: Temperature dependence of the electronic conductivity spectra of $LaMnO_3$.

tion features at ≈ 2 eV and $4-5$ eV characterize σ_1. These features agree well with earlier room temperature measurements.[39,44,88] The 2 eV feature exhibits a remark-

ably strong temperature dependence. As temperature lowers, the feature sharpens and increases in spectral weight, while no significant shift of the peak energy occurs. Strong temperature dependence persists to the high-frequency cutoff. However, the dependence of the K-K analysis on the high frequency extrapolation limits accurate determination of σ_1 above ≈ 4 eV. However, the 2 eV feature remains relatively insensitive to K-K extrapolations. Evidently the spectral weight increase of the 2 eV feature below room temperature balances with a decrease of spectral weight at higher energies. More recent optical measurements on *detwinned* crystals[90,91] confirm the results reported here. Both FTIR spectroscopy (Ref. 90) and ellipsometry (Ref. 91) report a decrease (increase) with increasing temperature in the 2 eV feature for the $E \parallel ab$ ($E \parallel c$) polarizations. In particular the more accurate ellipsometry data shows a correlation of the spectral weight with T_N.

Figure 3.3 shows temperature dependence of the peak position energy (circles) and the spectral weight (squares) for $LaMnO_3$. The peak position results from sub-

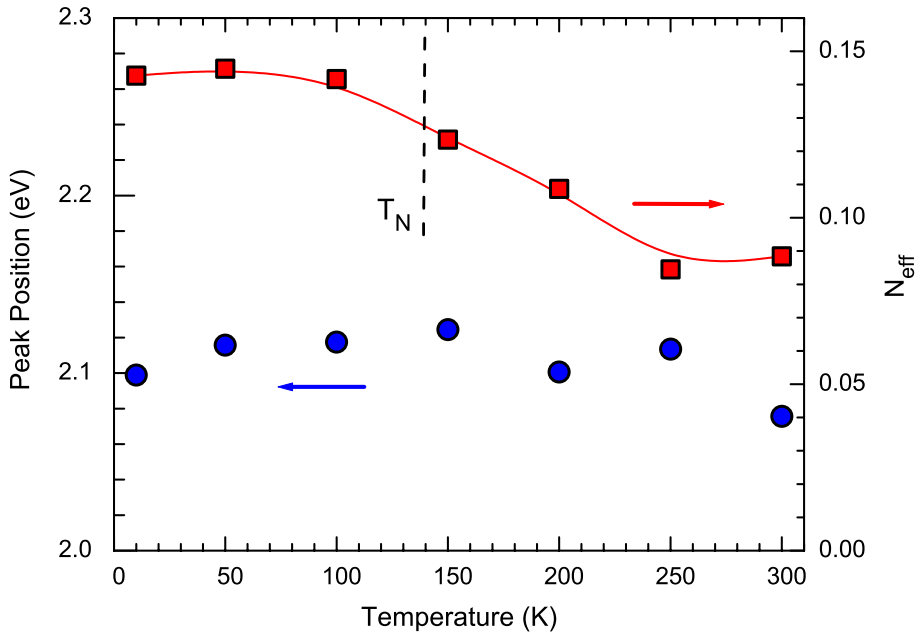

Figure 3.3: Temperature dependence of the 2 eV peak energy (circles) and spectral weight in N_{eff} (squares). Solid line guides the eye.

tracting the higher-energy $4\,$eV transition and fitting the remaining conductivity feature with a Gaussian function. While similar peak energies result from Lorentzian fits, the Gaussian fit better suites the data, suggesting this feature may represent several optical transitions.[91] As evidenced in Fig. 3.3, the peak positions shifts $< 2\,\%$ over the measured temperature range, remaining essentially constant within the measurement certainty. The behavior of the peak position contrasts sharply with the spectral weight [defined in Eq. (2.23)] of the $2\,$eV feature (conductivity integrated to $3\,$eV) shown in Fig. 3.3. The results expressed in Fig. 3.3 are given in terms of N_{eff}, the effective number of carriers per formula unit. At room temperature, N_{eff} decreases by $\approx 36\,\%$ of the low temperature value, showing a particularly rapid decrease and inflection point around T_N.

Phonon spectra

A simple sum of Lorentz oscillators given by Eq. (2.30) for the dielectric constant and Eq. (2.29) fits the far-IR reflectance spectra. The Lorentz model parameterizes each oscillator by the transverse optical (TO) frequency ω_{TO}, damping γ, and spectral weight A_j^2, resulting in 3 fitting parameters per phonon. Table 3.1 lists the phonon parameters resulting from a least-squares fit to the measured $\mathcal{R}$ at various temperatures. The inset of Fig. 3.4 shows the excellent agreement between the fitted and measured $\mathcal{R}$ spectra for room temperature.

The fit parameters in Table 3.1 define the complex dielectric constant $\tilde{\epsilon}$. The optical conductivity may be obtained from the dielectric constant, $\sigma_1(\omega) \propto \mathrm{i}\,\omega\,\epsilon_2(\omega)$. Figure 3.4 shows the real part of the optical conductivity σ_1 and the real part of the dielectric constant ϵ_1 in panels (a) and (b), respectively, in the far-IR for various temperatures. A large number of peaks (≈ 20), corresponding to transverse optical (TO) phonon vibrations of atoms, appear clearly in this spectral range. A comparison of the optical constants obtained from the fit parameters to that obtained from K-K

	Temperature (K)						
	10	50	100	150	200	250	300
$\omega_{TO,1}$	117.96	117.62	117.48	116.78	116.24	115.41	114.92
γ_1	3.84	3.09	3.90	3.01	3.68	5.90	6.51
A_1	64.51	56.78	65.57	55.54	61.90	78.18	78.50
$\omega_{TO,2}$	172.88	172.84	172.71	172.25	172.38	171.38	170.71
γ_2	3.08	3.02	2.99	2.94	3.49	4.51	5.30
A_2	432.23	427.77	429.58	380.28	413.76	414.43	401.66
$\omega_{TO,3}$	184.23	183.99	183.91	185.62	182.60	182.33	181.79
γ_3	4.47	4.54	4.37	10.96	5.47	6.31	7.00
A_3	211.41	219.62	217.09	199.43	215.11	209.20	200.23
$\omega_{TO,4}$	203.39	203.49	203.28	202.23	201.24	201.15	200.25
γ_4	8.97	7.30	7.47	10.39	10.18	7.92	8.00
A_4	78.64	66.23	67.28	89.81	86.42	66.05	61.44
$\omega_{TO,5}$	249.00	248.81	248.52	248.18	247.43	246.32	244.80
γ_5	6.95	8.05	9.02	7.16	6.79	8.39	7.47
A_5	178.18	179.17	184.06	177.73	161.52	153.21	132.07
$\omega_{TO,6}$	276.93	277.06	276.55	275.49	275.08	275.16	274.38
γ_6	11.08	11.21	11.64	11.22	10.98	12.46	12.81
A_6	403.35	389.11	394.43	414.65	398.78	369.55	341.75
$\omega_{TO,7}$	289.90	289.97	289.40	288.06	287.10	286.98	286.06
γ_7	6.89	7.32	7.89	9.17	10.41	11.50	12.67
A_7	156.48	159.28	163.58	186.42	203.26	196.32	219.81
$\omega_{TO,8}$	317.78	317.95	317.23	316.09	313.01	311.58	316.09
γ_8	4.64	4.34	4.53	2.89	2.47	0.00	8.46
A_8	77.85	64.68	61.79	48.04	34.88	0.53	0.00
$\omega_{TO,9}$	335.40	336.14	335.38	334.00	333.07	332.96	332.15
γ_9	13.35	14.60	14.46	14.62	13.99	14.21	15.04
A_9	438.69	448.19	443.56	492.44	464.77	425.89	437.92
$\omega_{TO,10}$	347.99	350.14	349.11	348.00	346.22	346.91	345.46
γ_{10}	18.34	19.04	19.32	19.09	18.92	21.07	20.76
A_{10}	404.94	405.67	412.81	428.03	442.60	460.66	435.44
$\omega_{TO,11}$	366.34	367.91	367.32	366.18	364.91	365.70	365.20
γ_{11}	22.41	19.33	21.94	20.12	22.70	21.01	23.11
A_{11}	404.83	366.14	384.75	343.42	370.58	349.72	355.22
$\omega_{TO,12}$	402.12	401.87	404.34	404.33	405.14	400.61	400.58
γ_{12}	21.52	25.42	25.67	27.17	30.32	37.65	28.68
A_{12}	158.51	183.39	167.53	169.26	174.68	210.46	175.21
$\omega_{TO,13}$	431.77	432.11	432.05	431.41	430.93	430.34	428.89
γ_{13}	12.43	12.15	12.19	12.31	12.11	12.91	13.33
A_{13}	164.06	162.04	160.18	155.32	150.05	150.36	146.27
$\omega_{TO,14}$	450.40	450.59	450.68	450.50	450.28	449.93	448.49
γ_{14}	11.24	11.26	11.10	10.77	12.48	12.72	14.78
A_{14}	92.32	93.04	87.59	72.83	70.78	68.15	75.68
$\omega_{TO,15}$	480.42	481.06	480.62	480.03	479.14	479.05	478.30
γ_{15}	18.34	17.72	18.72	19.80	21.82	23.06	23.31
A_{15}	163.75	161.66	166.41	172.35	176.05	166.00	165.99
$\omega_{TO,16}$	511.00	511.38	511.33	510.99	510.39	510.12	508.43
γ_{16}	6.58	5.95	6.75	7.95	9.95	9.79	11.59
A_{16}	91.61	84.61	92.48	102.77	108.45	94.59	106.87
$\omega_{TO,17}$	565.33	566.08	564.89	562.47	562.21	562.60	559.85
γ_{17}	15.39	13.78	15.46	18.74	18.87	20.06	23.76
A_{17}	492.70	487.90	505.53	544.22	517.31	529.15	503.76
$\omega_{TO,18}$	582.61	583.92	583.43	584.34	581.76	582.66	580.44
γ_{18}	31.78	29.82	30.99	30.05	34.00	33.88	36.02
A_{18}	355.56	363.82	337.22	259.61	306.09	293.24	287.83
$\omega_{TO,19}$	646.19	647.53	648.72	649.54	650.65	650.63	649.53
γ_{19}	38.33	36.87	36.59	34.27	33.44	38.28	39.54
A_{19}	159.45	152.55	144.14	127.98	122.28	129.79	119.87
ϵ_∞	6.68	6.63	6.58	6.53	6.52	6.41	6.02

Table 3.1: Fitting parameters for $LaMnO_3$ for various temperatures. Values are in cm^{-1} except for ϵ_∞.

analysis reveals no essential differences between the two methods.

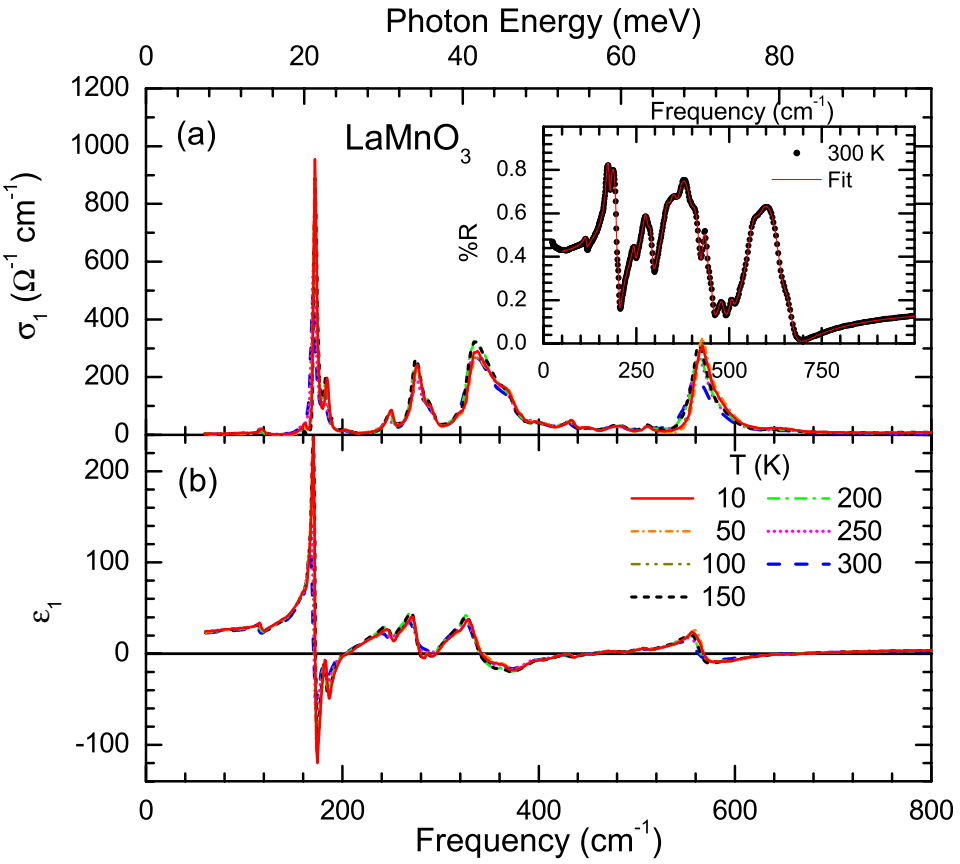

Figure 3.4: Real part of (a) the optical conductivity σ_1 and (b) the dielectric constant ϵ_1 of $LaMnO_3$ in the far-infrared for various temperatures. Inset shows the $300\,K$ data (circles) together with the Lorentzian fit (solid line).

A basic identification of the phonon modes results from considering ionic displacements in the harmonic approximation, in which the modes at lowest frequency correspond primarily to motion of the heavy La ions, while the modes at highest frequency (around $600\,cm^{-1}$) corresponds to motion of the light O ions. At intermediate frequencies, modes consist primarily of Mn ion displacements, in combination with O and La motion. More exact modal assignments can be made by analogy with those discussed in Refs. 92, 93, and 94. In the orthorhombic phase ($T < T_{JT} \approx 750\,K$),[95] $LaMnO_3$ crystallizes in the orthorhombic structure with space group $Pnma(D_{2h}^{16})$. A group-theoretical analysis[92] for the Γ-point phonon modes finds 25 IR active modes:

9 with B_{1u} symmetry, 7 with B_{2u} symmetry, and 9 with B_{3u} symmetry. Phonon modes with B_{1u}, B_{2u}, and B_{3u} symmetry corresponding to oscillations of the dipole moment along the z, y, and x axes respectively.[93]

Generally, the TO phonon frequencies ω_{TO} shift to higher frequency and the phonon widths sharpen with decreasing temperature. Several of the phonons resolve more clearly at lower temperatures, particularly for modes near 161, 184, 290, and 650 cm^{-1}. Raman studies report[96] a similar increase in the number of phonon modes at lower temperatures. An increase in the total number of phonon modes at lower temperatures might suggest a lowering of the crystal symmetry, consistent with the observation of a more cubic crystal structure in the paramagnetic state. However, Paolone *et al.*[93] argue that neutron diffraction experiments[95] observe no change in crystal symmetry below ≈ 750 K and hence the apparent increase in the number of modes results simply from an increased ability to resolve the narrower low-temperature phonons lines. Additional temperature dependence of the phonons, specifically ω_{TO}, is discussed in detail below.

3.2.4 Discussion

Origins and spectral weight of the 2 eV feature

Various interpretations of the origin of the 2 eV feature exist in the literature. Allen and Perebeinos interpret[87] the 2 eV feature as a phonon-assisted on-site electronic excitation between JT split Mn e_g orbitals. In cubic crystals optical selection rules forbid on-site d-d transitions. However, lattice distortions resulting from asymmetric oxygen breathing modes in $LaMnO_3$ provide p-orbital admixture and may allow for on-site Mn d-d transitions in $LaMnO_3$.[87] Electronic excitations from the JT ordered ground state self-trap by local distortions of the lattice. The predicted optical conductivity spectrum consists of a Franck-Condon series, *i.e.*, a broad Gaussian envelope of vibrational sidebands. The onset of absorption begins at Δ (or E_{JT}) the JT splitting

energy and peaks at 2Δ. Dispersion of phonons and electron states and phonon lifetime broadening (not included in the model) tend to smear the fine structure of the Franck-Condon spectra, leaving only the Gaussian envelope. Regarding temperature dependence, Allen and Perebeinos predict[87] very weak temperature effects near the peak of absorption at 2Δ. Specifically their model model does not depend on magnetic order and predicts no special dependence of either the peak energy or spectral weight near T_N. The temperature-dependent spectral weight observed in Fig. 3.3 and reported in Ref. 91 definitively contradict the predictions of the Franck-Condon model as put forth by Allen and Perebeinos.

Raman spectroscopy provides an additional experimental technique to measure the predicted[87] multiphonon behavior. Raman studies[97,98] on $LaMnO_3$ report evidence for weak multiphonons. While these results are consistent with a phonon-assisted optical absorption process, the Raman spectra provide no estimate of the spectral weight of the associated optical transition. Generally, such phonon-assisted optical transitions are much weaker than symmetry-allowed interband charge-transfer transitions expected in this class of materials.[40]

The failure of the Franck-Condon picture to predict the temperature dependence of the 2 eV feature suggests some other physics governs the low-lying electronic states in $LaMnO_3$. Solovyev *et al.*[41] employ the local-density approximation (LDA) plus electron-electron interactions (LDA+U) to determine the band structure. The authors report a model considering localized t_{2g} levels and itinerant e_g levels that well describes the observed physical properties. In their model, $U \approx 1.5$ eV and $J \approx 1$ eV. Furthermore, in these LDA+U calculations, the minimum optical gap in $LaMnO_3$ results from the excitation of electrons between the JT split e_g levels.[41] This theoretical treatment predicts a band structure and optical conductivity for the ground state only.

Consideration of the temperature dependence requires including effects on the

hopping amplitude of the charge-transfer e_g-e_g transition due to the spin-selection rules. In the ground state, the A-type antiferromagnetic order consists of ferromagnetically aligned spins in the ab plane and antiferromagnetically aligned spins along the c axis. Each Mn has six nearest-neighbors in the pseudocubic crystal, four in the plane and two along c. Hence the probability for transitions in the parallel spin manifold $e^1_{g\uparrow}$-$e^2_{g\uparrow}$ is $2/3$, while antiparallel $e^1_{g\uparrow}$-$e^2_{g\downarrow}$ is $1/3$. Far, above the magnetic ordering temperature T_N, spins align randomly in all directions. Nearest-neighbor Mn spins are equally likely to be parallel or antiparallel and the probabilities of $e^1_{g\uparrow}$-$e^2_{g\uparrow}$ and $e^1_{g\uparrow}$-$e^2_{g\downarrow}$ are both $1/2$. Thus, the spectral weight of the $2\,$eV feature should decrease by

$$\Delta S = \frac{S(10\,\mathrm{K}) - S(300\,\mathrm{K})}{S(10\,\mathrm{K})} = \frac{2/3 - 1/2}{2/3} = 25\,\%\,, \tag{3.2}$$

above T_N. Similarly, this simple model predicts that the higher transition (buried in the O $2p$ to Mn $3d$ transition) should increase by $50\,\%$. Fig. 3.3 shows the average spectral weight decreases by approximately $36\,\%$ from low temperature to well above T_N, in qualitative agreement. Moreover, polarization dependent ellipsometry[91] on a *detwinned* single crystal quantitatively supports these predictions.

While the addition of spin-selection rules to the LDA+U model provides a qualitative explanation of the temperature dependence, a more quantitative comparison requires a model taking into account the optical anisotropy of the e_g orbitals.[40] Ahn and Millis[99] offer such a realistic model. The authors considered a model Hamiltonian using a tight-binding parameterization of the band structure along with mean-field treatment of Hund, electron-electron, and electron-lattice coupling.[99] Predictions from this calculation are most easily compared to the measured optical response by consideration of the optical spectral weight, or equivalently the kinetic energy of the $2\,$eV feature. The kinetic energy K is given by Eq. (2.25) and the conductivity is integrated up to $3.0\,$eV to include the transition of interest. Table 3.2 compares the measured K with tight-binding predictions for temperatures $300\,$K and $10\,$K.

	Kinetic Energy (eV)	
T (K)	Experiment	Theory[a]
300	0.066	0.086
10	0.082	0.130[b]

[a] Theoretical predictions result from integration of revised Fig. 6 in Refs. 99, 100, and 101.
[b] Derived for $T = 0$.

Table 3.2: Spectral weight, expressed in units of kinetic energy, of the $2\,\text{eV}$ optical transition in $LaMnO_3$.

The parameter values used in the predictions are the following: $U = 1.59\,\text{eV}$, $\lambda \approx 1.38\,\text{eV/Å}$, and $2\,J_H\,S_c \approx 2.47\,\text{eV}$.[101] Both experiment and theory show an increase in K at low temperatures. In the theory, double exchange correlations between the spin-dependent hopping amplitudes drive the temperature dependence. The temperature dependence increases with the Hund's coupling energy $J_H\,S_c$ and the Coulomb energy U and decreases with increased coupling constant λ. Theoretical values listed in Table 3.2 overestimate the observed kinetic energy of the $2\,\text{eV}$ feature. This discrepancy may arise from the strength of Coulomb interactions.[99] The finite U employed in the model calculation substantially reduces K of the $2\,\text{eV}$ feature. However, theoretical values in Table 3.2 still exceed the experimental observations.

In addition to the tight-binding parameterization of the band-structure, Takahashi and Shiba report[102] a calculation of the e_g interband optical conductivity including the on-site Coulomb interaction effects to lowest order in perturbation theory. The calculated optical conductivity for small $U/6\,t_0$ extends to $\omega = 4\,t_0 \approx 2.4\,\text{eV}$, has a broad maximum at $\omega \approx 3\,t_0 \approx 2\,\text{eV}$, and is otherwise relatively featureless. The experimental data reported here and in Refs. 27 and 40 are in good qualitative and semi-quantitative agreement with the calculated conductivity, suggesting that the Coulomb effects are small.

The tight-binding model discussed above suggests the spectral weight of the

2 eV feature should correlate with the Mn spin order, changing abruptly at T_N and remaining constant at higher temperatures. However, the temperature dependence seen in σ_1 (Fig. 3.2) and N_{eff} (Fig. 3.3) continues above T_N. Note the optical transition depends on the nearest-neighbor spin-spin correlation function, which varies smoothly with temperature, not abruptly as does the long-range order probed in magnetization.[40] The observed changes in the optical spectral weight above T_N suggests the persistence of short-range order in $LaMnO_3$ perhaps extending beyond 300 K.

Phonon temperature dependence

Optically active phonons dominate the far-IR conductivity spectrum. Figure 3.5 shows the temperature dependence of the frequency shifts of ω_{TO} in panels (a) and (b) plotted relative to the phonon frequency at low temperature, $\Delta\omega_{\mathrm{TO}}(T) \equiv \omega_{\mathrm{TO}}(T) - \omega_{\mathrm{TO}}(10\,\mathrm{K})$. Panel (a) highlights phonons that harden smoothly with decreasing temperature, exhibiting no anomalous behavior around T_N. These phonons behave similarly to those undergoing the usual thermal shifts and lifetime effects resulting from lattice expansion and phonon anharmonicity observed in nonmagnetic materials.[40] However, several of the phonons do exhibit a temperature anomaly in ω_{TO} correlated with T_N. Specifically, $\omega_{\mathrm{TO}} = 277$, 290, 335, and 565 cm^{-1} phonons show inflection points near $T_N \approx 140$ K. This observation suggests that these modes couple strongest to the spin system. To highlight the similarity of this behavior, scaled frequency shifts, $-\Delta\omega(T)/\Delta\omega(300\,\mathrm{K})$, are plotted in Fig. 3.5 panels (c) and (d). Noise in ω_{TO} frequencies of several weaker phonons precludes investigation of an anomaly at T_N and are omitted from Fig. 3.5 for clarity. Lattice dynamical calculations[92,94] identify the symmetry of the IR allowed phonon modes. However, discrepancies in the calculated and experimentally observed phonon frequencies complicates identification of the specific modes exhibiting the magnetic anomaly.[93] In principle, polarization-dependent measurements on detwinned single crystals and

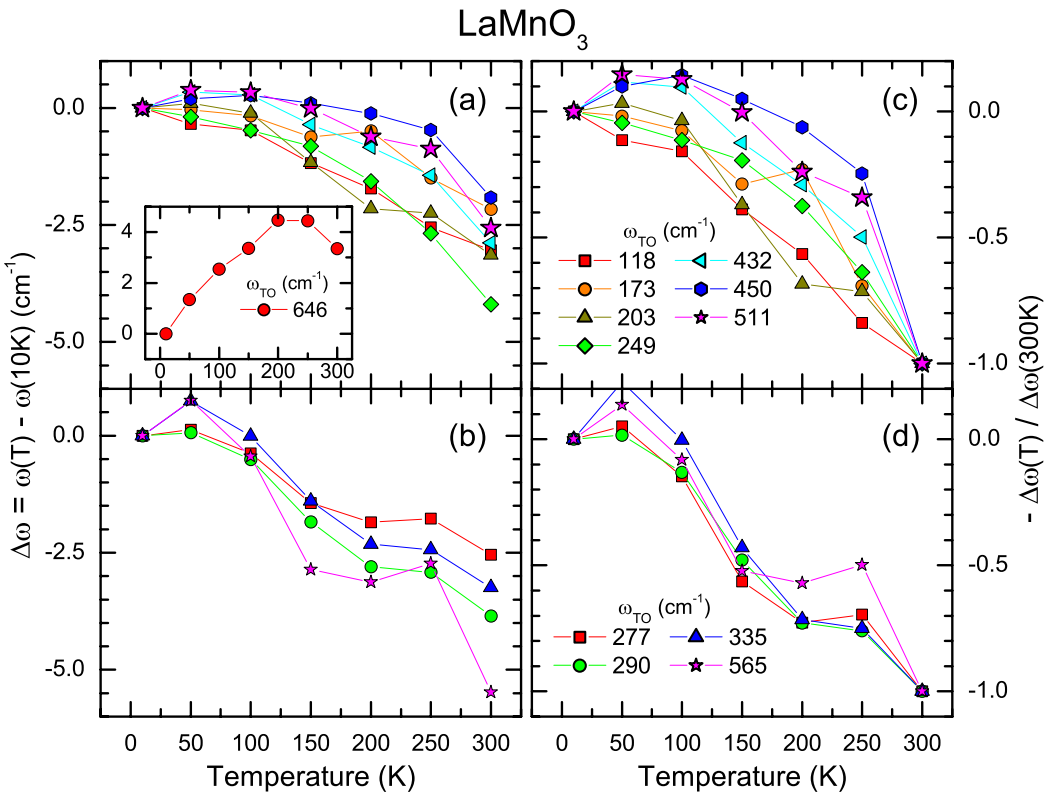

Figure 3.5: Temperature dependent shifts of TO phonon frequencies, $\Delta\omega(T) \equiv \omega(T) - \omega(10\,\mathrm{K})$ of $LaMnO_3$. Inset in (a) shows positive frequency shift with increasing temperature of the $645\,\mathrm{cm}^{-1}$ phonon. Scaled frequency shifts, $-\Delta\omega(T)/\Delta\omega(300\,\mathrm{K})$ shown in (c) and (d).

improved theoretical models would allow identification of the spin-coupled modes.

In addition to the observed hardening of the phonons with decreasing temperature, the $653\,\mathrm{cm}^{-1}$ phonon shown in the inset of Fig. 3.5(a) softens with decreasing temperature. Iliev *et al.*[92] observe a similar phonon in Raman spectroscopy. The breaking of inversion symmetry relaxes constraints on the generally mutually exclusive Raman and IR active phonon modes and may allow both spectroscopic techniques to observe the $645\,\mathrm{cm}^{-1}$ phonon. However, Iliev *et al.*[92] report the weak phonon varies among samples and thus appears to be of defect origin. Furthermore, Smirnova[94] suggests that theoretical calculations prohibit a single phonon mode of such high frequency. The exact nature of the $645\,\mathrm{cm}^{-1}$ mode remains uncertain.

The similarity of the frequency shift of the spin-coupled phonons and the temperature dependence of the spectral weight of the $2.0\,\mathrm{eV}$ feature (Fig. 3.3) suggests that both are related to the same, nearest-neighbor spin correlation function: $\langle \boldsymbol{S}_i \cdot \boldsymbol{S}_j \rangle(T)$. Phonon induced modulation of the exchange energy produced by the ion modal displacements provides an understanding of the phonon shifts. The change in exchange energy produces a corresponding change in the effective restoring force k and subsequently ω_{TO} for the phonon, $\Delta(\omega_{\mathrm{TO}}^2) \propto \Delta k$. Similar, stronger, spin-coupled phonons are observed in the hexagonal manganite $LuMnO_3$. Chapter 4 addresses the effects of the exchange interaction and spin-phonon coupling on ω_{TO} shifts in more detail.

3.3 CMR Alloys: Optical Conductivity and Spectral Weight

3.3.1 Introduction

This section presents a comparison of the optical conductivity derived from transmittance and reflectance measurements of thin films of $La_{0.7}Sr_{0.3}MnO_3$, $La_{0.7}Ca_{0.3}MnO_3$, and an oxygen-annealed $Nd_{0.7}Sr_{0.3}MnO_3$ as a function of temperature and for photon energies up to $5\,\mathrm{eV}$. The optical conductivity on these films show large shifts in spectral weight from visible to infrared frequencies as the temperature lowers through T_c, demonstrating large changes in electronic properties on an energy scale several orders of magnitude larger than $k_B T_c$. In the paramagnetic-insulating state, a broad maximum near $1\,\mathrm{eV}$ characterizes the optical conductivity at low energies and is interpreted in terms of the photon induced hopping of the Jahn-Teller small polaron. This spectral feature shifts to lower energy and grows in optical oscillator strength as the system enters into the ferromagnetic state, gradually transforming into a Drude-like response for $T \ll T_c$. Nevertheless, the polaron peak persists at temperatures substantially below T_c.

At higher frequencies, the spectrum of the real part of the optical conductivity

indicates the presence of a temperature dependent optical absorption feature centered at 3 eV and a large spectral feature at 4 eV which still has a weak temperature dependence. The 3-eV feature appears to be more prominent in the paramagnetic state. Additionally, the energy position of this feature suggests that it involves transitions between the Hund's rule spin-split e_g derived bands. The 4 eV feature most likely relates to a similar feature that observed in the undoped materials where it has been identified as a charge transfer transition between the O $2p$ and the Mn d derived bands.[44] Finally, this section presents an analysis of the magnitude and temperature dependence of the optical spectral weight.

3.3.2 Experimental

Sample Characterization

Pulsed laser deposition (PLD) provides thin films of $La_{0.7}Sr_{0.3}MnO_3$, $La_{0.7}Ca_{0.3}MnO_3$, and $Nd_{0.7}Sr_{0.3}MnO_3$ on $LaAlO_3$ substrates in an N_2O atmosphere.[103] X-ray diffraction reveals the epitaxial nature of the films and 3 MeV He^+ ion Rutherford backscattering channeling spectra with a minimum yield of $3.8\,\%$ indicates a high degree of crystallinity. Resistivity and ferromagnetic resonance measurements[104,105] provide additional characterization of these samples.

Figure 3.6 shows the temperature dependence of the resistivity, obtained using standard four-probe resistance measurements, for several CMR alloys. The temperature of peak resistivity, T_p, is 235 K for NSMO, 250 K for LCMO and 360 K for LSMO. Values of T_p coincide with the Curie temperatures T_c's in these samples, *i.e.*, $T_p \approx T_c$. In addition to the observed progression in T_p with dopant, the residual resistivity at low-temperature $\rho_0 \equiv \rho(10\,\mathrm{K})$. The values for ρ_0 are $350\,\mu\Omega$ cm for NSMO, $300\,\mu\Omega$ cm for LCMO, and $10\,\mu\Omega$ cm for the LSMO sample. Such low values for the residual resistivities indicate the high quality of these thin film samples. The observed low temperature resistivities correspond to conductivities greater than the Mott minimum

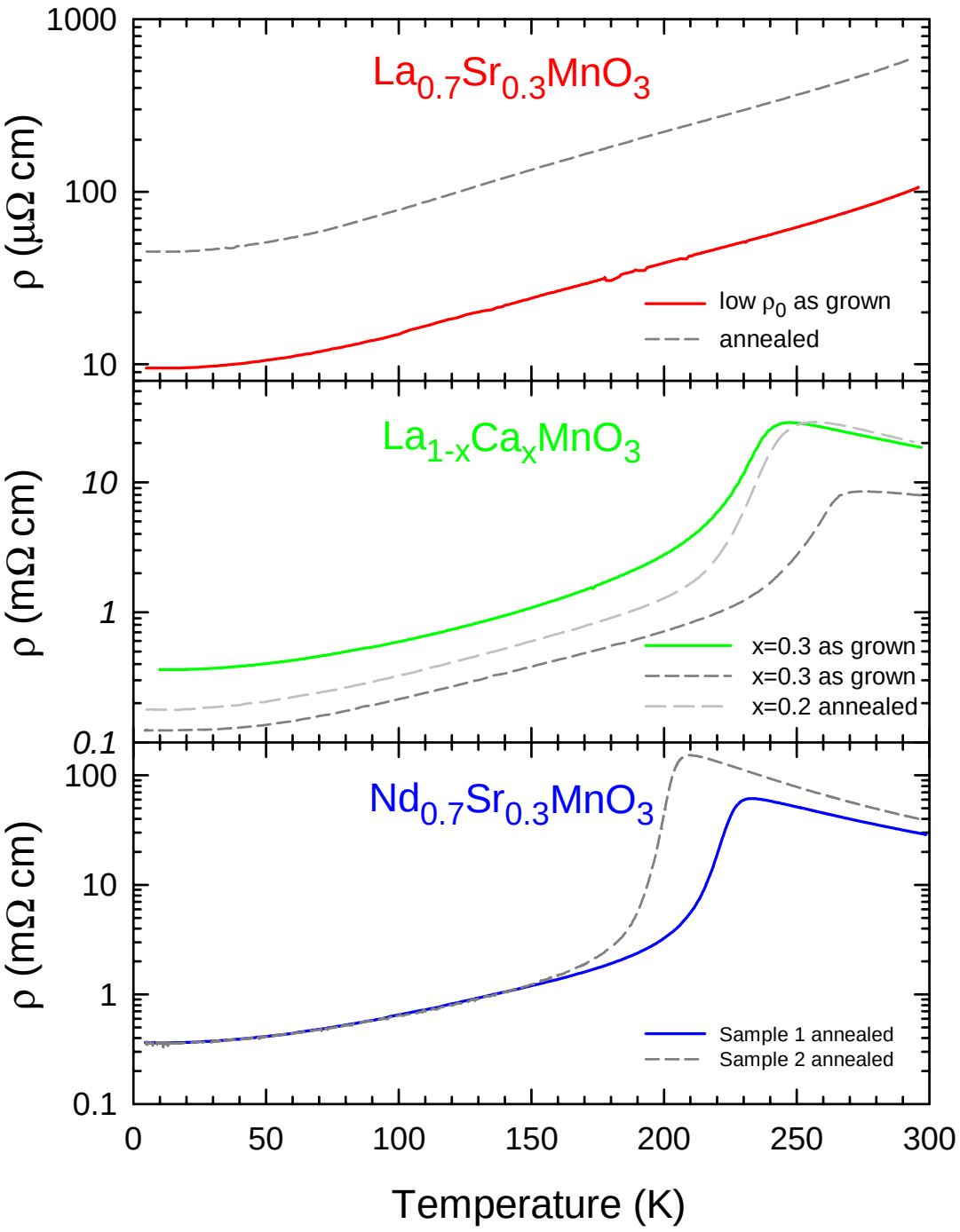

Figure 3.6: Temperature dependence of the resistivity for several hole-doped manganite alloys. The metal to insulator transition is apparent for the $Nd_{0.7}Sr_{0.3}MnO_3$ and $La_{0.7}Ca_{0.3}MnO_3$.

conductivity, $\sigma_{Mott} = 0.656\,(e^2/h)\,n^{1/3} \approx 500\,\Omega^{-1}\,\mathrm{cm}^{-1}$, where the carrier density n is determined by the divalent alkaline earth substitution. Low temperature resistivities previously reported in the literature for bulk and film samples generally correspond to conductivities below the Mott minimum conductivity, suggesting sample inhomogeneity.

Optical Techniques

Transmittance and reflectance measurements were performed using a Fourier transform spectrometer to cover the investigated regions of $5-25$ meV and $0.20-5$ eV. The measured frequency ranges correspond to the $LaAlO_3$ substrate transparency windows. At far-infrared (far-IR) frequencies the thin-film transmittance $\mathcal{T}_{\text{thin}}$ (transmission of the film/substrate $\mathcal{T}_{FS}$ divided by transmission of the bare substrate $\mathcal{T}_S$) is given by

$$\mathcal{T}_{\text{thin}}(\omega) \equiv \frac{T_{FS}}{T_S} = \frac{1}{\left|1 + \tilde{Z}(\omega)\,\tilde{\sigma}(\omega)\right|^2} \quad ; \quad \tilde{Z}(\omega) \equiv \frac{Z_0\,d_f}{\tilde{n}(\omega)+1}\,, \tag{3.3}$$

where $Z_0 = 377\,\Omega$ is the impedance of free space, d_f is the film thickness, $\tilde{\sigma}(\omega)$ is the complex optical conductivity, and $\tilde{n}(\omega)$ is the complex index of refraction of the substrate. The thin-film formula of Eq. (3.3) applies whenever the skin depth $\delta = \lambda/4\pi\kappa_f$ exceeds the film thickness $\delta \gg \lambda$, which is well satisfied in these thin film samples. Typical substrates (*e.g.*, $LaAlO_3$) exhibit negligible absorption ($\kappa \to 0$) at frequencies less than $100\,\mathrm{cm}^{-1}$. Hence the substrate index and complex impedance $\tilde{Z}$ become purely real. The resulting expression for $\mathcal{T}_{\text{thin}}$ given by Eq. (3.3) simplifies to the following

$$\mathcal{T}_{\text{thin}}(\omega) = \frac{1}{[1 + Z(\omega)\,\sigma_1(\omega)]^2 + [Z(\omega)\,\sigma_2(\omega)]^2}\,, \tag{3.4}$$

Note that to lowest order in the conductivity, $\mathcal{T}_{\text{thin}}$ depends linearly on σ_1 and quadratically on σ_2. Inverting Eq. (3.4), the measured $\mathcal{T}_{\text{thin}}$ determines σ_1,

$$\sigma_1(\omega) = \frac{1}{Z(\omega)}\left\{\sqrt{\mathcal{T}_{\text{thin}}(\omega) - [Z(\omega)\,\sigma_2(\omega)]^2} - 1\right\} \le \frac{1}{Z(\omega)}\left[\sqrt{\mathcal{T}_{\text{thin}}(\omega)} - 1\right] \tag{3.5}$$

The right side of Eq. (3.5) becomes an equality when $\sigma_2/\sigma_1 << 1$. In general, $\sigma_2 \to 0$ as $\omega \to 0$. Terahertz measurements on a $La_{0.7}Sr_{0.3}MnO_3$ sample[106] confirm that $\sigma_2/\sigma_1 << 1$ is a valid approximation in the regime of interest $\omega < 100\,\mathrm{cm}^{-1}$.

At higher frequencies, numerical inversion of the Fresnel formulae for a thin film on a weakly absorbing substrate yield the optical properties of the samples. Low spectral resolution averages the interference (étalon) effects. This procedure yields the index of refraction and extinction coefficient of the thin-film material, n_f and κ_f, respectively, using n and κ for the substrate. The results of n_f and κ_f are then used to derive the other optical constants, *e.g.*, the complex dielectric function, $\tilde{\epsilon}(\omega)$ or the complex optical conductivity $\tilde{\sigma}(\omega)$.[80] This technique avoids extrapolation errors associated with Kramers-Kronig analysis and permits reliable measurement of the optical conductivity up to the high frequency cutoff of the spectrometer ($5\,\mathrm{eV}$).

Figure 3.7 shows temperature dependence of transmittance $\mathcal{T}$ (top panel) and reflectance $\mathcal{R}$ (bottom panel) spectra for the $Nd_{0.7}Sr_{0.3}MnO_3$ sample. The spectra display several features common among the $x = 0.3$ doped alloys. First, both $\mathcal{T}$ and $\mathcal{R}$ display strong temperature dependence in the infrared ($\omega < 1\,\mathrm{eV}$) spectral range. In this region, $\mathcal{T}$ decreases upon cooling below T_c while $\mathcal{R}$ increases. At high frequencies (above $4\,\mathrm{eV}$), strong absorption produces nearly zero $\mathcal{T}$. This small $\mathcal{T}$ leads to noise in the subsequently determined optical constants. Finally, several temperature dependent features appear, particularly in $\mathcal{T}$, in the near-IR to visible spectral range.

In addition to the measured $\mathcal{T}$ and $\mathcal{R}$ shown in Fig. 3.7, the extraction of the film optical constants requires knowledge of the substrate n and κ. In all the measured LAO substrates, $n \approx 2.0$ (independent of sample) and roughly frequency independent in the $0.2 - 5\,\mathrm{eV}$ range.[107] Although the values for the extinction coefficient are small ($10^{-3} - 10^{-4}$) in this frequency range, κ varies for different samples of $LaAlO_3$, especially near the cutoff frequency of $0.2\,\mathrm{eV}$. The sufficiently large differences ne-

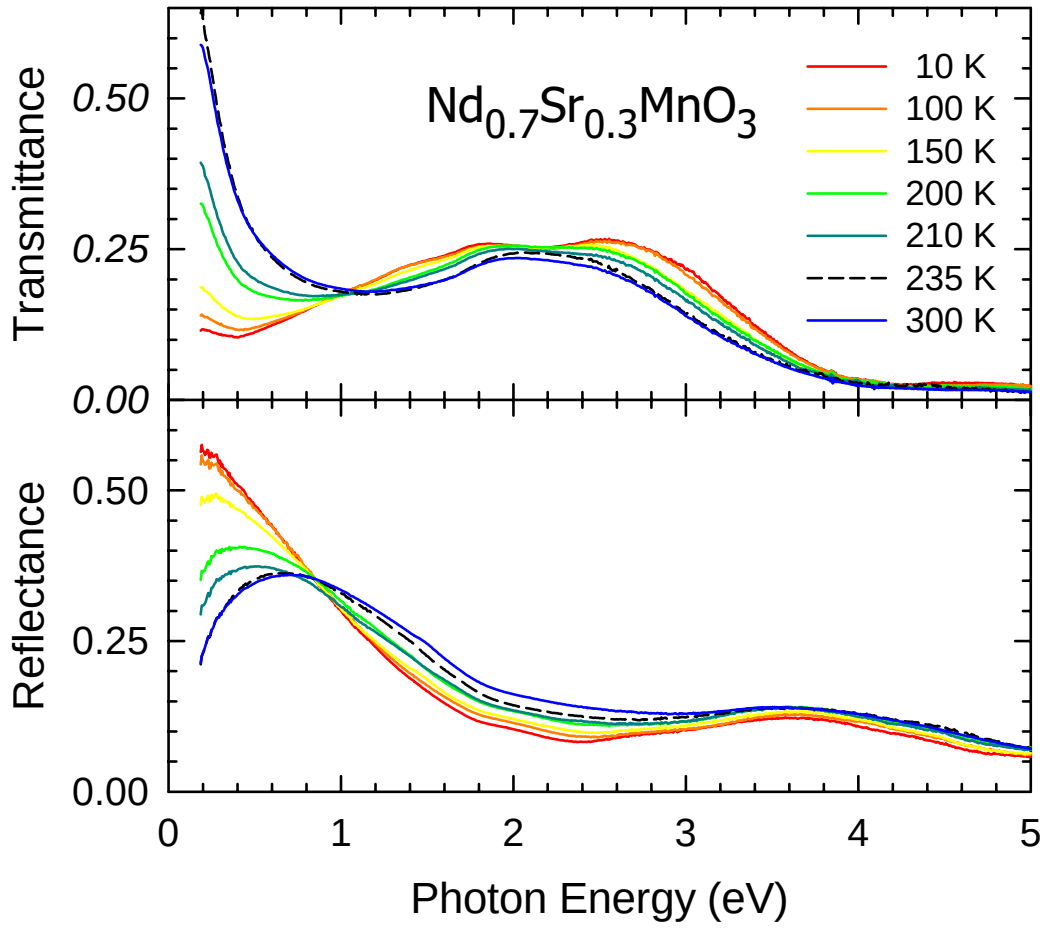

Figure 3.7: Transmittance and reflectance spectra of $Nd_{0.7}Sr_{0.3}MnO_3$ film for various temperatures.

cessitate using the values of n and κ for the substrate specific to each film sample in the analysis. Therefore, after measurement, films were removed from substrates and the $\mathcal{T}$ and $\mathcal{R}$ of the bare substrates were measured. This procedure ensures usage of the proper values of n and κ for the substrate in the final inversion of the data.

3.3.3 Results: Optical conductivity spectra

The optical conductivity in the far infrared was measured as described in Sec. 3.3.2. Because of the narrow range of the transmission window of the $LaAlO_3$ substrates these data provide only a low frequency data point to the broad band conductivity spectra shown below. An interesting analysis compares the far infrared

conductivity with the dc conductivity of identical samples. Figure 3.8 displays the measured dc conductivity together with the derived conductivities at $20\,\mathrm{cm}^{-1}$ using Eq. (3.5). A reasonable agreement exists between the ac and dc values for

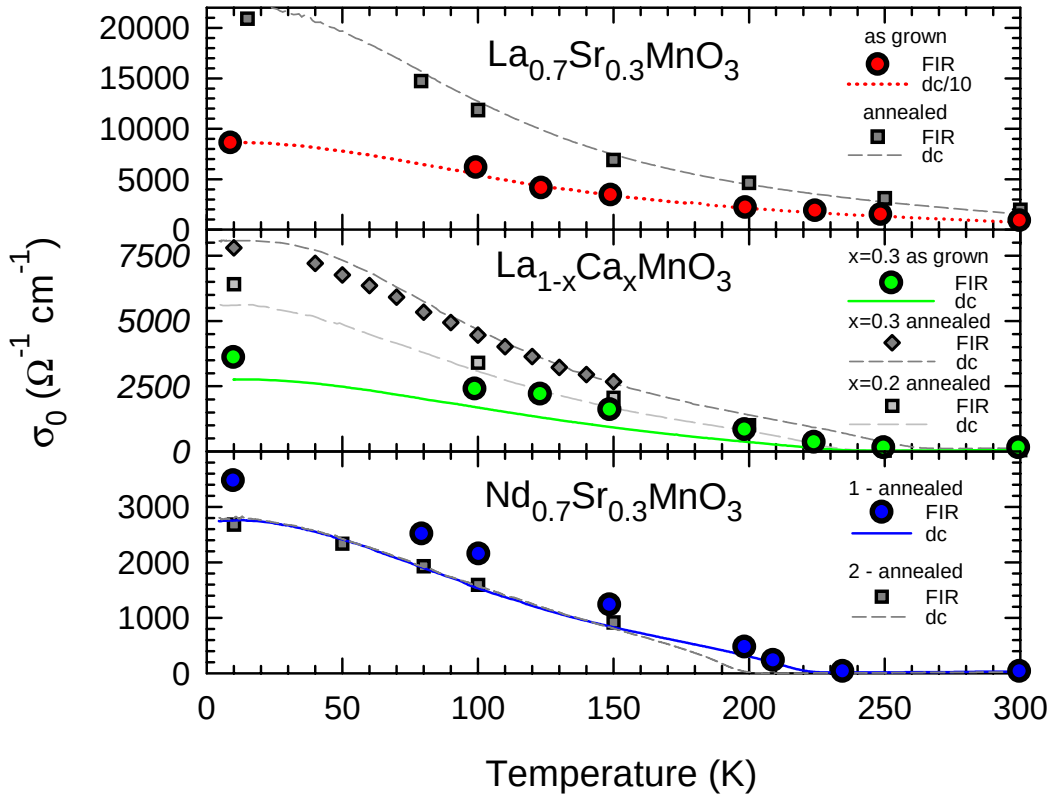

Figure 3.8: Comparison of the temperature dependence of the dc (solid lines) and ac (circles) conductivities at $20\,\mathrm{cm}^{-1}$ derived from Eq. (3.5). The dc conductivity for the $La_{0.7}Sr_{0.3}MnO_3$ sample (the dashed curve) has been divided by ~ 10 to fit the data on the same scale.

$La_{0.7}Ca_{0.3}MnO_3$ and $Nd_{0.7}Sr_{0.3}MnO_3$ samples. However, the $La_{0.7}Sr_{0.3}MnO_3$ sample exhibits a striking disagreement. The measured dc conductivity in this sample exceeds by roughly 10 times the ac value obtained at $20\,\mathrm{cm}^{-1}$. Similar results for $La_{0.7}Sr_{0.3}MnO_3$ films studied earlier[27] were attributed to an anisotropic conductivity resulting from substrate induced strain. However, subsequent measurement done in this study confirmed the spurious values occurred from errors in the dc resistivity measurements performed by the sample grower.[108] However, typical $La_{0.7}Sr_{0.3}MnO_3$

films have a resistivity of around $100\,\mu\Omega\,$cm in better agreement with the ac values.

The results of the real part of the optical conductivity $\sigma_1(\omega)$ for the three samples measured at different temperatures are shown in Fig. 3.9. The symbols near zero frequency result from the far-infrared transmittance measurements described above. The IR conductivity extrapolates reasonably to the far infrared value except for a downturn near the low-frequency IR cutoff. This downturn becomes more noticeable in the alloys with lower T_c, particularly for $Nd_{0.7}Sr_{0.3}MnO_3$. While care must be exercised extracting film optical constants near the onset of substrate absorption ($0.2\,$eV), Lee *et al.*[109] report similar results for $Nd_{0.7}Sr_{0.3}MnO_3$ single crystals. Near and above T_c, a broad maximum near $1\,$eV dominates σ_1, peaking with a value of roughly $600 - 700\,\Omega^{-1}\,$cm^{-1} and only slightly higher than the Mott minimum conductivity. Moreover, the $1\,$eV feature evolves in temperature similarly for the different alloys. These data indicate that this feature is universal in the hole-doped pseudocubic manganites. In all the samples, the broad maximum in the conductivity spectrum above T_c shifts lower in frequency and grows in oscillator strength as temperature decreases through T_c. The peak structure remains identifiable well below T_c, but as the temperature lowers further into the metallic range the low-frequency part fills in and eventually $\sigma_1(\omega)$ increases with decreasing frequency for $T \ll T_c$. This indicates a Drude response and coherent conduction at low temperatures and low frequencies in all the samples. The results for this oxygen annealed $Nd_{0.7}Sr_{0.3}MnO_3$ sample differ from results reported[28] on an unannealed sample, which did not show a Drude-like response even at the lowest temperature, although the $T > T_c$ behavior was similar to that observed here. The earlier sample had a lower T_c and a much higher dc resistivity ($\sigma_{DC} < \sigma_{Mott}$) than the present sample even at $10\,$K. Clearly, varying the oxygen concentration produced different behaviors in the dc transport and optical properties of $Nd_{0.7}Sr_{0.3}MnO_3$.

The other major spectral feature in observed σ_1 spectra is the strong peak near

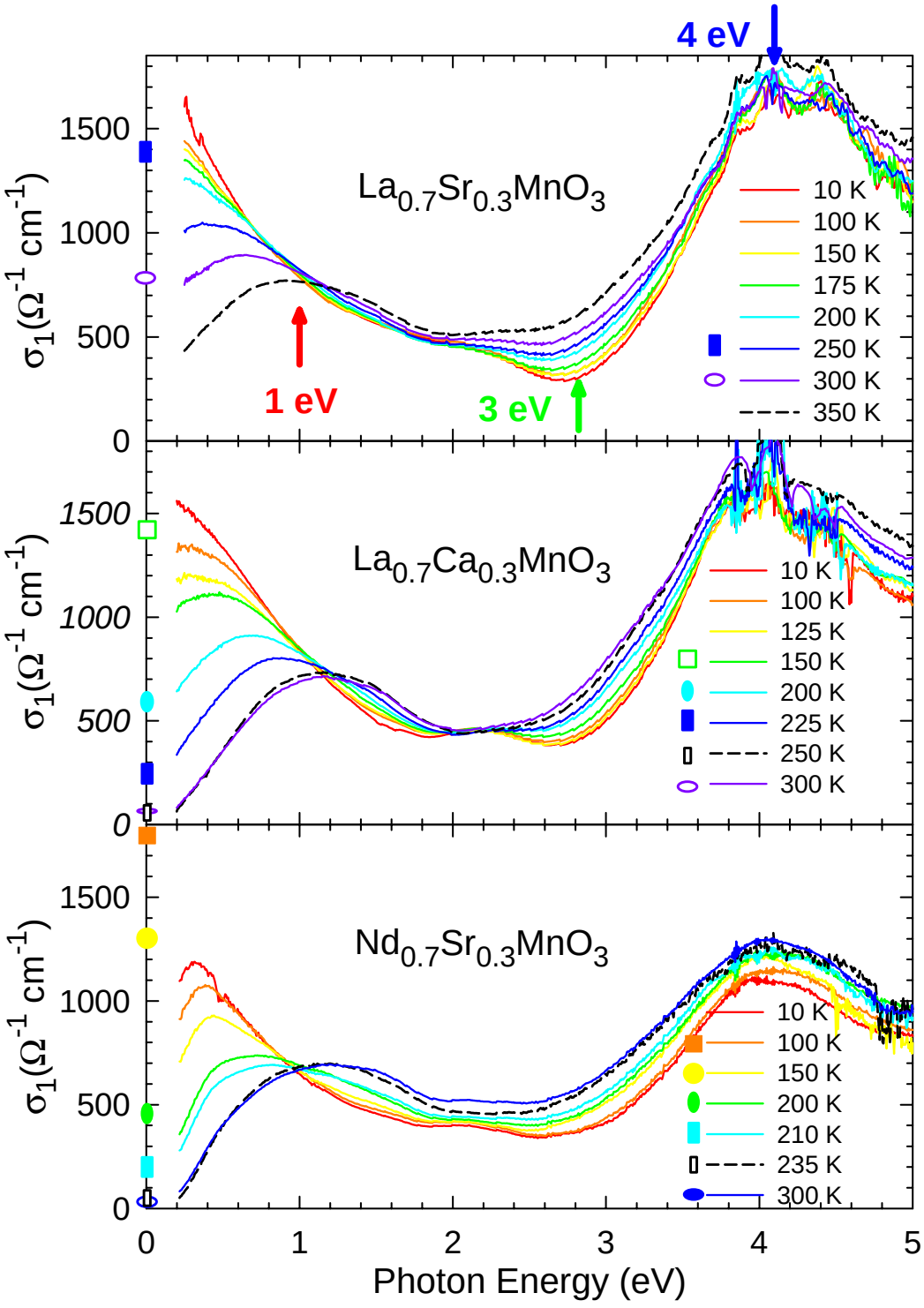

Figure 3.9: Frequency dependence of the real part of the optical conductivity, σ_1, for three $x = 0.3$ alloys at different temperatures.

4 eV. The noisy appearance of the conductivity data near the peak of this feature occurs as a consequence of the very small transmittance (strong absorption) of the films at the peak. A similar feature appears ubiquitously in other perovskite transition metal oxides.[44] A weak temperature dependence of the 4 eV absorption is observed outside of the measurement uncertainty. Additionally, the absorption appears noticeably weaker in $Nd_{0.7}Sr_{0.3}MnO_3$.

Throughout the measured spectral range, σ_1 dominates $\mathcal{T}$ and $\mathcal{R}$ of the films However, $\mathcal{T}$ and $\mathcal{R}$ remain relatively insensitive to ϵ_1 and consequently provide less reliable values of ϵ_1. In particular, ϵ_1 is prone to errors introduced by multiple roots in the numerical inversion of $\mathcal{T}$ and $\mathcal{R}$ (discussed in Chap. 2). Careful numerical inversion ensures the resulting ϵ_1 satisfies the K-K relations, *i.e.* ϵ_1 relates to the more reliably determined imaginary part of ϵ. Figure 3.10 shows the temperature dependence of ϵ_1 spectra typical for the doped alloys. At high frequencies, ϵ_1 exhibits little

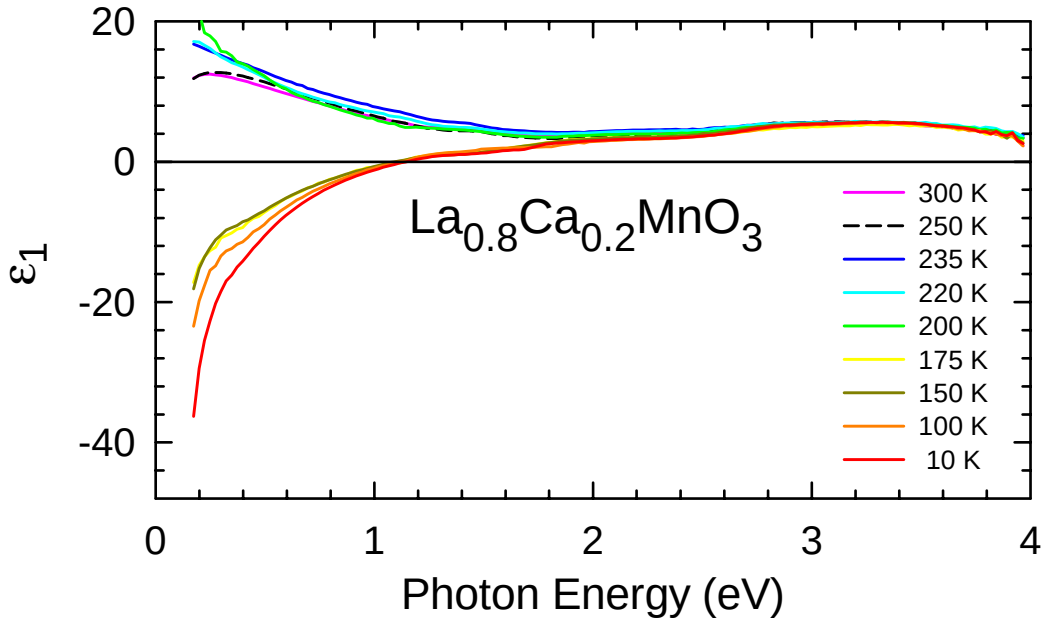

Figure 3.10: Real part of the dielectric constant ϵ_1 of $La_{0.8}Ca_{0.2}MnO_3$ for various temperature dependence.

temperature or frequency dependence, remaining nearly constant and positive down

to 1.8 eV. Below this point, ϵ_1 displays either insulating or metallic behavior, depending on temperature. From room temperature down to well below T_c, ϵ_1 increases slightly with decreasing temperature, while remaining positive (characteristic of an insulator). For temperatures well below T_c, ϵ_1 behaves more like a metal, becoming smaller with decreasing frequency and eventually going negative just above 1 eV. The apparent free-carrier response of $\sigma_1(\omega)$ at low temperature should tend to produce a negative ϵ_1 at frequencies below the plasma frequency, ω_p. However, the ω_p is predicted[110] to be much higher in frequency (≈ 3.5 eV). The observed behavior of ϵ_1 suggests interband transitions between the two e_g bands provide additional spectral weight in the infrared. This additional weight accounts for the relatively smaller contribution of the coherent component of the conductivity to the total spectral weight.

3.3.4 Assignment of optical transitions

This subsection addresses in detail several of the striking features of the optical conductivity data shown in Fig. 3.9, which consists of three main peaks at ≈ 1, 3, and 4 eV. Mn e_g and O $2p$ levels comprise the orbitals important to the low-lying electronic excitations. Allowed transitions involve motion of a charge either from one Mn site to another or from an O to a Mn. Jung *et al.*[39] argue that transitions from one e_g orbital to another *on-site* appear in the optical spectrum. However, these transitions have negligible oscillator strength given that the initial and the final states have d-symmetry with respect to the same origin. The following presents arguments that the 1 eV feature involves e_g-e_g transitions within the parallel spin manifold, the 3-eV feature results from e_g-e_g transitions to an antiparallel final state, and the 4-eV feature results from the e_g - O $2p$ charge transfer transition.

Several important energies are relevant to the lowest-lying optical transitions: (i) breathing distortion energy E_B, (ii) Jahn-Teller energy E_{JT}, (iii) on-site coulomb energy or "Hubbard U", (iv) Hund's energy J_H, and (v) charge transfer energy Δ. First,

a Mn-site with no e_g electrons experiences a symmetric "breathing" distortion of the surrounding oxygens. Evidence of breathing mode distortions appears whenever an electron hops to a Mn site with empty e_g orbitals on a timescale fast compared to phonon frequencies, as occurs in optical transitions. In this case the lattice does not have time to relax and the final state resides higher in energy by E_B. Next, the Jahn-Teller distortion splits the e_g levels by an amount E_{JT}. A singly occupied Mn e_g orbital experiences this local even-parity lattice distortion, which breaks cubic symmetry. In the low-temperature charge-ordered phase of $La_{0.5}Ca_{0.5}MnO_3$, both breathing and Jahn-Teller distortions occur.[111] The approximately equal amplitudes of these distortions suggests $E_B \approx E_{JT}$. A third energy results from coulomb interactions, or the "Hubbard U" repulsion,[112] between two e_g electrons on the same site. As discussed below, available evidence suggests that the effective U describing the low-energy ($\omega < 4\,\text{eV}$) physics of the e_g band remains weak. Another important energy, the Hund's coupling energy J_H governs the spin interaction between the Mn e_g electrons and the $S = 3/2$ core spin of the occupied t_{2g} orbitals. Electrons in e_g orbitals aligned with spins antiparallel to core spins reside higher than those aligned in parallel by an energy J_H. Finally, Δ describes the energy cost for the charge transfer from O_{2p} to Mn e_g levels. Such charge transfer transitions occur commonly in the manganites[44] and have already been seen in the parent compound in the previous section.

These characteristic energies play a crucial role in identifying the various transitions observed in the optical conductivity. Figure 3.11 shows a qualitative picture of the O $2p$ and Mn e_g (t_{2g} levels are not shown) states identified by the appropriate energy relative to the Fermi energy and the optical transitions observed in Fig. 3.9. The two fold degeneracy of the singly occupied e_g levels are assumed split by a local Jahn-Teller distortion with the splitting given by E_{JT}. The left-hand portion indicates an optical transition to a Mn that initially has no e_g electrons. In the case of a Mn-Mn charge transfer at low temperature (*i.e.*, parallel transition), the final state energy con-

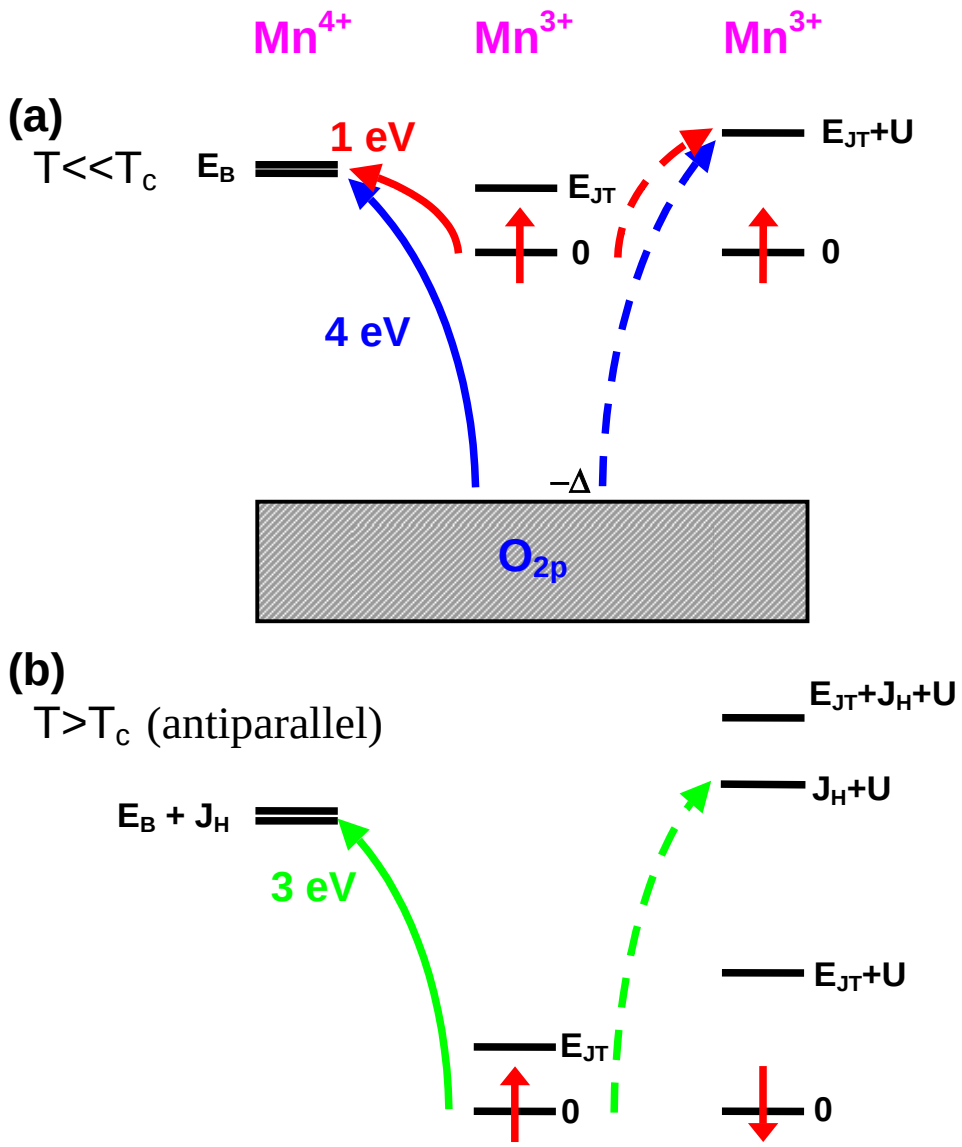

Figure 3.11: Schematic view of lowest-lying electronic transitions in $R_{1-x}A_x\mathrm{MnO}_3$. Central panel shows initial states while left and right panels show allowed optical transitions and final state energies referenced to the Fermi energy. The shaded box represents filled O p-bands and horizontal lines represent, in panels from left to right, Mn e_g levels on Mn^{4+}, Mn^{3+}, and Mn^{3+} sites. *Curved* arrows represent optical transitions corresponding to absorption observed in σ_1.

sists of the degenerate e_g levels shifted by the breathing distortion energy E_B. If the core spins on the Mn^{4+} site align antiparallel (as they do at temperatures above T_c), the hopping e_g electron must pay an additional Hund's energy cost J_H. Additionally, if

the transition to the unoccupied Mn originated from an O site, the final state energy would be raised an additional amount Δ. The right-hand panel indicates an optical transition in which charge moves from an O or Mn site to an already singly occupied Mn site, as occur exclusively in the undoped parent compound. These transitions to a Mn site containing an already singly occupied e_g level pay an additional energy cost U corresponding to the Coulomb interaction. Thus, the final state energy is the sum of the Jahn-Teller splitting E_{JT}, the e_g-e_g Coulomb repulsion U (and J_H and Δ if appropriate). Figure 3.11 allows identification of the energies: $E_B \approx 1$ eV, $E_{JT} \approx 1$ eV, $U \approx 1.2$ eV, $J_H S_c \approx 3$ eV, and $\Delta \approx 4$ eV

The broad absorption peak centered at ≈ 1 eV appears as the most striking feature of the data in this energy range. The features occurs in the paramagnetic phase of all samples. As T decreases below Tc, this feature loses intensity and shifts to lower frequency, eventually evolving into the observed Drude-like conduction. The oscillator strength, including T-dependence, of the 1-eV feature agrees with expectations for dipole allowed d-d charge transfer transitions between Mn ions on different sites. The insulating nature of the paramagnetic phase and the peak-like shape of the absorption suggests that it arises from the excitation of carriers out of bound states. Disorder induced carrier localization, as suggested in Ref. 113, offers a possible explanation. However, the universal appearance of the feature in manganites of widely varying dc conductivities[42,43] weakens this argument. The characteristic energy of the absorption feature in the paramagnetic state of the doped materials appears qualitatively similar to that observed in insulating $LaMnO_3$, where a ≈ 1.5 eV gap appears in the e_g manifold due to the presence of a long-range Jahn-Teller distortion. The feature observed in $LaMnO_3$ (see Fig. 3.2 on page 69) results from the e_g-e_g transition shown in the righthand panel of Fig. 3.11. The peak energy of approximately 2.2 eV corresponds to an energy $E_{JT} + U$. This peak thus exceeds the lowest electronic excitation in the doped manganites, *i.e.* $E_B \approx 1$ eV $< E_{JT} + U$.

Initial reports of the optical properties of doped manganites interpreted[43] the 1-eV feature as a "parallel" to "antiparallel" transition, implying a $J_H \approx 1.5$ eV. However, as noted by Millis *et al.*,[31] the temperature dependence of the spectral weight of the 1 eV feature is inconsistent with this interpretation. Selection rules for electric dipole matrix elements preserve spin and hence preclude the "antiparallel" final state in the fully polarized ferromagnetic ground state. The oscillator strength in the "antiparallel" transition, therefore, should decrease as T lowers below T_c. However, the observed intensity in the peak feature grows as T decreases below T_c, inconsistent with the "antiparallel" interpretation. Thus the 1-eV feature must involve parallel spin e_g-e_g transitions only. The temperature dependence of $\sigma_1(\omega)$ near ≈ 3 eV, however, is consistent with transitions to an e_g "antiparallel" final state. Figure 3.12 shows the difference conductivity $\Delta\sigma_1(T) \equiv \sigma_1(T) - \sigma_1(10\,\mathrm{K})$, which illustrates this behavior clearly. The peak at ≈ 3 eV gradually disappears in strength as the temperature lowers and the core spins align ferromagnetically.

In the range from $2 - 5$ eV, strong absorption dominates the conductivity at $\approx$ 4.0 eV. A comparison with the parent compound $LaMnO_3$ allows assignment of the optical process involved in this transition. In $LaMnO_3$, a similar peak in the optical conductivity has been observed (Fig. 3.2) at this frequency and assigned to a charge-transfer transition between the O $2p$ and the e_g derived bands.[39,44] Moreover, the data in Fig. 3.9 show a large redistribution of spectral weight from optical transitions occurring above 2 eV to below the 1 eV feature. The temperature dependence of $\sigma_1(\omega)$ extends to the upper measurement limit (5 eV). However, the T dependence of the 4 eV feature does not account for the missing spectral weight when the sample warms above T_c, as can be seen in Fig. 3.12. A full account of all the low-frequency oscillator strength in the ferromagnetic state requires including contributions up to and beyond the 5 eV limit of the present measurements.

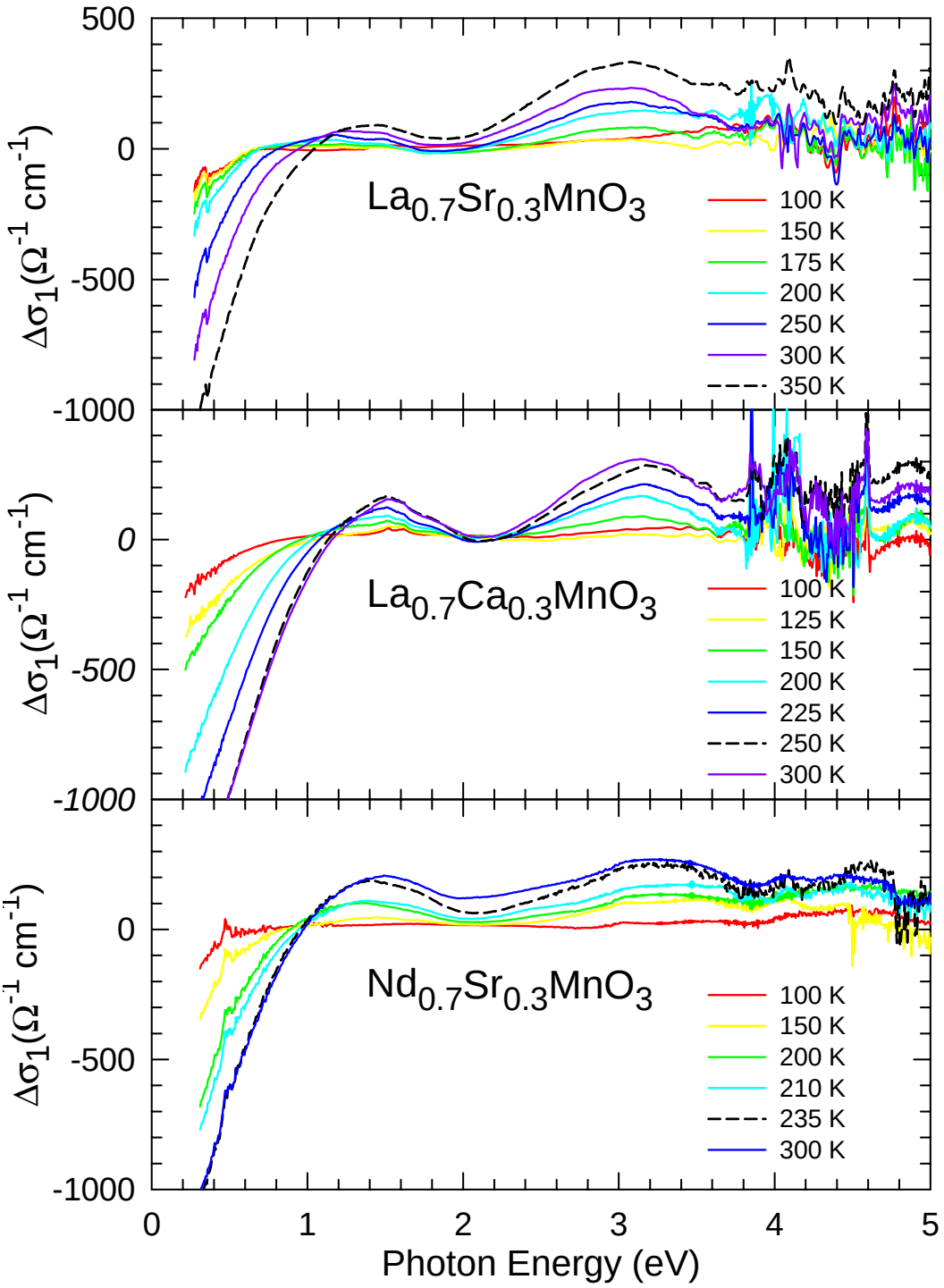

Figure 3.12: Difference in the optical conductivity $\Delta\sigma_1 \equiv \sigma_1(T) - \sigma_1(10\,\mathrm{K})$ for three $x = 0.3$ alloys. The ≈ 3.0 eV feature gradually disappears below T_c.

3.3.5 Jahn-Teller small polaron

Millis *et al*. predicted[30] doped materials in the paramagnetic phase would have lattice distortions similar to those occurring in $LaMnO_3$, but lacking the long range order. Neutron pair-distribution-function[29] and extended x-ray-absorption fine-structure (EXAFS)[114] experiments directly observed these distortions with an amplitude about $70\,\%$ of those in $LaMnO_3$. In this picture, the $1\,\mathrm{eV}$ feature observed at $T > T_c$ in doped samples results from the excitation of a carrier out of a bound state produced by a strong local lattice distortion. The polaron excitation hops to an adjacent Mn site whose e_g levels have been modified in energy by either the J-T distortion (singly occupied e_g) or the breathing mode distortion (empty e_g). Evidently, doping reduces the e_g electron concentration to less than one per site and allows transitions such as those shown in the left panel of Fig. 3.11. The observation of only one (broad) feature suggests that the energy shift due to the breathing distortion, E_B, is comparable to the Jahn-Teller plus Coulomb energy $E_{JT} + U$.

As the temperature decreases below T_c, the $1\,\mathrm{eV}$ feature grows in intensity and broadens, and eventually evolves into the low-temperature Drude-like response. This behavior corresponds to the collapse of the Jahn-Teller small polaron as the system goes into the ferromagnetic state. Millis, Mueller and Shraiman[30] propose an explanation with a model that incorporates double exchange and dynamic JT effects in the system. In this model, the dimensionless effective coupling constant λ controls the behavior of the system. The coupling constant is defined by

$$\lambda = \frac{E_{JT}}{t\,\langle\cos(\theta_{ij}/2)\rangle}, \tag{3.6}$$

where t is the hopping probability, and θ_{ij} is the relative angle between neighboring spins. The $\langle\cos(\theta_{ij}/2)\rangle$ factor, which goes from 1 in the ferromagnetic state (aligned spins) to $2/3$ in the paramagnetic state (randomly aligned spins), governs the temperature dependence. Within the DE and JT model, a qualitative description of the

data shown in Fig. 3.9 emerges. In the paramagnetic state, λ exceeds λ_c, the critical value for the formation of a small polaron. The $1\,$eV feature corresponds to the photo-ionization of the small polaron at E_B (see Fig. 3.11). As the temperature decreases, the spins align and $\lambda < \lambda_c$, leading to a collapse of the JT small polaron and resulting in coherent conduction. The optical conductivity calculated within this model[32] shows shifts in oscillator strength and linewidth as function of λ that compare well to the experimental results shown in Fig. 3.9 below $2\,$eV. The behavior of the resistivity, the Curie temperature, and the optical properties of these materials indicate that $La_{0.7}Sr_{0.3}MnO_3$, $La_{0.7}Ca_{0.3}MnO_3$, and $Nd_{0.7}Sr_{0.3}MnO_3$ have a progressively increasing JT coupling λ. In all samples, the JT small polaron feature remains for intermediate temperatures below T_c. Thermopower and EXAFS measurements also suggest evidence for small polaronic behavior in $La_{0.7}Ca_{0.3}MnO_3$ near T_c.[38,114] The downward shift in the polaron feature and the onset of metallic conductivity indicate a gradual transition from a small polaron to a large polaron and a correspondingly gradual growth of the coherent conductivity spectral weight.

3.3.6 Optical spectral weight: Comparison with theory

The spectral weight of low-lying electronic transitions affords a comparison of experimental conductivity results to predictions of theoretical models. Consider the spectral weight and subsequent kinetic energy given by Eq. (2.23) and Eq. (2.25), respectively. Figure 3.13 shows $K(\omega)$ for three $x = 0.3$ alloys at various temperatures. For the manganites the low-lying states of interest are the e_g electrons. The following analysis first determines a cutoff frequency ω_c such that $S(\omega_c)$ offers a good estimate of the spectral weight in the e_g-e_g transitions, next presents theoretical predictions, and finally draws a comparison between experimental results and theory of the magnitude and temperature dependence of the spectral weight.

The trend in kinetic energies shown in Fig. 3.13 agrees with the predictions of

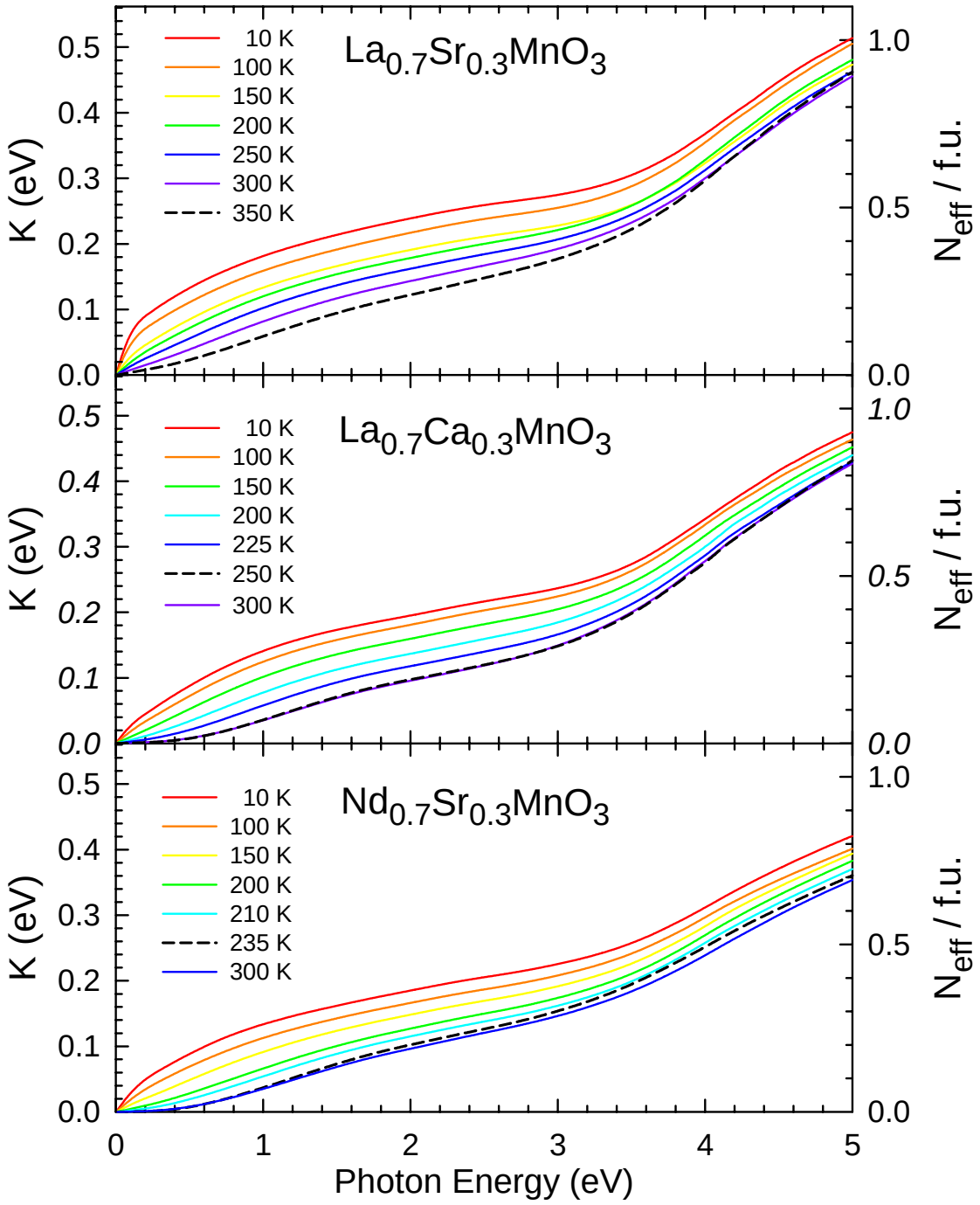

Figure 3.13: Integrated conductivity as a function of photon energy for various temperatures. The results are expressed in terms of the kinetic energy K and the carrier density per formula unit N_{eff}/f.u.

a theoretical model including DE and JT (discussed further below) where K scales with T_c. $La_{0.7}Sr_{0.3}MnO_3$ has the highest T_c and is the most metallic, consistent with its relatively large optically determined kinetic energy, while the opposite is true for $Nd_{0.7}Sr_{0.3}MnO_3$. Consideration of spectral weight temperature dependence provides further information on the relevant energy scales. As clearly seen in Fig. 3.13, large changes in temperature occur in the spectral weight at frequencies extending to the experimental limit.

A comparison of the observed oscillator strength to the band theory estimate requires identification of the e_g contribution to the absorption. As evidenced in the $T = 10$ K curves in Fig. 3.9, the Mn-O charge transfer transition dominates the absorption for $\omega > 2.7$ eV, particularly for the $La_{0.7}Sr_{0.3}MnO_3$ and $La_{0.7}Ca_{0.3}MnO_3$ samples. For all three $x = 0.3$ alloys, experimental estimates of the e_g kinetic energy at $T = 0$ result from integrating the data to a cutoff frequency $\omega_c = 2.7$ eV. Figure 3.14 shows temperature dependence of the oscillator strength N_{eff} at the cutoff ω_c for the three different $x = 0.3$ alloys. The temperature axis has been scaled to the ferromagnetic transition temperature T_c of each of the alloys. All three alloys exhibit a reduction in spectral weight with temperature from a maximum in the ferromagnetic ground state to $T/T_c = 1$, above which the behavior basically saturates. For comparison, a molecular mean-field calculation of the double-exchange bandwidth γ_{DE} derived by Kubo and Ohata[115] has been included. Qualitatively, N_{eff} and γ_{DE} exhibit similar temperature dependence. However, while DE predicts γ_{DE} should fall to only $3/4$ of its original value, N_{eff} for the alloys falls to nearly half of the low temperature value. Thus, the temperature dependence of the spectral weight suggests that DE alone does not explain the observed behavior and points to the necessity for including additional interactions in the theoretical models.

An absence of $\sigma(\omega, T)$ calculations, including both a realistic treatment of the e_g band structure and the effects of the electron-phonon interaction, focuses the the-

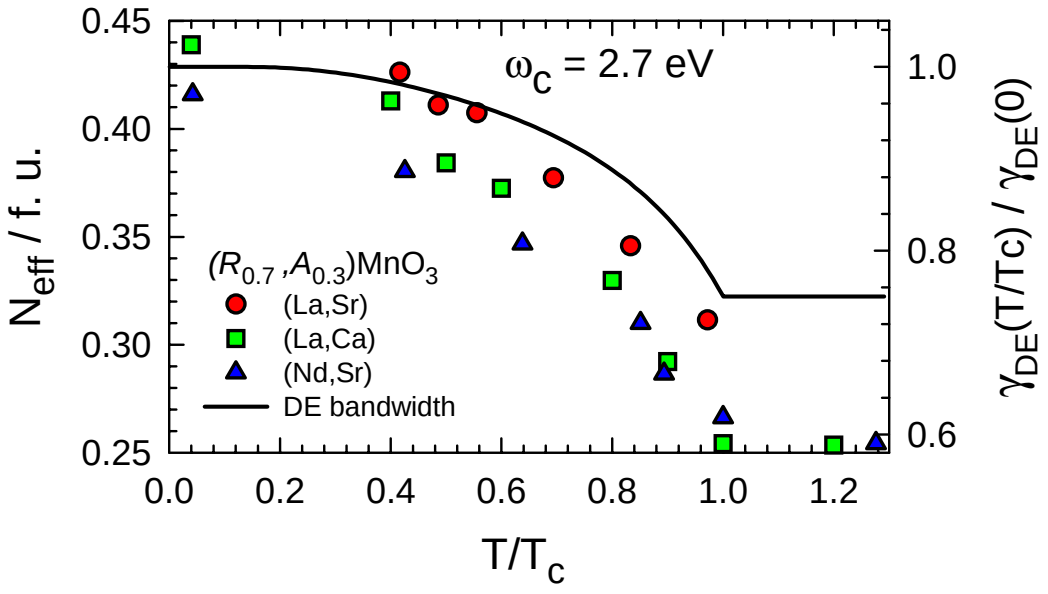

Figure 3.14: Temperature dependence of N_{eff} at 2.7 eV for three $x = 0.3$ alloys. Temperature scale normalized to T_c. Double exchange bandwidth γ_{DE} plotted on secondary y-axis (similarly scaled) for comparison.

oretical discussion on models approximating the band structure. A tight-binding parameterization[27,32,116] of the band structure[117] presents a model Hamiltonian from which the conductivity may be calculated. The model assumes the physics of interest is determined by carriers hopping between Mn e_g-symmetry d-levels on the sites of a simple cubic lattice (lattice constant a_0) and interacting with each other, with the lattice, and with Mn core spins of magnitude $S_c = 3/2$. The total Hamiltonian $\hat{H} = H_{band} + H_{J_H} + H_{int}$ consists of a hopping term H_{band}, a Hund's energy term H_{J_H}, and a term representing other interaction H_{int}. Writing $\hat{H}$ explicitly

$$\hat{H} = -\sum_{\substack{i\delta \\ ab}} t_{\delta}^{ab} \left[e^{i\frac{e}{c}\boldsymbol{A}\cdot\boldsymbol{\delta}} d_{ia\alpha}^{\dagger} d_{i+\delta b\alpha} + H.c. \right] - J_H \sum_{\substack{ia \\ \alpha\beta}} \boldsymbol{S}_{ci} \cdot d_{ia\alpha}^{\dagger} \boldsymbol{\sigma}_{\alpha\beta} d_{ia\beta} + H_{INT} \,. \qquad (3.7)$$

Here $d_{ia\alpha}^{\dagger}$ creates an electron with spin α in e_g orbital a on site i, J_H is the Hund's coupling between the itinerant electrons and the core spins, and $t_{\delta}^{ab} = t_{\delta}^{ba}$ represents the direction-dependent amplitude for an electron to hop from orbital b to orbital a on site $i + \boldsymbol{\delta}$. In the Peierls phase approximation employed in this model,[116] the vector poten-

tial $\boldsymbol{A}$ represents the electric field and the conductivity results from a linear response in $\boldsymbol{A}$ as usual. A hopping parameter $t_{\boldsymbol{\delta}}^{ab}$ involving only nearest neighbor hopping and only non-zero for one particular linear combination of orbitals fits well the calculated bandstructure.[27,117,118] Calculations[119] of the hopping amplitude find $t_0 \approx 0.67$ eV. Further details relating to this theoretical model are presented elsewhere.[27,32,116]

The kinetic energy will then be given by the expectation value of the hopping term in $\hat{H}$,

$$K = \frac{1}{6\,N_{sites}} \sum_{\substack{i\boldsymbol{\delta} \\ ab}} t_{\boldsymbol{\delta}}^{ab} \langle d_{ia\alpha}^{\dagger}\, d_{i+\delta b\alpha} + H.c. \rangle\,. \tag{3.8}$$

In general, the expectation value given in Eq. (3.8) and the spectral weight of other transitions may depend on temperature and interaction strength. Interestingly, the data in Fig. 3.12 suggest that transitions in addition to the e_g–O $2p$ are primarily responsible for restoring the optical spectral weight. The non-interacting (H_{int}=0) kinetic energy K_0 may be evaluated at $T = 0$. For doping concentration $x = 0.3$ ($n = 0.7$), K_0 is given by

$$K_0 = 0.46\, t_0 \approx 0.306\,\text{eV}. \tag{3.9}$$

K_0 results from finding an extrema of the kinetic energy assuming $H_{INT} = 0$ and a fully polarized ferromagnetic state for the Mn core spins. Spin disorder or $H_{INT} = 0$ will tend to reduce this value. Thus, K_0 represents an *upper bound* to the optical spectral weight of the model specified by Eq. (3.7), especially applicable to the e_g bands with negligible interaction effects. However, the sensitivity of the hopping amplitude to buckling of the Mn-O-Mn bond requires some caution in comparing t_0 obtained by fitting band calculations from ideal materials to various doped alloys that have slightly different unit-cell sizes and crystal structure.

Including temperature dependence in the model conductivity requires consideration of the Hund's coupling energy and the possibility of antiparallel transitions. In the $J_H \rightarrow \infty$ limit the antiparallel transitions may be neglected. From Fig. 3.12,

$J_H S_c \approx 3$ eV giving $J_H \approx 2$ eV. While not infinite, in practice $J_H S_c$ provides sufficient energy splitting to separately resolve the parallel and antiparallel absorptions. As T increases from 0, the spectral weight in the parallel spin transitions decreases both because the total kinetic energy decreases and because a portion of the remaining spectral weight transfers to the antiparallel transitions. For finite J_H and a more realistic band structure, statements can be made about the changes in spectral weights from $T = 0$ to $T > T_c$, where the core spins are expected to be completely uncorrelated from site to site. Calculations using the noninteracting model, Eq. (3.7) with $H_{INT} = 0$, show that for well-separated spin bands as the temperature is raised from $T = 0$ to $T > T_c$, the $J_H = \infty$ limit provides with good accuracy the change in spectral weight in the parallel spin transitions.[27] Furthermore, at $T > T_c$ the ratio of antiparallel to parallel spectral weights $K_{anti}/K_{par} \approx 2\,t_0/1.4\,J_H S_c \approx 1/3$ (using $t_0 = 0.67$ eV and $J_H S_c \approx 3$ eV). These conclusions, which have been verified in the noninteracting limit, should apply also to interacting models.[27]

A quantitative comparison of the expectations for the kinetic energy from the tight-binding model with that obtained from the measured conductivity requires identification of the various spectral weights. At low temperature, the total contributions of the e_g electrons already have been identified as originating from the conductivity at energies below 2.7 eV. In addition, separating the contributions resulting from parallel and antiparallel transitions involves examining the temperature dependent spectral weight. Figure 3.15 presents a schematic representation of the relevant kinetic energies. Shaded areas represent the integrated conductivity contributing to K_{tot}, K_{par}, and K_{anti}, respectively. K_{tot} and K_{par} are proportional to the integrated σ_1 from $0 - 2.7$ eV at temperature $T = 10$ K and $T = T_c$, respectively. The kinetic energy of the antiparallel transitions compares the change in oscillator strength of the 3 eV feature between $T = 0$ and $T > Tc$. K_{anti} is proportional to the integrated difference conductivity $\Delta\sigma_1(T_c)$ from $2.2 - 4$ eV.

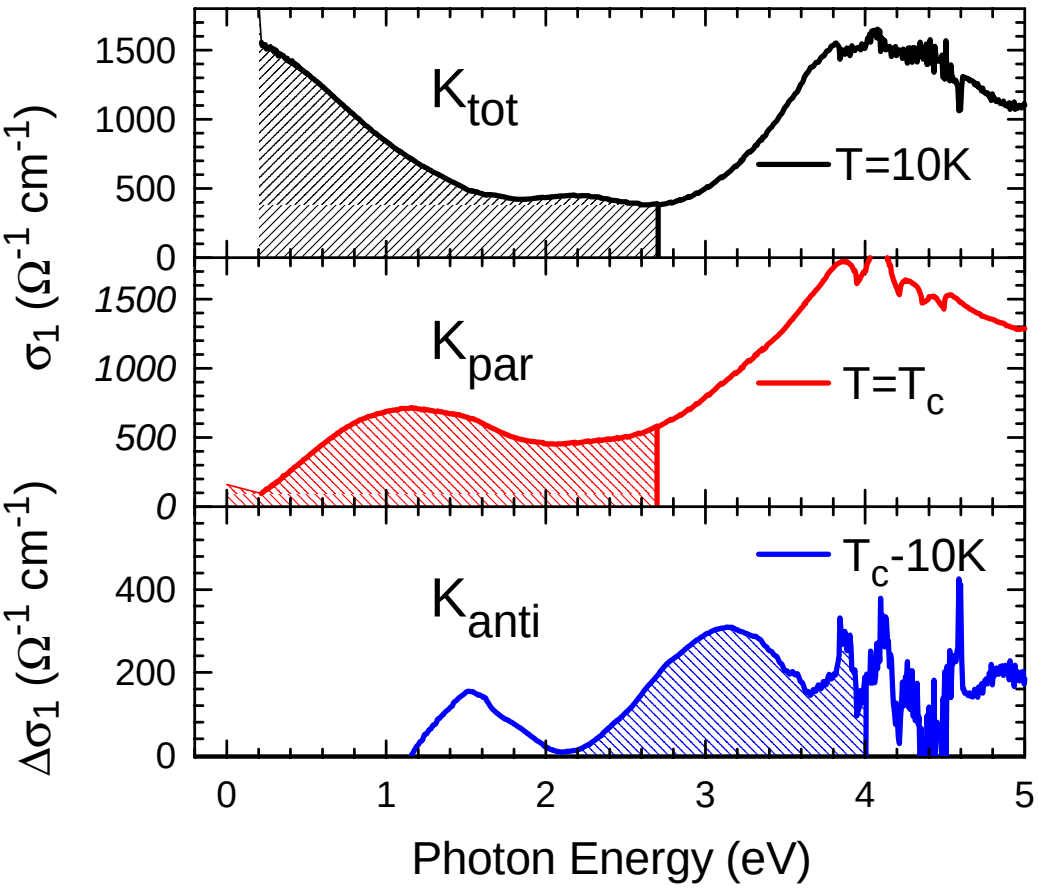

Figure 3.15: Shaded areas represent the integrated conductivity contributing to the kinetic energies K_{tot}, K_{par}, and K_{anti} in the top, middle, and bottom panels, respectively. $La_{0.7}Ca_{0.3}MnO_3$ data shown.

Table 3.3 presents the measured values and predictions from the tight-binding model. K_{tot} estimated from band theory exceeds all of the observed values, especially for (La,Ca) and (Nd,Sr). In addition to the kinetic energies, the ratios of the parallel to antiparallel kinetic energies K_{anti}/K_{par} and difference in kinetic energy between $T = 0$ and T_c, $\Delta K \equiv K_{tot}(T = 0) - K_{par}(T > T_c) = 1/4K_{tot}(T = 0)$, are presented. $K_{anti}/K_{par} \approx 1/3$ and $\Delta K/K_{tot} \approx 1/2$, in good agreement with theory. Further, the observed magnitude of ΔK validates the procedure determining K_{tot}. Different estimates of $K(T = 0)$ would lead to different estimates of $\Delta K/K_{tot}$, in disagreement with theory.

	$(La,Sr)MnO_3$	$(La,Ca)MnO_3$	$(Nd,Sr)MnO_3$	Theory
K_{tot}	260	220	200	306
K_{anti}	34	31	30	
K_{par}	125	100	100	
K_{anti}/K_{par}	0.27	0.31	0.30	1/3
$\Delta K/K_{tot}$	0.52	0.55	0.50	1/2
$\Delta\gamma_{DE}(T)/\gamma_{DE}(0)$				1/4

Table 3.3: Comparison of observed versus theoretical model predictions of kinetic energies (meV units) and kinetic energy ratios (dimensionless) for three $x = 0.3$ alloys.

In double-exchange only models such as Eq. (3.7) with $H_{INT} = 0$, the oscillator strength decreases by $1/4$ from low temperature to T_c. Models involving both double-exchange and electron-phonon coupling can produce a larger ΔK because of a feedback effect: decreasing K_{par} by increasing spin disorder increases the effective electron-phonon coupling, which decreases K_{par} still further. Millis *et al.*[32] distinguish between weak, intermediate, and strong electron-phonon couplings, with the intermediate coupling regime argued most relevant to CMR. In this regime, the phonon renormalization of the kinetic energy, which is small at low T where the behavior is metallic, increases at high T where the interactions localize the electrons. Including both DE and the JT interaction effects leads to a reduction in K_{par} giving $\Delta K/K \approx \frac{1}{2}$. Next, consider the antiparallel absorption. Table 3.3 lists K_{anti} and K_{anti}/K_{par}. This gives ratios of the antiparallel to the parallel spin absorptions of approximately $1/3$, in reasonable accord with the theoretical estimates. Moreover, the analysis suggests that at low T renormalizations of the kinetic energy resulting from electron-electron and electron-phonon interactions are not large. In view of the uncertainties involved, data and band theory correspond reasonably well.

3.4 Drude Weight

3.4.1 Purported anomalously small Drude weights

The previous section identified the low-lying electronic transitions and their relevant spectral weights and noted the transfer of spectral weight to a coherent response at temperatures below T_c. This section will focus on the properties of the low-frequency Drude-like conductivity at low temperatures. Below T_c, itinerant conduction resulting from ferromagnetic ordering increases the width of the e_g band and suppresses the JT effect. Evidence for charge and orbital ordering at different doping concentrations in the phase diagram (Fig. 1.3 on page 9) suggests the ground state may be the result of competition between interactions with the lattice and different types of ordering: ferromagnetic, charge, and orbital. At present, the exact nature of the low-temperature state is not fully understood.

Optical conductivity studies[27,28,42,43,109,120] have shown a shift in spectral weight from the visible to the infrared as the temperature is lowered below T_c. In the ferromagnetic state, the low-frequency optical spectrum is characterized by Drude-like conduction. Several groups have reported an anomalously small Drude weight in both $La_{0.7}Sr_{0.3}MnO_3$ and $La_{0.7}Ca_{0.3}MnO_3$.[42,43,120] Figure 3.16 shows low temperature (La,Sr)MnO_3 data for bulk ($x = 0.175$ single crystal) from Ref. 42 and for a thin film ($x = 0.3$) presented here. The bulk samples exhibit a large loss of spectral weight in the infrared, particularly the far-IR, relative to thin film samples. Note this discrepancy does not result from the differences in doping between the two samples shown in Fig. 3.16. A doping dependent study on bulk (La,Sr)MnO_3 reports[43] similar behavior for $x = 0.3$ bulk samples. Interpreting the small Drude weight in terms of an enhanced optical mass, the effective mass values reported on bulk samples exceed results from specific heat measurements.[121,122] Small apparent Drude weight may also be understood in terms of charge ordering. A charge density wave opens a par-

tial gap in the density of states at the Fermi level $N(E_f)$. Interpreting this reduction in $N(E_f)$ as a mass enhancement results in an optical mass increase, but a specific heat mass decrease. However, various groups[88,123] have cast doubts on these small Drude weights.

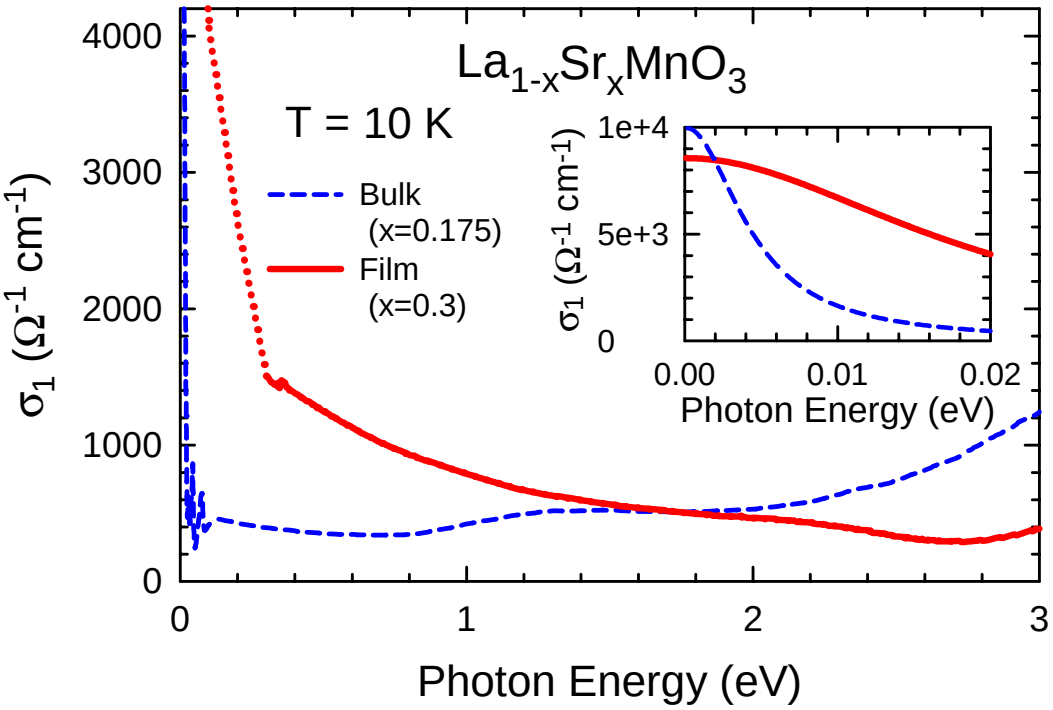

Figure 3.16: Comparison of low temperature optical conductivity from bulk single crystal ($x = 0.175$ from Ref. 42) versus thin film ($x = 0.3$) for (La,Sr)MnO_3.

The remainder of this section concentrates on the low-frequency optical conductivity, scattering rate, and mass enhancement of thin-film hole-doped manganites at temperatures below T_c. At these temperatures, the low-frequency conductivity exhibits a Drude-like behavior. The scattering rate and optical mass are obtained by fitting the far-infrared transmission data to a Drude model. Values for the plasma frequency disagree with the purportedly anomalously small Drude weights on bulk samples. The optical mass exceeds the specific heat mass, a result consistent with the presence of charge ordering in these optimally doped materials. Additionally, the

infrared spectral weight is compared to band-structure calculations.

3.4.2 Far-IR transmittance measurements

Thin films of $La_{0.7}Ca_{0.3}MnO_3$, $La_{0.7}Sr_{0.3}MnO_3$, $Nd_{0.7}Sr_{0.3}MnO_3$, and $La_{0.8}Ca_{0.2}MnO_3$ are grown on $LaAlO_3$ (LAO) substrates using pulsed laser deposition. The films (except $La_{0.7}Sr_{0.3}MnO_3$) were subsequently annealed in an O_2 environment.[124,125] Low residual resistivity $\rho(4\,\mathrm{K})$, and high resistivity peak temperature T_p indicate the excellent quality of the films.

Alloy	Doping, x	T_p (K)	$\rho(4\,\mathrm{K})$ ($\mu\Omega\,cm$)
(La,Sr)MnO_3	0.3	350	15
(La,Ca)MnO_3	0.3	275	124
	0.2	256	178
(Nd,Sr)MnO_3	0.3	210	367

Table 3.4: Residual resistivity $\rho(4\,\mathrm{K})$ and resistivity peak temperature T_p.

Transmittance $\mathcal{T}(\omega)$ and reflectance $\mathcal{R}(\omega)$ measurements of near normal incidence light were performed using a Fourier-transform spectrometer.[27] Temperature-dependent spectra from $10 - 150\,\mathrm{K}$ ($T < T_c$) are obtained. Two frequency ranges receive focus: the far-infrared (far-IR) $2.5 - 15\,\mathrm{meV}$ and the mid-infrared (mid-IR) $0.2 - 1.2\,\mathrm{eV}$. The spectral gap between 15 and $200\,\mathrm{meV}$ results from the opacity of LAO in this spectral range. Determination of the film conductivity in both frequency ranges requires knowledge of the index of refraction n and extinction coefficient κ of the substrate, which is measured separately.

In the far-IR, the thin-film transmittance (transmission of the film/substrate divided by transmission of the bare substrate) is given by Eq. (3.4). Given the metallic low-frequency behavior of the conductivity below T_c observed in these materi-

als,[27,109,120] a simple Drude model fits the measured $\mathcal{T}$ with conductivity given by

$$\tilde{\sigma}(\omega) = \frac{1}{4\pi}\frac{\omega_p^{*2}}{\gamma^* - \mathrm{i}\,\omega}\,, \tag{3.10}$$

where γ^* is the effective scattering rate and ω_p^* is the effective plasma frequency or spectral weight of the Drude conductivity.

Figure 3.17 shows transmittance curves in the far-IR (solid black lines) and fits to a Drude model (dashed blue lines) for several temperatures. The low-frequency

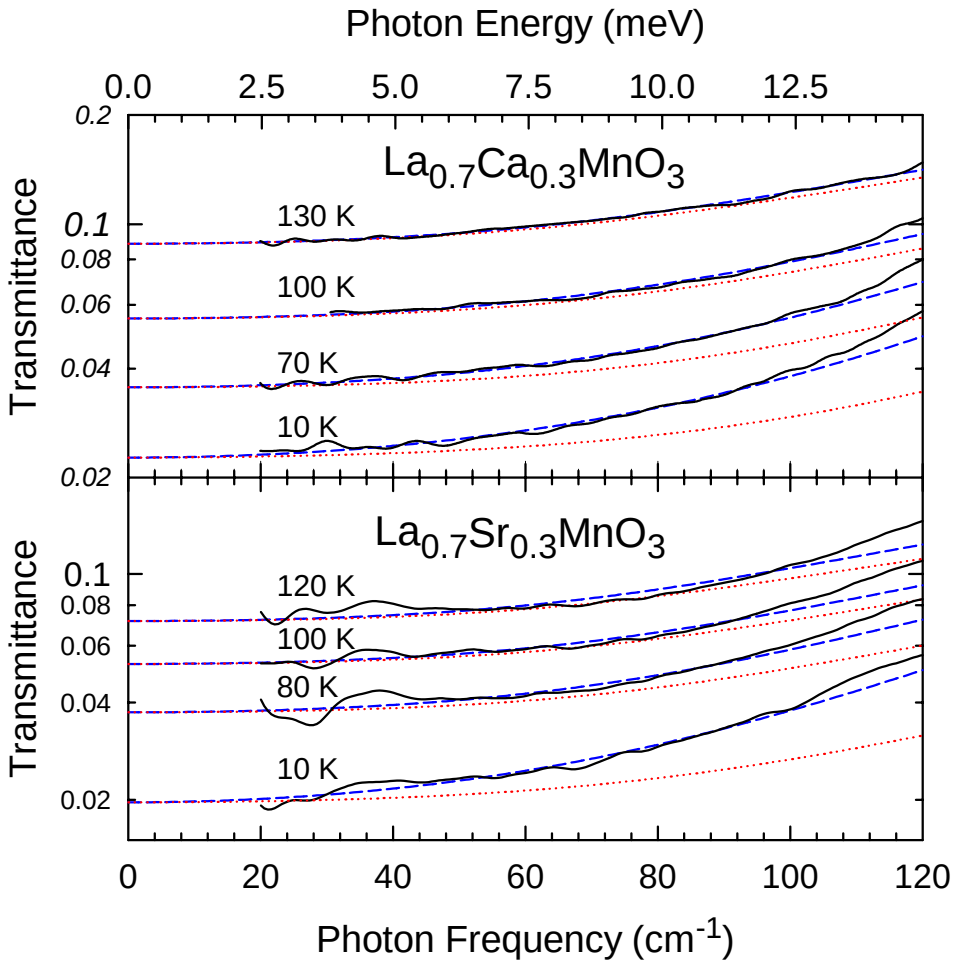

Figure 3.17: Transmittance of $La_{0.7}Ca_{0.3}MnO_3$ and $La_{0.7}Sr_{0.3}MnO_3$ as a function of photon energy for several temperatures. Solid lines are data, dashed lines are fits to a simple Drude model, and dotted lines are Drude fits in the limit, $\gamma^* \to \infty$.

$\mathcal{T}$ increases with temperature corresponding to a decrease in the conductivity. At

higher temperatures, $\mathcal{T}$ deviates less from the limiting value (dotted red lines) where $\gamma^* \to \infty$. In the infinite scattering-rate limit, $\sigma(\omega) \to \sigma_0$ and therefore the frequency dependence of the limiting case results from $n(\omega)$ of the LAO substrate. The slight upturn of the data relative to the fit curves (dashed lines) above $100\,\mathrm{cm}^{-1}$ appears independent of temperature. Note the uncertainty in $\mathcal{T}$ increases as the frequency nears the substrate cutoff around $120\,\mathrm{cm}^{-1}$. Transmittance curves for $La_{0.8}Ca_{0.2}MnO_3$ and $Nd_{0.7}Sr_{0.3}MnO_3$ (not shown) exhibit similar frequency dependence. However, even at lowest temperatures the data fail to deviate appreciably from the $\gamma^* \to \infty$ limit to allow extraction of the Drude parameters. Nevertheless, the data allows *upper* limits to be placed on the mass enhancement (discussed below) for $La_{0.8}Ca_{0.2}MnO_3$ and $Nd_{0.7}Sr_{0.3}MnO_3$.

Fitting the measured $\mathcal{T}$ in Fig. 3.17 with Eq. (3.10) determines the temperature dependence of the resulting γ^* and ω_p^*. Figure 3.18 shows the temperature dependence of the resulting fitting parameters. Solid lines represent a T^2 temperature dependent fit to the scattering rate,

$$\gamma^*(T) = \gamma_0^* + (k_B T)^2 / W\,, \tag{3.11}$$

where the fitting parameters are the defect scattering rate at zero temperature γ_0 and the characteristic energy for inelastic scattering W, and k_B is Boltzmann's constant. W values for $La_{0.7}Ca_{0.3}MnO_3$ and $La_{0.7}Sr_{0.3}MnO_3$ are listed in Table 3.5 on page 112.

As temperature increases, $\mathcal{T}$ approaches the limiting value and the uncertainty in determining both γ^* and ω_p^* increases. Error bars in Fig. 3.18 for γ^* in (a) and ω_p^* in (b) quantize this increase in uncertainty. At the highest temperatures ($140\,\mathrm{K}$ and $150\,\mathrm{K}$ for $La_{0.7}Ca_{0.3}MnO_3$ and $La_{0.7}Sr_{0.3}MnO_3$, respectively), γ^* falls below the T^2 fit. Currently, the cause of this decrease in the scattering rate and whether it persists above $150\,\mathrm{K}$ remains uncertain. While γ^* exhibits a strong temperature dependence,

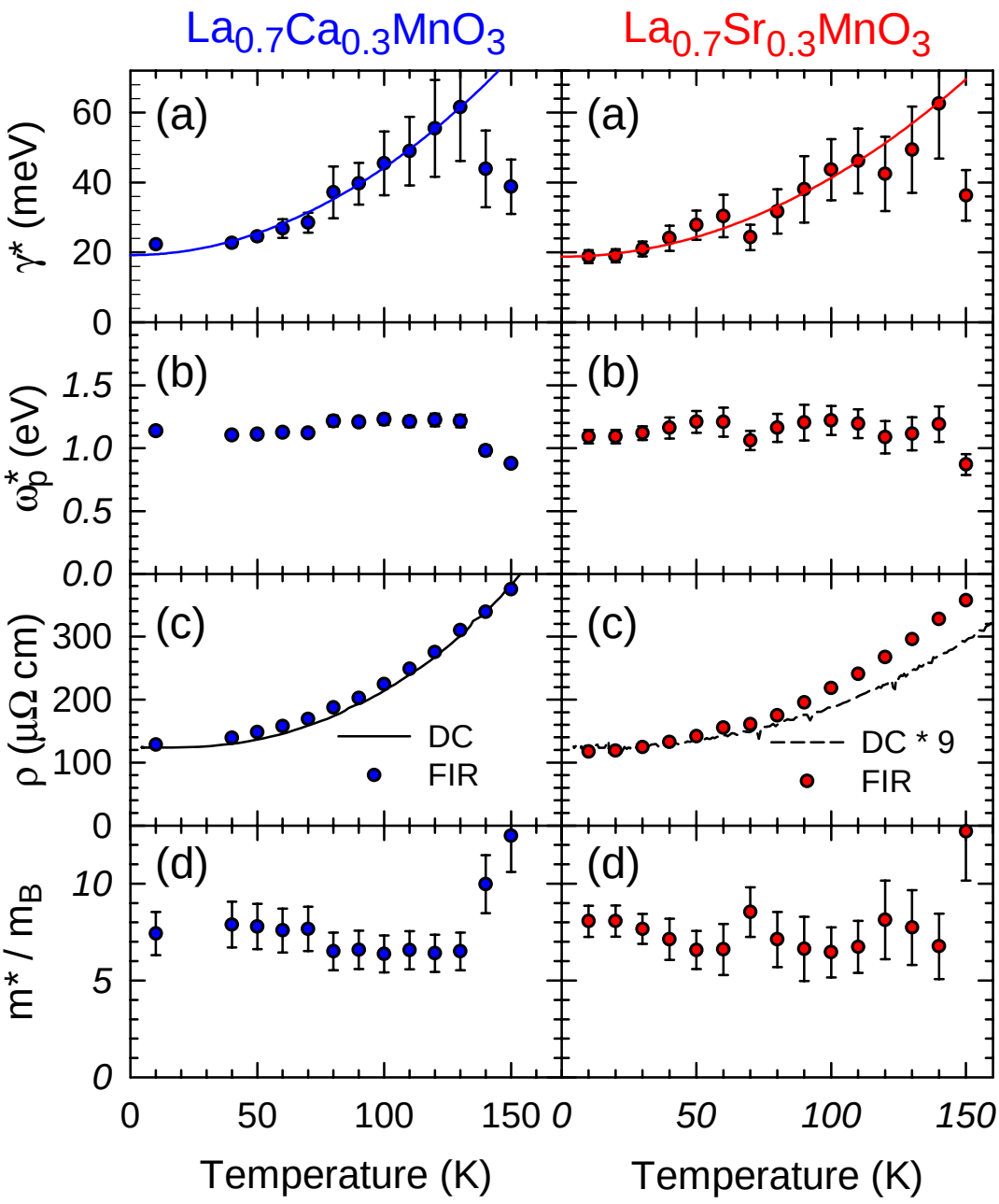

Figure 3.18: Temperature dependence of the (a) scattering rate γ^*, (b) plasma frequency ω_p^*, (c) resistivity ρ, and (d) mass enhancement m^*/m_B obtained from fitting the far-IR transmittance using a Drude conductivity. T^2 fit to γ^* shown in (a) as a solid line. The dc resistivity in (c) is plotted (lines) for comparison (note for $La_{0.7}Sr_{0.3}MnO_3$ dc resistivity is multiplied by a factor of 9). Error bars are shown explicitly in (a), (b), and (d) and are nominally the size of the solid circles in (c).

ω_p^* exhibits relatively weak temperature dependence.

Recent THz measurement[126] on thin films observed a similar T^2 dependence of γ^*, although with a higher residual scattering rate due to poorer crystal quality. However, the THz films show a measurable decrease of ω_p with temperature not observed in the present study. Moreover, the T^2 dependence of γ^* and relative T-independence of m^*/m_B differs with results reported on a $La_{0.7}Ca_{0.3}MnO_3$ polycrystalline sample.[120] The discrepancy with these bulk samples likely results from the effects of surface damage introduced during the polishing. Several groups[88,109,123] have since discussed the importance of polishing and surface scattering effects in measuring bulk reflectivity for polycrystalline and single-crystal samples. They found the optical properties of these materials depend sensitively on surface preparation. Specifically, polishing produced a decrease in mid-IR reflectivity and the apparent spectral weight. Cleaving or annealing the polished surfaces removes these effects, bringing the results on bulk samples in reasonable agreement with thin films.

The fit parameters γ^* and ω_p^* determine the zero-frequency resistivity

$$\rho = \frac{4\pi\gamma^*}{\omega_p^{*2}} = \frac{4\pi\gamma}{\omega_p^2} \,. \tag{3.12}$$

Figure 3.18(c) shows the temperature dependence of ρ. Plotting both the far-IR values (solid circles) derived from Eq. (3.12) and the dc values (lines) from standard four-probe resistance measurements affords comparison of the two results. Far-IR and dc values agree reasonably well in $La_{0.7}Ca_{0.3}MnO_3$, however, the dc value for $La_{0.7}Sr_{0.3}MnO_3$ has been scaled by a factor of 9, owing to similar problems with the dc measurement discussed in the previous section. Uncertainty in the far-IR ρ (error bars are nominally the size of the points) results from uncertainty in the film thickness and detector noise.

3.4.3 Mass enhancement

The optical mass enhancement is defined by

$$m^*/m_B \equiv (\omega_p^B/\omega_p^*)^2 = 1 + \lambda \,, \tag{3.13}$$

where λ is the mass enhancement factor and the plasma frequencies, ω_p^B and ω_p^*, are obtained from band structure calculations and far-IR measurements, respectively. Pickett and Singh[110] predict $\omega_p^B = 3.1\,\text{eV}$ for $La_{0.7}Ca_{0.3}MnO_3$. A tight binding parameterization of the band structure with hopping parameter $t_0 = 0.67\,\text{eV}$ gives similar results.[116] Taking $\omega_p^B = 3.1\,\text{eV}$, mass enhancement as a function of temperature is found to be approximately 8 for both materials. Table 3.5 compares low-temperature results for the alloys and Fig. 3.18(d) shows the temperature dependence. Optical

		m^*/m_B		
Alloy	Doping, x	Optics[a]	Specific Heat[b]	W (meV)
(La,Sr)MnO_3	0.3	7.9 ± 0.6	2.10 ± 0.06	3.3
(La,Ca)MnO_3	0.3	7.4 ± 0.4	2.84 ± 0.04	3.0
	0.2	$\lesssim 13$	3.88 ± 0.06	
(Nd,Sr)MnO_3	0.3	$\lesssim 13$	15[c]	

[a] $T = 10\,\text{K}$
[b] Ref. 121
[c] Ref. 127

Table 3.5: Mass enhancements from optics and specific heat and characteristic scattering-rate energies.

masses for $La_{0.8}Ca_{0.2}MnO_3$ and $Nd_{0.7}Sr_{0.3}MnO_3$ represent *upper* bounds owing to the large residual scattering rate as mentioned above.

The T^2 temperature dependence of the scattering suggests that γ^* and hence m^* (see below) may also be frequency dependent. The analysis presented above assumes a frequency-independent γ^* and ω_p^*. Consideration of a frequency dependent γ^* necessitates modification of the Drude theory in order to obtain an optical

conductivity that is a proper response function satisfying Kramers-Kronig relations. Specifically, a frequency dependent scattering rate must include a real and imaginary part, $\tilde{\gamma}(\omega) = \gamma_1(\omega) + \mathrm{i}\,\gamma_2(\omega)$, where $\gamma_2(\omega) = -\omega\,\lambda(\omega)$. This leads to the extended Drude model[128]

$$\tilde{\sigma}(\omega) = \frac{1}{4\pi}\frac{\omega_p^2}{\gamma_1(\omega) - \mathrm{i}\,\omega[1+\lambda(\omega)]} = \frac{1}{4\pi}\frac{\omega_p^*(\omega)^2}{\gamma^*(\omega) - \mathrm{i}\,\omega} \tag{3.14}$$

with a renormalized scattering rate, $\gamma^*(\omega) = \gamma_1(\omega)/[1+\lambda(\omega)]$, and a renormalized plasma frequency, $\omega_p^*(\omega) = \omega_p/\sqrt{1+\lambda(\omega)}$. Thus, the frequency-dependent scattering gives rise to a concomitant frequency-dependent mass enhancement, $m^*/m_B(\omega) = 1 + \lambda(\omega)$.

Obtaining $m^*/m_B(\omega)$ for these transmission measurements requires an assumed form (given the lack of a direct measurement) for the frequency dependence of γ. The squared power law temperature dependence of γ^* implies a similar ω^2 dependence at low-frequency.[129] This gives the full temperature and frequency dependent scattering rate, $\gamma^*(\omega, T) \propto \omega^2 + (p\,\pi\,T)^2$. Gurzhi calculated $p = 2$ for electron-electron scattering,[130] while for heavy fermion systems, experimental data[129] is consistent with $p \leq 1$. Sulewski *et al.* proposed a simple phenomenological model,

$$\tilde{\gamma}(\omega) = \gamma_0 + \frac{\lambda_0\,\omega_s\,\omega}{(\omega + \mathrm{i}\,\omega_0)}\,, \tag{3.15}$$

which satisfies the ω^2 behavior at low frequencies and saturates at the characteristic frequency ω_s. Using W from the T^2 fits to γ^* (see Fig. 3.18) and a value for p, ω_s may be determined from Eq. (3.15). For $p = 1$, frequency dependent scattering results in less than a 15% effect on the mass enhancement and $\omega_s \gg 15\,\mathrm{meV}$, the high-frequency cutoff of the far-IR measurements. Thus, in the far-IR, the frequency dependence of γ^* and m^*/m_B is not significant.

A comparison of the mass enhancement obtained from optical measurements reported here with those obtained from specific heat measurements proves interest-

ing. The low-temperature ($3 < T < 8$ K) specific heat is given by

$$C_H = \gamma_{el}\, T + \delta\, T^{3/2} + \beta\, T^3\,, \tag{3.16}$$

where the three terms arise from charge carriers, magnons, and phonons, respectively.[122] The coefficient of the linear (electronic) term is $\gamma_{el} = \pi^2 k_B^2 N(E_f)/3 \propto m^*$. For $La_{0.7}Ca_{0.3}MnO_3$ and $La_{0.7}Sr_{0.3}MnO_3$, γ_{el} is 4.5 ± 0.1 and 3.4 ± 0.15 mJ/mole K^2, respectively. Relating the experimental γ_{el} to band theory predictions gives the specific heat mass enhancement,

$$m^*/m_B \equiv \gamma_{el}/\gamma_{el}^B = 1 + \lambda\,, \tag{3.17}$$

analogous to the optical enhancement in Eq. (3.13). Band structure calculations by Pickett and Singh[110] predict $N(E_f) = 0.47$ states/eV for the majority spin band, giving $\gamma_{el}^B = 1.1$ mJ/mole K^2. Table 3.5 shows mass enhancements calculated using this γ_{el}^B. Including the $N(E_f)$ for the minority spin bands (smaller than the majority by approximately a factor of 2) increases γ_{el}^B and $(\omega_p^B)^2$. This tends to reduce the specific heat mass enhancement while increasing the optical mass enhancement. However, cation disorder tends to localize minority carriers.[110] Hence, the minority spin bands are not included.

A comparison of m^*/m_B from optics ($T = 10$ K) and specific heat as shown in Table 3.5 indicates the optical mass exceeds the specific heat mass by a factor of $2 - 3$. This observation contrasts with the earlier results of other groups on $La_{0.7}Ca_{0.3}MnO_3$[120] and $La_{0.7}Sr_{0.3}MnO_3$[42,43] bulk samples where much larger optical masses are reported. Thus, the larger optical mass enhancement observed in Table 3.5 suggests that charge ordering correlations may be present in the ground state of the CMR manganite alloys around $x = 0.3$ doping.

The small value of W in Table 3.5, $W \ll E_f \approx 1$ eV, indicates strong inelastic scattering. For electron-electron scattering, W is typically on the order of E_f. This is

consistent with the relatively large mass enhancement in these materials in comparison with conventional metals. The value of the characteristic frequency ω_0 reasonably agrees with the expectations of electron-phonon interactions where typically ω_0 would be somewhat larger than the average phonon frequency of the system. Explanations for the temperature dependence of the scattering rate include magnons[115,131] and phonons.[132] However, the exact origin of the T^2 scattering remains unclear.

3.4.4 Mid-IR conductivity

In the mid-IR, numerical inversion of the Fresnel $\mathcal{T}$ and $\mathcal{R}$ formulae for a film on an absorbing substrate[86] determine optical constants, such as $\tilde{\sigma}(\omega)$ or the dielectric constant $\tilde{\epsilon}(\omega)$, without the need for Kramers-Kronig analysis.[80] Figure 3.19 shows the real part of the optical conductivity σ_1 and the real part of the dielectric constant ϵ_1 (inset) in the mid-IR for $La_{0.7}Ca_{0.3}MnO_3$. The observed negative ϵ_1 is characteristic

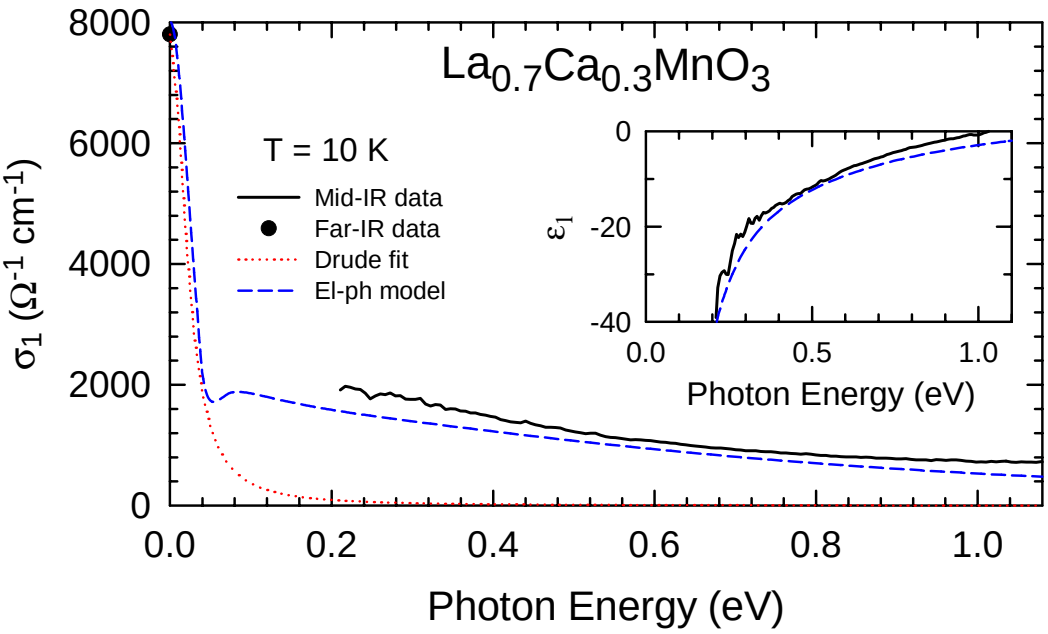

Figure 3.19: Frequency dependence of the real part of the optical conductivity $\sigma_1(\omega)$ for $La_{0.7}Ca_{0.3}MnO_3$. Simple and extended Drude conductivity are shown as a dotted and dashed line, respectively. The inset shows the real part of the dielectric constant $\epsilon_1(\omega)$.

of a metal. For $T < 150\,\mathrm{K}$, σ_1 exhibits negligible temperature dependence and conse-

quently Fig. 3.19 shows only the $T = 10$ K data (solid line). In this spectral range, σ_1 increases at low frequency and eventually must extrapolate to the far-IR value (solid circle). For comparison, the Drude conductivity resulting from the fit parameters, γ^* and ω_p^* is shown as a dotted line. The extrapolated conductivity associated with the Drude model falls well short of the observed mid-IR value.

While the mass enhancement analysis does not support an anomalously small Drude weight, a comparison of the observed far-IR Drude weight with the total spectral weight predicted from band structure calculations proves interesting. The kinetic energy K given in Eq. (2.25) on page 53 serves well for this comparison. If ω is chosen to include all the optical transitions within the e_g bands, K represents the kinetic energy of the Mn e_g electrons. As discussed previously,[27] the e_g contribution to the conductivity in these materials occurs in the frequency range $0 - 2.7$ eV. To estimate K, the measured far-IR and mid-IR conductivity for the $La_{0.7}Ca_{0.3}MnO_3$ sample shown in Fig. 3.19, combined with the sample discussed in the previous section in the range from $1 - 2.7$ eV, provides σ_1 over the required spectral range.[133] The observed K for $La_{0.7}Ca_{0.3}MnO_3$ is 280 meV, which agrees reasonably well with the tight-binding prediction shown in Eq. (3.9). Considering only the contribution from the Drude conductivity, Eq. (2.25) gives $K_{\text{Drude}} = a_0/(4\pi e^2)\,\omega_p^{*2}$. Thus, K_{Drude} from the far-IR is 28 meV, smaller than the band structure value of 207 meV by the mass enhancement factor $1 + \lambda$.

What is the source of the remaining spectral weight in the infrared? The earlier consideration of a frequency dependent scattering resulting from electron-electron interactions found little effect on the conductivity in the far-IR region. While these effects increase with frequency, el-el scattering cannot account for all of the missing spectral weight. Other mechanisms, *e.g.* electron-phonon or electron-magnon coupling, may be responsible for the additional absorption. In particular, the dynamic JT effect plays a critical role in determining the IR conductivity and coupling with the

lattice has proven to be important in these systems.

Incorporation of electron-phonon coupling effects in the low frequency conductivity requires a scattering rate with contributions from both impurities and phonon scattering. A straightforward model consists of the Holstein[134] electron-phonon (el-ph) interaction. Figure 3.20(a) illustrates the model schematically. An incident photon

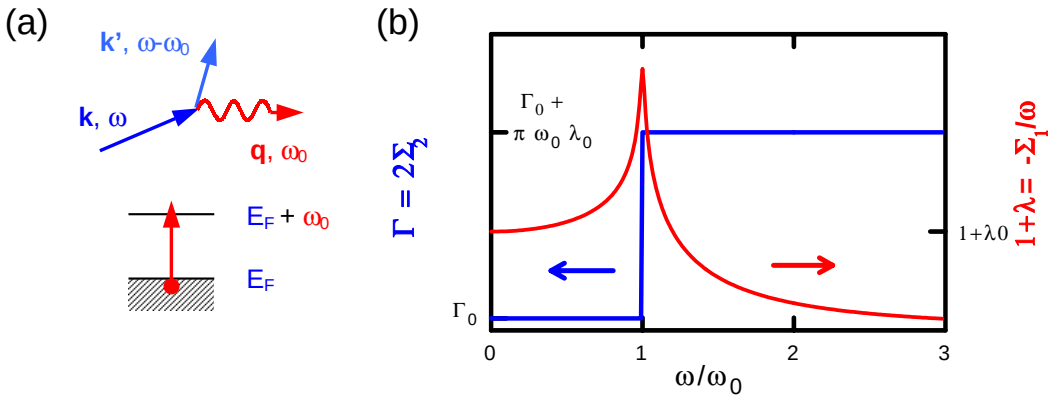

Figure 3.20: Holstein model of electron-phonon interaction. (a) Scattering of incident photon with wavevector $\boldsymbol{k}$ and energy $\hbar\omega$ by a phonon with wavevector $\boldsymbol{q}$ and energy $\hbar\omega_0$. (b) Single particle scattering rate Γ and electron phonon coupling strength λ versus incident photon energy in units of the characteristic phonon frequency, ω_0.

of wavevector $\boldsymbol{k}$ and energy $\hbar\omega$ scatters off a phonon of wavevector $\boldsymbol{q}$ and phonon energy $\hbar\omega_0$. The electron final state is given by wavevector $\boldsymbol{k}'$ and energy $\hbar(\omega - \omega_0)$. For simplicity, the model assumes an Einstein phonon density of states, *i.e.*, a single phonon characteristic frequency ω_0. In this one phonon model, the single particle self energy $\tilde{\Sigma}(\omega)$ consists[34] of a real part Σ_1 (proportional to the mass enhancement) and an imaginary part Σ_2 (proportional to the scattering rate) given by

$$\begin{aligned} \Sigma_1(\omega) &= \frac{1}{2}\,\omega_0\,\lambda_0\,\ln\left|\frac{\omega_0-\omega}{\omega_0+\omega}\right| \\ \Sigma_2(\omega) &= \frac{1}{2}\,\Gamma_{\text{imp}} + \frac{\pi}{2}\times\begin{cases} 0 & ,\ \omega < \omega_0 \\ \omega_0\,\lambda_0 & ,\ \omega \geq \omega_0 \end{cases} \end{aligned} \tag{3.18}$$

Figure 3.20(b) shows the single particle scattering rate $\Gamma = 2\,\Sigma_2$ and mass enhancement, $1 + \lambda = 1 - \Sigma_1/\omega$, as a function of frequency normalized to the characteristic

phonon frequency ω_0. The optical conductivity is written in terms of the single particle self energies as a sum over the allowable transitions. Using the self-energy of Eq. (3.18), the optical conductivity is then given by[101]

$$\tilde{\sigma}(\omega) = \frac{A}{\omega}\int_{-\omega}^{0} \mathrm{d}\omega' \, \frac{1}{2\,\Sigma_2(\omega') - \mathrm{i}[\omega - \Sigma_1(\omega+\omega') + \Sigma_1(\omega')]}\,, \tag{3.19}$$

where $A \propto (\omega_p^B)^2$ is the spectral weight of the infrared conductivity. This single-particle free-electron-like model neglects vertex corrections. Figure 3.19 shows the predicted σ_1 and ϵ_1 (dashed curves) from Eq. 3.19 using parameter values: $\omega_0 = 300\,\mathrm{cm}^{-1}$, $\lambda_0 = 4$, and $\omega_p^B = 3.1\,\mathrm{eV}$. Note that $m^*/m_B(0) = 1 + \lambda_0 = 5$, smaller than the value obtained in the far-IR but still larger than the specific heat mass (see Table 3.5).

Having determined the model conductivity, the average scattering rate and mass enhancement may be extracted using the extended Drude form of the conductivity [see Eq. (3.14)].

$$\begin{aligned} \Gamma(\omega) &= \frac{(\omega_p^B)^2}{4\pi}\,\frac{\sigma_1(\omega)}{\sigma_1(\omega)^2 + \sigma_2(\omega)^2} \\ m^*/m_B\,(\omega) &= 1 + \lambda(\omega) \\ &= \frac{(\omega_p^B)^2}{4\pi}\,\frac{\sigma_2(\omega)/\omega}{\sigma_1(\omega)^2 + \sigma_2(\omega)^2}\,, \end{aligned} \tag{3.20}$$

where the plasma frequency is taken to be the band value, $\omega_p \approx 3.1\,\mathrm{eV}$. Figure 3.21 shows the frequency-dependent scattering rate and mass enhancement for $La_{0.7}Ca_{0.3}MnO_3$ obtained using Eq. (3.20) with the data (points) and model (lines). Reasonable agreement between theory and model, particularly for frequencies below $0.5\,\mathrm{eV}$. Above $0.5\,\mathrm{eV}$ the scattering rate begins to deviate from this simple picture. This may suggest the onset of interband transitions.

By definition, including frequency-dependent scattering in the extended Drude model to recover the intraband spectral weight leads to the result shown as a dashed line in Fig. 3.19. However, the Drude conductivity alone, even including the effects of inelastic scattering, does not account for all of the mid-IR σ_1, particularly above

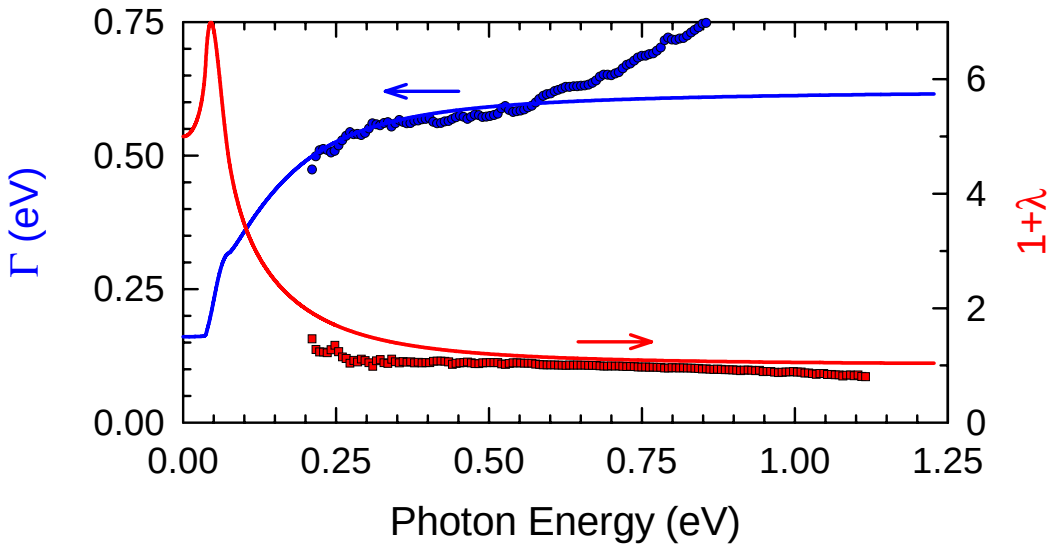

Figure 3.21: Frequency-dependent scattering rate Γ and mass enhancement $1+\lambda$ from model conductivity predictions (solid curves) compared with mid-IR data (points). Model parameter values are $\omega_0 = 300\,\mathrm{cm}^{-1}$, $\lambda_0 = 4$, and $\omega_p = \omega_p^B = 3.1\,\mathrm{eV}$. $La_{0.7}Ca_{0.3}MnO_3$ data at $10\,\mathrm{K}$ shown.

$1\,\mathrm{eV}$. The remaining spectral weight most likely originates from interband transitions occurring between the two Mn e_g bands. The total infrared conductivity then represents the sum of a Drude term from coherent carriers, an electron phonon term from inelastic scattering, and a term from interband transitions, $\sigma = \sigma_{\mathrm{Drude}} + \sigma_{\mathrm{el\text{-}ph}} + \sigma_{\mathrm{IB}}$.

3.5 Conclusions

Temperature dependent optical conductivity studies of $LaMnO_3$, the parent compound of the colossal magnetoresistance manganites, reveal interesting properties in the electronic and phonon spectral regions. The temperature dependence of the spectral weight of the optical transition at $2\,\mathrm{eV}$ correlates with T_N. The double-exchange picture, counting nearest-neighbor spin alignment, provides a semi-quantitative description of the observed temperature-dependent changes in oscillator strength. These observations contradict the predictions of Allen and Perebeinos, which explain this optical transition as arising from on-site transitions of

a self-trapped exciton. On the contrary, the present optical studies suggest charge-transfer hopping between nearest-neighbor Mn ions dominates the spectral weight of the 2 eV feature. In the far-IR spectral range, several of the symmetry-allowed phonons exhibit TO phonon shifts that correlate with the antiferromagnetic ordering.

Having identified the relevant optical transitions in the parent compound, optical studies of the changes with doping provide insight into the nature of the CMR effect. In particular, Section 3.3 presented the optical conductivity and spectral weight of several $x = 0.3$ hole-doped manganites $Nd_{0.7}Sr_{0.3}MnO_3$, $La_{0.7}Ca_{0.3}MnO_3$, and $La_{0.7}Sr_{0.3}MnO_3$, including the identification of the physical origin of the various features in the absorption spectrum and determination of their variation with temperature and alloy material. A broad maximum near 1 eV characterizes the low-energy optical conductivity in the paramagnetic-insulating state of these materials. This feature shifts to lower energy and grows in optical oscillator strength as the temperature lowers into the ferromagnetic state. It persists well below T_c and transforms eventually into a Drude-like response. This optical behavior and the activated transport in the paramagnetic state of these materials are consistent with a Jahn-Teller small polaron.

A comparison of the spectral weight with predictions from a tight-binding parameterization of the band structure including both DE and JT effects provides important insight into the physics governing these materials. Specifically, the e_g electron kinetic energy is largest and the effective electron-phonon interaction weakest in $La_{0.7}Sr_{0.3}MnO_3$, while the kinetic energy is smallest and the electron-phonon interaction strongest in $Nd_{0.7}Sr_{0.3}MnO_3$, with $La_{0.7}Ca_{0.3}MnO_3$ being intermediate. This kinetic energy roughly scales with T_c in these materials in qualitative agreement with theory. In all compounds at lowest temperature the e_g kinetic energy approximately equals the band theory value. As temperature increases to above T_c, the change in e_g kinetic energy between lowest temperature and T_c exceeds the expectations of

models involving only double exchange. However, the optical spectra and oscillator strength changes compare well with models that include both double exchange and the dynamic Jahn-Teller effect in the description of the electronic structure, suggesting the importance of electron-phonon coupling.

In the far-IR at low-temperatures a Drude analysis of the measured optical properties determines γ^* and ω_p^* as a function of temperature. ω_p^* exhibits little temperature dependence while γ^* shows a strong T^2 temperature dependence. The value of ω_p^* in thin film samples suggest the anomalously small Drude weight reported for bulk samples arises from spurious surface preparation effects. The optical mass enhancement exceeds the mass enhancement found from specific heat, indicating that charge ordering correlations may be present in the ferromagnetic ground state of the CMR manganites. At frequencies above the far-IR, frequency-dependent scattering due to the strong electron-phonon coupling observed in this system serves to account for a majority of the IR spectral weight. A comparison of the Drude weight with the measured total spectral weight finds that the infrared conductivity is consistent with conventional contributions from coherent Drude carriers, inelastic electron-phonon scattering processes, and interband transitions.

Chapter 4

Hexa-Manganite $LuMnO_3$

The colossal magnetoresistance compounds, discussed in the previous chapter, attracted a great deal of attention owing to their interesting physical properties and potential applications. Another series of RMnO$_3$ manganites (R=Ho, Er, Tm, Yb, Lu, Y, Sc, and In) have a smaller rare-earth ionic radius R^{3+} and crystallize in the hexagonal lattice. Several groups report[52,135–139] various aspects of the electromagnetic response in hexa-manganites. However, none of these earlier reports present a detailed study of the optical spectra of quality single-crystal samples as a function of temperature. This chapter presents a systematic study of the linear optical response of single crystals of LuMnO$_3$, which elucidates the origin of the ϵ_0 anomalies and the effects of the Mn-Mn exchange energy on the electrodynamics of this system. The following sections show that the exchange interaction manifests itself in an antiferromagnetic resonance, spin-phonon coupling, and the temperature dependence of a 1.7 eV on-site Mn d-d optical transition. The results provide a comprehensive view of the magnetic and electronic structure of this interesting ferroelectric and strongly frustrated antiferromagnetic material.

4.1 Experiment

4.1.1 Sample preparation

Single crystals of LuMnO$_3$ were grown using the travelling floating zone method and characterized by magnetization, resistivity, and x-ray powder diffraction.[140] The

lattice constants as well as the observed macroscopic properties agree well with measurements reported in the literature.[50,53] In general, hexagonal manganites displays insulating behavior in transport. The resistivity of $LuMnO_3$ increases with decreasing temperature, characteristic of an insulator. Additionally, there exists an anisotropy[53] between the in-plane ρ_{ab} and out-of-plane ρ_c resistivities, $\rho_c \gtrsim 10\,\rho_{ab}$.

In order to study the inherent optical anisotropy of the hexagonal crystal structure, samples with surfaces perpendicular (001) and parallel (110) to the c-axis were prepared. The 001 samples cleave as thin platelets. Polishing with $0.3\,\mu$m diamond paste provides flat surfaces. After polishing, samples are annealed.[140] The 001 sample studied in this work is $5 \times 1.5\,\text{mm}^2 \times 25\,\mu$m thick. Such a thin sample affords transmission measurements in regions lacking strong absorption. The 110 sample studied is much thicker, having dimensions $2 \times 4 \times 1.5\,\text{mm}^3$.

4.1.2 Extracting optical constants

Temperature dependent ($4 - 300\,\text{K}$) transmittance $\mathcal{T}$ and reflectance $\mathcal{R}$ in a frequency range from $1.2\,\text{meV}$ to $5.6\,\text{eV}$ ($10 - 45000\,\text{cm}^{-1}$) are obtained using FTIR spectroscopic techniques detailed in Chap. 2. Isolating the incident polarization of the electric field E relative to the crystallographic c-axis for the 110-oriented requires several different linear polarizers to operate over the entire spectral range. In the visible range, dichroic sheets polarize the incident light. In the far-IR, a combination of wire grids on Mylar and KRS-5 substrates polarize the incident beam. For the 001-oriented sample, the near-normal incident electric field lies in the plane (*i.e.*, $E \perp c$) without requiring additional polarizers. In the remainder of the chapter wherever specific mention of the sample crystallographic orientation is absent, $E \perp c$ refers to the in-plane response of the 001-oriented sample and $E \parallel c$ refers to the $E \parallel c$ response of the 110-oriented sample.

Employing a variety of measurement techniques affords extraction of the op-

tical constants, *e.g.*, the dielectric constant $\tilde{\epsilon}$ or optical conductivity $\tilde{\sigma}$. For regions where the transmittance tends to zero, Kramers-Kronig (KK) analysis of the measured bulk reflectance together with low and high frequency extrapolations provides the reflectance phase θ. At low frequency ($\omega < 10\,\mathrm{cm}^{-1}$), the reflectance extrapolates to zero as a constant, consistent with the insulating nature of the dc-resistivity. As described in Chap 2, the interband frequency dependence β and the onset frequency of free electron behavior ω_{FE} characterize the high-frequency extrapolations. For the $E \perp c$ sample, $\beta \approx 0.75$ and $\omega_{FE} \approx 3 \times 10^6\,\mathrm{cm}^{-1}$ best match the optical constants in the near-infrared (near-IR) region determined using other methods described below.

In the mid-infrared (mid-IR) transparency widow, numerically inverting the Fresnel coefficients (see Chap. 2 and Appendix A) for $\mathcal{T}$ and $\mathcal{R}$ of a finite thickness slab determines n and κ. These curves may be patched together to obtain the predicted bulk reflectance shown as the dashed curve in Fig. 4.1. Well inside the transparency window (where $\kappa \approx 0$), the thin platelet sample acts a Fabry-Pérot resonant cavity. The resulting $\mathcal{T}$ and $\mathcal{R}$ will display interference (étalon) maxima and minima. Peak fits to the transmittance maxima determine the index of refraction n given by Eq. (2.36) on page 59. Accurate identification of n requires precise knowledge of the peak number m. This becomes more difficult as frequency increases. Thus, the low end of the IR transparency window more accurately determines the index of refraction.

4.1.3 $E \perp c$ measured spectra

Reflectance

The room-temperature reflectance spectrum for the $E \perp c$ orientation on the thin platelet sample is shown in Fig. 4.1 (solid curve). Electronic transitions dominate the optical spectrum of $E \perp c$ $LuMnO_3$ in the visible to ultraviolet (UV) frequency range ($\omega \gtrsim 1\,\mathrm{eV}$). Two main features emerge from the reflectance spectrum: (i) a narrow feature centered around $1.7\,\mathrm{eV}$ and (ii) a broad feature at higher frequencies

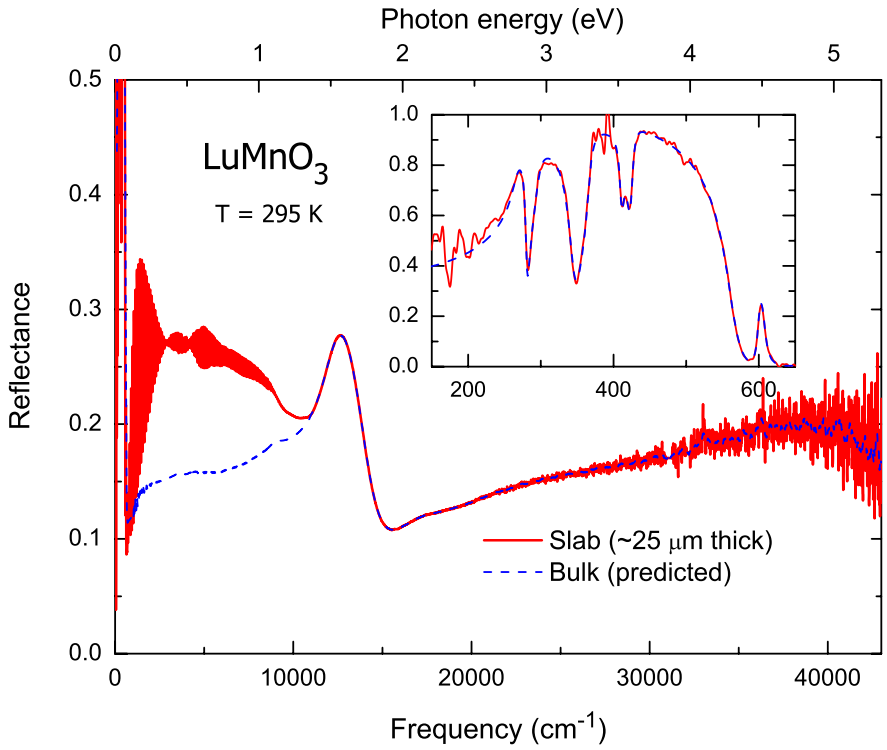

Figure 4.1: Frequency dependence of the room-temperature reflectance of $LuMnO_3$ in the $E \perp c$ polarization. Measured spectrum (solid curve) and bulk reflectance spectrum (dashed curve) predicted from n and κ determined independently (see text). Inset highlights phonons in the far-infrared spectrum.

≈ 5 eV. Reflectance spectra in the range $10 - 300$ K (not shown) reveal a strong temperature dependence of the 1.7 eV feature while the 5 eV feature remains relatively unchanged.

Below the electronic transitions in the infrared spectral range ($1000 - 10000\,\mathrm{cm}^{-1}$), the sample transmittance becomes nonzero. As a result, étalon interference effects appear below $\approx$ 1 eV. In this region, the measured $\mathcal{R}$ (solid red curve in Fig. 4.1) no longer represents the bulk reflectance of a semi-infinite sample (dashed blue curve). As described above, inversion of both $\mathcal{T}$ and $\mathcal{R}$ spectra determine the optical constants and hence predict the bulk reflectance using Eq. (2.29). The inset of Fig. 4.2 shows the predicted bulk reflectance obtained using

this method. The predicted bulk $\mathcal{R}$ values merge well with the measured $\mathcal{R}$ spectra for frequencies where $\mathcal{T} \to 0$.

In the $250 - 700\,\mathrm{cm}^{-1}$ frequency range, several phonons appear clearly in the reflectance. The inset of Fig. 4.1 shows the room temperature spectrum in this far-IR region. The $\mathcal{R}$ spectra are well-described by Eq. (2.29) with $\tilde{\epsilon}(\omega)$ given by the product form in Eq. (2.31). The relatively strong, wide-band phonons in the $E \perp c$ polarization require the product form rather than the simpler sum of Lorentzians given by Eq. (2.30). The peak frequencies of these phonons exhibit strong temperature dependence (not shown), which will be discussed below. Outside the phonon range $\omega \lesssim 200\,\mathrm{cm}^{-1}$ and $\omega \gtrsim 650\,\mathrm{cm}^{-1}$ (not shown) the sample again becomes transparent, demonstrating étalon interference peaks.

Transmittance in the mid-IR

Figure 4.2 shows transmittance in the mid to near-IR region. The transmittance drops precipitously at the onset of electronic transitions ($\approx 1.1\,\mathrm{eV}$). A temperature independent absorption onset $\approx 1.2\,\mathrm{eV}$ likely represents the tail of the $5\,\mathrm{eV}$ feature observed in reflectance. Above this onset, additional absorption due to the $1.7\,\mathrm{eV}$ feature displays strong temperature dependence. The inset of Fig. 4.2 highlights this feature.

Weak étalon peaks, appearing below $\approx 1\,\mathrm{eV}$ in Fig. 4.2, strengthen at lower IR frequencies. Figure 4.3 shows these transmission peaks from $1000 - 3000\,\mathrm{cm}^{-1}$ at room temperature. Thickness variations and a lack of perfectly parallel edges of the platelet sample result in the beat pattern superimposed on the étalon interference peaks. Nevertheless, a number of well-defined $\mathcal{T}$ peaks exist in this spectral range. Fitting the peaks and using Eq. (2.36) accurately determines the index n. Having n affords determination of the real part of the dielectric constant, $\epsilon_1 = n^2 + \kappa^2 \approx n^2$ for $\kappa \approx 0$ in this weakly absorbing spectral range. In the far-IR, ϵ_1 changes drastically

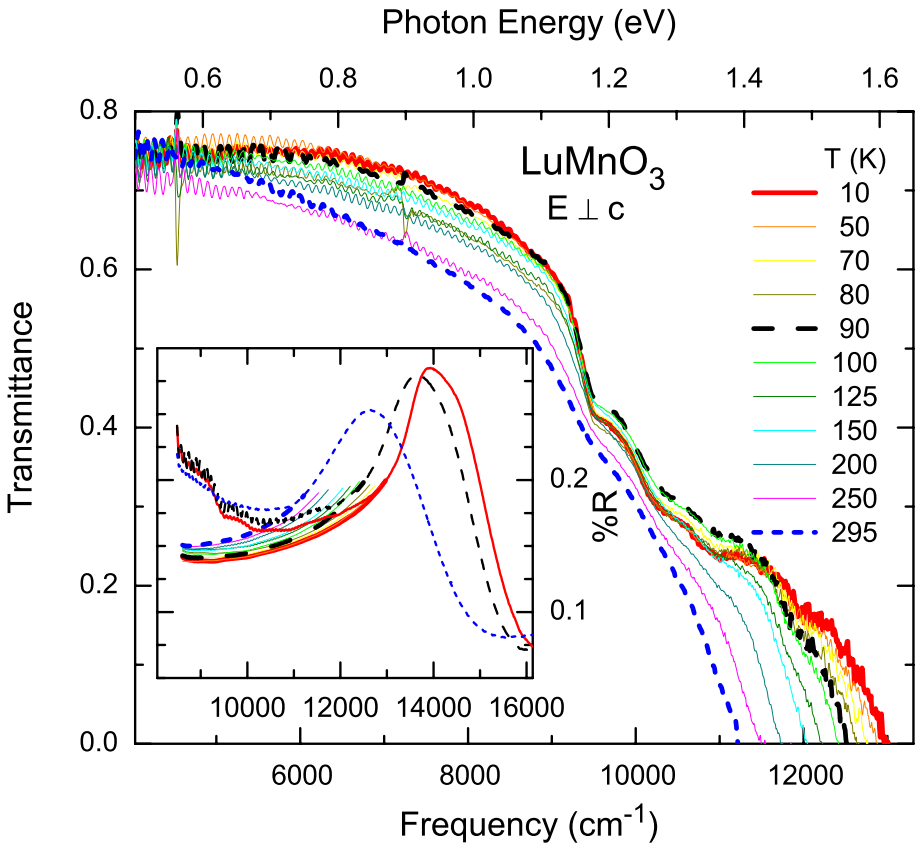

Figure 4.2: Near-infrared to visible transmittance ($E \perp c$) of $LuMnO_3$ at various temperatures. Inset shows the measured reflectance spectra for 10, 90, and 295 K shown together with bulk reflectance (all temperatures) predicted from n and κ determined independently (see text).

throughout the observed phonon resonances. However at frequencies well above the phonons, the dielectric constant saturates to a relatively constant value, $\epsilon_\infty \equiv \epsilon_1(\sim 2700\,\mathrm{cm}^{-1})$, before the onset of interband transitions. The inset of Fig. 4.3 shows the temperature dependence of ϵ_∞. A clear anomaly in ϵ_∞ appears at T_N and will be addressed further in Sec. 4.3.

Transmittance in the far-IR

At frequencies below the phonons ($\lesssim 200\,\mathrm{cm}^{-1}$), another transparency window opens and $\mathcal{T}$ again becomes nonzero. Several étalon peaks in the far-IR $\mathcal{T}$ are visible. Figure 4.4 shows the first-order ($m = 1$) peak. As discussed above, the peak

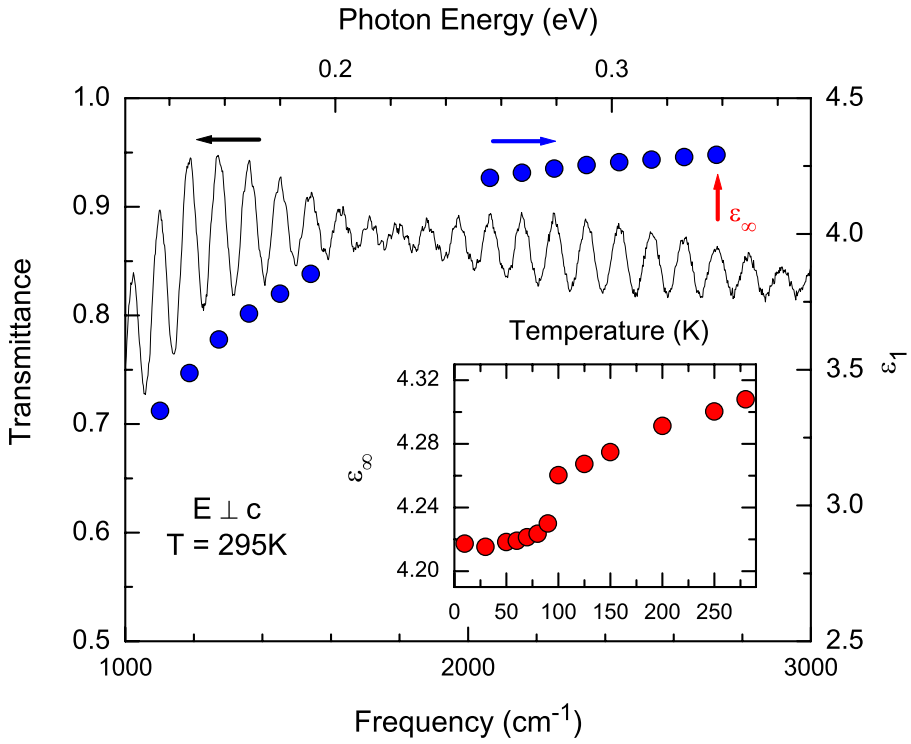

Figure 4.3: Infrared transmittance spectrum (solid curve) in $E \perp c$ orientation of $LuMnO_3$ at room temperature exhibiting étalon peaks and resulting ϵ_1 (circles). Inset shows temperature dependence of $\epsilon_\infty \equiv \epsilon_1(\approx 2700\,\text{cm}^{-1})$.

location determines n using Eq. (2.36). The quasi-static dielectric constant ϵ_0 is then given by the value of ϵ at the first order peak, $\epsilon_0 \equiv \epsilon_1(\approx 52\,\text{cm}^{-1})$. The inset of Fig. 4.4 shows the temperature dependence of ϵ_0 determined in this way. Similar to ϵ_∞, the quasi-static ϵ_0 exhibits strong temperature dependence with an anomaly at T_N.

In addition to the étalon peaks, a weak and narrow absorption appears around $50\,\text{cm}^{-1}$ at low temperatures ($T < T_N$) as shown in Fig. 4.4. This feature shifts to lower frequencies and broadens as T increases, effectively disappearing around $T \approx 60\,\text{K}$.

4.1.4 $E \parallel c$ measured spectra

Reflectance in the near-IR to visible

Single crystals in the 110-orientation afford study of the anisotropy between in-plane and out-of-plane optical response by using polarizations $E \perp c$ and $E \parallel c$,

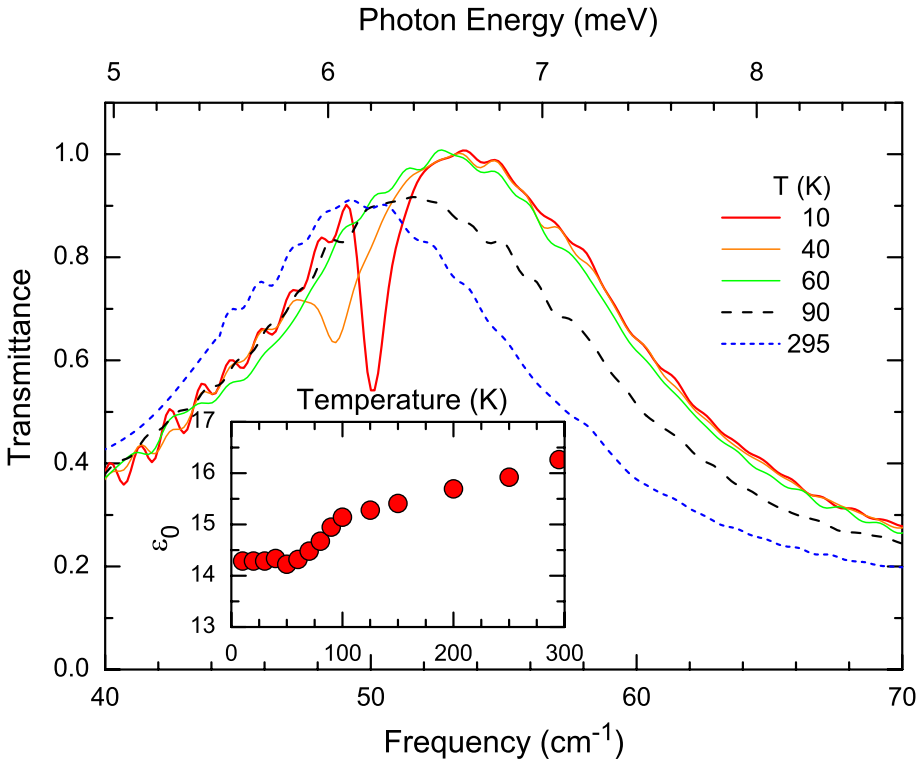

Figure 4.4: First-order étalon peak in the far-infrared transmittance spectra ($E \perp c$) of $LuMnO_3$ for several temperatures. A small absorption feature appears ($\approx 50\,\text{cm}^{-1}$) for temperatures less than T_N. Inset shows temperature dependence of $\epsilon_0 \equiv \epsilon_1(\approx 52\,\text{cm}^{-1})$.

respectively. Figure 4.5 shows the near-IR to visible $\mathcal{R}$ spectra for both 110 and 001-oriented crystals at room temperature and for various polarizations. Note that the 001 sample displays no in-plane anisotropy and hence no additional in-plane polarization is shown. On the 110-oriented crystal with $E \perp c$ polarized light (dashed curve), the 1.7 feature appears similar, although reduced in intensity, to that observed in the 001-oriented sample (dotted curve). Incident light polarized in $E \parallel c$ (solid curve) displays no signature of the 1.7 eV feature. Evidently, this feature exhibits an anisotropy relative to the polarization of the incident electric field, vanishing in the $E \parallel c$ polarization.

Above the 1.7 eV feature, the optical anisotropy in $\mathcal{R}$ diminishes. Additionally,

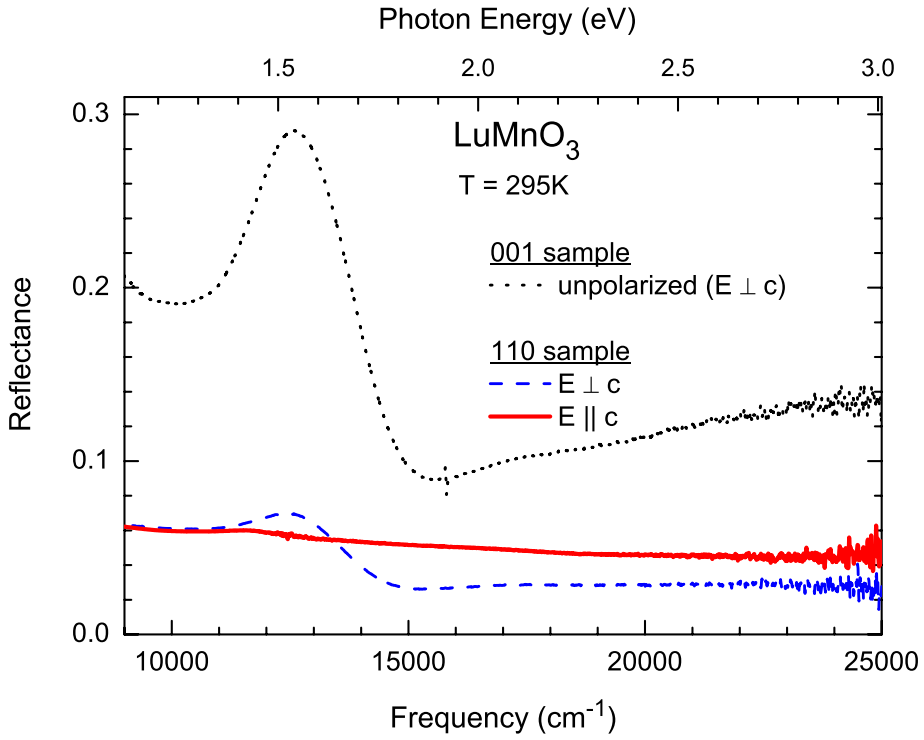

Figure 4.5: Room temperature reflectance spectra of 110-oriented $LuMnO_3$ in two polarization states: $E \parallel c$ (solid curve) and $E \perp c$ (dashed curve). 001-oriented sample with E in-plane shown for comparison (dotted curve).

the overall $\mathcal{R}$ signal falls off with increasing frequency as a result of poor surface quality. Diffusive scattering of incident light from surface imperfections increases with frequency, hence reducing specular reflection. Extracting the optical constants in such samples requires accounting for scattering losses. The standard correction technique[141] involves measuring the sample reflectance, overcoating with a reflective metal (*e.g.*, Au or Al), and remeasuring $\mathcal{R}$ on the overcoated sample. For $LuMnO_3$ in the near-IR to visible spectrum, the anisotropy of the 1.7 eV feature appears evident in the raw $\mathcal{R}$ spectrum without requiring additional overcoating and analysis. At longer wavelengths (*e.g.*, the far-IR), scattering losses resulting from surface imperfections vanish.

Reflectance in the far-IR

Figure 4.6 shows the measured reflectance for room temperature data (points) in the $E \parallel c$ polarization. The phonon spectra display a clear anisotropy between the

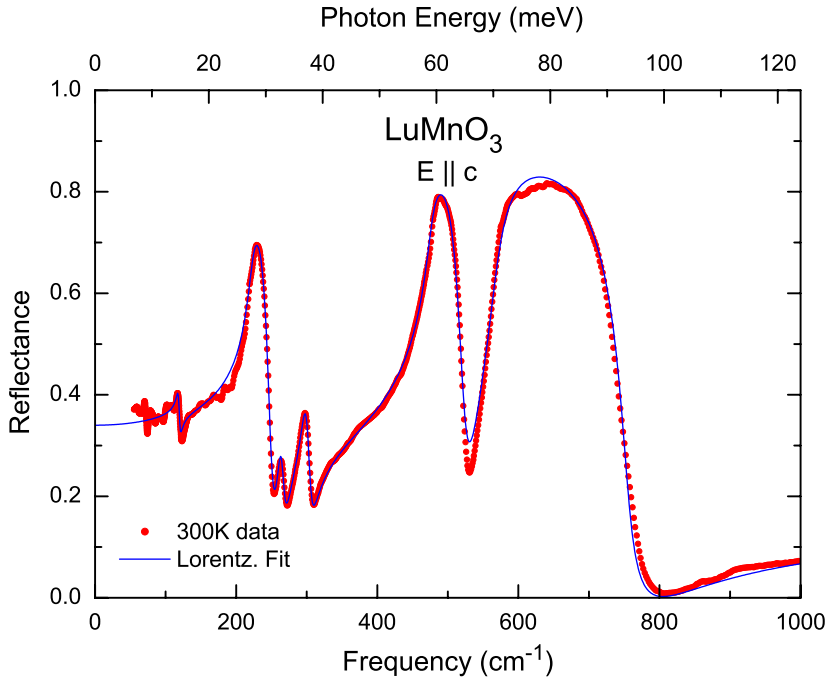

Figure 4.6: Far-infrared reflectance ($E \parallel c$) at room temperature for $LuMnO_3$. Measured data (points) compared to a fit using the Lorentz oscillator sum model (line).

in-plane ($E \perp c$) versus out-of-plane ($E \parallel c$) orientations. In the $E \perp c$ polarization, the reflectance spectra of the 110 sample (not shown) agree with the results on the 001 sample shown in the inset to Fig. 4.1. For the much thicker 110-oriented crystal, étalon effects appear well below the phonon region. Several phonons are easily visible, including a weak phonon around $125\,\mathrm{cm}^{-1}$. The $\mathcal{R}$ data are fit using the sum of Lorentzians model for $\tilde{\epsilon}(\omega)$ given by Eq. (2.30). The model fit (solid curve) well describes the data. The resulting fitting parameters and dielectric constant, including their temperature dependence, will be discussed below.

4.2 Results

4.2.1 Electronic spectra

In the frequency range of electronic transitions, extraction of optical constants is possible only for the 001 sample ($E \perp c$) with higher surface quality. Figure 4.7 shows the real part of the optical conductivity $\sigma_1(\omega)$ for $LuMnO_3$ at 10 and 300 K calculated using Kramers-Kronig relations from the reflectance spectra. The lowest electronic

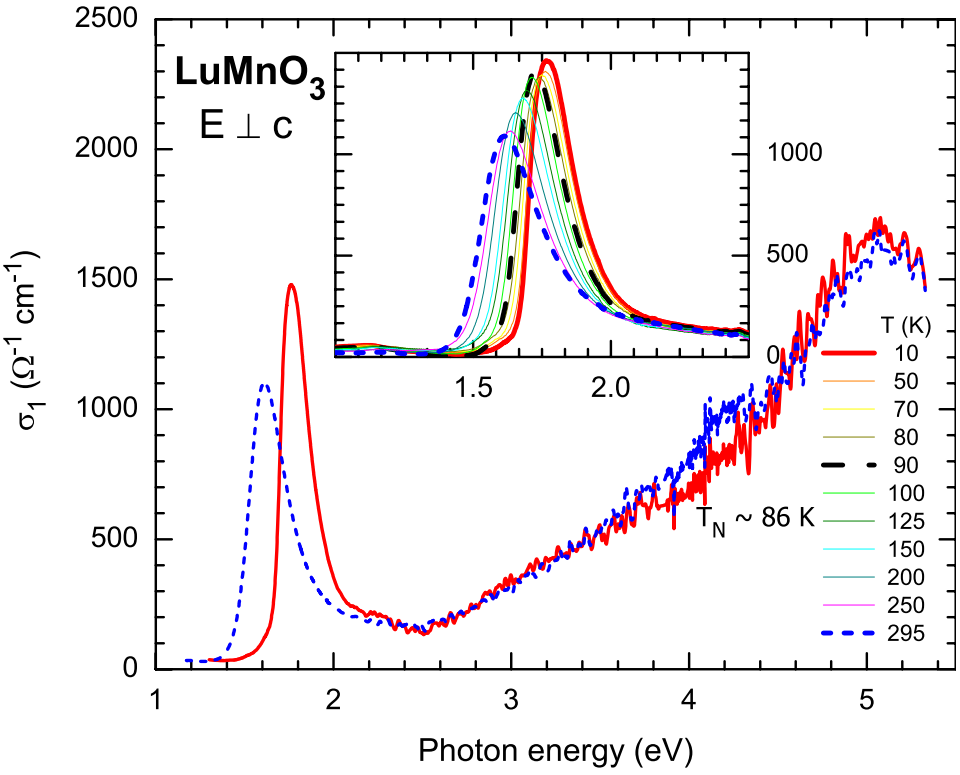

Figure 4.7: Electronic conductivity spectra of $LuMnO_3$ at 300 K (dashed line) and 10 K (solid line). Inset highlights the temperature dependence of the 1.7 eV feature.

excitation centered at $\approx$ 1.7 eV depends strongly on temperature, as highlighted in the inset of Fig. 4.7. This feature displays a strong anisotropy, disappearing in the $E \parallel c$ orientation. Yi *et al.*[138] report a similar feature in hexa-$YMnO_3$ for room temperature measurements, which is absent or very weak in ortho-$YMnO_3$. The 1.7 eV transition sits near the foot of a larger spectral feature centered around 5 eV. A sim-

ilar transition is also observed in the ortho-manganites.[27,40] The weak, but sharp, absorption onset begins around 1.1 eV and exhibits little temperature dependence, as seen in the infrared $\mathcal{T}$ spectra shown in Fig. 4.2. The spectral weight of the 5 eV peak remains independent of temperature to within the measurement accuracy. Just above the 1.7 eV peak sits a small shoulder around 2-2.5 eV. This shoulder may represent an additional weak transition. Around 4 eV, σ_1 becomes particular noisy, which is not observed in the room temperature measurement performed without windows. This spurious feature results from the CaFl vacuum windows used in the cryostat.

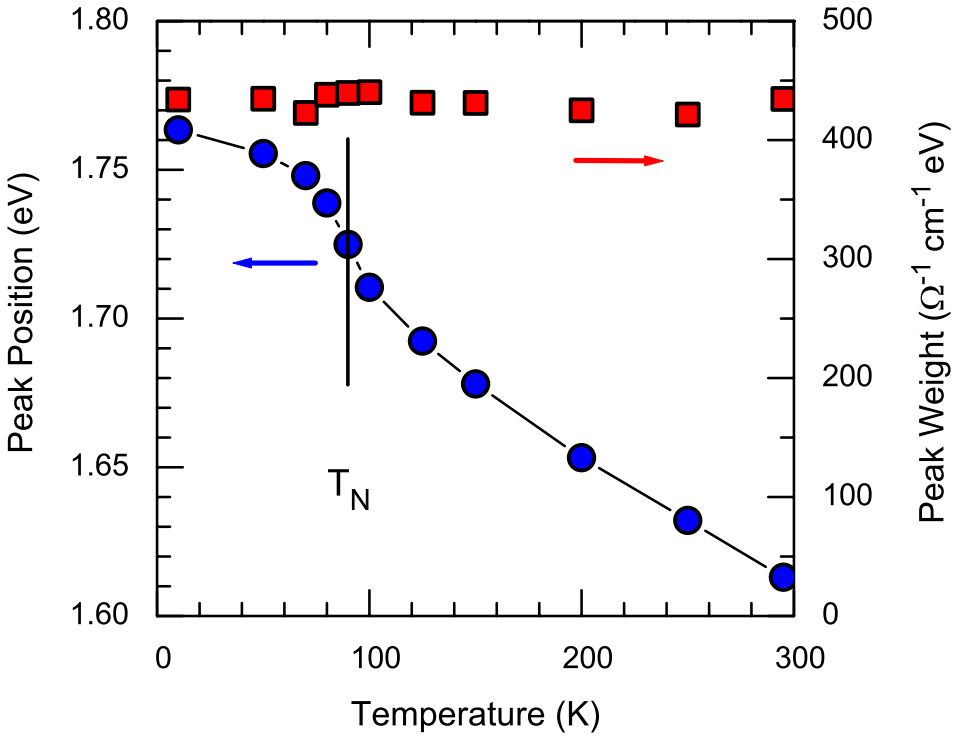

Figure 4.8: Temperature dependence of the 1.7 eV peak energy (circles) and spectral weight (squares).

Fitting the 1.7 eV transition with a Lorentzian affords tracking the temperature dependence of the peak energy. The resonance energy decreases monotonically with temperature, having an inflection point at $T_N \approx 90$ K as seen in Fig. 4.8 (circles). The peak shifts by 0.15 eV ($\gtrsim 10\,\%$ change) over the measured temperature range $0 - 300$ K with 0.05 eV of the shift occurring below the antiferromagnetic ordering

temperature T_N.

The temperature dependence of the spectral intensity, or integrated conductivity, provides additional information regarding the nature of 1.7 eV feature. The spectral weight S of this transition is defined by the restricted sum-rule [see Eq. (2.23)]

$$S = \frac{2}{\pi} \int_{1.25\,\mathrm{eV}}^{2.5\,\mathrm{eV}} \sigma_1(\omega)\, d\omega \,, \tag{4.1}$$

where the limits (1.25-2.5 eV) include the appropriate spectral range. A small contribution from the tail of the higher energy transition little affects the temperature dependence of S and consequently has not been subtracted from the integral. The squares in Fig. 4.8 represent the spectral weight as defined by Eq. (4.1). While the peak energy shifts strongly with temperature and correlates with T_N, the integrated spectral intensity of this excitation remains constant to within the experimental accuracy of $3\,\%$.

4.2.2 Phonon spectra

Equation (2.29) and an appropriate model for the dielectric constant fit the far-IR reflectance spectra. The resulting $\tilde{\epsilon}$ agrees well with that obtained from Kramers-Kronig analysis. In the $E \perp c$ orientation, sufficiently wide phonon bands necessitate the FPSQ model of Eq. (2.31). The FPSQ model ϵ parameterizes each oscillator by the frequency and damping of the phonon LO and TO modes, resulting in four parameters per phonon. Given the 6 oscillators observed in the $\mathcal{R}$ spectrum, the fit involves 24 phonon parameters in addition to the background dielectric at high frequency ϵ_∞. For the thin platelet sample measured in this polarization, étalon peaks in the IR transmittance accurately determine ϵ_∞ (see Fig. 4.3) and these ϵ_∞ values are used in Eq. (2.31). Table 4.1 lists the parameters obtained from a least-squares fitting of the measured $E \perp c$ $\mathcal{R}$ spectra at various temperatures. The inset of Fig. 4.1 shows the excellent agreement between the fitted and measured spectra for room temperature.

	Temperature (K)										
	10	50	70	80	90	100	125	150	200	250	300
$\omega_{TO,1}$	273.37	272.22	271.25	270.71	270.33	269.62	269.13	268.24	267.74	266.00	266.16
$\gamma_{TO,1}$	11.72	9.75	8.34	8.44	9.62	10.96	9.20	6.33	6.43	8.48	13.02
$\omega_{LO,1}$	283.27	283.16	283.08	283.13	282.89	282.77	282.47	282.21	281.69	281.02	280.76
$\gamma_{LO,1}$	1.84	1.93	1.96	2.14	2.15	2.29	2.28	2.76	3.59	4.09	4.60
$\omega_{TO,2}$	305.16	304.03	303.35	303.15	302.17	301.54	300.64	299.98	299.10	297.37	297.01
$\gamma_{TO,2}$	17.67	13.67	10.16	9.85	10.84	11.19	9.18	6.00	6.02	7.34	10.60
$\omega_{LO,2}$	347.99	347.89	347.66	347.73	347.39	347.01	346.51	346.45	345.89	345.67	345.57
$\gamma_{LO,2}$	5.69	6.03	6.55	7.10	6.96	7.04	8.08	9.48	11.99	13.84	16.68
$\omega_{TO,3}$	369.00	368.88	368.80	368.50	368.45	368.44	367.91	368.00	367.69	367.48	367.43
$\gamma_{TO,3}$	7.50	7.00	6.50	6.12	6.20	7.55	7.68	5.30	5.34	6.89	7.71
$\omega_{LO,3}$	564.65	565.42	566.24	566.17	566.45	566.28	566.28	565.81	564.78	564.16	563.95
$\gamma_{LO,3}$	14.00	14.10	14.10	14.20	14.23	14.37	15.71	16.15	18.41	21.01	25.76
$\omega_{TO,4}$	415.38	415.31	414.82	415.00	415.14	415.03	414.68	413.30	411.87	412.00	412.41
$\gamma_{TO,4}$	2.92	3.47	4.43	3.90	3.65	4.30	4.02	5.90	7.06	7.30	7.60
$\omega_{LO,4}$	413.40	413.31	412.87	412.99	413.16	412.90	412.96	411.52	410.46	410.50	410.73
$\gamma_{LO,4}$	2.42	2.87	3.03	2.91	3.06	3.53	3.61	3.94	4.74	5.60	6.50
$\omega_{TO,5}$	428.48	428.31	428.17	428.33	427.78	427.74	427.67	427.32	426.98	426.00	425.36
$\gamma_{TO,5}$	4.49	4.35	3.74	3.85	4.38	3.92	4.06	4.22	5.29	6.00	7.31
$\omega_{LO,5}$	424.81	424.81	425.09	424.99	424.43	424.54	424.42	424.50	424.31	423.00	422.48
$\gamma_{LO,5}$	4.65	4.66	4.32	4.67	4.74	4.59	5.68	5.98	8.47	9.30	10.16
$\omega_{TO,6}$	602.15	601.57	600.76	601.35	600.89	600.84	600.34	599.84	599.58	599.26	598.85
$\gamma_{TO,6}$	2.00	2.25	2.50	2.50	2.57	2.69	4.10	5.45	6.89	7.10	7.94
$\omega_{LO,6}$	610.14	610.46	609.84	610.30	609.89	609.96	609.42	609.25	608.49	607.94	607.40
$\gamma_{LO,6}$	8.00	9.00	11.09	10.00	11.52	12.30	8.27	7.61	6.73	7.88	9.79

Table 4.1: Fitting parameters for the $E \perp c$ reflectance of $LuMnO_3$ for various temperatures. Values are in cm^{-1}.

Phonons in the $E \parallel c$ orientation differ from those in $E \perp c$. Being more isolated (narrower band), the simple sum of Lorentz oscillators given by Eq. (2.30) fits well the out-of-plane $\mathcal{R}$ spectra. The classical Lorentz model parameterizes each oscillator by the TO frequency, damping, and spectral weight, resulting in three parameters per phonon. Table 4.2 lists the phonon parameters resulting from of a least-squares fit to the measured $E \parallel c$ reflectance at various temperatures. The fitted reflectance spectra agree well with measurements as illustrated in Fig. 4.5 for room temperature. The thicker 110-crystal precludes determining ϵ_∞ from étalon in $\mathcal{T}$ and hence least-squares fits include ϵ_∞ as a free parameter. ϵ_∞ obtained in this manner, however, lacks the accuracy of that obtained from étalon analysis.

The fit parameters in Tables 4.1 and 4.2 define the complex dielectric constant $\tilde{\epsilon}$ for the $E \perp c$ and $E \parallel c$ orientations, respectively. The optical conductivity may be obtained using Eqs. 2.13 and 2.14 and the dielectric constant from fitting $\mathcal{R}$. The frequency dependence of σ_1 and ϵ_1 at 10 and 300 K is shown in Fig. 4.9. Panels (a)

	Temperature (K)										
	10	50	65	80	90	100	125	150	200	250	300
$\omega_{TO,1}$	124.36	124.15	124.11	123.92	123.74	123.73	123.27	122.82	121.73	120.37	118.65
γ_1	3.27	3.24	3.02	3.27	3.06	2.94	3.01	3.50	3.72	3.91	4.55
A_1	27.63	26.99	25.20	27.27	27.17	25.93	28.22	31.13	37.77	44.01	59.99
$\omega_{TO,2}$	229.33	229.23	228.12	228.60	228.38	228.80	228.29	227.60	226.41	225.13	223.08
γ_2	4.95	4.55	5.33	5.45	5.35	5.77	6.83	6.24	8.54	11.69	14.92
A_2	407.70	409.81	415.90	412.30	412.08	413.61	413.97	421.13	423.27	429.32	430.10
$\omega_{TO,3}$	266.80	267.17	267.06	267.14	267.15	267.04	266.86	266.37	265.52	264.77	263.41
γ_3	5.22	5.04	4.60	5.13	4.88	5.44	5.54	6.53	7.76	9.71	10.44
A_3	131.78	129.83	121.78	123.90	122.10	123.85	120.57	120.16	120.88	114.14	105.54
$\omega_{TO,4}$	303.72	303.48	303.47	303.31	303.10	302.89	302.59	301.97	301.09	299.65	298.27
γ_4	6.25	5.90	6.50	6.42	6.48	6.39	7.00	7.23	8.44	11.36	12.06
A_4	174.01	178.15	175.53	174.99	176.24	176.26	175.24	179.02	176.68	185.81	180.69
$\omega_{TO,5}$	478.50	479.06	477.83	478.92	478.84	478.25	478.39	478.19	477.83	476.93	476.48
γ_5	10.04	9.64	10.32	10.75	10.46	10.38	11.25	10.88	13.77	15.66	17.59
A_5	868.80	877.45	865.33	872.39	867.96	878.14	881.81	885.06	877.56	875.17	855.54
$\omega_{TO,6}$	571.21	570.85	571.41	570.98	571.18	571.11	570.58	570.55	569.82	568.88	567.82
γ_6	28.12	26.46	28.66	27.66	28.02	25.43	24.47	24.04	26.30	28.16	30.95
A_6	742.60	749.23	740.90	751.60	754.09	753.72	757.93	762.01	767.48	759.45	756.94
ϵ_∞	4.95	5.04	4.92	5.00	4.97	5.02	5.04	5.08	5.08	5.04	4.92

Table 4.2: Fitting parameters for the $E \parallel c$ reflectance of $LuMnO_3$ for various temperatures. Values are in cm^{-1} except for ϵ_∞.

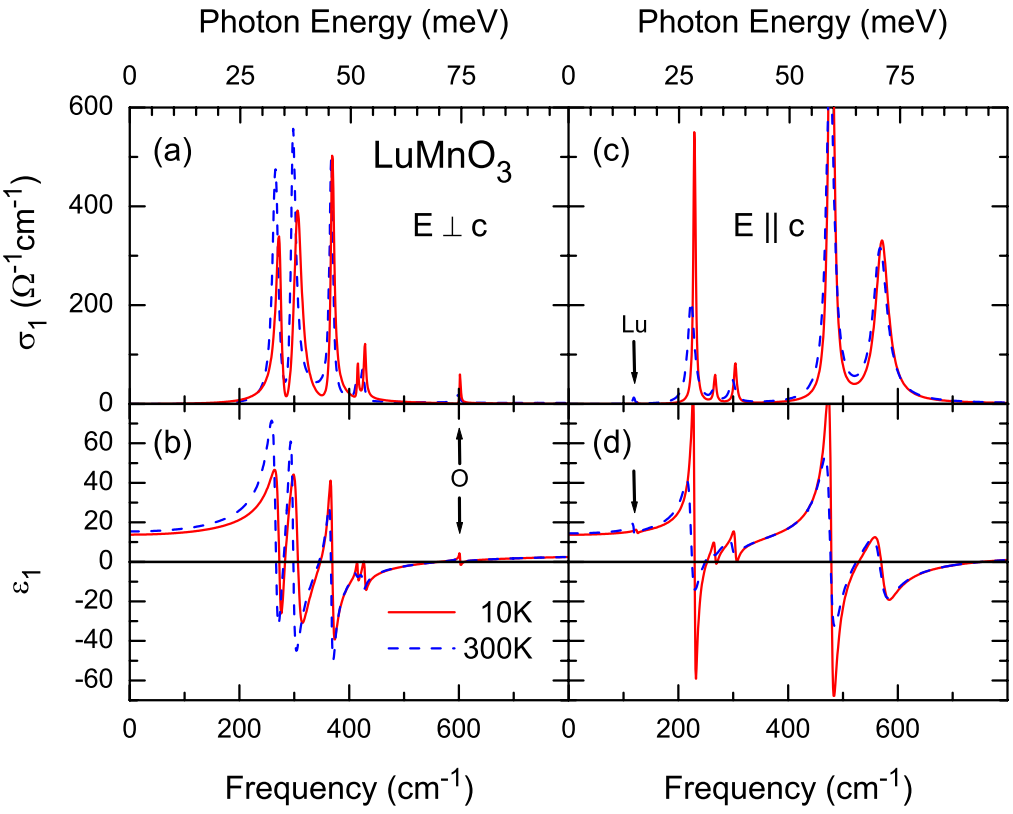

Figure 4.9: Real part of the optical conductivity σ_1 and dielectric constant ϵ_1 of $LuMnO_3$ in the phonon spectral range for 10 K (solid) and 300 K (dashed).

and (b) present σ_1 and ϵ_1, respectively, for $E \perp c$ and panels (c) and (d) present σ_1 and ϵ_1, respectively, for $E \parallel c$. In $E \perp c$, several phonons exhibit large shifts with temperature. Detailed temperature-dependent shifts of ω_{TO} will be presented and discussed in Sec. 4.3.

A basic identification of phonon modes results from considering ionic displacements in the harmonic approximation. The resonant frequency is inversely proportional to the square root of the ionic mass, $\omega_{\mathrm{TO},i} \propto 1/\sqrt{M_i}$. Thus, the mode at lowest frequency corresponds primarily to motion of the heavy Lu ions, while the mode at highest frequency corresponds to motion of the light O ions. A weak Lu phonon at $\approx 125\,\mathrm{cm}^{-1}$ appears in the $E \parallel c$ conductivity in Fig. 4.9 (right panels). O modes appear around $600\,\mathrm{cm}^{-1}$ in both crystal orientations, though the in-plane mode is much weaker. At intermediate frequencies, modes consist primarily of Mn ion displacements, in combination with O and Lu motion. More exact modal assignments can be made by analogy with those in $YMnO_3$.[137] In the ferroelectric phase ($T < T_c$), $LuMnO_3$ crystallizes in the hexagonal structure with space group $P6_3cm$. A group-theoretical analysis for the Γ-point phonon modes of space group $P6_3cm$ finds 23 IR active modes: 9 with A_1 symmetry and 14 with E_1 symmetry.[137] Modes with A_1 symmetry consist primarily of ionic motion out-of-plane, while those with E_1 symmetry consist primarily of in-plane displacements. However, coupling of modes allows some mixing. The optical measurements presented herein display 6 in-plane ($E \perp c$) phonon modes and 6 out-of-plane ($E \parallel c$) modes.

4.2.3 Antiferromagnetic resonance

For the weak feature in the far-IR $\mathcal{T}$ around $50\,\mathrm{cm}^{-1}$, several observations suggest this to be a magneto-dipole transition. First, Penney *et al.*[136] purported a similar feature in $YMnO_3$ at $\approx 43\,\mathrm{cm}^{-1}$ to be an antiferromagnetic resonance (AFMR), though no data was presented. In addition, the feature has the symmetry expected

for magnon excitations in the plane,[142] present for polarizations where $B \perp c$, but absent for $B \parallel c$. Inelastic neutron scattering[143] observes a magnon peak in $YMnO_3$ at $5.3\,\text{meV}$ ($\approx 43\,\text{cm}^{-1}$), which supports the assignment of this transition as an AFMR. Figure 4.10 shows the temperature dependence of this feature in the measured $\mathcal{T}$ spectra (symbols). The background étalon peak has been divided out for clarity.

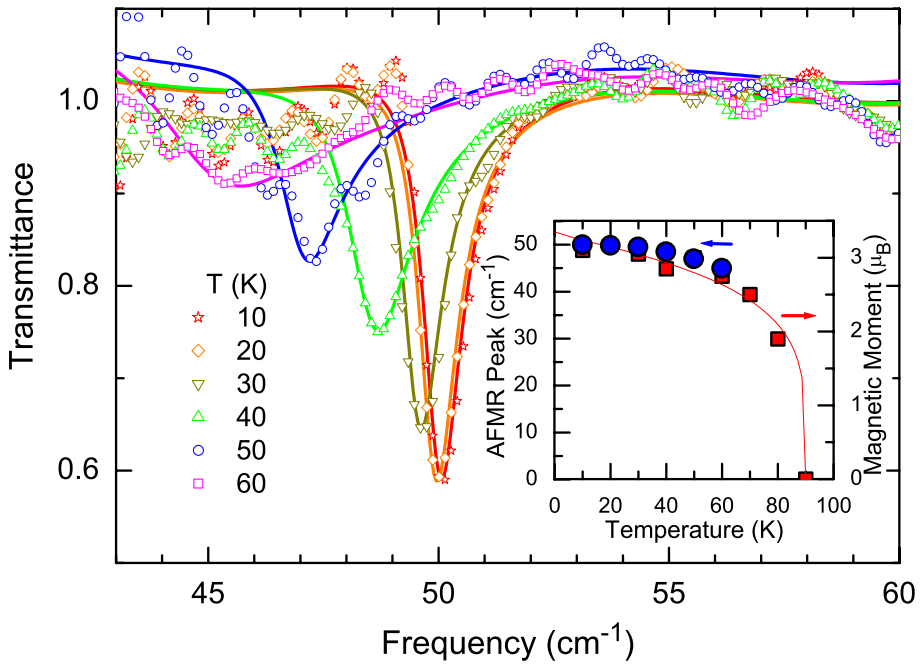

Figure 4.10: Antiferromagnetic resonance in the far-infrared transmission ($E \perp c$) of $LuMnO_3$. Background étalon have been divided out. Inset shows temperature dependence of the antiferromagnetic resonance frequency (circles) along with magnetic moment data (squares) taken from Ref. 50 for comparison.

In general, magneto-dipole transitions will be weaker than electro-dipole transitions. The relative sizes of the transitions may be estimated by considering the transition rate from initial state i to final state f given by $W_{i\to f} = 2\pi/\hbar\,|M|^2\,\delta(E_f - E_i - \hbar\omega)$, where M represents the appropriate matrix element between the two states. The electric dipole matrix element, with selection rules that the initial and final angular momentum state differ by 1 (*i.e.*, $l_f = l_i \pm 1$), is given by $M_E = \langle\psi_l|\boldsymbol{p}\cdot\boldsymbol{E}|\psi_{l\pm1}\rangle =$

$e\,E\langle\psi_l|\boldsymbol{r}|\psi_{l\pm1}\rangle \sim e\,E\,a_B$, where $a_B = \hbar^2/(m\,e^2)$ is the Bohr radius. For the magnetic dipole transition, the matrix element M_B for the incident EM wave to flip a spin will be given by $M_B = \langle\uparrow|\boldsymbol{m}\cdot\boldsymbol{B}|\downarrow\rangle \sim \mu_B\,B$, where $\mu_B = e\,\hbar/(2\,m\,c)$ is the Bohr magneton. The ratio of the transition rates is then given by

$$\frac{W_B}{W_E} = \frac{|M_B|^2}{|M_E|^2} = \frac{\mu_B^2\,B^2}{e^2\,a_B^2\,E^2} = \frac{1}{4}\,\alpha^2 \approx 3\times10^{-5}\,, \tag{4.2}$$

where $\alpha = e^2/(\hbar^2c^2)$ is the fine structure constant. Thus one expects magneto-dipole transitions to be much weaker than electro-dipole transitions. However, occasions arise where the ratio may approach unity: (i) the oscillator strength of the electro-dipole transitions is small (*e.g.*, weak phonon mode) or (ii) if the magneto-dipole transition is enhanced (*e.g.*, large spin S or g-factor). It is possible, in principle, to distinguish the nature of a weak optical absorption feature as either electro- or magneto-dipole in origin from the response of the bulk reflectance.[144] In order to distinguish the two transitions from the measured $\mathcal{R}$ spectra, ϵ_∞ must differ appreciably from μ_∞.

Given the evidence suggesting the $50\,\mathrm{cm}^{-1}$ feature derives from a magneto-dipole transition, the feature is modeled analogously to the phonon transitions in $\tilde{\epsilon}$ with a Lorentz oscillator model [Eq. (2.30)]. Here the AFMR consists of single resonance in the complex magnetic permeability $\tilde{\mu}$ given by,

$$\tilde{\mu} = \mu_\infty + \frac{A^2}{\omega_0^2 - \omega^2 - \mathrm{i}\,\gamma\,\omega}\,, \tag{4.3}$$

where μ_∞ is the background permeability above any magnon excitations. Performing a least squares fit of the temperature-dependent $\mathcal{T}$ feature results in the parameter values listed in Table 4.3. Note the μ_∞ values were taken to be unity *a priori* to the least squares fit. Results of the fit using the parameter values listed in Table 4.3 are shown as solid lines in Fig. 4.10. With increasing temperature, the AFMR energy decreases and the feature broadens, eventually disappearing $\approx 70\,\mathrm{K}$ ($< T_N$). The inset

	Temperature (K)					
	10	20	30	40	50	60
ω_0	50.0	49.9	49.55	48.55	46.9	45.0
γ	0.8	0.8	0.85	1.5	1.5	3.7
A	2.0	2.0	1.9	2	1.8	2.1

Table 4.3: Fitting parameters for the antiferromagnetic resonance of $LuMnO_3$ for various temperatures. Values are in cm^{-1}.

of Fig. 4.10 compares the temperature dependent AFMR energy with the magnetic moment M reported by Katsufuji *et al.* in Ref. 50. The solid line corresponds to a fit of the magnetic moment, $M = A(1 - T/T_N)^{\beta}$, where the critical exponent $\beta \approx 0.22$.

4.3 Discussion

4.3.1 Electronic transitions

The two main features of the electronic conductivity spectrum are understood as: (1) a broad band of charge transfer transitions from the hybridized oxygen p-levels to the Mn $d_{3z^2-r^2}$ levels centered at ≈ 5 eV and (2) an on-site Mn d-d transition centered at ≈ 1.7 eV. The fact that this feature appears in $YMnO_3$ in the hexagonal phase but not the orthorhombic phase remains consistent with selection rules for the on-site Mn d-d transitions in hexagonal and cubic (or pseudo-cubic) symmetry. The relative temperature insensitivity of the spectral weight of this feature rules out its interpretation as a charge transfer transition. Contrast this with the ≈ 2.1 eV Mn-Mn intersite transition observed in $LaMnO_3$, where the oscillator strength exhibits strong temperature dependence correlated with T_N. In this case, the spin dependence of the charge transfer matrix elements leads to a strong temperature dependence of the spectral weight, which is not observed in the hexagonal system.

Ligand-field theory[101] predicts the energies and spectral intensities of electronic transitions in the MnO_5 complex. The electronic states are taken to be the manganese d-orbitals coupled to the oxygen p_σ orbitals. Setting the $d_{x^2-y^2,\,xy}$ orbital pair

as the energy zero, ligand-field theory predicts the O p-orbital energy $\Delta = -3\,\text{eV}$ and the $d_{3z^2-r^2}$ orbital crystal field energy $\Delta_{\text{CF}} = 0.7\,\text{eV}$. For the symmetric (paraelectric) structure, the hybridization is $t_1 = t_2 = 1.9\,\text{eV}$ for apical and $t_3 = t_4 = 1.7\,\text{eV}$ for in-plane oxygens. The symmetry-allowed optical transitions for the $E \perp c$ polarization of light are: $d'_{x^2-y^2,\,xy} \rightarrow d'_{3z^2-r^2}$ at $1.6\,\text{eV}$ and the two in-plane bonding O $p \rightarrow$ Mn $d'_{3z^2-r^2}$ at $6.3\,\text{eV}$, where primes denote the corresponding d-states hybridized with the oxygen orbitals. The calculated spectral weights of both transitions agree in their ratio, but underestimate measurements by a factor of four. This discrepancy may be attributed to the neglect of the Mn p-orbitals and s-orbitals, which also couple to the O p-states in the hexagonal symmetry. In the case of $E \parallel c$ polarization of incident light, the optical matrix elements for the $d'_{x^2-y^2,\,xy} \rightarrow d'_{3z^2-r^2}$ transitions vanish, as observed experimentally.

The temperature dependence of the $1.7\,\text{eV}$ peak energy shown in Fig. 4.8 raises an interesting question as to the origin of such a large shift ($\approx 0.15\,\text{eV}$). The anomaly at T_N indicates that at least part of the shift associates with the magnetic phase transition. The magnetic part of the shift may be attributed to the effects of the exchange interactions between the Mn ions. Figure 4.11 illustrates the localized Mn $3d$ levels and the filled O $2p$ bands (shaded) for temperatures below (left panel) and above (right panel) T_N. Curved arrows indicate the symmetry-allowed on-site Mn d-d optical transitions from the occupied $d'_{x^2-y^2,\,xy}$ levels to the unoccupied $d'_{3z^2-r^2}$ levels. Shifts of the Mn d-levels due to superexchange between Mn neighbors result from a lowering of the $d'_{x^2-y^2,\,xy}$ levels in the antiferromagnetic state by the exchange energy E_{ex}. The relatively isolated $d'_{3z^2-r^2}$ orbital remains essentially unaffected by the magnetic ordering. The observed shift in the resonance energy between $4\,\text{K}$ and T_N ($\approx 0.05\,\text{eV}$) likely underestimates the exchange energy due partly to short-range antiferromagnetic correlations in this frustrated magnetic system, which are expected and observed to persist to higher temperatures.[53,143]

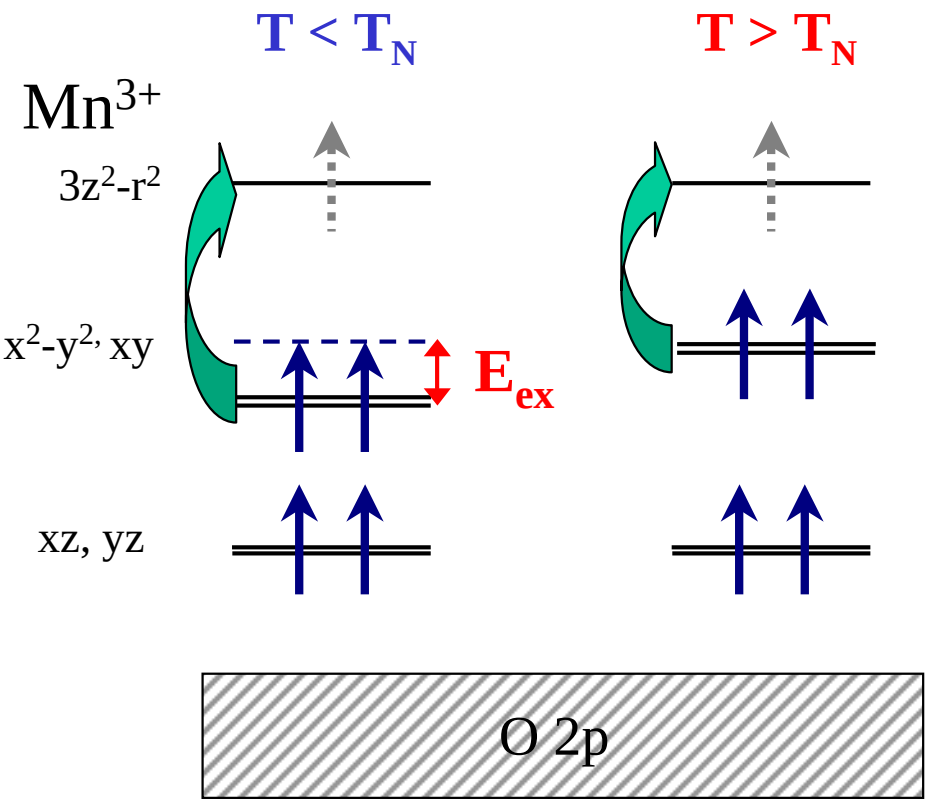

Figure 4.11: Schematic view of the lowest-lying electronic transitions in $LuMnO_3$.

In addition to exchange effects, thermal expansion and magnetostriction may contribute to a spectral shift. Considering first thermal expansion above T_N, the observed shift exceeds values typically observed in interband features in solids where changes in the transition energy scale directly with changes in the lattice constant,[145] $\delta E/E = \alpha\,\delta a/a$ and $\alpha \sim 1$. In $LuMnO_3$, the strong overlap of the the hybridized orbitals suggests that $\delta t/t \sim \delta a/a$. Given that ligand field theory predicts changes in the transition energies on the order of changes in the hybridization, $\delta\Delta_{CF}/\Delta_{CF} \sim \delta t/t$, changes in the transition energy due to thermal expansion effects should be on the order of the changes in the lattice constant, $\delta\Delta_{CF}/\Delta_{CF} \sim \delta a/a$. From x-ray diffraction measurements[50] above room temperature, extrapolated changes from 300 K to T_N in the in-plane lattice parameter a are small, $\delta a/a \approx 0.3\,\%$ and changes in the out-of-

plane parameter c are smaller still by a factor of 10. The absence of a shift in the 5 eV feature also precludes such a large thermal shift in the 1.7 eV feature since both features share the same $d'_{3z^2-r^2}$ final state. Furthermore, the extremely weak decrease in the oscillator strength of the 1.7 eV feature argues against a strong thermal expansion effect since this optical transition, allowed only due to the hybridization with the O p-states, depends more sensitively on thermal changes in the lattice constant than does the peak energy. However, the experiment presently cannot separate exchange effects from thermal expansion effects on the optical transition energy. For temperatures below the magnetic ordering, magnetostriction also changes the lattice constant and may produce level shifts. However, Muñoz *et al.*[51] report the changes in the lattice constant for $YMnO_3$ from 0 to T_N are smaller by about a factor of 10 than the effects due to thermal expansion.[50] Thus magnetostriction effects are not responsible for the additional shift of the peak energy below T_N.

Measuring shifts of the 1.7 eV optical transition provides an estimate of the exchange interaction in $LuMnO_3$. In addition to optics, inelastic neutron scattering and magnetic susceptibility also offer estimates for the exchange energy of the Mn spins. Inelastic neutron-scattering measurements reported by Sato *et al.*[143] find an in-plane antiferromagnetic coupling $J \approx -3.4$ meV, resulting in an estimate of the exchange energy $E_{ex} \approx 120$ meV. Magnetic susceptibility measurements determine the Curie-Weiss temperature in the susceptibility. From molecular field theory, $k_B \theta_{\mathrm{CW}} = z J_{NN} S(S+1)/3$, where $z = 6$ is the number of Mn nearest neighbors, J_{NN} is the nearest neighbor antiferromagnetic coupling, and S is the spin. The exchange energy for the manganese ion is then given by $E_{ex} \approx 3 k_B \theta_{\mathrm{CW}}$. In the literature, θ_{CW} data for $LuMnO_3$ range between -519 K (Ref. 55) and -887 K (Ref. 53). Taking these values for θ_{CW} gives a range for the exchange energy, $140 \lesssim E_{ex} \lesssim 240$ meV, which is somewhat larger than that estimated from the optical shifts ($E_{ex} \gtrsim 50$ meV). As noted earlier, this estimate ignored the additional shifts expected above T_N due to frustra-

tion effects. Moreover, these two estimations represent different manifestations of the exchange interaction. Exchange estimated from θ_{CW} represents the ground state exchange energy between the Mn moments, while the optical shift represents the change in exchange energy of the Mn ion between the ground and excited state of the Mn^{3+} ion. Thus, the exchange estimates agree satisfactorily, supporting the assignment of the temperature shift of the 1.7 eV peak to the difference in exchange interaction between the ground and excited optical states of a given Mn ion.

4.3.2 Spin-phonon coupling

Optically active phonons dominate the far-IR conductivity spectrum. The frequencies of the TO phonons ω_{TO} in the $E \perp c$ orientation exhibit a temperature anomaly around T_N similar to the 1.7 eV optical transition. Figure 4.12 shows the temperature dependence of the frequency shifts for $E \perp c$ and $E \parallel c$ in panels (a) and (b), respectively. Shifts are plotted relative to the phonon frequency at low temperature, $\Delta\omega_{\mathrm{TO}}(T) \equiv \omega_{\mathrm{TO}}(T) - \omega_{\mathrm{TO}}(10\,\mathrm{K})$. The two lowest frequency vibrational modes ($\omega_{\mathrm{TO}} \approx 270, 305\,\mathrm{cm}^{-1}$) in the $E \perp c$ polarization display the strongest absolute frequency shifts ($\Delta\omega_{\mathrm{TO}}$), relative frequency shifts ($\Delta\omega_{\mathrm{TO}}/\omega_{\mathrm{TO}}$), and inflection points at T_N. This observation suggests that these modes couple strongest to the spin system. Additionally, scaled frequency shifts, $-\Delta\omega(T)/\Delta\omega(300)\,\mathrm{K}$, in Fig. 4.12(c) show that other $E \perp c$ phonons display similar behavior. Noise in ω_{TO} frequencies of the weak phonons at $\omega_{\mathrm{TO}} \approx 416, 429\,\mathrm{cm}^{-1}$ in $E \perp c$ precludes observation of the anomaly at T_N. In the $E \parallel c$ polarization, measurements of the phonon spectrum on the 110-sample exhibit no anomaly at T_N. There exists a clear anisotropy between the in-plane and out-of-plane phonon behavior, which correlates with the in-plane spin ordering. The similarity of the frequency shift of the spin-coupled phonons and the temperature dependence of the 1.7 eV feature suggests that both are related to the same, nearest-neighbor spin correlation function $\langle \boldsymbol{S}_i \cdot \boldsymbol{S}_j \rangle(T)$.

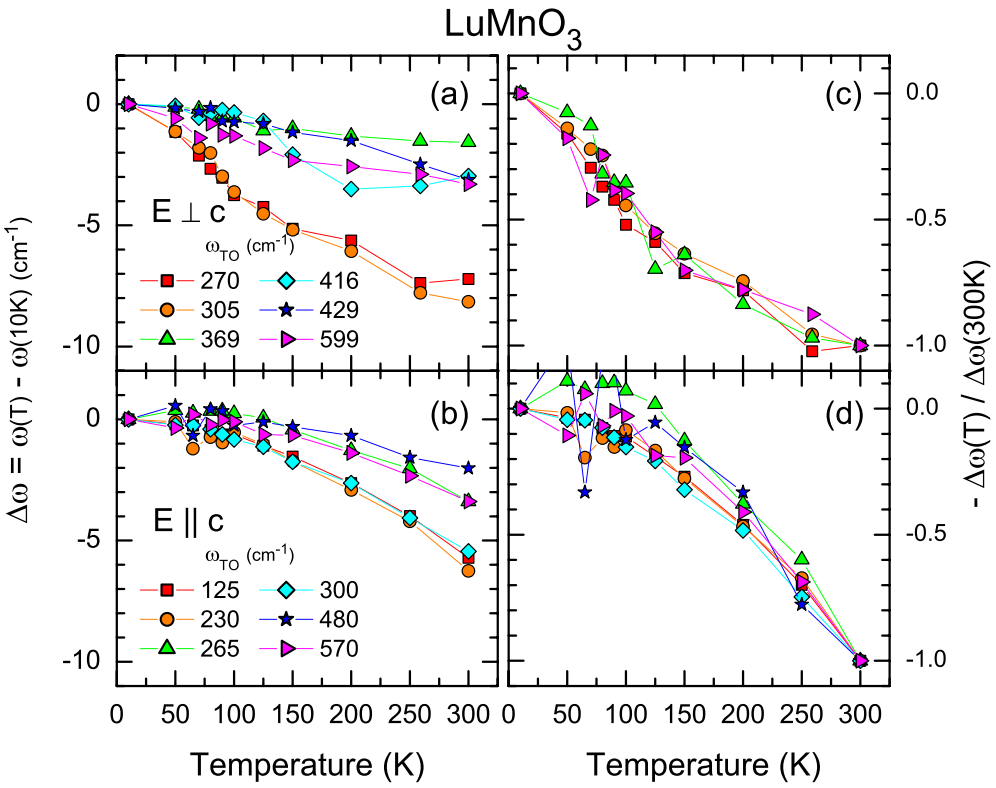

Figure 4.12: Temperature-dependent shifts of the TO phonon frequencies, $\Delta\omega(T) \equiv \omega(T) - \omega(10\,\mathrm{K})$ for (a) $E \perp c$ and (b) $E \parallel c$. Scaled frequency shifts, $-\Delta\omega(T)/\Delta\omega(300\,\mathrm{K})$ for (c) $E \perp c$ and (d) $E \parallel c$.

Phonon induced modulation of the exchange energy produced by the ion modal displacements provides an understanding of the phonon shifts. The change in exchange energy produces a corresponding change in the effective restoring force k for the phonon. This change in k results in a ω_{TO} shift given by $\Delta(\omega_{\mathrm{TO}}^2) = \Delta k/\mu$, where $\Delta k(T) \propto \langle \boldsymbol{S}_i \cdot \boldsymbol{S}_j \rangle(T)$ is the exchange energy contribution to the force constant and μ is the reduced mass of the phonon mode. Superexchange between nearest neighbor Mn ions separated by O dominates the exchange energy. However, the complexity of the hybridized Mn d-states allows both ferromagnetic and antiferromagnetic contributions that differ for in-plane and out-of-plane neighbors.

4.3.3 Dielectric constant anomaly

Several authors[54,56] consider the observed anomaly in the temperature dependence of the static in-plane dielectric constant below the Néel temperature as evidence of a manifestation of coupling between magnetic and ferroelectric order parameters in ferroelectromagnets. As provided by the optical sum rule for the dielectric constant in Eq. (2.22), all of the oscillators present in the optical response of the system determine $\epsilon_0 \equiv \epsilon_1(\omega = 0)$. Unlike quasi-static measurements, the present optical studies afford identification of an individual oscillator's contribution to the quasi-static dielectric constant of $LuMnO_3$. Three groups of oscillators participate: ferroelectric domains, phonons, and electronic transitions. The antiferromagnetic resonance contributes a minimal correction to ϵ_0.[146] Contributions from ferroelectric domains fall off with frequency, becoming negligible at the megahertz frequencies of the quasi-static electrical measurements[54] and decrease further at far-IR frequencies. Figure 4.13 shows the temperature dependence of the real part of the dielectric constant of $LuMnO_3$. The top curve in panel (a) reproduces the quasi-static in-plane data of Katsufuji *et al.*[53] taken at $100\,\text{kHz}$. The bottom plot (circles) in panel (a) results from the measured frequency shift of the first étalon maximum in the transmittance spectrum (Fig. 4.4) centered at $53\,\text{cm}^{-1}$ ($\approx 6.6\,\text{meV}$). At this low frequency, all IR active phonons and all electronic transitions provide input to ϵ_1. Panel (b) shows ϵ_1 obtained from the interference fringes in the mid-IR transparency region (Fig. 4.3) midway between the phonon and electronic absorption bands at $2700\,\text{cm}^{-1}$ ($\approx 0.335\,\text{eV}$). Electronic transitions determine the value of ϵ_1 at this frequency, $\epsilon_\infty \equiv \epsilon(0.335)\,\text{eV}$. Finally, panel (c) shows an estimation of the input to the dielectric constant from the $1.7\,\text{eV}$ electronic peak using a restricted sum-rule for ϵ_0

$$\Delta\epsilon_1 = \frac{2}{\pi}\int_{1\,\text{eV}}^{2.5\,\text{eV}} \frac{\epsilon_2(\omega)}{\omega}\,\mathrm{d}\omega\,. \tag{4.4}$$

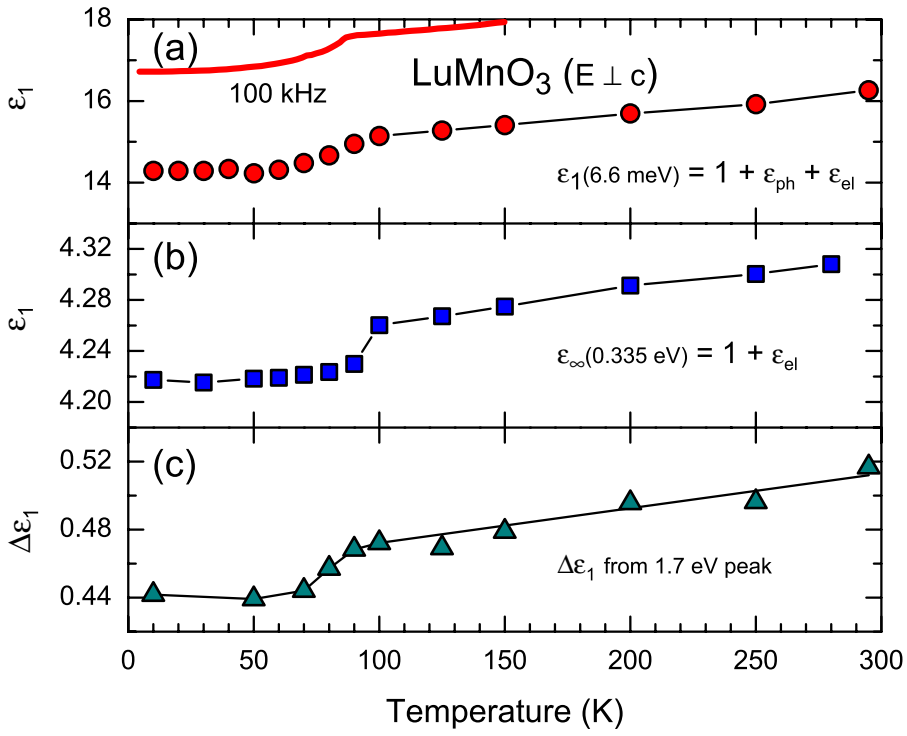

Figure 4.13: Temperature dependence of the dielectric constant ϵ_1 of $LuMnO_3$. Top (a) and middle (b) panels represent ϵ_1 measured from the étalon interference effect in the far-IR and mid-IR, respectively. Panel (c) shows the contribution of the 1.7 eV peak to ϵ_1 determined from the optical sum rule. The lines guide the eye. 100 kHz data from Katsufuji *et al.* (Ref. 53)

As evident from ϵ_1 plots in Fig. 4.13, phonon hardening produces practically all of the $\Delta\epsilon$ below T_N. Comparing panels (a) and (b), only $\approx 5\%$ of this change comes from the shift of the 1.7 eV electronic peak. Furthermore, panels (b) and (c) in Fig. 4.13 show that the temperature dependence of ϵ_∞ results, almost entirely, from the 1.7 eV feature, *i.e.*, higher energy electronic transitions remain relatively insensitive to magnetic ordering and provide only a temperature independent background to ϵ_1.

The absence of a magnetic anomaly in phonons with the $E \parallel c$ polarization (Fig. 4.12) agrees with the observed anisotropy in the static dielectric constant[53] and ω_{TO} phonon shifts. Toward developing an understanding of this anisotropy of the spin-lattice coupling, note that important distinctions in the exchange modulation ex-

ist between the $E \parallel c$ and $E \perp c$ polarizations. In the case of $E \parallel c$ polarization, in-plane Mn and O ions displace transversely relative to their bond. Furthermore, bond stretching occurs only with the apical oxygen, primarily affecting the empty Mn $d_{3z^2-r^2}$ orbital. Contrast this with $E \perp c$, where the incident electric field induces both transverse and bond stretching Mn-O displacements, which involve occupied in-plane orbitals. This observation suggests that the in-plane bond stretching displacements dominate the spin-phonon interaction effects.

4.3.4 Order parameter coupling

More generally the question of a coupling between the FE P and AFM l order parameters of this material remains interesting. Within the Landau theory of phase transitions, there are symmetry allowed terms in the free energy describing the coupling between the magnetic and ferroelectric order.[45] The experimental data on the quasi-static dielectric constant implies that this term is of the form $\delta F \approx l^2 P^2 (E_x^2 + E_y^2)$. Zhong and Jiang report[57] polarization induced by magnetic coupling provides for the electric susceptibility anomaly. Coupling of the form $g\, u_k^2\, \boldsymbol{S}_i \cdot \boldsymbol{S}_j$, or for the susceptibility $\chi = \chi_0(1 - \alpha \langle \boldsymbol{S}_i \cdot \boldsymbol{S}_j \rangle)$, results from a model that includes a soft-mode theory for FE and a mean-field approximation for AFM.

Not all authors agree that a dielectric anomaly implies coupling of the order parameters. Tomuta *et al.*[55] argue against direct coupling, but rather attribute the ϵ anomaly to small changes in the ferroelectric domain wall mobility. Indeed, Smolenskii and Chupis[45] cite the ϵ_0 anomaly as a necessary but not sufficient condition for order parameter coupling. Materials with magnetic but no FE ordering exhibit anomalies in the TO phonon frequencies and quasi-static dielectric constant similar to those observed for the hexamanganites. The antiferromagnetic CuO displays anomalies in TO phonon frequencies[147] and in the dielectric constant[148] associated with the magnetic ordering temperature. In the pseudo-cubic manganites, shifts in the O-

phonon modes observed in far-IR spectra (see Fig. 3.5) and in Raman spectra[149] of $LaMnO_3$ correlate with T_N. Additionally, the doped manganite $La_{0.7}Ca_{0.3}MnO_3$ shows TO phonon shifts at the ferromagnetic ordering temperature.[36] In these other magnetically ordered systems, anomalies in ω_{TO} and ϵ_0 attributed to spin-phonon coupling exist in the absence of a ferroelectric order parameter.

Nonlinear optics has provided the strongest evidence in support of the coupling of the order parameters P and l. Fiebig *et al.*[150] observe coupled ferroelectric and AFM domains in second harmonic generation (SHG). Symmetry properties allow separate identification of the two order parameters: P obeys time-reversal symmetry and l does not.[150] In nonlinear optics, the SHG source term $\boldsymbol{S}(2\omega)$ couples to the incident electric field $\boldsymbol{E}(\omega)$ in the following way, $\boldsymbol{S}(2\omega) = \epsilon_0[\hat{\chi}(0) + \hat{\chi}(P) + \hat{\chi}(l) + \hat{\chi}(P\,l)\,\boldsymbol{E}(\omega)\boldsymbol{E}(\omega)]$. The SHG spectra in Ref. 150 manifest the first examples of a nonlinear optical process coupling simultaneously to an electric and magnetic order parameter, *i.e.*, observation of a susceptibility term dependent on coupling $\hat{\chi}(P\,l)$. Moreover, the coupling of order parameters leads to the formation of AFM domains, which are dominated by the product $P\,l$ rather than by l alone.

Establishing the coupling of order parameters and relating it to the microscopic physics remains a key issue in the study of this class of materials. The present experiments confirm an anomaly in the static dielectric constant below the T_N. Measurements of the dynamical ϵ find that phonon contributions prevail. Thus, spin-phonon coupling dominates the ϵ anomaly. Uncertainties persist in the current understanding of the relation between the ϵ anomaly and order parameter coupling.

4.3.5 Electron phonon coupling

The strong spin-phonon coupling observed in $LuMnO_3$ naturally motivates consideration of other forms of coupling. In particular, electron phonon coupling may allow for the observation of Franck-Condon spectra, where small molecules have ex-

cited electronic states leading to multiphonon sidebands in the electronic spectra.[87] In order to observe these effects, the occupied ground state wavefunction must have a different coordinate space minimum than the optically excited state. Then optical absorption occurs before the lattice can react (*i.e.*, vertical transition in the coordination configuration picture).[82] The excited state relaxes to the coordinate minimum through phonon emission before eventually reemitting at a lower frequency. Multiphonon processes produce observable signatures in Raman and photoluminescence spectroscopies.

Raman spectroscopy provides an experimental technique to measure the predicted[87] multiphonon behavior. In cubic crystals (*e.g.*, the pseudo-cubic manganite $LaMnO_3$), optical selection rules forbid on-site d-d transitions. However, lattice distortions resulting from asymmetric oxygen breathing modes in $LaMnO_3$ provide orbital admixture and allow for on-site d-d transitions in this system.[87] Raman studies[97,98] on $LaMnO_3$ report evidence for weak multiphonons. In the hexa-manganites, the symmetry allowed on-site Mn d-d transition in $LuMnO_3$ appears a natural candidate to observe similar Franck-Condon physics. Nevertheless, preliminary Raman measurements[151] find no evidence for multiphonon sidebands in hexagonal $YMnO_3$. Higher order Raman phonons do not correspond to first-order phonon harmonics. Furthermore, the ratio of the intensities of second order to first order phonons depends strongly on temperature, in contradiction to Franck-Condon model predictions and the behavior of the pseudo-cubic manganites.[98]

In addition to Raman spectroscopy, the Frank-Condon model predicts effects on the photoluminescence (PL) and photoluminescence excitation (PLE) spectra.[87] Despite these predictions, PL measurements[151,152] on hexagonal $YMnO_3$ find no evidence of multiphonon emission sidebands, even at low temperatures. Preliminary PL and PLE measurements do observe a Stokes-shifted emission peak lower in energy and with a frequency dependence similar to the excitation spectrum.[151] However, the

emitted intensity is many orders of magnitude lower than expected for on-site luminescence.[142] The observed PL spectra likely correspond to emission of a delocalized exciton trapped in potential well (*e.g.*, an impurity).

Raman and PL results on $LuMnO_3$ and $YMnO_3$ suggest the Franck-Condon picture may not be applicable to hexa-manganites. Rather one should consider the electronic excitations in a delocalized exciton band picture. Furthermore, electron phonon coupling remains weak in this system. These findings contrast the observations in the pseudo-cubic manganites.

4.4 Conclusions

In conclusion, this chapter presents optical evidence of a strong coupling of the antiferromagnetism in $LuMnO_3$ to a sharp low energy interband transition and to the infrared phonon spectrum. Optical measurements from $1.2\,\text{meV}$ to $5.6\,\text{eV}$ ($10 - 45000\,\text{cm}^{-1}$) at temperatures $4 - 300\,\text{K}$ reveal a symmetry-allowed on-site Mn d-d transition near $1.7\,\text{eV}$. The optical feature blueshifts ($\approx 0.1\,\text{eV}$) with the antiferromagnetic ordering, which is due to the effects of superexchange interaction on the on-site Mn d-d transition. Similar anomalies in the temperature dependence of the TO phonon frequencies are attributed to the effects of spin-phonon coupling. Furthermore, these phonon contributions overwhelmingly dominate the known anomaly in temperature dependence of the quasi-static dielectric constant ϵ_0 below the Néel temperature ($T_N \approx 90\,\text{K}$).

Chapter 5

Co-Doped Titanium Dioxide: A Diluted Ferromagnetic Oxide

This chapter addresses clustering and the optical properties of well-characterized thin films of anatase $Ti_{1-x}Co_xO_{2-\delta}$. Section 5.1 examines the implications of cobalt clustering on the optical properties. Given the evidence[66] supporting limited Co solubility, Sec. 5.2 presents measurements on low-doped samples with $x \leq 0.02$. For low Co concentrations, these as-grown films exhibit no signs of clustering. Section 5.3 presents the optical absorption of low-doped films. Interband absorption above the band gap at $3.6\,\text{eV}$ dominates the optical spectra. The observed band gap blue shifts with Co doping and no magnetic impurity states appear in the gap. Finally, Sec. 5.4 discusses the implications of these results related to band structure calculations and compares the measured band edge shift to other optical studies.

5.1 Optical Response of Cobalt Clusters

The experimental evidence supporting Co clustering in these films naturally raises the question of how this clustering might be observed in the optical data. Effective medium theory (EMT) models the optical response of inhomogeneous media.[153–157] Simple Maxwell Garnett theory (MGT)[153,154,158] treats spherical inclusions in a dielectric host background to determine an effective dielectric constant, ϵ given

by

$$\epsilon = \epsilon^{(\mathrm{I})} \frac{(\epsilon^{(\mathrm{II})} + 2\epsilon^{(\mathrm{I})}) + 2f(\epsilon^{(\mathrm{II})} - \epsilon^{(\mathrm{I})})}{(\epsilon^{(\mathrm{II})} + 2\epsilon^{(\mathrm{I})}) - f(\epsilon^{(\mathrm{II})} - \epsilon^{(\mathrm{I})})}, \tag{5.1}$$

where f is the volume fraction of inclusions in a host medium, $\epsilon^{(\mathrm{II})}$ is the dielectric constant of the inclusions, and $\epsilon^{(\mathrm{I})}$ is the dielectric constant of the host. In the Co-doped TiO_2 system, $\epsilon^{(\mathrm{II})}$ and $\epsilon^{(\mathrm{I})}$ represents the dielectric constant of Co metal and TiO_2, respectively. The effective ϵ predicted by MGT does not depend on the radius of the inclusions a, provided that a is large enough to include several unit cells and $a \ll \delta$, where δ is the penetration depth of the incident light in the metallic inclusion. For Co in the near-IR to visible (1-4 eV) range, $\delta \approx 20$ nm.

A comparison of the predictions of MGT to the measured σ_1 for $x = 0.07$ requires values for the parameters in Eq. (5.1). Values for $\epsilon^{(\mathrm{II})}$ are taken from the literature[159,160] and values of $\epsilon^{(\mathrm{I})}$ are taken from measurements of the undoped TiO_2 films. For $x = 0.07$ (*i.e.*, assuming all of the doped cobalt forms clusters) the resulting volume fraction is given by

$$f = x \frac{\Omega_{\mathrm{Co}}}{\Omega_{\mathrm{TiO_2}}} = 0.07 \frac{1.1 \times 10^{-23}}{3.4 \times 10^{-23}} = 0.023\,, \tag{5.2}$$

where Ω is the volume per formula unit (cm^3/f.u.). Figure 5.1 shows the predicted σ_1 (solid curve) using Eqs. (5.1) and (5.2) with $f = 0.023$. MGT predicts enhanced absorption below the band edge of TiO_2, but shows no significant frequency shift of the edge. Contrary to the prediction, the measured conductivity (dashed curve Fig. 5.1) exhibits a noticeable shift of the band edge, but no such enhanced absorption. To consider the possibility of filamentary Co (as proposed in a theoretical paper by Yang *et al.*[161]), the MGT model is extended to consider the clustered Co as ellipsoids of revolution.[155] As the aspect ratio of the ellipsoids increases, the optical conductivity below the energy gap spreads to lower frequencies. Even with an aspect ratio of $100:1$, there exists no appreciable reduction of σ_1 in the visible frequency range nor shift of the band edge. Thus, EMT fails to capture the optical behavior of the Co-

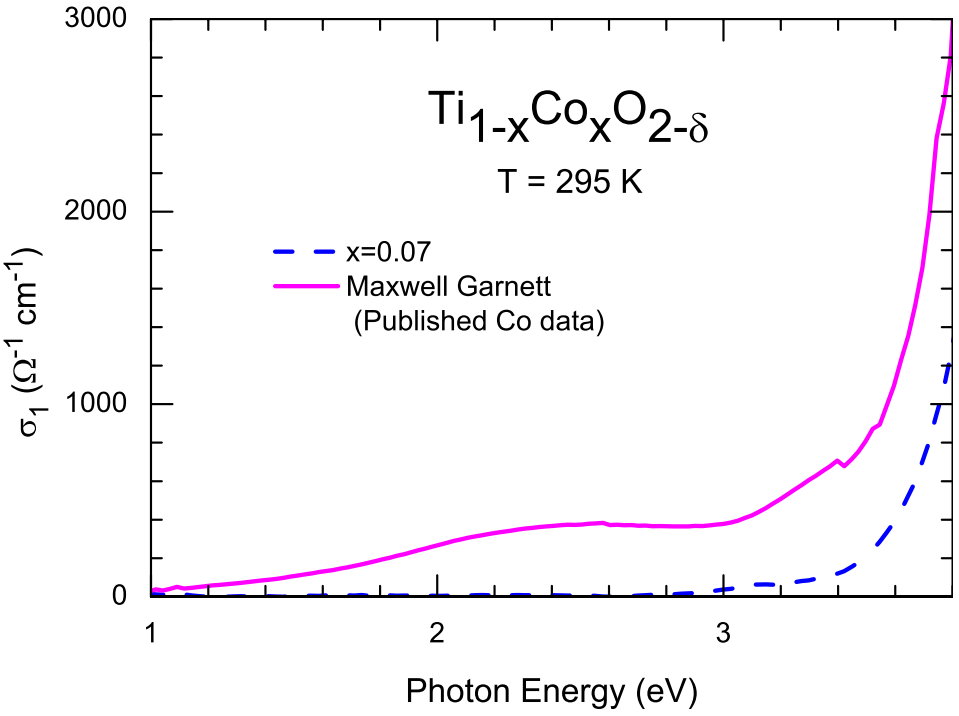

Figure 5.1: Frequency dependent σ_1 from Maxwell Garnett effective medium theory (solid curve) and data (dashed curve) for $Ti_{0.93}Co_{0.07}O_2$.

clustered films, indicative of the cluster size exceeding the penetration depth, $a \geq \delta$, as observed in TEM.

For larger Co clusters, $a \geq \delta$, losses due to the skin effect become important and the cluster separation increases. In this case, Mie's treatment[162] of light incident on a sphere represents a more appropriate model than the effective dielectric from MGT.[156] A conducting sphere causes both scattering and absorption processes. The total or extinction cross section of light incident on the sphere σ_{ext} then represents a sum of the scattering σ_{sc} and absorption σ_{ab} cross sections, $\sigma_{ext} = \sigma_{sc} + \sigma_{abs}$. Mie theory provides expressions for these various cross sections,[156, 162, 163] which are

given by

$$\frac{\sigma_{sc}}{\pi a^2} = \frac{2}{q^2}\sum_{l=1}^{\infty}(2l+1)(|\alpha_l|^2+|\beta_l|^2) \tag{5.3}$$

$$\frac{\sigma_{abs}}{\pi a^2} = \frac{2}{q^2}\sum_{l=1}^{\infty}(2l+1)\left(1/2-|\alpha_l-1/2|^2-|\beta_l-1/2|^2\right) \tag{5.4}$$

$$\frac{\sigma_{ext}}{\pi a^2} = \frac{2}{q^2}\sum_{l=1}^{\infty}(2l+1)\Re e\left\{\alpha_l+\beta_l\right\}, \tag{5.5}$$

where $q = 2\pi/\lambda^{(\mathrm{I})}\, a = 2\pi\sqrt{\epsilon^{(\mathrm{I})}}\nu\, a$ and α_l and β_l are the complex partial-wave coefficients. Boundary value conditions at the surface of the sphere give α_l and β_l in terms of the Ricatti-Bessel functions (ψ_l and ζ_l) and their derivatives,

$$\begin{aligned}\alpha_l &= \frac{\hat{n}\,\psi_l'(q)\,\psi_l(\hat{n}\,q)-\psi_l(q)\,\psi_l'(\hat{n}\,q)}{\hat{n}\,\zeta_l'(q)\,\psi_l(\hat{n}\,q)-\zeta_l(q)\,\psi_l'(\hat{n}\,q)}\\ \beta_l &= \frac{\hat{n}\,\psi_l(q)\,\psi_l'(\hat{n}\,q)-\psi_l'(q)\,\psi_l(\hat{n}\,q)}{\hat{n}\,\zeta_l(q)\,\psi_l'(\hat{n}\,q)-\zeta_l'(q)\,\psi_l(\hat{n}\,q)},\end{aligned} \tag{5.6}$$

where $\psi_l(x) = \sqrt{\pi x/2}\, J_{l+1/2}(x)$, $\zeta_l(x) = \sqrt{\pi x/2}\, H^{(1)}_{l+1/2}(x)$, and $\hat{n} = \sqrt{\epsilon^{(\mathrm{II})}}/\sqrt{\epsilon^{(\mathrm{I})}}$ is the ratio of complex indexes of refraction. Limiting forms for the scattering cross section given in Eq. (5.3) are readily attainable[83,156,163] and intermediate values may be determined using numerical methods, *e.g.* Mathematica™. In the long wavelength limit $q \ll 1$, σ_{sc} reduces to the Raleigh scattering result $\sigma_{sc} \propto q^4$. For short wavelengths $q \gg 1$, Eq. (5.3) reduces to the classical short-wave result $\sigma_{sc} = 2\pi\, a^2$.

The intermediate wavelength limit $q \approx 1$ best represents the visible frequency region (below the band gap) of Co-doped TiO_2. Fig. 5.2 shows the frequency dependence of σ_{ext} given by Eq. (5.5). Values for the extinction cross section are normalized to πa^2 for a Co sphere in TiO_2 with constant index, $n^{(\mathrm{I})} = \sqrt{\epsilon^{(\mathrm{I})}} = 2$. Curves for several cluster sizes corresponding to the range observed in TEM, $10 \le a \le 25\,\mathrm{nm}$, are shown. As the cluster size increase the onset of the cross section moves to lower frequencies. At high frequencies (short wavelengths), $\sigma_{sc} \sim 2\pi a^2$ and $\sigma_{abs} \sim 0$, giving $\sigma_{ext} \sim \sigma_{sc} \sim 2\pi a^2$. For the region below the band gap of TiO_2 ($\nu < 3\times10^4\,\mathrm{cm}^{-1}$), any nonzero σ_{ext} represents a decrease in intensity of the incident light beam. The

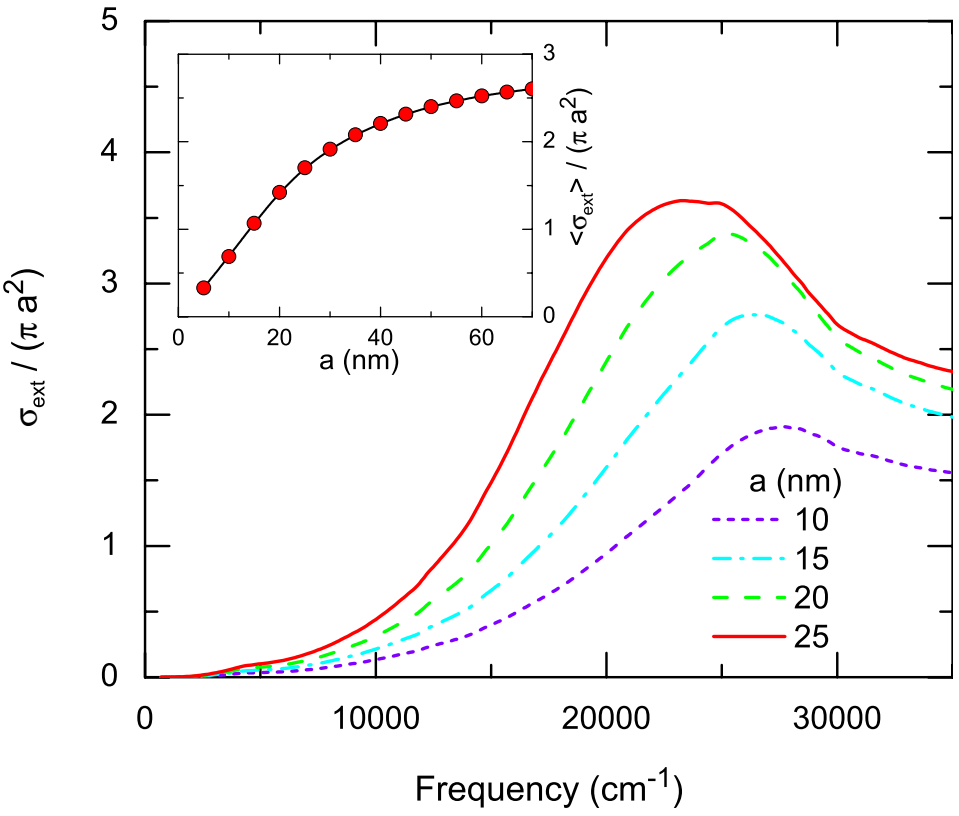

Figure 5.2: Normalized extinction cross section from Mie theory for TiO_2 host with Co spheres of radii: $a = 10, 15, 20$, and 25 nm. Inset shows the normalized extinction cross section averaged from $0\text{-}3 \times 10^4$ cm^{-1} as a function of cluster size (solid line guides the eye).

average total cross section $\langle \sigma_{ext} \rangle$ proves useful to estimate the affect of scattering and absorption of Co spheres in the mid gap region. The inset of Fig. 5.2 shows normalized values of $\langle \sigma_{ext} \rangle$ as a function of a. For $10 \leq a \leq 25$ nm, the average extinction cross section grows linearly with the cluster size $\langle \sigma_{ext} \rangle / \pi a^2 = \mu\, a$, where the slope $\mu \approx 0.067$ nm^{-1}.

While rigorously solved for a single sphere, Mie theory must be extended to include the multiple scatters (and absorbers) appropriate to the Co clustered TiO_2 systems. The total absorption cross sections for multiple spheres involves a sum of the individual σ_{abs} given by Eq. (5.4). However, scattering from a number of small particles involves, in general, the coherent addition of scattering cross sections. The

resulting total σ_{sc} has a term proportional to the phase difference between scatterers $e^{i\,\boldsymbol{q}\cdot(\boldsymbol{r}_i-\boldsymbol{r}_j)}$, where $\boldsymbol{q}$ is the vectorial change in the incident and scattering wave vector and $\boldsymbol{r}_i$ and $\boldsymbol{r}_j$ are the position vectors from the i-th and j-th scatterer, respectively. In the case of randomly distributed scattering centers, appropriate to clustered Co-doped TiO_2, the phase factors for $i \neq j$ contribute negligibly to the sum.[83] Thus, an incoherent addition of scattering centers better suites the present system. For incoherent addition, the total cross section due to all clusters is a simple sum

$$\sigma_{\text{total}} = \sum_i \sigma_i = N_A\,\sigma_i\,, \tag{5.7}$$

where N_A is the total number of inclusions in an incident beam of light with area A and σ_i is the average extinction cross section of a single inclusion. As discussed above, $\langle\sigma_i\rangle \approx \mu\,a\,\pi a^2$ in the interband region. The number of clusters in a given area A depends on the cluster density, $N_A = \eta\,t\,A$, where η is the cluster number density and t is the film thickness.

The Co doping concentration x and the relative number densities of Co metal and TiO_2 provide an estimate the cluster density η. The number of Co atoms in a given cluster N_{cl} is given by $N_{cl} = \eta^{(\text{II})}\,\frac{4}{3}\,\pi a^3$. The cluster density is then the density of Co in TiO_2 due to doping divided by N_{cl}

$$\eta = \frac{\eta_x}{N_{cl}} = \frac{x}{\frac{4}{3}\,\pi a^3}\,\frac{\eta^{(\text{I})}}{\eta^{(\text{II})}}\,, \tag{5.8}$$

where $\eta^{(\text{I})} = 2.91\times10^{22}\,\text{cm}^{-3}$ and $\eta^{(\text{II})} = 9.1\times10^{22}\,\text{cm}^{-3}$ represent the number densities of Ti in TiO_2 and Co in bulk metallic Co, respectively. The average separation r between Co clusters (solving $\frac{4}{3}\,\pi r^3\,\eta = 1$) is

$$r = \left(\frac{1}{\frac{4}{3}\,\pi\,\eta}\right)^{1/3} = a\left(\frac{1}{x}\,\frac{\eta^{(\text{II})}}{\eta^{(\text{I})}}\right)^{1/3}. \tag{5.9}$$

For clusters with $a = 20\,\text{nm}$ and $x = 0.07$ doping, Eq. (5.8) and Eq. (5.9) give $\eta \approx 6.7\times10^{14}\,\text{cm}^{-3}$ and $r \approx 70\,\text{nm}$, respectively. Comparing with TEM measurements,

the micrograph in Fig. 1.12(a) represents a nearly 2D slice of thickness $t \approx 10\,\text{nm}$, less than a typical cluster radius. From the micrograph, $\eta^{2D} \approx 1.8 \times 10^9\,\text{cm}^{-2}$. The resulting cluster density is then $\eta^{2D}/t \approx 1.8 \times 10^{15}\,\text{cm}^{-3}$, higher than the estimation from Eq. (5.8) by a factor of two. However, uncertainties in t and the small number of clusters in the micrograph lead to uncertainties in the number density of Co clusters estimated from TEM.

The cluster density calculated from Eq. (5.8) allows estimation of the total extinction cross section together with Eq. (5.7). The ratio of the total extinction cross section to the area of the incident light beam is then

$$\frac{\sigma_{\text{total}}}{A} = \frac{N_A \times \sigma_i}{A} = \frac{\eta\, t\, A \times \mu\, a\, \pi a^2}{A} = \frac{3}{4}\frac{\eta^{(\text{I})}}{\eta^{(\text{II})}}\, x\, \mu\, t\,. \tag{5.10}$$

This ratio represents the relative observable optical signal, *i.e.*, the ratio of the total scattered and absorbed light to the incident light. For $x = 0.07$, $10 \leq a \leq 25\,\text{nm}$, and $t = 80\,\text{nm}$, Eq. (5.10) estimates $\sigma_{\text{total}}/A \approx 0.09$. A relative loss of signal due to scattering and absorption of this magnitude should be observable in optical transmittance $\mathcal{T}$ and reflectance $\mathcal{R}$. Yet no such loss appears in the resulting optical conductivity for the $x = 0.07$ film shown in Fig. 5.1. Indeed the optical absorptance, $\mathcal{A} = 1 - (\mathcal{T} + \mathcal{R})$, remains zero in the mid gap region to within the experimental accuracy. $\mathcal{T}$ and $\mathcal{R}$ are measured to within $\pm 1\%$ and $\pm 2\%$, respectively, and the corresponding uncertainty in absorptance is $\Delta\mathcal{A} \approx 2.2\%$.

In light of the experimental evidence for scattering from TEM and the predictions of optical behavior from Mie theory, the absence of a measurable effect on the mid gap optical spectrum remains puzzling. Two possible scenarios may explain the optical data: (i) the amount of Co that clusters is less than the total Co-doping and/or (ii) the cluster sizes are larger than expected from TEM. Both scenarios imply the micrograph in Fig. 1.12(a) does not accurately represent clustering in the films. For the first scenario, not all of the doped cobalt x goes into metallic Co clusters. In

order for the predicted extinction cross section from Eq. (5.10) to be reduced inside the measured optical absorption sensitivity ($\Delta\mathcal{A} \approx 0.022$), only approximately $1/4\,x$ of the doped Co would form clusters. Indeed, approximately $x = 0.02$ of the Co is soluble in the TiO_2 lattice.[66] Additionally, the Co clusters may not consist entirely of bulk Co metal. Cobalt on the outer surface of the clusters likely forms a Co-oxide layer surrounding the spheres of bulk Co. In the second scenario, the average cluster radius must be larger than observed in Fig. 1.12(a) by roughly a factor of two. If $30 \leq a \leq 60$, the slope of the normalized $\langle\sigma_{ext}\rangle$ decreases to $\mu \approx 0.014$. Substituting into Eq. (5.10) gives $\sigma_{\text{total}} \lesssim 0.02$, an effect not observable with the present optical measurement certainty. Thus, scenario (ii) offers a plausible explanation consistent with the reported behavior of Co clusters[66] and the optical data showing no evidence of scattering or absorbtion by these clusters.

High-T magnetization and TEM experiments have provided direct evidence of Co clustering in the $x = 0.07$ samples. The large T_c reported from VSM likely results from bulk Co in these clusters. Optical measurements find no clustering evidence as predicted by either effective medium theory or Mie theory. In Mie theory, the reduced cross section suggests either a lower concentration of Co in clusters than expected from the doping level or an average cluster radius larger than that observed in the TEM micrograph. For low-doped samples, $x \leq 0.02$, the clustering story appears different. In these low-doped systems, T_c lies much lower than bulk Co and TEM exhibits no clustering. Given the limited Co solubility in the TiO_2 matrix for concentrations $x > 0.02$ and the reported sensitivity of $Ti_{1-x}Co_xO_{2-\delta}$ films to sample preparation (O_2-annealing[66] and growth temperature) the remaining sections of this chapter focus on low-doped samples.

5.2 Experiment

5.2.1 Sample characterization

Thin film samples of $Ti_{1-x}Co_xO_{2-\delta}$ with $x = 0, 0.01,$ and 0.02 were grown on $SrLaGaO_4$ (SLGO) substrates using pulsed laser deposition (PLD). Additionally, a pure TiO_2 film was grown on $LaAlO_3$ (LAO) for comparison. Films were deposited with an oxygen partial pressure of 10^{-5} Torr (corresponding to $\delta \ll 1$). Rutherford backscattering measurements (RBS) determined the film thicknesses to be $1470, 1350, 1400,$ and 1580 Å (to better than 5 %) for the $x = 0, 0.01, 0.02$ on SLGO, and $x = 0$ on LAO, respectively. 4-probe dc resistance measurements exhibit insulating behavior with room temperature resistivity $\rho_{295K} \gtrsim 0.1\,\Omega$ cm. X-ray diffraction (XRD) measurements[66] of both pure and doped TiO_2 films show peaks corresponding to those observed in bulk anatase TiO_2. Figure 5.3a illustrates the narrow XRD peaks (inset highlights anatase 004 peak) for doped $Ti_{1-x}Co_xO_{2-\delta}$ indicative of high-quality films. Values of the in-plane and out-of-plane (d_{004}) lattice constants obtained from XRD are discussed later in the chapter. No direct evidence

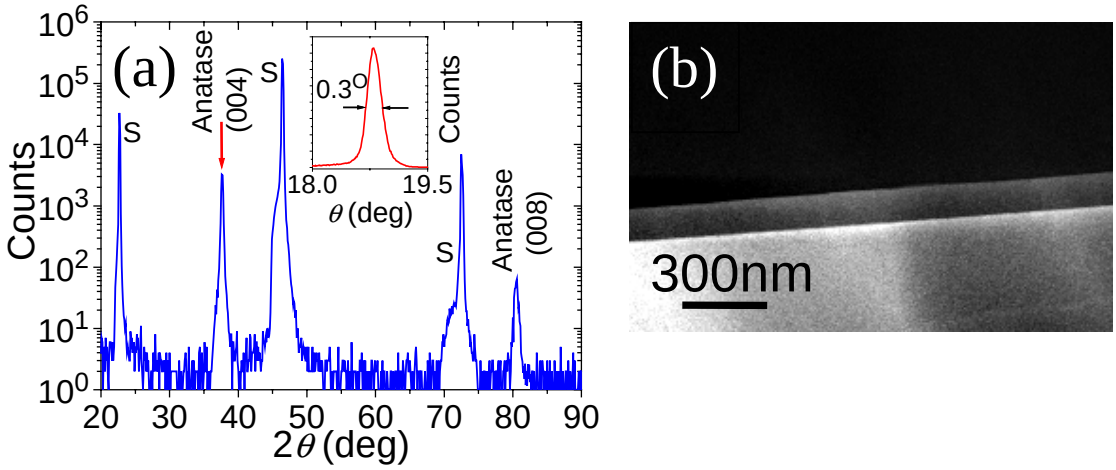

Figure 5.3: $Ti_{0.99}Co_{0.01}O_{2-\delta}$ films. (a) XRD rocking curves. Inset highlights the Anatase 004 peak. (b) TEM showing an absence of Co clusters.

of Co clustering is observed in these low-doped ($x \leq 0.02$) films as confirmed by the

TEM micrograph shown in Fig. 5.3b.

Films produced using PLD typically display rough surface topology. A high-energy laser ablates a target pellet of the material to be deposited. The laser pulse removes large chunks of material from the target and deposits those boulders on the substrate material. Often this process results in a rough film surface.

Atomic Force Microscopy (AFM) characterizes the film surface roughness. Results of an AFM surface scan of a $10 \times 10\,\mu$m area of a $x = 0.02$ film studied herein are shown in Fig. 5.4. While most of the surface remains flat to within ± 20 nm, several large boulders of material are easily seen. These boulders persist in films of all doping concentrations, but are not observed on the bare substrates. The line scan in Fig. 5.4 shows a typical height profile of the boulders, which extends to greater than 100 nm above the average film surface. Despite the large height of the boulders relative to the film thickness, the area of these regions remains small (less than a few percent). Therefore, the resulting thickness variations only minimally affect the optical properties.

5.2.2 Transmission and reflection measurements

Room temperature transmission $\mathcal{T}(\omega)$ and reflection $\mathcal{R}(\omega)$ measurements of near-normal incidence light at frequencies from 0.25 to 5 eV are performed using a FTIR spectrometer[27,164] described in detail in Chap. 2. Figure 5.5 shows the room-temperature $\mathcal{T}$ and $\mathcal{R}$ spectra for doping $x = 0, 0.01$, and 0.02. Several features characterize the spectra. First, below ≈ 3 eV, $\mathcal{T}$ and $\mathcal{R}$ sum to unity, indicative of negligible absorption or scattering. In this region, $\mathcal{T}$ and $\mathcal{R}$ exhibit oscillations resulting from interference (étalon) in the thin films. The period of this étalon ($\Delta\nu$) together with the index of refraction n gives the film thickness using Eq. (2.36) on page 59. Film thicknesses determined from étalon agree with RBS measurements. Above the transparency window, $\mathcal{T}$ drops precipitously and the étalon behavior disappears,

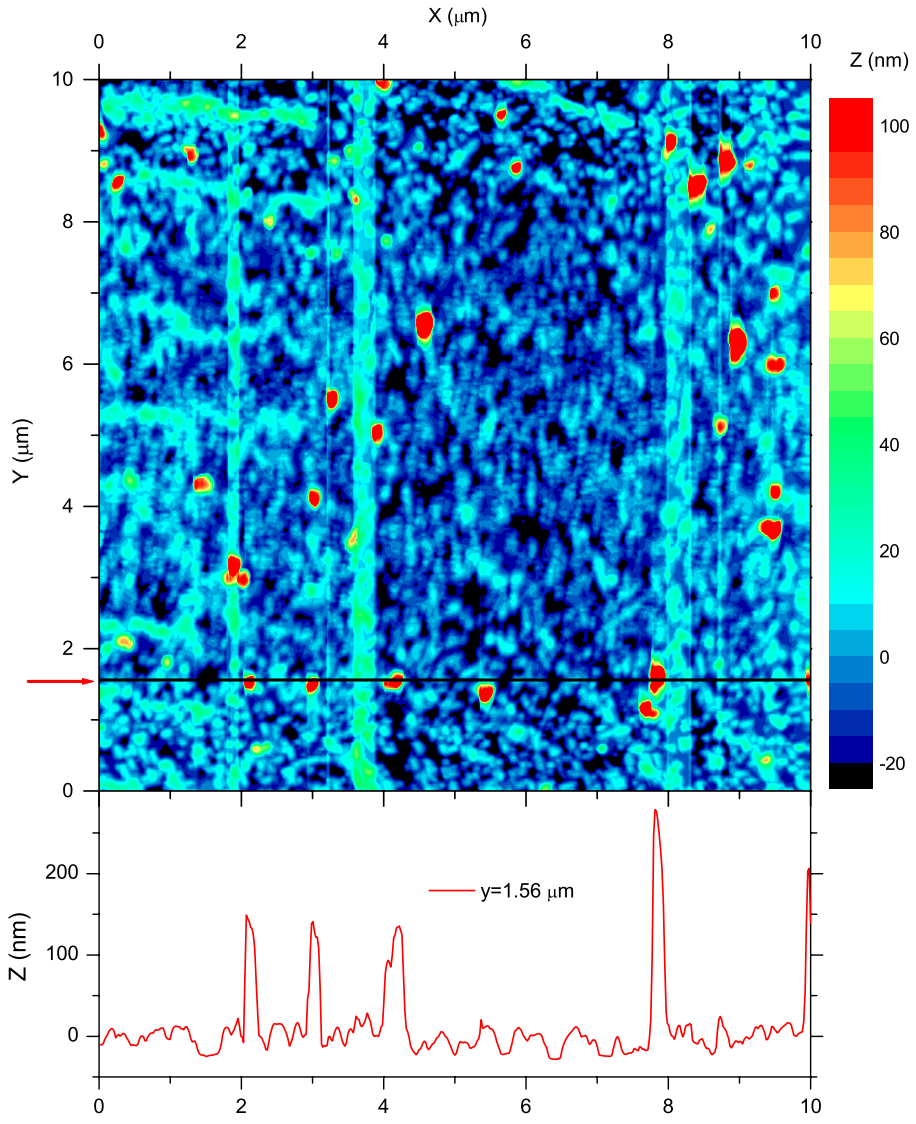

Figure 5.4: AFM film surface scan of $Ti_{0.98}Co_{0.02}O_{2-\delta}$. Scan area is $10 \times 10\,\mu$m and height contours are in nm. Several boulders of deposited material are visible. A line scan ($y = 1.56\,\mu$m) illustrates the height of the boulders.

characteristic of the onset of absorption. Finally, this absorption onset shifts to higher frequencies with x, as seen in $\mathcal{T}$.

As described in Chap. 2, numerical inversion of the Fresnel formulas[86] for $\mathcal{T}$ and $\mathcal{R}$ obtains directly the complex index of refraction. In the transparency window (below $3\,$eV), the small value of κ complicates the numerical inversion procedure. As a result, multiple roots arise in the solutions of $\mathcal{T}$ and $\mathcal{R}$ (see Fig. 2.11). The

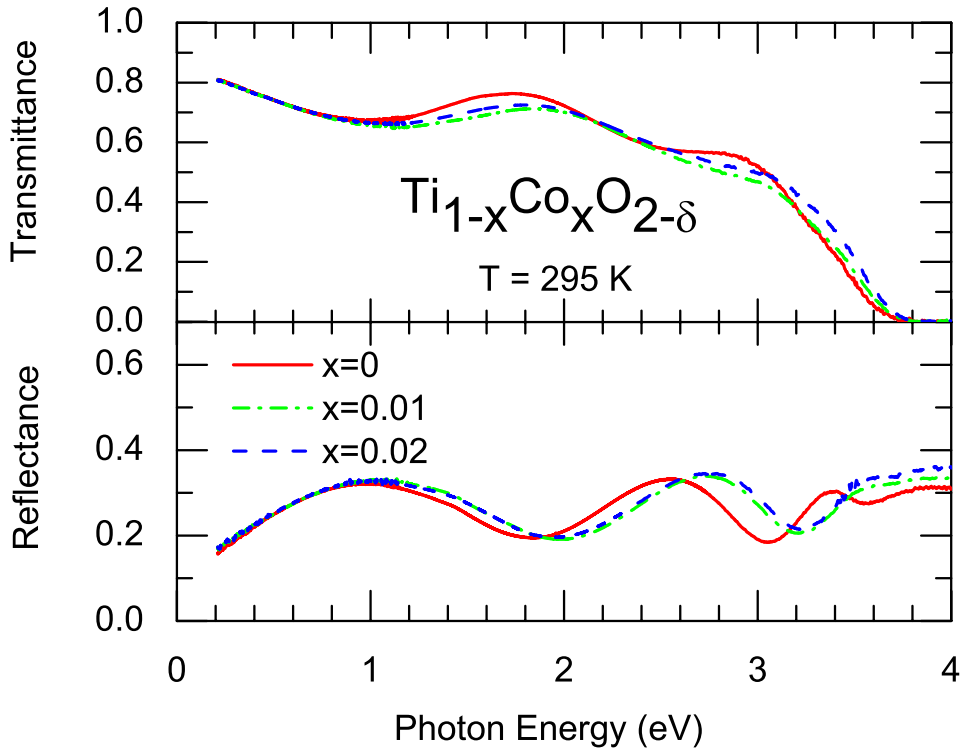

Figure 5.5: Transmittance and reflectance spectra of $Ti_{1-x}Co_xO_{2-\delta}$ films at room temperature for Co concentrations $x = 0, 0.01$, and 0.02.

n values are particularly sensitive to these roots, while κ remains roughly constant. These complications vanish above the absorption onset. Having determined $\tilde{n}(\omega)$, additional optical constants may be derived, *e.g.*, the optical absorption $\alpha(\omega)$ or the complex optical conductivity $\tilde{\sigma}(\omega)$. The following section discusses the resulting optical constants.

5.3 Results

5.3.1 Absorption coefficient

Historically, the spectral dependence of the band edge is characterized using the absorption coefficient α given by Eq. (2.9). At photon energies above the band gap E_g, $\alpha \propto (\hbar\omega - E_g)^{1/2}$ for a direct gap while $\alpha \propto (\hbar\omega - E_g)^2$ for an indirect gap.[165] Band structure calculations[166] predict a direct gap at energies just lower than the on-

set of indirect transitions in TiO_2. In a detailed study of the absorption edge of single crystal anatase TiO_2, Tang *et al.*[167] report a band edge extrapolated from an Urbach tail behavior with $E_g = 3.420$ eV and tentatively assign the transition to a direct gap. Consistent with the behavior of a direct gap, Fig. 5.6 plots α^2 versus frequency. Extrapolations to zero absorption of the linear fits above the band edge onset give

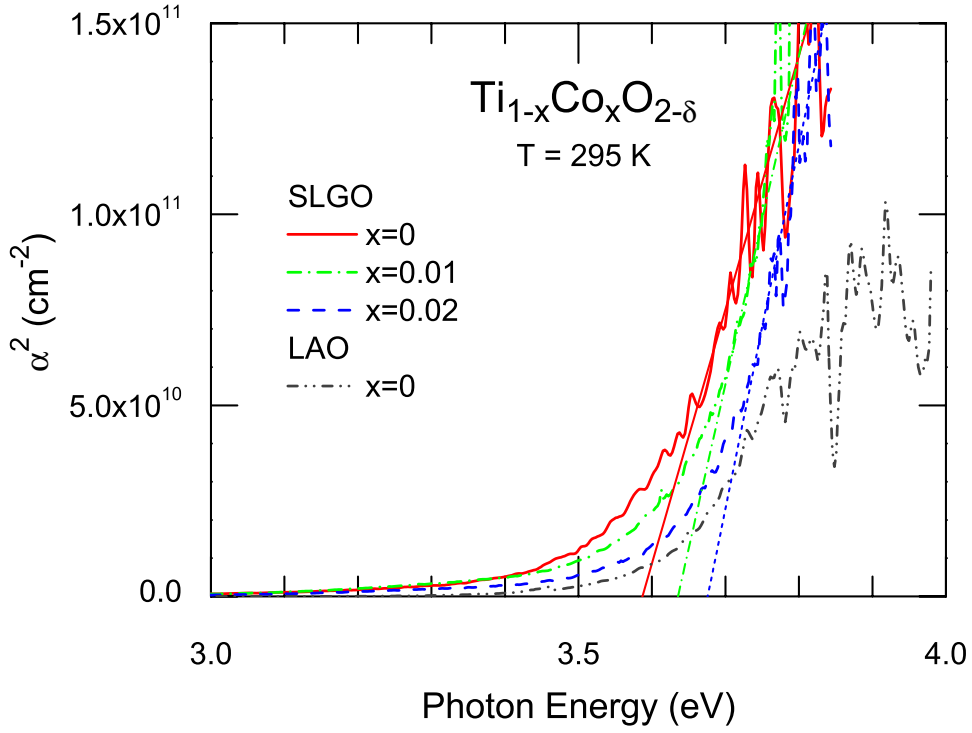

Figure 5.6: Frequency dependence of the square of the absorption coefficient α at room temperature for Co concentrations $x = 0, 0.01$, and 0.02. Straight lines represent linear fits. An undoped TiO_2 sample grown on a $LaAlO_3$ substrate is shown for comparison.

the direct band gap energy E_g. Pure TiO_2 exhibits $E_g = 3.6$ eV. With increased Co concentration x, the band edge shifts to higher frequencies, showing a maximum shift of 100 meV for $x = 0.02$. Apart from a band edge tail, there appears no evidence for strong absorption at frequencies below the gap. Additionally, direct band gap energies are compared to results of α fits appropriate to an indirect gap ($\sqrt{\alpha}$) and for an Urbach tail[167] (semilog α). Figure 5.7 shows $\sqrt{\alpha}$ versus frequency and correspond-

ing linear fits. While the absolute position of E_g depends on the assumed frequency dependence of α, the observed blue shift of E_g with Co doping remains quantitatively unaffected. While the exact nature of the gap (direct or indirect) remains uncertain, that the edge shifts does not. In a related work on Co-doped rutile TiO_2, Park *et al.*[68]

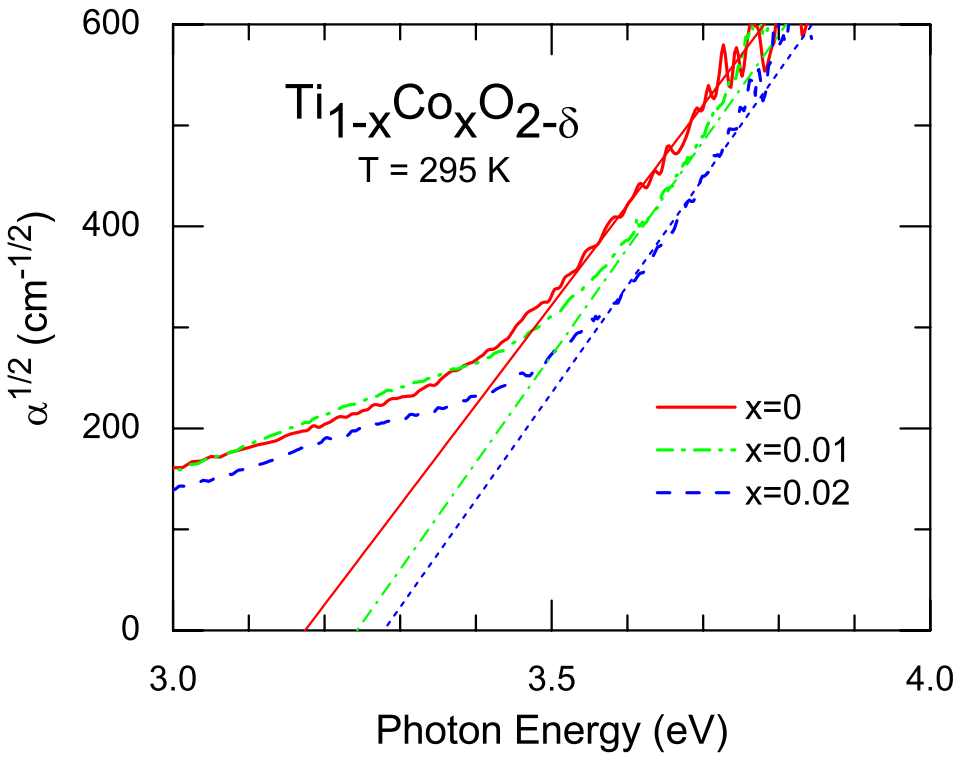

Figure 5.7: Frequency dependence of the square root of the absorption coefficient α at room temperature for Co concentrations $x = 0, 0.01$, and 0.02. Straight lines represent linear fits.

find no appreciable band edge shift with Co doping up to $x = 0.12$. However, the maximum blue shift of 100 meV observed in the present study falls within the error bars reported on the rutile phase, so the two results may be consistent.

5.3.2 Optical conductivity

While α well characterizes the band edge onset, the optical conductivity better suites to compare experimental results to the predictions of band theory. In particular, the real part of the optical conductivity is given by $\sigma_1(\omega) \propto 2nk\omega$, where n and

k are the real and imaginary part of the complex index of refraction, respectively, and ω is the frequency. Figure 5.8 shows the frequency dependence of σ_1 at room temperature for several Co concentrations. Throughout the mid-infrared (mid-IR) to

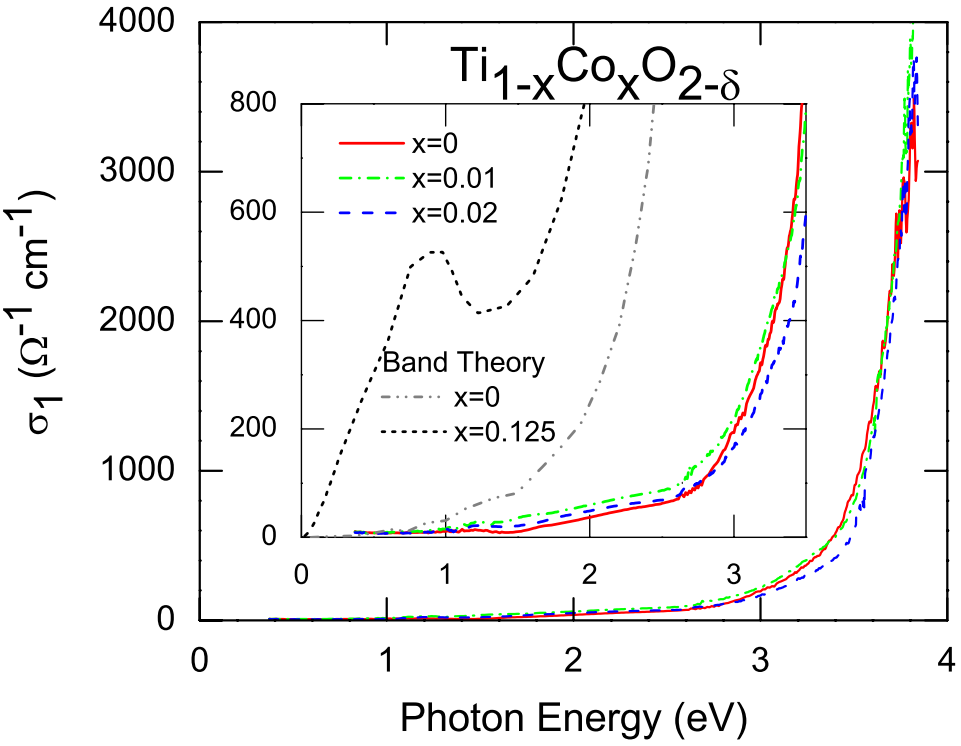

Figure 5.8: Frequency dependence of the real part of the optical conductivity σ_1 at room temperature for Co concentrations $x = 0, 0.01$, and 0.02. Inset expands the region just below the band edge. Band theory calculations from Yang *et al.*[161] are shown for $x = 0$ and $x = 0.125$.

visible frequency range (0.25 to $3\,$eV), σ_1 remains essentially zero, consistent with the negligible dc conductivity ($\sigma_{dc} \lesssim 0.1\,\Omega^{-1}\,\text{cm}^{-1}$). At frequencies larger than $3\,$eV, σ_1 increases rapidly, corresponding to the increase in absorption as seen in Fig. 5.6. The expanded view in the inset of Fig 5.8 further elucidates the minimal mid gap conductivity. Although no strong conductivity in the spectral range $1 \leq \hbar\omega \leq 3\,$eV is observed, σ_1 increases slightly near the edge, albeit non-monotonically, with the addition of Co. Such an increase may result from the Co levels in the gap or disorder effects on the Urbach tail[167] of the fundamental absorption edge.

5.4 Discussion

5.4.1 Photoluminescence data

An interesting results arises from the comparison of the optical conductivity and band edge shifts with photoluminescence (PL) spectra. PL studies[168–170] find a broad peak centered around 2.3 eV for anatase TiO_2. The peak in the PL spectrum is Stokes shifted 1.3 eV lower than the onset of interband transitions in the optical conductivity and the peak in the PL excitation spectrum. Tang *et al.*[170] assign the Stokes shift to a self-trapped exciton (STE) where the exciton loses energy nonradiatively to the lattice. In this interpretation, the peak in the PL spectrum resulting from the STE should follow the shifts in the band edge. Indeed, the PL peak blue shifts with Co doping.[168] Doping dependent shifts in the band edge and the PL peak are plotted together in Fig. 5.9 for comparison. Both the direct band gap energy and the PL peak increase monotonically with doping for $x \leq 0.02$, while the PL peak saturates above $x = 0.02$. The saturation of the shift at higher doping concentrations is consistent with the limited solubility of Co in TiO_2 as reported earlier.[66]

5.4.2 Pressure-dependent optical studies

A pressure-dependent optical study[171] of single crystal anatase TiO_2 reports similar shifts of the band edge with Co as observed here. Sekiya *et al.*[171] observe a blue shift of the band edge upon the application of hydrostatic pressure. For an applied pressure of 3.9 GPa, the edge shifts to higher energy by ≈ 50 meV. The change in the TiO_2 lattice resulting from the hydrostatic pressure is estimated by introducing the bulk modulus $B = -V\Delta P/\Delta V$, where V is the volume, ΔV is the change in volume, and P is the applied pressure. Taking $B = 180$ GPa for anatase TiO_2 from Ref. 172, the applied hydrostatic pressure of 3.9 GPa introduces a volume decrease of $\approx 2\%$.

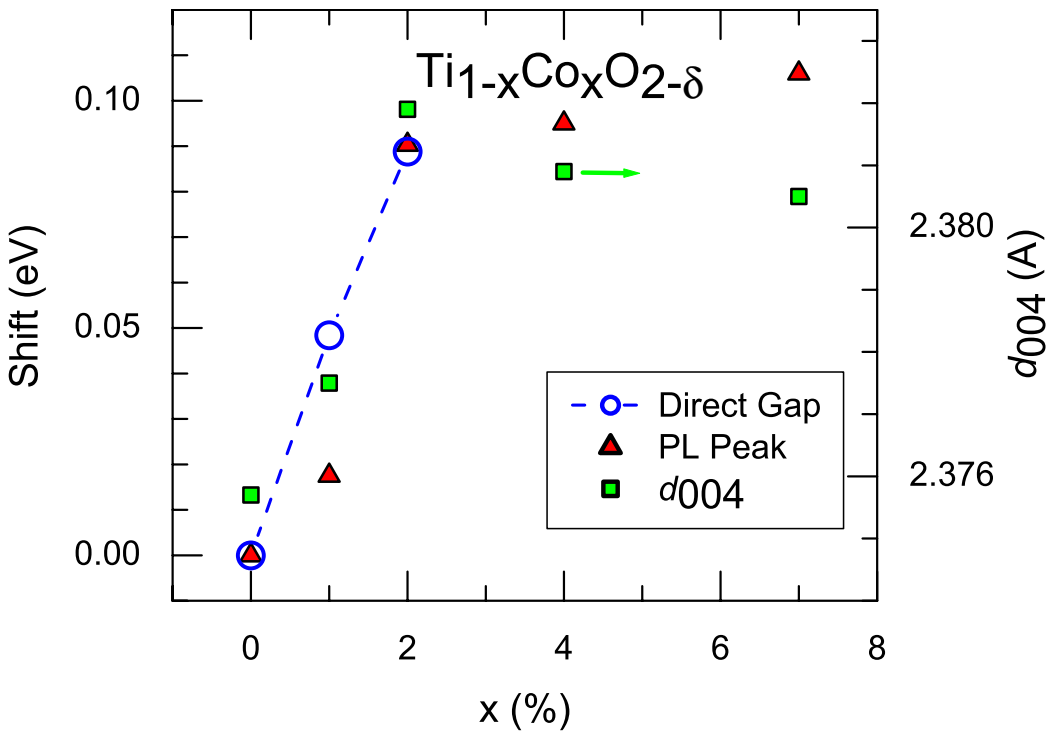

Figure 5.9: Shifts with cobalt doping of the direct band edge (circles with a dashed line as a guide for the eye) and photoluminescence peak from Guha *et al.*[168] (triangles). For comparison the out of plane lattice constant[66] d_{004} for films grown on $LaAlO_3$ is plotted on a separate y-axis (squares).

5.4.3 Substrate strain

The blue shift of the band edge with increasing pressure or equivalently decreasing lattice size suggests consideration of lattice strain induced by the substrate or the addition of cobalt. First regarding the substrate, the thin films studied suffer strain due to lattice mismatch with the substrates. For epitaxial films, the initial layers grow coherently with the substrate. Defects gradually relax the induced strain, allowing the films to grow more like bulk. Values of the in-plane lattice constant a for bulk TiO_2, LAO, and SLGO are listed in Table 5.1. Both LAO and SLGO substrates have a larger in-plane lattice parameter than bulk TiO_2, introducing a tensile strain in the films of approximately 0.12% and 1.5%, respectively. The tensile stress tends to expand the TiO_2 lattice in the plane. For materials with a typical Poisson

ratio, an in-plane expansion results in a reduction of the out-of-plane lattice constant, d_{004}. Indeed XRD measurements of the TiO_2 films reveal such a decrease of d_{004}, as shown in Table 5.1. The film on SLGO, with the larger in-plane tensile strain, exhibits

	a (Å)	d_{004} (Å)
TiO_2 Bulk[1]	3.7851	2.3780
$LaAlO_3$ substrate	3.79	
$SrLaGaO_4$ substrate	3.84	
TiO_2 film on $LaAlO_3$		2.376 [2]
TiO_2 film on $SrLaGaO_4$		2.367 [2]

[1] Ref. 172.
[2] X-ray diffraction measurement.

Table 5.1: TiO_2 and substrate in-plane (a) and out-of-plane (d_{004}) lattice parameters.

a larger reduction in d_{004} relative to bulk TiO_2 (0.45%) compared with the film on LAO (0.08%). To explore the effects of lattice strain on the band edge, the absorption of a TiO_2 film grown on LAO is shown in Fig. 5.6. The band edge of the film on LAO with the smaller in-plane lattice is blue shifted ($\gtrsim 100$ meV) relative to the TiO_2 film grown on SLGO, consistent with the blue shift resulting from the application of hydrostatic pressure discussed above.

5.4.4 Lattice expansion with doping

Examining the change in size of the lattice with doping addresses the effect of cobalt substitution on the shift of the band edge. Cobalt appears in the doped TiO_2 system in the $2+$ formal oxidation state as determined from x-ray absorption spectroscopy.[67] The atomic radii of Co^{2+} and Ti^{4+} are 0.82 Å and 0.69 Å, respectively.[173] Substitution of the larger Co^{2+} for Ti^{4+} should expand the lattice. XRD measurements[66] of films grown on LAO (plotted in Fig. 5.9) show d_{004} increases with x, saturating at about $x = 0.02$. The increase of d_{004} supports the prediction of an increase in the size of the lattice with Co doping. For the films grown on SLGO, d_{004} remains relatively constant with Co, $d_{004} = 2.3674 \pm 0.0002$ Å. An increasing (films on

LAO) or relatively constant (films on SLGO) lattice size with x should result in either a red shift or no shift of the band edge. Therefore, the observed blue shift with Co doping cannot be ascribed simply to a change of the lattice size.

5.4.5 Band structure and electronic transitions

A comparison of the measured conductivity to theoretical predictions of the electronic structure of both pure and Co-doped TiO_2 provides insight towards understanding the observed blue shift of the band edge. Band structure calculations[68,174] indicate the valence band derives primarily from oxygen p-levels, the conduction band derives from the Ti d-levels, and that the crystal-field split Co d-levels fall within the energy gap.[68,175] These mid gap states would lead to below band gap optical absorption in a non-interacting electron picture of optical transitions. Using a first-principles density-functional approach, Yang *et al.*[161] investigates nonuniform distribution of Co. The resulting σ_1 for $x = 0.125$ and pure TiO_2 are shown in the inset of Fig. 5.8 for comparison.

The predicted increase in conductivity below the band gap results from transitions to cobalt levels. The effective Co number density N_{eff} may be estimated using the partial optical sum rule given by Eq. (2.24), where N_{eff} in general will be somewhat less than the cobalt number density N. The cobalt number density N as a function of x is given by $N = fx/V$, where $f = 4$ is the number of Ti per unit cell and $V = 136.85\,\text{Å}^3$ is the unit cell volume. Estimating N_{eff} from the predicted conductivity using Eq. (2.24) and comparing to N, approximately 0.75 of the total Co spectral weight appears in the predicted mid gap absorption feature. To estimate the Co spectral weight from the experimental data, the difference in σ_1 due to doping is taken to be a constant $\approx 10\,\Omega^{-1}\,\text{cm}^{-1}$ (corresponding to the measurement error) over the frequency range from 1 to $3\,\text{eV}$. Substituting into Eq. (2.24) provides an experimental upper bound of $N_{eff} \approx 10^{20}\,\text{cm}^{-3}$. Comparing this to the number density N

results in an *upper* bound on the observed density of Co, which is roughly 0.15 times the expected total. The absence of below gap optical excitations in the measured conductivity may be understood either as evidence that the band calculations fail to capture the electronic structure of this material under the assumed charge state of the cobalt or that the on-site Coulomb energy U for adding another electron to the Co ion is large. In the second scenario the experiment implies $U \gtrsim 3\,\text{eV}$.

Taken together, the absence of spectral weight associated with cobalt levels in the gap and the blue shift of the band edge suggest possible strong interaction effects on the optical transitions involving the Co ion. First, interpretations that consider the alloy within a rigid band picture are rejected. In this case a shift in the band edge results from uniform shifts of the conduction band due to the average Ti/Co potentials. Since the atomic potentials for Co are larger that those of Ti, the Ti/Co band would be lower than the pure Ti bands in TiO_2 resulting in a red shift of the band edge, contrary to observation. Indeed the rigid band approach more appropriately describes delocalized states. For the transition metal ions in $Ti_{1-x}Co_xO_{2-\delta}$, a localized picture is more appropriate. Therefore, the following discussion considers the processes operating on the optical transitions involving the Co levels within a localized picture. Figure 5.10 shows a schematic view of the band structure.

In pure TiO_2, the band edge E_g consists of the energy difference between the filled O p-levels (shaded) and the empty Ti d-levels with $E_g \approx 3.6\,\text{eV}$ (as discussed above). With the addition of cobalt, charge transfer transitions from the O p-levels to the empty localized Co^{2+} d-levels become possible. Allowed transitions from occupied Co levels to the Ti levels should be weaker since they involve a virtual transition through the O p-levels. The energy E_1 of the oxygen to cobalt transition is the sum of the charge transfer energy Δ_{Co} plus the on-site Coulomb energy U; $E_1 = \Delta_{\text{Co}} + U$. The observed absence of below band gap absorption indicates that E_1 is greater than the band gap in the alloy E_g'. This is reasonable since the U is estimated to be

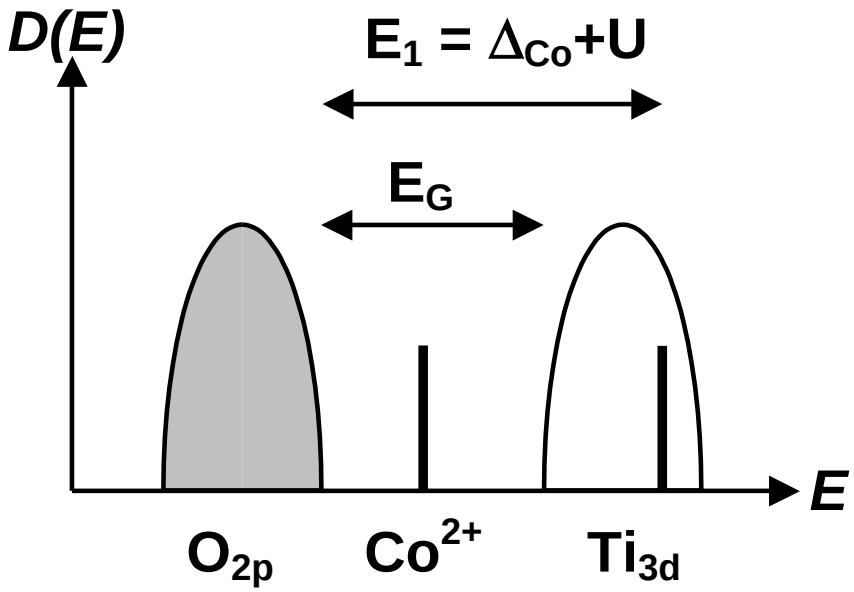

Figure 5.10: Schematic energy level diagram of $Ti_{1-x}Co_xO_{2-\delta}$.

≈ 3 eV and the empty Co levels are ≈ 2 eV above the oxygen band.[68]

Considering now the observed band edge shift, $\Delta E_g = \xi x$, where $\xi = 5$ eV. If the O and Ti band edges are not affected by the substitution of Co, this shift would be understood in terms of the reduction of the interband oscillator strength upon Ti dilution by Co and the extra absorption at E_1. However, this scenario leads not to a shift in the band edge but essentially to a change in the slope of α^2, contrary to observation. Therefore the O and Ti bands must separate upon Co substitution. The large rate of separation ($\xi = 5$ eV) implies strong level repulsion that might occur for interstitial incorporation of the Co. This large band edge shift is especially interesting because it implies strong interactions which are also required to provide the large exchange interaction and associated high ferromagnetic T_c observed in this material.[175]

5.5 Conclusions

Summarizing, Chap. 5 presents optical measurements in the spectral range $0.2 \leq \hbar\omega < 5$ eV on anatase $Ti_{1-x}Co_xO_{2-\delta}$ films. As-grown films doped at concentra-

tions $x > 0.02$ exhibit a limited Co solubility, as clearly demonstrated in TEM. However, optical measurements in the mid gap region find no evidence for absorption or scattering processes as predicted from either Maxwell-Garnet or Mie scattering theories. This suggests the TEM micrograph in Fig. 1.12 is not representative of clustering in these systems. Possible explanations include less metallic Co in the clusters or the average cluster size exceeds that shown in the micrograph. In low-doped films ($0 \leq x \leq 0.02$) exhibiting no clustering, optical measurements have revealed a shift of the band edge with Co doping and an absence of mid gap absorption. For well oxygenated films ($\delta \ll 1$) the optical conductivity is characterized by an absence of optical absorption below an onset of interband transitions at $3.6\,\text{eV}$ and a blue shift of the optical band edge with increasing Co concentration.

Current theoretical models predict mid gap magnetic impurity bands. Thus, the absence of below band gap absorption implies strong Coulomb interaction effects on the optical processes involving the Co ions. Furthermore, the origin of the observed blue shift remains puzzling. Changes in the lattice size with Co substitution suggest an additional mechanism must produce the observed shift. Identification of the mechanism responsible for modifying the band structure may provide insight towards understanding the unusually high T_c in Co-doped TiO_2.

Chapter 6

Conclusions

Strongly interacting electron systems offer wide-ranging phenomena of interest to condensed matter physics and potential applications in novel electronic devices. Magnetic transition metal oxides (TMO) represent archetypical strongly correlated systems. The optical studies presented in the preceding chapters focus on three such magnetic TMOs: the orthorhombic manganites including the parent compound $LaMnO_3$ and the hole-doped colossal magnetoresistant alloys, the multiferroic hexagonal manganite $LuMnO_3$, and the diluted magnetic oxide (DMO) Co-doped TiO_2. The experimental efforts concentrated on understanding the underlying physics of these systems through their response to light under varying experimental parameters, namely frequency, temperature, and electric field polarization.

6.1 Experimental Techniques

The measurements discussed herein employed a variety of spectroscopic methods to determine most accurately the optical properties of the investigated materials. Specifically, the measurements entailed extensive experience with FTIR spectroscopy and knowledge of the optical properties of elements utilized for beamsplitters, windows, polarizers, and filters from the far infrared to ultraviolet spectral range. Thin film samples required development and characterization of a technique to extract the optical constants by measuring both transmission and reflection and inverting the Fresnel coefficients.

Thin film samples offer several advantages over bulk samples. First, the numerical inversion technique extracts the complex optical conductivity at measured frequencies without the need for extrapolations required by the standard Kramers-Kronig (K-K) method. Furthermore, typical dimensions for films grown by pulsed laser deposition ($5 \times 5\,\mathrm{mm}^2$) exceed that of single crystal bulk samples. Large samples increase the signal to noise ratio, which is especially important in the far-infrared spectral range. In addition to a large surface area, films offer an optically flat surface area without requiring polishing.

While the thin film inversion process avoids extrapolation errors, determining the physically relevant roots from multiple solutions often proves difficult in practice. In contrast, K-K of bulk samples readily produces values for the optical constants. Furthermore, extracting optical constants from films requires both transmittance and reflectance measurements plus knowledge of the substrate optical constants, as opposed to only one quantity (reflectance) required for bulk samples. Finally, substrates opacity in the phonon frequency region limits the useful spectral range.

6.2 Orthorhombic Manganites

The hole-doped pseudocubic manganites, $R_{1-x}A_x\mathrm{MnO}_3$, exhibit a rich phase diagram that includes, in addition to colossal magnetoresistance (CMR), various types of magnetic, charge, and orbitally ordered phases. Temperature dependent optical conductivity studies of the parent compound LaMnO_3 reveal interesting properties in the electronic and phonon spectral regions. The strong correlation of the $2\,\mathrm{eV}$-feature spectral weight with T_N agrees with models considering this transition as a Mn-Mn *inter-site* charge-transfer transition, in contradiction with models considering the transition as on-site. In the far-infrared, several of the infrared active phonons exhibit temperature shifts of the transverse optical phonon frequencies that correlate with the antiferromagnetic ordering below T_N.

For the CMR manganites ($0.2 \leq x \leq 0.4$), a broad maximum near $1\,\text{eV}$ characterizes the infrared optical conductivity in the paramagnetic-insulating state of these materials. The transition red shifts and grows in optical oscillator strength as the temperature lowers into the ferromagnetic state, eventually transforming into a Drude-like response. This optical behavior is consistent with a crossover from activated small polaron transport in the paramagnetic state to itinerant conduction of a large polaron in the ferromagnetic ground state. The observed optical spectra and oscillator strength changes compare well with models that include both double exchange and the dynamic Jahn-Teller effect in the description of the electronic structure.

A Drude-model analysis of far-infrared transmission finds a T^2 temperature dependence of the scattering rate and an optical mass enhancement that exceeds specific heat results. The enhanced optical mass may result from charge ordering correlations. The presence of charge density waves at low temperatures suggests the competition of various types of ordering in the ferromagnetic metallic ground state. At higher energies, frequency-dependent scattering due to the strong electron-phonon coupling accounts for a majority of the IR spectral weight.

6.3 Hexagonal Manganites

Manganites with a small rare-earth ionic radius (*e.g.*, Lu) result in a hexagonal crystal structure and a multiferroic ground state in which ferroelectricity and antiferromagnetism occur simultaneously. The results reported here offer the first thorough optical study of $LuMnO_3$. The optical conductivity of this hexagonal manganite exhibits an *on-site* Mn d-d transition near $1.7\,\text{eV}$ allowed by the low crystalline symmetry. The transition peak energy blueshifts ($\approx 0.1\,\text{eV}$) in the antiferromagnetic state displaying an inflection point at T_N. In the far infrared, transverse optical phonon frequencies exhibit a similar temperature dependent anomaly arising from spin-phonon interaction effects. Further, these phonons overwhelmingly contribute to the known

temperature dependent anomaly below T_N of the quasi-static dielectric constant. The similarity of the frequency shift of the spin-coupled phonons and the temperature dependence of the 1.7 eV feature suggests that both are related to the same, nearest-neighbor spin correlation function.

Hexa-manganites exhibit similarities in the electronic spectrum with the orthorhombic manganites. Optical conductivity of both crystal structures reveals an O $2p$ to Mn $3d$ charge transfer transition above ≈ 4 eV. Additionally, a lower-lying Mn-Mn transition occurs in both manganite classes. However, the temperature dependence and underlying mechanism of the observed transitions differ. In $LuMnO_3$ the peak energy shifts with temperature while the spectral weight remains relatively constant, exactly the opposite occurs in $LaMnO_3$. Thus, while both low-lying electronic transitions are Mn-Mn, the transition is a symmetry allowed *on-site* in $LuMnO_3$ and a *inter-site* in $LaMnO_3$.

The optical properties of $LuMnO_3$ reported here contribute significantly to understanding the nature of coupling between magnetic and ferroelectric ordering in multiferroic materials. Moreover, the results demonstrate that optical spectroscopy provides a powerful tool in the study of exchange interaction effects in the strongly frustrated magnetic system of the hexagonal manganites.

6.4 Co-Doped Titanium Dioxide

Cobalt-doped titanium dioxide offers a promising new dilute magnetic system. The results presented here represent the first optical conductivity studies on thin films of anatase-phase $Ti_{1-x}Co_xO_{2-\delta}$. Optical measurements on higher doped samples ($x > 0.02$) with known cobalt solubility problems find no evidence for absorption or scattering processes in the mid gap region as predicted from either Maxwell-Garnet or Mie scattering theories. The discrepancy suggests either a lower concentration of metallic Co in clusters or a larger average cluster size than determined by TEM. The

optical conductivity on low-doped ($x \leq 0.02$) films reveals an absence of absorption below an onset of interband transitions at 3.6 eV and a blue shift of the band edge with increasing Co concentration. These observations remain inconsistent with theoretical models, which contain mid gap magnetic impurity bands, and suggest that strong on-site Coulomb interactions shift the O-band to Co-level optical transitions to energies above the gap. The large observed shift in the band edge with doping may provide insight towards understanding the unusually high T_c in these diluted magnetic oxide systems.

6.5 Future Work

The optical studies summarized above have provided insight into the physical mechanisms governing several strongly correlated TMO systems. However, fundamental questions still remain and further studies are required.

At low frequencies the near unity reflection of materials with metallic-like conductivity complicates accurate extraction of the optical constants. A novel technique to extract the conductivity of thin films in the far infrared by measuring the amplitude and phase of reflection and analyzing the frequency shift of the substrate étalon has been developed. Appendix B presents a description of the experimental method and preliminary results on metal films. The technique proves especially powerful for extracting the imaginary part of the conductivity, which appears squared in the reflectance and tends to zero with decreasing frequency.

The history of clustering in diluted magnetic semiconductors/oxides necessitates a technique for characterizing the intrinsic nature of the ferromagnetism. A recent study reports[176] observation of an anomalous Hall effect signals present in clustered rutile phase $Ti_{1-x}Co_xO_{2-\delta}$. Hence, other experimental methods such as electric field modulation of magnetism or magnetic circular dichroism (MCD) offer promise for ruling out clustering. An extension of the present optical studies on DMOs in-

volves developing magnetic circular dichroism (MCD) measurement capabilities. The project consists of the design, construction, and application of a broadband (1-5 eV) optical system to measure MCD in these materials. Sensitive heterodyne detection utilizing a photo-elastic polarization modulator and lock-in amplifiers measures the complex Faraday angle. A compact electromagnet produces moderate magnetic fields ($\gtrsim 1$ T) and an optical cryostat allows for temperature dependent measurements (4-425 K). The system affords field-dependent transmission and reflection measurements in both the Faraday and Voigt geometries. In addition to characterizing the intrinsic nature of the ferromagnetism, MCD measurements provide information regarding the band structure and electronic states important to understanding magnetic ordering in these novel systems.

Appendix A

Applications of Maxwell's Equations to Boundaries

A.1 Maxwell's Equations

A brief review of electrodynamics facilitates the derivation of Fresnel's coefficients at dielectric boundaries. Maxwell's equations of electrodynamics provide the necessary laws governing the interaction of light with matter. For linear isotropic media, the macroscopic Maxwell's equations (in cgs units) are given by

$$\left.\begin{aligned} \boldsymbol{\nabla}\cdot\boldsymbol{D} &= 4\pi\rho_{\text{ext}} \\ \boldsymbol{\nabla}\cdot\boldsymbol{B} &= 0 \\ \boldsymbol{\nabla}\times\boldsymbol{E} &= -\tfrac{1}{c}\tfrac{\partial}{\partial t}\boldsymbol{B} \\ \boldsymbol{\nabla}\times\boldsymbol{H} &= \tfrac{1}{c}\tfrac{\partial}{\partial t}\boldsymbol{D} + \tfrac{4\pi}{c}\boldsymbol{J} \end{aligned}\right\}, \tag{A.1}$$

where $\boldsymbol{E}$ and $\boldsymbol{H}$ are the electric and magnetic fields, ρ_{ext} denotes the free charge density, and $\boldsymbol{J}$ represents the current density. For isotropic media in the linear approximation, the electric displacement $\boldsymbol{D}$ and magnetic induction $\boldsymbol{B}$ are given in terms of $\boldsymbol{E}$ and $\boldsymbol{H}$ by

$$\left.\begin{aligned} \boldsymbol{D} &= \epsilon\,\boldsymbol{E} \\ \boldsymbol{B} &= \mu\,\boldsymbol{H} \end{aligned}\right\}, \tag{A.2}$$

where ϵ is the dielectric constant and μ is the magnetic permeability. Additionally, for conducting media Ohm's law relates the current density $\boldsymbol{J}$ to the electric field $\boldsymbol{E}$ through the conductivity σ,

$$\boldsymbol{J} = \sigma\,\boldsymbol{E}\,. \tag{A.3}$$

The solution to Eq. (A.1) for source-free media (*i.e.*, $\rho_{\rm ext} = 0$ and $\boldsymbol{J} = 0$) is a propagating electromagnetic plane wave with spatial and time dependence given by

$$\boldsymbol{E}(\boldsymbol{r}, t) = \boldsymbol{E}_0 \, \mathrm{e}^{\mathrm{i}(\boldsymbol{k}\cdot\boldsymbol{r} - \omega t)} \tag{A.4}$$

$$\boldsymbol{H}(\boldsymbol{r}, t) = \sqrt{\frac{\tilde{\epsilon}}{\tilde{\mu}}}\, \hat{\boldsymbol{k}} \times \boldsymbol{E}(\boldsymbol{r}, t) \equiv \frac{1}{\tilde{Z}} \hat{\boldsymbol{k}} \times \boldsymbol{E}(\boldsymbol{r}, t)\,, \tag{A.5}$$

where $\tilde{Z} = \sqrt{\frac{\mu}{\epsilon}}$ represents the complex impedance. For free space, $Z = 4\pi/c$ in cgs units and $Z = 377\,\Omega$ in MKS units. The interaction of propagating electromagnetic waves with boundaries between optical medium will be of prime importance in the remainder of this appendix.

A.2 Fresnel Coefficients

Consider first the case of a single boundary between optical media designated by 0 and 1. Figure A.1 shows a schematic representation of an electromagnetic wave incident from the left on the boundary between media with indices of refraction n_0 and n_1. For $n_0 \neq n_1$, the incident wave will experience both reflection and transmission from the interface. Solving for the relative magnitude of the transmission and reflection requires boundary conditions.

At the boundary, Maxwell's equations, Eq. (A.1), provides continuity of the normal D and B and the tangential E and H fields. Writing these conditions out explicitly for the boundary between media 0 and 1 gives

$$\left.\begin{aligned} \hat{\boldsymbol{n}} \cdot (\boldsymbol{D}_1 - \boldsymbol{D}_0) &= 4\pi\sigma \\ \hat{\boldsymbol{n}} \cdot (\boldsymbol{B}_1 - \boldsymbol{B}_0) &= 0 \\ \hat{\boldsymbol{n}} \times (\boldsymbol{E}_1 - \boldsymbol{E}_0) &= 0 \\ \hat{\boldsymbol{n}} \times (\boldsymbol{H}_1 - \boldsymbol{H}_0) &= \tfrac{4\pi}{c}\boldsymbol{K} \end{aligned}\right\}, \tag{A.6}$$

where $\hat{\boldsymbol{n}}$ represents the unit normal vector at the boundary and σ and $\boldsymbol{K}$ represents a surface charge density and a surface current density, respectively. In the case of

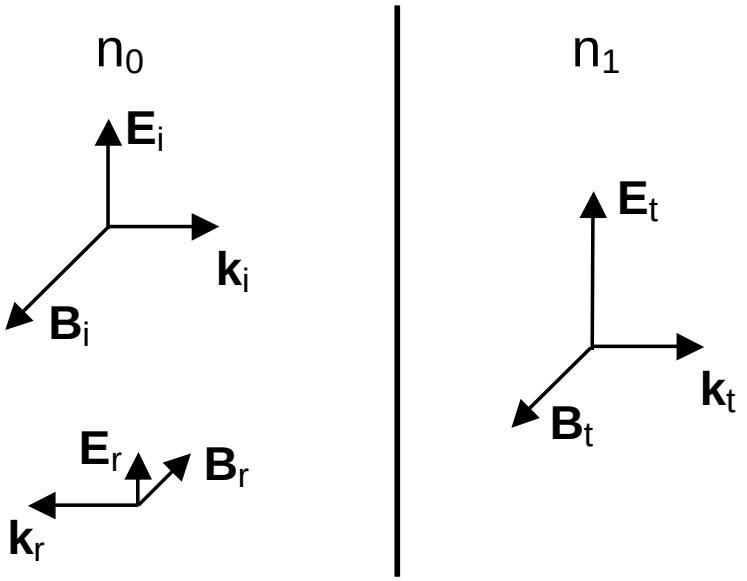

Figure A.1: Electromagnetic wave incident on a dielectric boundary between media with indices n_0 and n_1. Note here $n_0 > n_1$ so the reflected wave experiences no π phase shift of the electric field.

normally incident light with no surface charges or currents, consideration of only the tangential components results in the following simplified boundary conditions

$$E_i + E_r = E_t \tag{A.7}$$

$$H_i - H_r = H_t \rightarrow \frac{1}{\tilde{Z}_0}(E_i - E_r) = \frac{1}{\tilde{Z}_1}E_t\,, \tag{A.8}$$

where the right side of Eq. (A.8) utilizes the complex impedance $\tilde{Z}$.

Solving Eqs. (A.7) and (A.8) gives the Fresnel coefficients for the transmission t_{01} and reflection r_{01} of normally incident light on a plane boundary between two semi-infinite media with complex indexes of refraction $\tilde{n}_0$ and $\tilde{n}_1$. Here t_{01} (r_{01}) represent the amplitude ratio of the transmitted (reflected) to the incident electric field. The Fresnel coefficients are given by

$$t_{01} = \frac{E_t}{E_i} = \frac{2\tilde{Z}_0}{\tilde{Z}_0 + \tilde{Z}_1} \rightarrow \frac{2\tilde{n}_0}{\tilde{n}_0 + \tilde{n}_1} \tag{A.9}$$

$$r_{01} = \frac{E_r}{E_i} = \frac{\tilde{Z}_1 - \tilde{Z}_0}{\tilde{Z}_0 + \tilde{Z}_1} \rightarrow \frac{\tilde{n}_0 - \tilde{n}_1}{\tilde{n}_0 + \tilde{n}_1}\,, \tag{A.10}$$

where the subscripts 01 indicate light incident from medium 0 onto medium 1. Note that the equations are not mirror symmetric, $r_{ij} = -r_{j1}$ and $t_{ij} = n_i/n_j\, t_{ji}$. The right-hand sides of Eqs. (A.9) and (A.10) represent the result for $\mu = 1$. This condition is satisfied for most materials at frequencies from the far-infrared and above. This condition may be violated in the vicinity of weak magneto-dipole transitions (see anti-ferromagnetic resonance in Chap. 4).

The Fresnel coefficients represent the amplitude ratios of the transmitted and reflected E-fields to the incident E-field. Optical detectors typically measure intensity rather than amplitude. In this case, the transmittance $\mathcal{T}$ and reflectance $\mathcal{R}$ represent the ratio of the transmitted and reflected intensities to the incident intensity. The transmittance $\mathcal{T}$ and reflectance $\mathcal{R}$ are given by

$$\mathcal{T}_{01} = \frac{n_1}{n_0}\left|\frac{E_t}{E_i}\right|^2 = \frac{n_1}{n_0}\,|t_{01}|^2 = \frac{n_1}{n_0}\,\frac{4(n_0^2+\kappa_0^2)}{(n_0+n_1)^2+(\kappa_0+\kappa_1)^2} \tag{A.11}$$

$$\mathcal{R}_{01} = \left|\frac{E_r}{E_i}\right|^2 = |r_{01}|^2 = \frac{(n_0-n_1)^2+(\kappa_0-\kappa_1)^2}{(n_0+n_1)^2+(\kappa_0+\kappa_1)^2}\,. \tag{A.12}$$

Note the extra ratio of indexes in the formula for $\mathcal{T}$ necessary for energy conservation. The Poynting vector $\boldsymbol{S}$ gives the power in a given medium, $\boldsymbol{S} = c/(4\pi)\,\boldsymbol{E}\times\boldsymbol{H} = c/(4\pi)\,n\,|E|^2\,\hat{\boldsymbol{k}}$, and hence the additional factor of n.

A.3 Bounded Dielectric Slab

A Fabry-Pérot cavity consists of a slab of material of finite thickness d_1 with parallel edges and index of refraction $\tilde{n}_1$ bounded by two semi-infinite medium of indexes $\tilde{n}_0$ and $\tilde{n}_2$ respectively. In general, an incident electromagnetic wave will experience multiple reflections from the boundaries. Figure A.2 represents schematically the multiple passes in a slab with limited absorption. For each pass through the medium, the beam acquires a phase ϕ_1 given by

$$\phi_1 = 2\pi\,\tilde{n}_1\,\nu\,d_1\,, \tag{A.13}$$

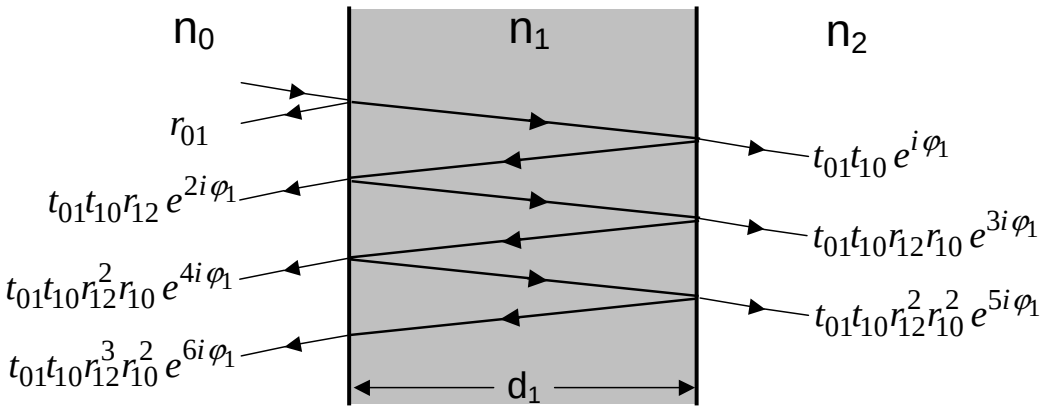

Figure A.2: Schematic view of Fabry-Perot resonant cavity illustrating the first few terms in the infinite series of multiple passes.

where $\nu = 1/\lambda$ is the frequency of the light in wavenumbers. The real part of ϕ_1 represents oscillations of the E-field while the imaginary part represents attenuation.

Adding the multiple passes in the cavity results in an infinite series of terms, which for the transmission amplitude is given by

$$\begin{aligned} t &= t_{01}t_{12}\mathrm{e}^{\mathrm{i}\phi_1} + t_{01}t_{12}r_{12}r_{10}\mathrm{e}^{3\mathrm{i}\phi_1} + t_{01}t_{12}r_{12}^2r_{10}^2\mathrm{e}^{5\mathrm{i}\phi_1} + \cdots \\ &= t_{01}t_{12}\mathrm{e}^{\mathrm{i}\phi_1}(1 + r_{12}r_{10}\mathrm{e}^{2\mathrm{i}\phi_1} + r_{12}^2r_{10}^2\mathrm{e}^{4\mathrm{i}\phi_1} + \cdots) \\ &= \frac{t_{01}t_{12}\mathrm{e}^{\mathrm{i}\phi_1}}{1 - r_{12}r_{10}\mathrm{e}^{2\mathrm{i}\phi_1}} \end{aligned} \tag{A.14}$$

and for the reflection amplitude is given by

$$\begin{aligned} r &= r_{01} + t_{01}t_{10}r_{12}\mathrm{e}^{2\mathrm{i}\phi_1} + t_{01}t_{10}r_{12}^2r_{10}\mathrm{e}^{4\mathrm{i}\phi_1} + t_{01}t_{10}r_{12}^3r_{10}^2\mathrm{e}^{6\mathrm{i}\phi_1} + \cdots \\ &= r_{01} + t_{01}t_{10}r_{12}\mathrm{e}^{2\mathrm{i}\phi_1}(1 + r_{12}r_{10}\mathrm{e}^{2\mathrm{i}\phi_1} + r_{12}^2r_{10}^2\mathrm{e}^{4\mathrm{i}\phi_1} + \cdots) \\ &= r_{01} + \frac{t_{01}t_{10}r_{12}\mathrm{e}^{2\mathrm{i}\phi_1}}{1 - r_{12}r_{10}\mathrm{e}^{2\mathrm{i}\phi_1}} = \frac{r_{01} + r_{12}\mathrm{e}^{2\mathrm{i}\phi_1}}{1 - r_{12}r_{10}\mathrm{e}^{2\mathrm{i}\phi_1}}\,. \end{aligned} \tag{A.15}$$

The last line in Eq. (A.15) results from the conservation of energy, $t_{01}t_{10} + r_{01}^2 = 1$. Intensities result from the amplitudes as before [see Eq. (A.11)], giving $\mathcal{T} = n_2/n_0\,|t|^2$ and $\mathcal{R} = |r|^2$.

In the typical case where the medium represents a slab of material (*e.g.*, a substrate for thin film growth), air comprises the surrounding media and thus $\tilde{n}_0 =$

$\tilde{n}_2 = n_{air} \approx 1$ and $r_{12} = r_{10} = -r_{01}$. In general, $\Im m\{\tilde{n}\} \neq 0$ and attenuation occurs in the slab. In this case, the Fresnel coefficients are complex $r_{10} \equiv r_{10}\,\mathrm{e}^{-\mathrm{i}\,\theta_1}$. The absorption coefficient α describes the attenuation per unit length and is given by Eq. (2.9). The resulting intensities from Eqs. (A.14) and (A.15) give for the transmittance

$$\begin{aligned}\mathcal{T} &= \left|\frac{t_{01}t_{12}\,\mathrm{e}^{\mathrm{i}\,\phi_1}}{1 - r_{10}^2\,\mathrm{e}^{2\mathrm{i}\,\phi_1}}\right|^2 \\ &= \frac{\mathcal{T}_{01}\mathcal{T}_{12}\mathrm{e}^{-\alpha_1 d_1}}{1 - 2\mathcal{R}_{10}\cos\left[2(\phi_1 + \theta_1)\right]\,\mathrm{e}^{-\alpha_1 d_1} + \mathcal{R}_{10}^2\mathrm{e}^{-2\alpha_1 d_1}}\end{aligned} \tag{A.16}$$

and for the reflectance

$$\begin{aligned}\mathcal{R} &= \left|r_{01} + \frac{t_{01}t_{10}r_{12}\,\mathrm{e}^{\mathrm{i}\,2\phi_1}}{1 - r_{10}^2\,\mathrm{e}^{2\mathrm{i}\,\phi_1}}\right|^2 = \left|\frac{r_{01}\left(1 - \mathrm{e}^{\mathrm{i}\,2\phi_1}\right)}{1 - r_{10}^2\,\mathrm{e}^{\mathrm{i}\,2\phi_1}}\right|^2 \\ &= \frac{\mathcal{R}_{01}\left[1 - 2\cos(2\phi_1)\,\mathrm{e}^{-\alpha_1 d_1} + \mathrm{e}^{-2\alpha_1 d_1}\right]}{1 - 2\mathcal{R}_{10}\cos\left[2(\phi_1 + \theta_1)\right]\,\mathrm{e}^{-\alpha_1 d_1} + \mathcal{R}_{10}^2\mathrm{e}^{-2\alpha_1 d_1}}\,.\end{aligned} \tag{A.17}$$

These values represent the intensity for the coherent addition of the multiple reflections illustrated in Fig. A.2. Note that the denominators of both $\mathcal{T}$ and $\mathcal{R}$ have an oscillatory term in frequency given by the phase. Peaks in the transmission occur whenever the phase ϕ is an integer multiple of π. The index at the m-th peak is given by

$$n_m = \frac{m}{2\,\nu_m\,d}\,, \tag{A.18}$$

where d is the slab thickness and ν_m is the frequency in cm^{-1} of the m-th peak. Of course to obtain n from this method requires knowledge of the order m of the phase. In principle when the étalon is measured in the far-IR sufficiently near $0\,\mathrm{cm}^{-1}$, m may be determined by extrapolating the data to zero frequency.

This technique is particularly well-suited for determining the index of refraction of materials to be used as substrates in thin film growth. Fitting the resulting transmission spectrum with a series of Lorentzians obtains the peak frequencies. Figure A.3 shows results for $SrLaGaO_4$. Transmittance data at room temperature is shown as circles and the series of Lorentzians are shown as the solid lines.

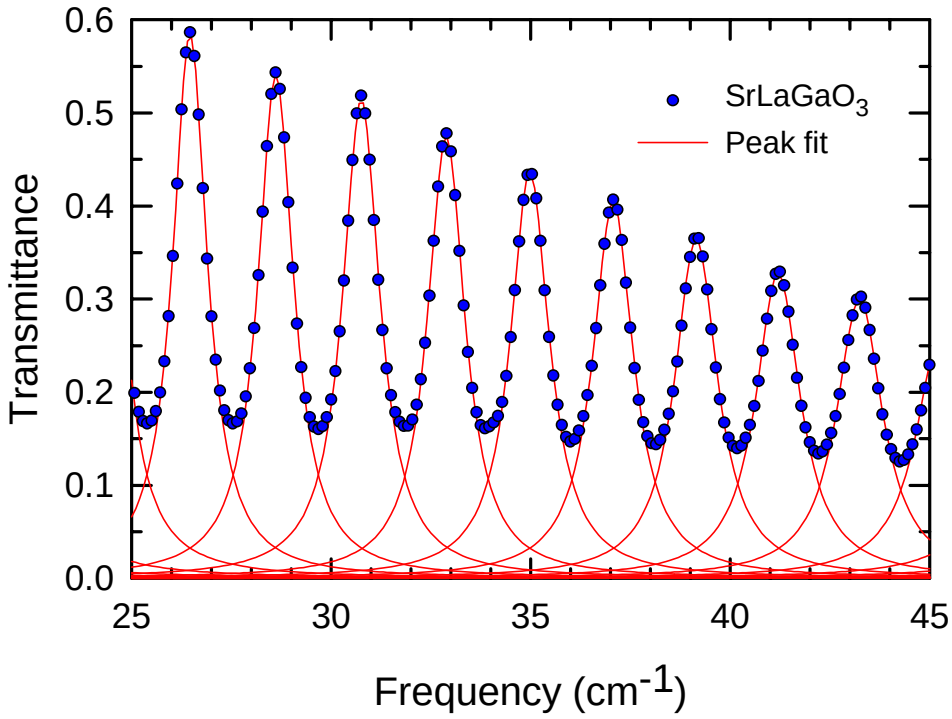

Figure A.3: Transmission étalon peaks of LSGO fit to Lorentzians.

Using the method described above together with Eq. (A.18), the far-IR indexes for several substrate materials are plotted in Fig. A.4. Data are for room temperature with the exception of $LaAlO_3$ which displays temperatures $294\,\mathrm{K}$ and $100\,\mathrm{K}$.

A.4 Coherent vs. Incoherent Addition

For optical measurements of thin films on relatively transparent substrates, the étalon behavior of the Fabry-Pérot cavity formed by the substrate is of little interest. Rearranging Eq. (A.18) gives the frequency difference between peaks. For typical substrates, $d \approx 0.05\,\mathrm{cm}$ and $n \approx 2$ in the infrared to visible frequency range. The corresponding frequency difference between étalon peaks is approximately $5\,\mathrm{cm}^{-1}$. The optical properties studied herein concern features broader than $5\,\mathrm{cm}^{-1}$ (with the exception of narrow phonon lines in the far-IR). Thus the substrate étalon behavior may be averaged.

Experimentally, restricting the scanning mirror travel in the FTIR spectrometer

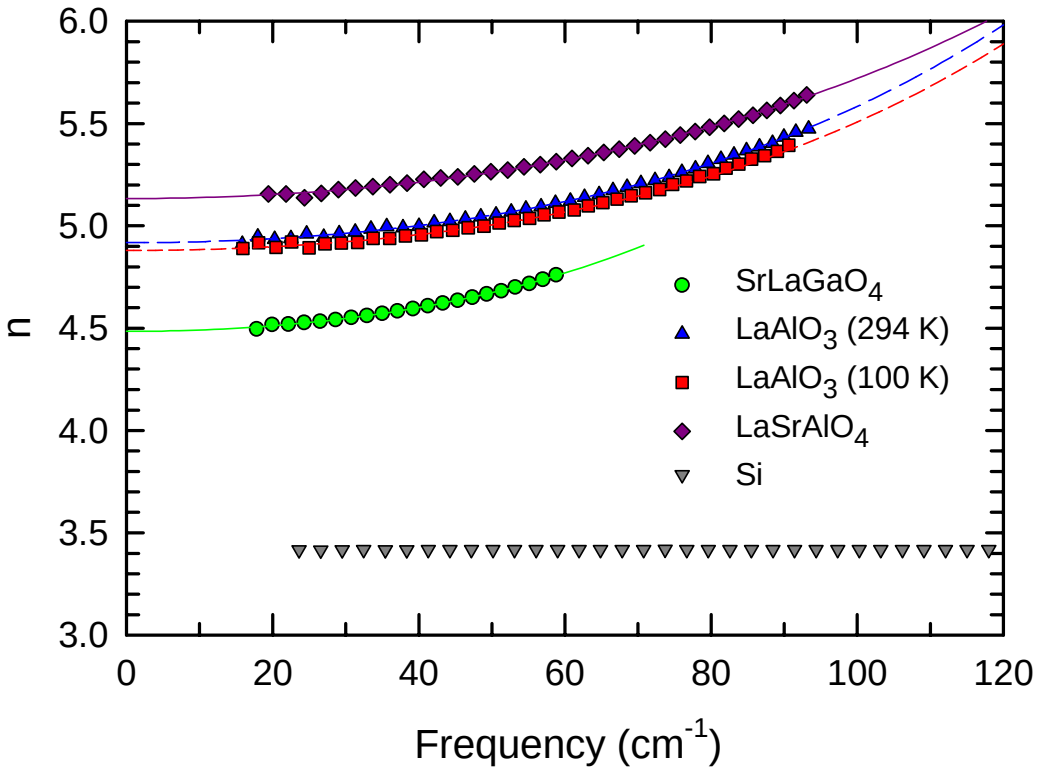

Figure A.4: Index of refraction for several common substrate materials obtained from étalon transmission peaks in the far-infrared.

to a distance $L < 0.1\,\text{cm}$ limits the resolution to $1/(2L) > 5\,\text{cm}^{-1}$ and effectively averages the substrate étalon. Extracting the film and substrate optical constants from this physically averaged spectrum requires a model that effectively averages the substrate étalon. In principle, a simple average of the $\mathcal{T}$ or $\mathcal{R}$ response over the frequency range $\Delta\nu$ should suffice. However, inversion of the $\mathcal{T}$ and $\mathcal{R}$ equations to obtain the optical coefficients already presents computational challenges.

A simpler model considers the incoherent addition of the multiple reflections in the slab, dropping the real part of the phase ϕ. Here the multiple passes are treated as a sum of the *intensities* of the Fresnel coefficients ($\mathcal{T}_{ij} = |t_{ij}|^2$ and $\mathcal{R}_{ij} = |r_{ij}|^2$) at

the boundaries. For incoherent addition, $\mathcal{T}$ and $\mathcal{R}$ are given by

$$\mathcal{T} = \frac{\mathcal{T}_{01}\mathcal{T}_{12}\,\mathrm{e}^{-\alpha_1 d_1}}{1-\mathcal{R}_{01}^2\,\mathrm{e}^{-2\alpha_1 d_1}} \tag{A.19}$$

$$\mathcal{R} = \mathcal{R}_{01} + \frac{\mathcal{T}_{01}\mathcal{T}_{10}\mathcal{R}_{12}\,\mathrm{e}^{-2\alpha_1 d_1}}{1-\mathcal{R}_{01}^2\,\mathrm{e}^{-2\alpha_1 d_1}}\,, \tag{A.20}$$

where the bounding media 0 and 2 are taken to be the same such that $\mathcal{R}_{01} = \mathcal{R}_{10} = \mathcal{R}_{12}$.

Questions regarding the rigorous nature of this simplified model naturally arise. In the limit of zero absorption and for a dispersionless index ($\kappa = 0$ and $n \neq n(\nu)$), the incoherent addition exactly represents an average over the étalon. For example, consider average transmittance over one étalon period (from m-th to $m+1$-th peak given by

$$\frac{1}{\pi}\int_{m\pi}^{(m+1)\pi} \frac{\mathcal{T}_{01}\mathcal{T}_{12}}{1-2\mathcal{R}_{01}\,\cos(2\phi)+\mathcal{R}_{01}^2}\,\mathrm{d}\phi = \frac{\mathcal{T}_{01}\mathcal{T}_{12}}{1-\mathcal{R}_{01}^2}\,. \tag{A.21}$$

Comparing with Eq. (A.19) for zero absorption (*i.e.*, $\alpha_1 = 0$), the incoherent addition exactly equals the average $\mathcal{T}$ over one étalon peak. When the restricted behavior of n is lifted, the incoherent addition no longer remains rigorously exact. However, the incoherent addition performs remarkable well in practice for finite absorption and dispersive n, provided neither has strong frequency dependence over an etalon spacing.

A.5 Thin Film on a Substrate

As a final boundary configuration, consider the case of a thin film on a substrate where both are potentially absorbing. Define the media numbering 0-3 from left to right as follows: the bounding media are 0 and 3, the film is 1, and the substrate is 2. The coherent transmittance and reflectance (intensities) are given by

$$\begin{aligned}\mathcal{T} &= |t|^2 = \left|\frac{t_{01}\,t_{12}\,t_{23}\,\mathrm{e}^{\mathrm{i}(\phi_1+\phi_2)}}{1+r_{01}\,r_{12}\,\mathrm{e}^{2\mathrm{i}\,\phi_1}+r_{01}\,r_{23}\,\mathrm{e}^{2\mathrm{i}(\phi_1+\phi_2)}+r_{12}\,r_{23}\,\mathrm{e}^{2\mathrm{i}\,\phi_2}}\right|^2 \\ \mathcal{R} &= |r|^2 = \left|\frac{r_{01}+r_{12}\,\mathrm{e}^{2\mathrm{i}\,\phi_1}+r_{23}\,\mathrm{e}^{2\mathrm{i}(\phi_1+\phi_2)}+r_{01}\,r_{12}\,r_{23}\,\mathrm{e}^{2\mathrm{i}\,\phi_2}}{1+r_{01}\,r_{12}\,\mathrm{e}^{2\mathrm{i}\,\phi_1}+r_{01}\,r_{23}\,\mathrm{e}^{2\mathrm{i}(\phi_1+\phi_2)}+r_{12}\,r_{23}\,\mathrm{e}^{2\mathrm{i}\,\phi_2}}\right|^2\end{aligned} \tag{A.22}$$

where the fresnel coefficients for $t_{j-1\,j}$ and $r_{j-1\,j}$ are given by Eqs. (A.9) and (A.10) and the phases ϕ_j are given by Eq. (A.13). Equation (A.22) results from consideration of multiple passes in both the film and the substrate by splitting the system into two successive stages.[86,177] First consider multiple passes in just the film to obtain Fresnel coefficients for the front surface of the substrate. Alternatively, these may be derived from the multi-layer treatment or by accounting for the complete multiple passes at once.

As for the case of the bounded slab, a simplified formula for $\mathcal{T}$ and $\mathcal{R}$ results for the film on substrate by considering incoherent addition in the substrate. Here the multiple passes are treated as a sum of the *intensities* of the Fresnel coefficients ($\mathcal{T}_j = |t_j|^2$ and $\mathcal{R}_j = |r_j|^2$) at the boundaries. The resulting film on substrate $\mathcal{T}$ and $\mathcal{R}$ considering incoherent substrate addition are

$$\begin{aligned} \mathcal{T} &= \frac{\mathcal{T}'\,\mathcal{T}_{23}\,\mathrm{e}^{-\alpha_2 d_2}}{1-\mathcal{R}''\,\mathcal{R}_{23}\,\mathrm{e}^{-\alpha_2 d_2}} \\ \mathcal{R} &= \mathcal{R}' + \frac{\mathcal{T}'\,\mathcal{T}''\,\mathrm{e}^{-2\alpha_2 d_2}}{1-\mathcal{R}''\,\mathcal{R}_{23}\,\mathrm{e}^{-\alpha_2 d_2}} \end{aligned} \tag{A.23}$$

where the primed and double primed $\mathcal{T}$ and $\mathcal{R}$ result from separate consideration of the coherent addition in the film,

$$\begin{aligned} \mathcal{T}' &= |t'|^2 = \left|\frac{t_{01}\,t_{12}\,\mathrm{e}^{\mathrm{i}\phi_1}}{1+r_{01}\,r_{12}\,\mathrm{e}^{2\mathrm{i}\phi_1}}\right|^2 \\ \mathcal{T}'' &= |t''|^2 = \left|\frac{(n_2/n_0)\,t_{01}\,t_{12}\,\mathrm{e}^{\mathrm{i}\phi_1}}{1+r_{01}\,r_{12}\,\mathrm{e}^{2\mathrm{i}\phi_1}}\right|^2 \\ \mathcal{R}' &= |r'|^2 = \left|\frac{-(r_{01}+r_{12}\,\mathrm{e}^{2\mathrm{i}\phi_1})}{1+r_{01}\,r_{12}\,\mathrm{e}^{2\mathrm{i}\phi_1}}\right|^2 \\ \mathcal{R}'' &= |r''|^2 = \left|\frac{-(r_{12}+r_{01}\,\mathrm{e}^{2\mathrm{i}\phi_1})}{1+r_{01}\,r_{12}\,\mathrm{e}^{2\mathrm{i}\phi_1}}\right|^2 . \end{aligned} \tag{A.24}$$

Note that the film coefficients depend on the traversal direction across the boundary, hence the primed and double-primed coefficients.

Extending this model to multilayer composite samples (beyond the film on substrate) becomes increasingly difficult. In this case the multilayer approach using prop-

agation matrices is more appropriate. Schmadel[178] and Jenkins[179] provide additional details regarding this technique.

Appendix B

Étalon Peak Shifts

For metallic films, the real part of the optical conductivity σ_1 dominates the low-frequency conductivity, while $\sigma_2/\sigma_1 \to 0$ with decreasing frequency. Moreover, both $\mathcal{T}$ and $\mathcal{R}$ depend linearly on σ_1 but quadratically on σ_2. The thin film transmittance formula, Eq. (3.4), illustrates this clearly. Thus, determining the imaginary part of the optical conductivity σ_2 in the far-infrared requires a sensitive measurement technique. The remainder of this appendix presents a novel technique to accurately determine σ_2 of thin films by measuring the phase shifts of the substrate étalon induced by the films.

B.1 Substrate Thickness Changes

To qualify the experimental technique and establish the sensitivity, first consider the shift of étalon peaks of a substrate upon changing the thickness. Shifts of the étalon peaks with frequency determine the change in thickness. Let d' represent the new thickness, $d' = d + \Delta d$. If the substrate material has been removed (*e.g.*, by polishing) then $\Delta d < 0$. From Eq. (A.18) the new frequency of the m-th peak ν'_m is given by

$$\nu'_m = \nu + \Delta\nu_m = \frac{m}{2\,n'_m(d+\Delta d)} \approx \frac{m}{2\,n\,d}\left(1 - \frac{\Delta d}{d}\right) = \nu_m\left(1 - \frac{\Delta d}{d}\right), \tag{B.1}$$

where $\Delta d/d \ll 1$ satisfies the approximation. In this case the relative shift of the peaks will be equal to negative the relative change in the thickness

$$\frac{\Delta\nu}{\nu} = -\frac{\Delta d}{d}\,. \tag{B.2}$$

Figure B.1 shows peak shifts versus frequency for two different silicon substrates with differing Δd. The inset shows the raw transmittance data for the Si substrates

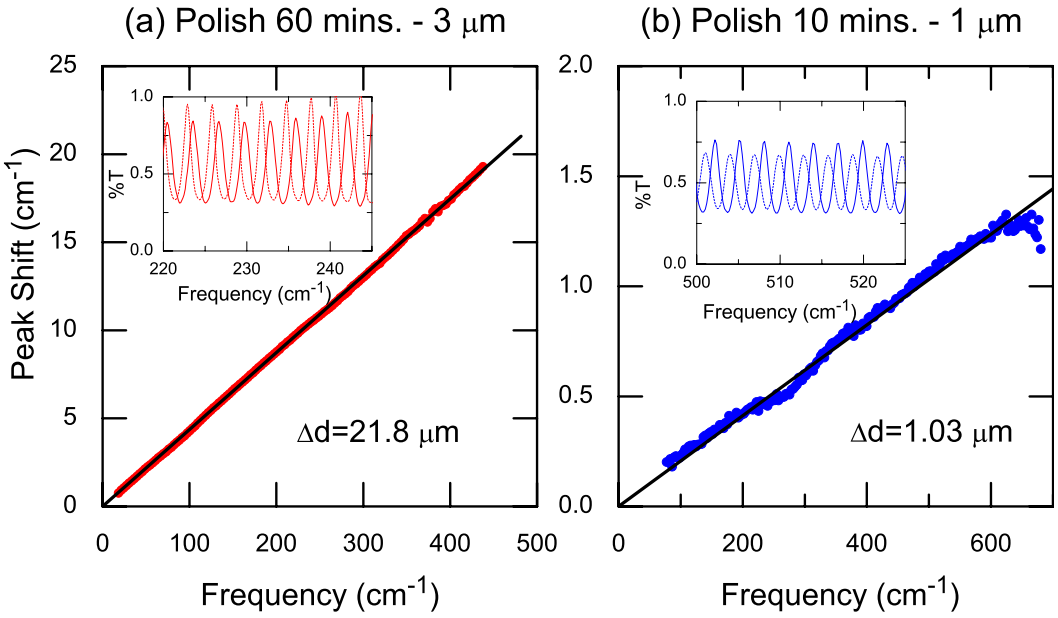

Figure B.1: Étalon peak shifts as a function of frequency for polished Si substrates with different polishing configurations: (a) $3\,\mu$m diamond paste for 60 minutes. (b) $1\,\mu$m for 10 minutes. Insets show transmittance data of polished (solid line) and unpolished (dashed line) substrates over a limited frequency window.

before (dashed curve) and after (solid curve) polishing. A Buehler Minimet automatic polisher (described in detail in Chap. 2) reduced the substrate thickness using constant applied pressure with (a) $3\,\mu$m diamond paste for 60 minutes and (b) $1\,\mu$m diamond paste for 10 minutes. The peak shifts exhibit linear dependence with frequency in accord with Eq. (B.2). Linear fits together with a knowledge of the original substrate thickness $d \approx 500\,\mu$m provide an accurate determination of the change in thickness Δd from polishing. The absolute experimental accuracy is better than $0.05\,\text{cm}^{-1}$ throughout the measurement range. This corresponds to a maximum sensitivity of roughly $1:10^4$.

B.2 Thin Film on Transparent Substrate

Next, consider a very thin conducting film on a non-absorbing substrate. In the far-infrared where the film thickness t is much less than the skin-depth, $t \ll \delta = \lambda/(4\pi k)$, the film may be represented as an infinitely thin conducting sheet. The usual boundary conditions, Eq. (A.6), at the n_0-film and film-n_1 interfaces give continuity in the tangential E-field and the jump in the tangential H-field due to the sheet conductance. These two boundary conditions result in two equations relating the incident, transmitted, and reflected electric fields

$$E_i + E_r = E_t \tag{B.3}$$

$$n_0 E_i - n_0 E_r = (n_1 + \tilde{y}) E_t , \tag{B.4}$$

where $\tilde{y} = Z_0 \tilde{\sigma} t$. Solving these equations gives the Fresnel coefficients for transmission and reflection amplitude ratios

$$t = \frac{E_t}{E_i} = \frac{2n_0}{n_0 + n_1 + \tilde{y}} \tag{B.5}$$

$$r = \frac{E_r}{E_i} = \frac{n_0 - n_1 - \tilde{y}}{n_0 + n_1 + \tilde{y}} . \tag{B.6}$$

Notice that for $n_0 > n_1$, there exists the possibility of zero reflection from the interface if $\tilde{y} = n_0 - n_1$. The film then serves as an anti-reflection (AR) coating. AR coatings are particular useful for removing often undesirable étalon in optical elements. In this case, the coating should be deposited such that $R_\square = Z_0/(n_0 - n_1)$, where $R_\square$ is the sheet resistance of the film.

For a thin film on a substrate bounded by air, $n_0 = n_2 = 1$ and $n_1 = n_s$. The ratio of the transmitted and reflected to incident intensity, denoted by $\mathcal{T}$ and $\mathcal{R}$, respectively, are then

$$\mathcal{T} = \frac{n_1}{n_0} \left| \frac{2\, n_0}{n_0 + n_1 + \tilde{y}} \right|^2 = \frac{4\, n_1\, n_0}{(n_0 + n_1 + Z_0\, \sigma_1\, t)^2 + (Z_0\, \sigma_2\, t)^2} \tag{B.7}$$

$$\mathcal{R} = \left| \frac{n_0 - n_1 - \tilde{y}}{n_0 + n_1 + \tilde{y}} \right|^2 = \frac{(n_0 - n_1 - Z_0\, \sigma_1\, t)^2 + (Z_0\, \sigma_2\, t)^2}{(n_0 + n_1 + Z_0\, \sigma_1\, t)^2 + (Z_0\, \sigma_2\, t)^2} . \tag{B.8}$$

For non-absorbing substrates of finite thickness, the incident light will reach the back surface. Here an expression for the ratio of the film-substrate configuration to the bare substrate may be obtained. The resulting thin-film transmittance of the film/substrate combination is given by Eq. (3.4).

The thin-film transmittance formula ignores étalon effects in the substrate. For the absorbing film, the coefficient for reflection from the substrate-film surface r_{10} becomes complex and is now given by Eq. (B.6), $r_{10} = r$. Rewriting the complex substrate-film reflection coefficient

$$\tilde{r}_{10} = \rho\, \mathrm{e}^{2\,\mathrm{i}\,\theta}\,, \tag{B.9}$$

where $2\,\theta$ denotes the phase, makes obvious the additional phase factor contributing in the denominator of $\mathcal{T}$ in Eq. (B.7). This phase factor will be given by $2\,\theta = \tan^{-1}\left(\Im m\{\tilde{r}_{10}\}/\Re e\{\tilde{r}_{10}\}\right)$.

For metallic, or semi-metallic, films in the far-infrared, $\tilde{y} = Z_0\,\tilde{\sigma}\,t \gg n - 1$. Rewriting Eq. (B.6) and expanding in the small parameter $(n/\tilde{y})$ gives

$$\begin{aligned} r &= \frac{-1 - \dfrac{(1-n)}{\tilde{y}}}{1 + \dfrac{n+1}{\tilde{y}}} \\ &\approx -\left(1 + \frac{1-n}{\tilde{y}}\right)\left(1 - \frac{n+1}{\tilde{y}}\right) = -\left[1 - \frac{2n}{\tilde{y}} + \mathcal{O}\left(\frac{n}{\tilde{y}}\right)^2\right] \\ &\approx -\mathrm{e}^{-2\,n/\tilde{y}} = \mathrm{e}^{-2\,n\,\Re e\{1/\tilde{y}\}}\,\mathrm{e}^{\mathrm{i}(\pi\,-\,2\,n\,\Im m\{1/\tilde{y}\})} \end{aligned} \tag{B.10}$$

The additional phase factor θ resulting from the very thin film is proportional to the $\Im m\{1/\sigma\}$. Specifically,

$$2\,\theta = \pi - \frac{2\,n}{Z_0\,t}\,\Im m\{1/\tilde{\sigma}\}\,. \tag{B.11}$$

The Drude conductivity model well-describes the far-IR conductivity of metals,

$$\tilde{\sigma}_{\text{Drude}} = \frac{N\,e^2/m^*}{\gamma^* - \mathrm{i}\omega} = \frac{1}{4\,\pi}\,\frac{\omega_p^{*\,2}}{\gamma^* - \mathrm{i}\,\omega} \tag{B.12}$$

where N is the number density of electrons, m^* is the effective mass, e is the electronic charge, γ^* is the effective scattering rate, and ω_p^{*2} is the effective plasma frequency.

Taking the imaginary part of the inverse Drude conductivity in Eq. (B.12) gives

$$\Im m\{1/\sigma_{\text{Drude}}\} = -\frac{m^*}{N\,e^2}\,\omega. \tag{B.13}$$

Hence the additional phase factor θ is directly proportional to the effective mass m^*. Both the additional phase θ resulting from the metal film and the regular étalon phase ϕ of the substrate are directly proportional to frequency. Therefore θ manifests itself as a shift of the étalon peak position that increases with frequency.

B.3 Antimony Film on Silicon

Evaluating the technique requires an appropriate sample material. The semimetal antimony serves as good test case having a conductivity similar to metallic transition metal oxides, *e.g.*, the hole-doped pseudocubic manganites. The DA3 spectrometer (described in detail in Chap. 2) measures high-resolution ($\approx 0.1\,\text{cm}^{-1}$) reflectance of the substrate-film relative to an aluminum mirror. Figure B.2 shows the raw reflectance of the antimony film (red circles) on the backside of a silicon substrate. The reflectance of the bare silicon substrate is shown (blue circles) for comparison. Note that the valleys in reflectance show the sharpest finesse. The curves shown in Fig. B.2 represent signal averaging of several hours. Transmission of the film/substrate combination exhibits similar étalon shifts. However, the decreased signal in transmission mode, owing to the large σ_1 of the film, greatly reduces the signal to noise ratio. The antimony film shown here was deposited using thermal vapor deposition to a thickness $t \approx 644\,\text{Å}$ and with a sheet resistance $R_\square \approx 12\,\Omega$.

Shifts of the étalon arising from the imaginary part of the film conductivity in addition to the π phase shift are determined by fitting the reflectance valleys with inverted Lorentzians. The constant π-phase shift [see Eq. (B.11)] of the metallic

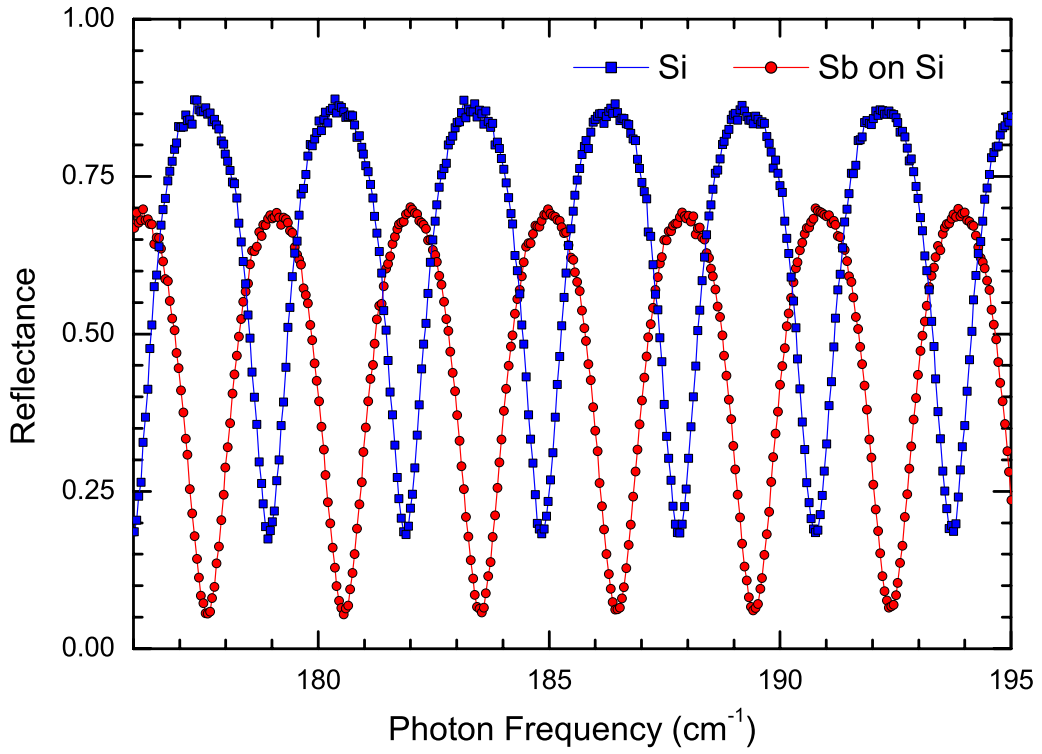

Figure B.2: Raw reflectance of antimony film on silicon. Reflectance of bare silicon substrate shown for comparison.

film is effectively subtracted out by averaging adjacent valleys in the bare substrate traces. Figure B.3 shows the additional shift of the reflectance minima of the Sb film relative to the silicon substrate. Circles represent the shift at a given valley in the reflectance spectrum. The solid line represents a linear fit assuming the Drude conductivity of Eq. (B.12). The slope of the linear curve provides an estimate for the free carrier plasma frequency ω_p^* or mass enhancement m^* given by Eq. (B.13). From the linear least-squares fit, $\omega_p^* = 1.791$ eV. This result is slightly higher than that estimated from Drude fits to the low-resolution thin-film transmittance.

The Fermi surface of semi-metallic antimony appears complicated. Both the valence and conduction bands cross the Fermi surface, which consists of both electron and hole like pockets. Moreover, these pockets display a strong anisotropy. Nevertheless, band structure calculations[180] for the carrier density agree well with

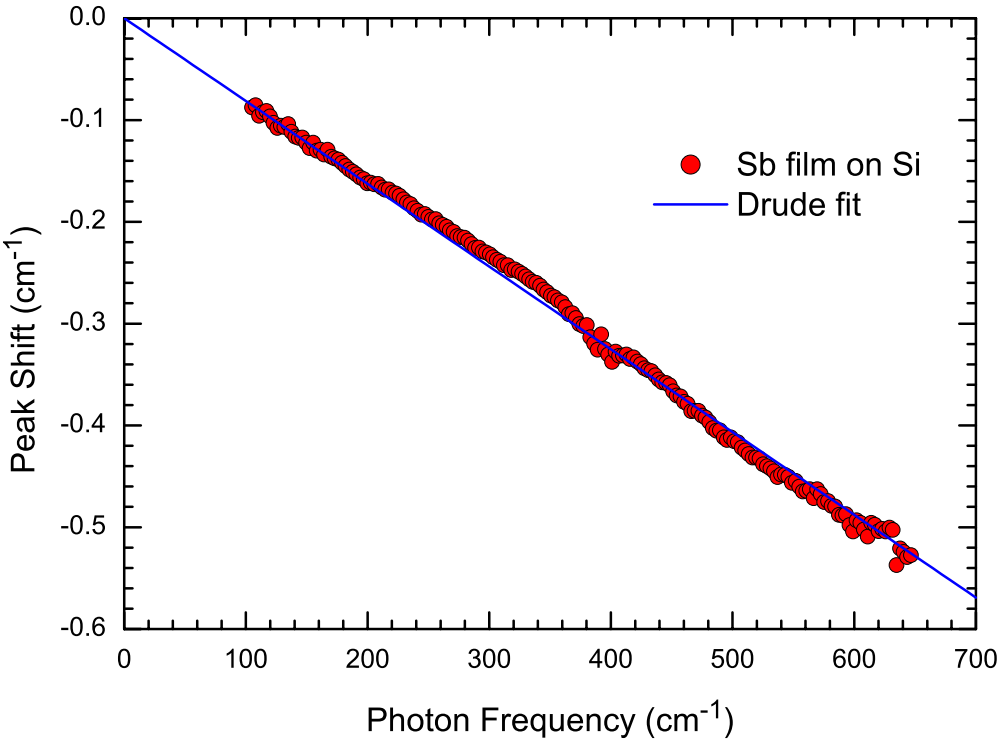

Figure B.3: Shifts of the reflectance minima for Sb film.

reported[181] experimental values. Liu and Allen calculate[180] $N \approx 5\times10^{20}$ cm^{-3} for both electrons and holes. Taking this value together with ω_p^* obtained from the étalon peak shifts provides an average mass enhancement relative to the free electron mass of $m^*/m_e \approx 0.043$, smaller than values from cyclotron resonance[182] by approximately a factor of two. The exact nature of this discrepancy remains unknown at present.

Bibliography

[1] J. G. Bednorz and K. A. Muller, Z. Phys. B **64**, 189 (1986).

[2] C. N. R. Rao and B. Raveau, *Transition Metal Oxides* (VCH Publishers, New York, 1995).

[3] A. J. Millis, Nature **392**, 147 (1998).

[4] S. A. Wolf, D. D. Awschalom, R. A. Buhrman, J. M. Daughton, S. von Molnár, M. L. Roukes, A. Y. Chtchelkanova, and D. M. Treger, Science **294**, 1488 (2001).

[5] G. E. Moore, Electronics **38** (1965).

[6] Data prior to 2000 from Ref. 7. Recent data represents an approximate storage capacity of the high end 5.25 in. hard drives offered by several major manufacturers.

[7] T. Claasen, Semiconductor International **July 1** (1998).

[8] G. A. Prinz, Science **282**, 1660 (1998).

[9] M. N. Baibich, J. M. Broto, A. Fert, F. Nguyen Van Dau, f. Petroff, P. Eitenne, G. Creuzet, A. Friederich, and J. Chazelas, Phys. Rev. Lett. **61**, 2472 (1998).

[10] D. D. Awschalom and R. K. Kawakami, Nature **408**, 923 (2000).

[11] H. Ohno, D. Chiba, F. Matsukura, T. Omiya, E. Abe, T. Dietl, Y. Ohno, and K. Ohtani, Nature **408**, 944 (2000).

[12] N. Hur, S. Park, P. A. Sharma, J. S. Ahn, S. Guha, and S-W. Cheong, Nature **429**, 392 (2004).

[13] A. J. Millis, J. Electron Spectrosc. Relat. Phenom. **114-116**, 669 (2001).

[14] R. D. Shannon, Acta Cryst. **A32**, 751 (1976).

[15] R. M. Kusters, J. Singleton, D. A. Keen, R. Mcgreevy, and W. Hayes, Physica B **155**, 362 (1989).

[16] R. Von Helmholt, J. Wecker, B. Holzapfel, L. Schultz, and K. Samwer, Phys. Rev. Lett. **71**, 2331 (1993).

[17] K. I. Chahara, T. Ohno, M. Kasai, and Y. Kozono, Appl. Phys. Lett. **63**, 1990 (1993).

[18] S. Jin, T. H. Tiefel, M. McCormack, R. A. Fastnacht, R. Ramesh, and L. H. Chen, Science **264**, 413 (1994).

[19] H. L. Ju, C. Kwon, Qi Li, R. L. Greene, and T. Venkatesan, Appl. Phys. Lett. **65**, 2108 (1994).

[20] P. Schiffer, A. P. Ramirez, W. Bao, and S.-W. Cheong, Phys. Rev. Lett. **75**, 3336 (1995).

[21] Y. Murakami, J. P. Hill, D. Gibbs, M. Blume, I. Koyama, M. Tanaka, H. Kawata, T. Arima, and Y. Tokura, Phys. Rev. B **81**, 582 (1998).

[22] A. M. Glazer, Acta Cryst. B **28**, 3384 (1972).

[23] Y. Tokura, editor, *Colossal Mangenetoresistive Oxides* (Gordon and Breach Science Publishers, The Netherlands, 2000).

[24] H. Sawada, Y. Morikawa, K. Terakura, and N. Hamada, Phys. Rev. B **56**, 12154 (1997).

[25] C. Zener, Phys. Rev. B **82**, 403 (1951).

[26] P. W. Anderson and H. Hasegawa, Phys. Rev. **100**, 675 (1955).

[27] M. Quijada, J. Černe, J. R. Simpson, H. D. Drew, K. H. Ahn, A. J. Millis, R. Shreekala, R. Ramesh, M. Rajeswari, and T. Venkatesan, Phys. Rev. B **58**, 16093 (1998).

[28] S. Kaplan, M. Quijada, H. D. Drew, D. B. Tanner, G. C. Xiong, R. Rames, C. Kwon, and T. Venkatesan, Phys. Rev. Lett. **77**, 2081 (1996).

[29] S. J. L. Billinge, R. G. DiFrancesco, G. H. Kwei, J. J. Neumeier, and J. D. Thompson, Phys. Rev. Lett. **77**, 715 (1996).

[30] A. J. Millis, Boris I. Shraiman, and R. Mueller, Phys. Rev. Lett. **74**, 5144 (1995).

[31] A. J. Millis, Boris I. Shraiman, and R. Mueller, Phys. Rev. Lett. **77**, 175 (1996).

[32] A. J. Millis, Boris I. Shraiman, and R. Mueller, Phys. Rev. B **54**, 5389 (1996).

[33] H. R. Roder, Jun Zang, and A. R. Bishop, Phys. Rev. Lett. **76**, 1356 (1996).

[34] G. D. Mahan, *Many-Particle Physics* (Plenum Press, New York, 1981), Chap 4.

[35] David Emin, Phys. Rev. B **48**, 13691 (1993).

[36] K. H. Kim, J. Y. Gu, E. J. Choi, G. W. Park, and T. W. Noh, Phys. Rev. Lett. **77**, 1877 (1996).

[37] A. Asamitsu, Y. Moritomo, Y. Tomioka, T. Arima, and Y. Tokura, Nature (London) **373**, 407 (1995).

[38] M. Jaime, M. B. Salamon, K. Pettit, M. Rubinstein, R. E. Treece, J. S. Horwitz, and D. B. Chrisey, Appl. Phys. Lett. **68**, 1576 (1996).

[39] J. H. Jung, K. H. Kim, T. W. Noh, E. J. Choi, and J. Yu, Phys. Rev. B **57**, 11043 (1998).

[40] M. Quijada, J. R. Simpson, L. Vasiliu-Doloc, J. W. Lynn, H. D. Drew, Y. M. Mukovskii, and S. G. Karabashev, Phys. Rev. B **64**, 224426 (2001).

[41] I. Solovyev, N. Hamada, and K. Terakura, Phys. Rev. B **53**, 7158 (1996).

[42] Y. Okimoto, T. Katsufuji, T. Ishikawa, A. Urushibara, T. Arima, and Y. Tokura, Phys. Rev. Lett. **75**, 109 (1995).

[43] Y. Okimoto, T. Katsufuji, T. Ishikawa, T. Arima, and Y. Tokura, Phys. Rev. B **55**, 4206 (1997).

[44] T. Arima, Y. Tokura, and J. B. Torrance, Phys. Rev. B **48**, 17006 (1993).

[45] G. A. Smolenskii and I. E. Chupis, Usp. Fiz. Nauk **136-138**, 415 (1982), [Sov. Phys. Usp. **25**, 475 (1982)].

[46] The T_c here refers to the ordering of electric moments and should not be confused with the Curie temperature for the ordering of magnetic moments. Whether T_c refers to ferroelectric or ferromagnetic ordering will be clear from the context.

[47] T. Kimura, T. Goto, H. Shintani, K. Ishizaka, T. Arima, and Y. Tokura, Nature **426**, 55 (2003).

[48] E. F. Bertaut and M. Mercier, Phys. Lett. **5**, 27 (1963).

[49] B. B. van Aken, A. Meetsma, and T. T. M. Palstra, Acta. Cryst. E **57**, 101 (2001).

[50] T. Katsufuji, M. Masaki, A. Machida, M. Moritomo, K. Kato, E. Nishibori, M. Takata, M. Sakata, K. Ohoyama, K. Kitazawa, and H. Takagi, Phys. Rev. B **66**, 134434 (2002).

[51] A. Munoz, J. A. Alonso, M. J. Martinez-Lope, M. T. Casais, J. L. Martinez, and M. T. Fernandez-Diaz, Phys. Rev. B **62**, 9498 (2000).

[52] M. Fiebig, D. Fröhlich, K. Kohn, S. Leute, T. Lottermoser, V. V. Pavlov, and R. V. Pisarev, Phys. Rev. Lett. **84**, 5620 (2000).

[53] T. Katsufuji, S. Mori, M. Masaki, Y. Moritomo, N. Yamamoto, and H. Takagi, Phys. Rev. B **64**, 104419 (2001).

[54] Z. J. Huang, Y. Cao, Y. Y. Sun, Y. Y. Xue, and C. W. Chu, Phys. Rev. B **56**, 2623 (1997).

[55] D. G. Tomuta, S. Ramakrishnan, G. J. Nieuwenhuys, and J. A. Mydosh, J. Phys. Condens. Matter **13**, 4543 (2001).

[56] N. Iwata and K. Kohn, J. Phys. Soc. Jpn. **67**, 3318 (1998).

[57] C. Zhong and Q. Jiang, J. Phys.: Condens. Matter **14**, 8605 (2002).

[58] H. Ohno, Science **281**, 951 (1998).

[59] M. A. Ruderman and C. Kittel, Phys. Rev. **96**, 99 (1954).

[60] B. Lee, T. Jungwirth, and A. H. MacDonald, Phys. Rev. B **61**, 15606 (2000).

[61] J. König, H. H. Lin, and A. H. MacDonald, Phys. Rev. Lett. **84**, 5628 (2000).

[62] H. Akai, Phys. Rev. Lett. **81**, 3002 (1998).

[63] J. Inoue, S. Nonoyama, and H. Itoh, Phys. Rev. Lett. **85**, 4610 (2000).

[64] T. Dietl, H. Ohno, F. Matsukura, J. Cibert, and D. Ferrand, Science **287**, 1019 (2000).

[65] Y. Matsumoto, M. Murakami, T. Shono, T. Hasegawa, T. Fukumura, M. Kawasaki, P. Ahmet, T. Chikyow, S. Koshihara, and H. Koinuma, Science **291**, 854 (2001).

[66] S. R. Shinde, S. B. Ogale, S. Das Sarma, J. R. Simpson, H. D. Drew, S. E. Lofland, C. Lanci, J. P. Buban, N. D. Browning, V. N. Kulkarni, J. Higgins, R. P. Sharma, R. L. Greene, and T. Venkatesan, Phys. Rev. B **67**, 115211 (2003).

[67] S. A. Chambers, S. Thevuthasan, R. F. C. Farrow, R. F. Marks, J. U. Thiele, L. Folks, M. G. Samant, A. J. Kellock, N. Ruzycki, D. L. Ederer, and U. Diebold, Appl. Phys. Lett. **79**, 3467 (2001).

[68] M. S. Park, S. K. Kwon, and B. I. Min, Phys. Rev. B **65**, R161201 (2002).

[69] P. B. Fellgett, J. Phys. Radium **92**, 197 (1958).

[70] P. Jacquinot, Appl. Opt. **8**, 497 (1967).

[71] G. Gruner, editor, *Millimeter and Submillimeter Wave Spectroscopy of Solids* (Springer-Verlag, Berlin, 1998), Chap. 5.

[72] A. A. Michelson, Amer. J. Sci **22**, 3 (1881).

[73] M. L. Forman, J. Opt. Soc. Am. **56**, 978 (1966).

[74] R. H. Norton and R. Beer, Journal of the Optical Society of America **66**, 259 (1976).

[75] G. W. Chantry, *Long-wave Optics: The Science and Technology of Infrared and Near-millimetre Waves* (Academic Press Inc., London, 1984).

[76] *Spectrometer System Manual* (Bomem, Québec, 1991).

[77] *PCDA Software User's Guide Rev. 1.1* (Bomem, Québec, 1993).

[78] D. C. Schmadel, A. B. Sushkov, and H. D. Drew, (private communication).

[79] N. W. Aschcroft and N. D. Mermin, *Solid State Physics* (Saunders College Publishing, New York, 1976).

[80] F. Wooten, *Optical Properties of Solids* (Academic Press, New York, 1972).

[81] H. D. Drew and P. Coleman, Phys. Rev. Lett. **78**, 1572 (1997).

[82] J. M. Ziman, *Principles of the Theory of Solids* (Cambridge University Press, Cambridge, 1972).

[83] J. D. Jackson, *Classical Electrodynamics, 2nd Edition* (John Wiley and Sons, New York, 1975).

[84] Jr. A. S. Barker, Phys. Rev. **136**, 1290 (1964).

[85] F. Gervais and B. Piriou, J. Phys. C: Solid State Phys. **7**, 2374 (1974).

[86] O. S. Heavens, *Optical Properties of Thin Solid Films* (Dover Publications Inc., New York, 1991), Chap. 4.

[87] P. B. Allen and V. Perebeinos, Phys. Rev. Lett. **83**, 4828 (1999).

[88] K.Takenaka, K.Iida, Y.Sawaki, S.Sugai, Y.Moritomo, and A.Nakamura, J. Phys. Soc. Jpn. **68**, 1828 (1999).

[89] Far-IR measurements performed on a Bruker IFS 113v spectrometer and higher frequency IR to UV measurements performed on a Bomem DA3 spectrometer.

[90] K. Tobe, T. Kimura, Y. Okimoto, and Y. Tokura, Phys. Rev. B **64**, 184421 (2001).

[91] N. N. Kovaleva an A. V. Boris, C. Bernhard, A. Kulakov, A. Pimenov, A. M. Balbashov, G. Khaliullin, and B. Keimer, Phys. Rev. Lett. **93**, 147204 (2004).

[92] M. N. Iliev, M. V. Abrashev, H.-G. Lee, V. N. Popov, Y. Y. Sun, C. Thomsen, R. L. Meng, and C. W. Chu, Phys. Rev. B **57**, 2872 (1998).

[93] A. Paolone, P. Roy, A. Pimenov, A. Loidl, O. K. Mel'nikov, and A. Y. Shapiro, Phys. Rev. B **61**, 11255 (2000).

[94] I. S. Smirnova, Physica B **262**, 247 (1999).

[95] J. Rodgríguez-Carvajal, M. Hennion, F. Moussa, A. H. Moudden, L. Pinsard, and A. Revoclevschi, Phys. Rev. B **57**, 3189 (1998).

[96] V. B. Podobedov, A. Weber, D. B. Romero, J. P. Rice, and H. D. Drew, Phys. Rev. B **58**, 43 (1998).

[97] D. B. Romero, Y. Moritomo, J. F. Mitchell, and H. D. Drew, Phys. Rev. B **63**, 123404 (2001).

[98] L. Martín-Carrón and A. de Andrés, Phys. Rev. Lett. **92**, 175501 (2004).

[99] K. H. Ahn and A. J. Millis, Phys. Rev. B **61**, 13545 (2000).

[100] K. H. Ahn and A. J. Millis, Phys. Rev. B **63**, 209902(E) (2001).

[101] A. J. Millis (private communication).

[102] A. Takahashi and H. Shiba, Eur. Phys. J. B. **5**, 413 (1998).

[103] G. C. Xiong, Q. Li, H. L. Ju, S. N. Mao, L. Senapati, X. X. Xi, R. L. Greene, and T. Venkatesan, Appl. Phys. Lett. **66**, 1427 (1995).

[104] S. E. Lofland, S. M. Bhagat, H. L. G. C. Xiong, T. Venkatesan, R. L. Greene, and S. Tyagi, J. Appl. Phys. **79**, 5166 (1996).

[105] S. Lofland and S. Bhagat, (private communication).

[106] A. G. Markelz, (private communication).

[107] Z. M. Zhang, B. I. Choi, M. I. Flik, and A. C. Anderson, J. Opt. Soc. Am. B **11**, 2252 (1994).

[108] Errors in dc measurements resulted from Ag print layers on the substrate back surfaces applied to enhance thermal conductivity during the growth process. Excess Ag print, not removed before dc measurements, shorted electrical contacts on the films, resulting in erroneously low values of resistivity. The polishing procedure applied before ac measurements ensures none of the optical results reported here suffer from this problem.

[109] H. J. Lee, J. H. Jung, Y. S. Lee, J. S. Ahn, T. W. Noh, K. H. Kim, and S-W. Cheong, arXiv:cond-mat/9904173 (unpublished).

[110] W. E. Pickett and D. J. Singh, J. Magn. Magn. Mater. **172**, 237 (1997).

[111] P. G. Radaelli, D. E. Cox, M. Marecio, and S.-W. Cheong, Phys. Rev. B **55**, 3015 (1997).

[112] A. Chainani, M. Mathew, and D. D. Sarma, Phys. Rev. B **47**, 15397 (1993).

[113] L. Sheng, D. Y. Xing, D. N. Sheng, and C. S. Ting, Phys. Rev. Lett. **79**, 1710 (1997).

[114] C. H. Booth, F. Bridges, G. H. Kwei, J. M. Lawrence, A. L. Cornelius, and J. J. Neumeier, Phys. Rev. Lett. **80**, 853 (1998).

[115] Kenn Kubo and Nagao Ohata, J. Phys. Soc. Jpn. **33**, 21 (1972).

[116] B. Michaelis and A. J. Millis, Phys. Rev. B **68**, 115111 (2003).

[117] W. E. Pickett and D. Singh, Phys. Rev. B **53**, 1146 (1996).

[118] L. F. Matheiss, (unpublished).

[119] Theoretical predictions of the tight-binding hopping amplitude t_0 and the band plasma frequency ω_p^B continue to evolve. The latest values, $t_0 \approx 0.67\,\text{eV}$ and $\omega_p^B \approx 3.1\,\text{eV}$ from Ref. 116 corrects earlier works,[27,99,110] which reported $t_0 \approx 0.6\,\text{eV}$ and $\omega_p^B \approx 1.9\,\text{eV}$.

[120] K. H. Kim, J. H. Jung, and T. W. Noh, Phys. Rev. Lett. **81**, 1517 (1998).

[121] V. N. Smolyaninova, *PhD Thesis* (University of Maryland, College Park, 1999).

[122] J. J. Hamilton, E. L. Keatley, H. L. Ju, A. K. Raychaudhuri, V. N. Smolyaninova, and R. L. Greene, Phys. Rev. B **54**, 14926 (1996).

[123] O. R. Mercier, R. G. Buckley, A. Bittar, H. J. Trodahl, E. M. Haines, J. B. Metson, and Y. Tomioka, Phys. Rev. B **64**, 035106 (2001).

[124] M. Rajeswari, R. Shreekala, A. Goyal, S. E. Lofland, S. M. Bhagat, K. Ghosh, R. P. Sharma, R. L. Greene, R. Ramesh, and T. Venkatesan, Appl. Phys. Lett. **73**, 2672 (1998).

[125] A. Goyal, M. Rajeswari, R. Shreekala, S. E. Lofland, S. M. Bhagat, T. Boettcher, C. Kwon, R. Ramesh, and T. Venkatesan, Appl. Phys. Lett. **71**, 2535 (1997).

[126] N. Kida, M. Hangyo, and M. Tonouchi, Phys. Rev. B **62**, 11965 (2000).

[127] J. E. Gordon, R. A. Fisher, Y. X. Jia, N. E. Phillips, S. F. Reklis, D. A. Wright, and Z. Zettl, Phys. Rev. B **59**, 127 (1999).

[128] J. W. Allen and J. C. Mikkelsen, Phys. Rev. B **15**, 2952 (1977).

[129] P. E. Sulewski, A. J. Sievers, M. B. Maple, M. S. Torikachvili, J. L. Smith, and Z. Fisk, Phys. Rev. B **38**, 5338 (1988).

[130] R. N. Gurzhi, Sov. Phys.–JETP **8**, 673 (1959).

[131] M. Jaime, P. Lin, M. B. Salamon, and P. D. Han, Phys. Rev. B **58**, R5901 (1998).

[132] A. A. Abrikosov, L. P. Gorkov, and I. E. Dzyaloshinski, *Methods of Quantum Field Theory in Statistical Physics* (Dover, New York, 1975).

[133] A linear interpolation from the far-IR data to 0.2 eV approximates the spectral gap resulting from LAO opacity. K exhibits little sensitivity to the choice of interpolation in this relativels small frequency range.

[134] T. Holstein, Ann. Phys. (N.Y.) **8**, 325 (1959).

[135] K. Kritayakirana, P. Berger, and R. V. Jones, Opt. Commun. **1**, 95 (1969).

[136] T. Penney, P. Berger, and K. Krytayakirana, J. Appl. Phys. **40**, 1234 (1969).

[137] M. N. Iliev, H.-G. Lee, V. N. Popov, M. V. Abrashev, A. Hamed, R. L. Meng, and C. W. Chu, Phys. Rev. B **56**, 2488 (1997).

[138] W.-C. Yi, S.-I. Kwun, and J.-G. Yoon, J. Phys. Soc. Jpn. **69**, 2706 (2000).

[139] J. Takahashi, K. Hagita, K. Kohn, Y. Tanabe, and E. Hanamura, Phys. Rev. Lett. **89**, 076404 (2002).

[140] S. W. Cheong, (private communication).

[141] J. H. Jung, K. H. Kim, D. J. Eom, T. W. Noh, E. J. Choi, J. Yu, Y. S. Kwon, and Y. Chung, Phys. Rev. B **55**, 15489 (1997).

[142] A. B. Sushkov, (private communication).

[143] T. J. Sato, S.-H. Lee, T. Katsufuji, M. Masaki, S. Park, J. R. D. Copley, and H. Takagi, Phys. Rev. B **68**, 014432 (2003).

[144] A. A. Mukhin, A. Y. Pronin, A. S. Prokhorov, G. V. Kozlov, V. Zelezny, and J. Petzelt, Phys. Lett. A **153**, 499 (1991).

[145] The arguments for $\delta E/E = \alpha\,\delta a/a$, with $\alpha \sim 1$ must be modified for semiconductors with large bandwidths W compared to the band gap E_g. In this case while $\delta W/W \sim \delta a/a$, the relative change in the gap energy may be rather large compared to the relative change in the lattice constant. For GaAs ($E_g \approx 1.4$ eV), optical measurements of the gap under hydrostatic pressure[183] find $\delta E_g/E_g \approx 20\,\delta a/a$ ($\alpha \approx 20$). Compare this to titanium oxide TiO_2 with a larger gap (≈ 3.6 eV), where similar pressure-dependent optical studies[171] report $\alpha \approx 2$.

[146] In the far-infrared, the lowest étalon peak in transmittance determines the index of refraction, which depends both on the electric permittivity and the magnetic permeability, $n = \mathcal{R}e\left\{\sqrt{\tilde{\mu}\,\tilde{\epsilon}}\right\}$. An accurate determination of ϵ_0 requires knowledge of both n and $\tilde{\mu}$. The relatively weak antiferromagnetic resonance observed in the hexamanganites changes the magnetic permeability negligibly from the vacuum value $\mu = 1$ (cgs units). Thus, including the antiferromagnetic resonance offers only a small correction to ϵ_0.

[147] A. B. Kuz'menko, D. van der Marel, P. J. M. van Bentum, E. A. Tishchenko, C. Presura, and A. A. Bush, Phys. Rev. B **63**, 094303 (2001).

[148] X. G. Zheng, Y. Sakurai, Y. Okayama, T. Q. Yang, L. Y. Zhang, X. Yao, K. Nonaka, and C. N. Xu, J. Appl. Phys. **92**, 2703 (2002).

[149] E. Granado, A. García, J. A. Sanjurjo, C. Rettori, and I. Torriani, Phys. Rev. B **60**, 11879 (1999).

[150] M. Fiebig, T. Lottermoser, D. Frölich, A. V. Goltsev, and R. V. Pisarev, Nature **419**, 818 (2002).

[151] D. B. Romero and A. B. Sushkov, (private communication).

[152] J. Takahashi, K. Kohn, and E. Hanamura, J. Lumin. **100**, 141 (2002).

[153] J. C. Maxwell Garnett, Phil. Trans. R. Soc. London, Ser. A **203**, 385 (1904); **205**, 237 (1906).

[154] D. A. G. Bruggeman, Ann. Phys. (Leipzig) **24**, 636 (1935).

[155] P. O'Neill and A. Ignatiev, Phys. Rev. B **18**, 6540 (1978).

[156] T. C. Choy, *Effective Medium Theory: Principles and Applications* (Clarendon Press, Oxford, 1999).

[157] K. D. Cummings, J. C. Garland, and D. B. Tanner, Phys. Rev. B **30**, 4170 (1984).

[158] The effective medium approximation (EMA) by Bruggeman[154] improves upon that established by Maxwell Garnett. EMA treats the two composites symmetrically, gives rise to a critical volume fraction, and adapts easily to include multiple components.[156] In the low f limit (satisfied by the $x \leq 0.07$ Co-doping levels in these samples), EMA reduces to MGT.

[159] A. Y-C. Yu, T. M. Donovan, and W. E. Spicer, Phys. Rev. **167**, 670 (1968).

[160] E. D. Palik, editor, *Handbook of Optical Constants of Solids II* (Academic Press, San Diego, 1991).

[161] Z. Yang, G. Liu, and R. Wu, Phys. Rev. B **67**, 060402(R) (2003).

[162] G. Mie, Ann. Phys. (Leipzig) **25**, 377 (1908).

[163] M. Born and E. Wolf, *Principles of Optics, 7th edition* (Cambridge University Press, Cambridge, 1999).

[164] J. R. Simpson, H. D. Drew, V. N. Smolyaninova, R. L. Greene, M. C. Robson, A. Biswas, and M. Rajeswari, Phys. Rev. B **60**, R16263 (1999).

[165] P. Y. Yu and M. Cardona, *Fundamentals of Semiconductors* (Springer-Verlag, Berlin, 1996).

[166] R. Asahi, Y. Taga, W. Mannstadt, and A. J. Freeman, Phys. Rev. B **61**, 7459 (2000).

[167] H. Tang, F. Lévy, H. Berger, and P. E. Schmid, Phys. Rev. B **52**, 7771 (1995).

[168] S. Guha, K. Ghosh, J. G. Keeth, S. B. Ogale, S. R. Shinde, J. R. Simpson, H. D. Drew, and T. Venkatesan, Appl. Phys. Lett. **83**, 3296 (2003).

[169] H. Tang, H. Berger, P. E. Schmid, and F. Lévy, Solid State Commun. **87**, 847 (1993).

[170] H. Tang, H. Berger, P. E. Schmid, and F. Lévy, Solid State Commun. **92**, 267 (1994).

[171] T. Sekiya, S. Ohta, and S. Kurita, Int. J. Mod. Phys. B **15**, 3952 (2001).

[172] T. Arlt, M. Bermejo, M. A. Blanco, L Gerward, J. Z. Jiang, J. Staun Olsen, and J. M. Recio, Phys. Rev. B **61**, 14414 (2000).

[173] J. Emsley, *The Elements* (Clarenden Press, Oxford, 1998).

[174] S.-D. Mo and W. Y. Chin, Phys. Rev. B **51**, 13023 (1995).

[175] E. H. Hwang, A. J. Millis, and S. Das Sarma, Phys. Rev. B **65**, 233206 (2002).

[176] S. R. Shinde, S. B. Ogale, J. S. Higgins, H. Zheng, A. J. Millis, V. N. Kulkarni, R. Ramesh, R. L. Greene, and T. Venkatesan, Phys. Rev. Lett. **92**, 166601 (2004).

[177] P. Rouard, Ann. d. Physique **7**, 271 (1937).

[178] D. C. Schmadel, *PhD Thesis* (University of Maryland, College Park, 2002).

[179] G. S. Jenkins, *PhD Thesis* (University of Maryland, College Park, 2003).

[180] Y. Liu and E. Allen, Phys. Rev. B **52**, 1566 (1995).

[181] L. R. Windmiller, Phys. Rev. **149**, 472 (1966).

[182] W. R. Datars and J. Vanderkooy, IBM J. Res. Dev. **8**, 247 (1964).

[183] A. Kangarlu, G. Guarriello, R. Berney, and P. W. Yu, Appl. Phys. Lett. **59**, 2290 (1991).

Jeffrey R. Simpson

Department of Physics
University of Maryland • College Park, MD 20742
Phone: 301-405-7278 • Fax: 301-314-9465
Email: simpson@physics.umd.edu
http://www2.physics.umd.edu/~simpson

Objective

Seeking a tenure-track position in academia teaching physics and involving undergraduates in current research projects.

Education

Ph.D. Physics
University of Maryland, *College Park, MD*, Fall 2004
Thesis topic: Optical Properties of Magnetic Transition Metal Oxides
Thesis advisor: Professor H. Dennis Drew
GPA: 3.38

B.A. Physics
B.A. Mathematics/Computer Science
Shippensburg University, *Shippensburg, PA*, December 1994
GPA: 3.96 Graduated Summa Cum Laude

Professional Experience

Graduate Research Assistant, *Magneto-optics Group, University of Maryland*, Summer 1997 until present

- Specializing in measuring the optical constants of magnetic transition metal oxides using a variety of Fourier Transform spectroscopic techniques in a frequency range from far-infrared to UV.
- Designing and constructing a magneto-circular dichroism experiment to study novel magnetic materials, *e.g.* diluted magnetic semiconductors.
- First reported study attributing the anomaly in the static dielectric constant temperature dependence of $LuMnO_3$ to infrared active phonons. Identified a symmetry-allowed on-site Mn-Mn optical transition at ~ 1.7 eV and found a similar spin-correlated temperature dependence.
- Contributed to the understanding of the electronic structure of the diluted magnetic semiconductor, Co-doped TiO_2, through observation of a shift of the band edge with Co-doping and an absence of Co-impurity states in the gap.
- Developed a novel technique to obtain the complex optical conductivity in the far-infrared of thin films by measuring the reflection amplitude and phase.
- Refuted the purported anomalously-small Drude optical spectral weight in colossal magnetoresistant (CMR) manganites.
- Reported strong optical evidence supporting Double-Exchange coupled with Jahn-Teller interaction as the relevant physical mechanism responsible for CMR in hole-doped manganites.

Teaching Fellow, *Materials Research Science and Engineering Center, University of Maryland*, 2001-2003

- Originated a high school electronics course curriculum covering analog and digital circuits using both discrete and integrated components.
- Developed and conducted a summer workshop for high school students on the physics and engineering of roller coasters.

- Implemented an after-school electronics club with a local high school teacher Stan Eisestein. Developed and conducted mini-labs, short lectures, and presented demonstrations on electronics and related physics topics. Assisted students with completion of individual AM transistor radios.
- Performed Physics is Phun lecture demonstrations shows at local area schools (K-12) in collaboration with Prof. Richard Berg, director of physics lecture demonstration facility
- Developed and presented lectures, demonstrations, tutorials, and laboratories for students at local secondary schools as part of the NSF sponsored GK-12 educational outreach program .

Instructor, *Department of Physics, University of Maryland*, Summer 2001

- Responsible for teaching duties of the introductory physics course for engineers, PHYS161 General Physics: Mechanics and Particle Dynamics.
- Created lessons plans, developed homework and exams, and provided in-class demonstrations.

Teaching Assistant, *Department of Physics, University of Maryland*, 1995 - 1997

- Taught physics majors, engineers, and non-majors in five introductory physics courses: PHYS262 General Physics: Vibrations, Waves, Heat, Electricity and Magnetism, PHYS161, PHYS122 Fundamentals of Physics II with Lab, PHYS171 Introductory Physics: Mechanics and Relativity, PHYS262A lab.
- Duties included running labs, teaching recitations and tutorials, and grading.
- Received teaching awards from the University and the Physics Department.

Research Assistant, *Los Alamos National Laboratory, Los Alamos, NM*, January to August 1995

- Characterized a digital radiography technique utilizing high energy x-rays for use in the plutonium stockpile stewardship program.
- Developed FORTRAN code to aide benchmarking of x-ray simulation program XRSIM.
- Awarded a DOE Research Semester (SERS).

Lab Technician, *Proctor and Gamble Division of Cosmetics and Fragrances, Hunt Valley, MD*, Summers 1991-93, 1994 and Winter 1993

- Evaluated new and current products in several research and development groups including chemical and physical package evaluation, chemical analysis, and spectroscopic analysis.
- Developed a test method for spectroscopic analysis of liquid make-up foundation shades.

Lab Technician, *EA Engineering, Hunt Valley, MD*, Winter 1991

- Evaluated toxicity of wastewater effluents chemically and biologically.

Publications

Optical band edge shift of anatase $Ti_{1-x}Co_xO_{2-\delta}$, J. R. Simpson, H. D. Drew, S. R. Shinde, R. J. Choudhary, S. B. Ogale, and T. Venkatesan, Phys. Rev. B **69**, 193205 (2004).

Temperature-dependent optical studies of $Ti_{1-x}Co_xO_2$, S. Guha, K. Ghosh, J. G. Keeth, S. B. Ogale, S. R. Shinde, J. R. Simpson, H. D. Drew, and T. Venkatesan, Appl. Phys. Lett. **83**, 3296 (2003).

High Temperature Ferromagnetism with a Giant Magnetic Moment in Transparent Co-doped $SnO_{2-\delta}$, S. B. Ogale, R. J. Choudhary, J. P. Buban, S. E. Lofland, S. R. Shinde, S. N. Kale, V. N. Kulkarni, J. Higgins, C. Lanci, J. R. Simpson, N. D. Browning, S. Das Sarma, H. D. Drew, R. L. Greene, and T. Venkatesan, Phys. Rev. Lett. **91**, 077205 (2003).

Exchange Interaction Effects on the Optical Properties of $LuMnO_3$, A. B. Souchkov, J. R. Simpson, M. Quijada, H. Ishibashi, N. Hur, J. S. Ahn, S. W. Cheong, A. J. Millis, and H. D. Drew, Phys. Rev. Lett. **91**, 027203 (2003).

Ferromagnetism in laser deposited anatase $Ti_{1-x}Co_xO_{2-\delta}$ films, S. R. Shinde, S. B. Ogale, S. Das Sarma, J. R. Simpson, H. D. Drew, S. E. Lofland, C. Lanci, J. P. Buban , N. D. Browning, V. N. Kulkarni, J. Higgins, R. P. Sharma, R. L. Greene, and T. Venkatesan, Physical Review B **67**, 115211 (2003).

Temperature dependence of low-lying electronic excitations of $LaMnO_3$, M. A. Quijada, J. R. Simpson, L. Vasiliu-Doloc, J. W. Lynn, H. D. Drew, Y. M. Mukovskii, and S. G. Karabashev, Phys. Rev. B **64**, 224426 (2001).

Midinfrared Hall effect in thin-film metals: Probing the Fermi surface anisotropy in Au and Cu, J. Cerne, D. C. Schmadel, M. Grayson, G. S. Jenkins, J. R. Simpson, and H. D. Drew, Phys. Rev. B **61**, 8133 (2000).

The AC Hall effect in YBCO: temperature and frequency dependence of Hall scattering, J. Cerne, M. Grayson, D. C. Schmadel, J. Simpson, H. D. Drew, R. Hughes, J. S. Preston, and P. J. Kung, Physica B **284-288**, 941 (2000).

Temperature-dependent scattering rate and optical mass of ferromagnetic metallic manganites, J. R. Simpson, H. D. Drew, V. N. Smolyaninova, R. L. Green, M. C. Robson, Amlan Biswas, and M. Rajeswari, Phys. Rev. B **60**, R16263 (1999).

Optical conductivity of manganites: Crossover from Jahn-Teller small polaron to coherent transport in the ferromagnetic state, M. Quijada, J. Cerne, J. R. Simpson, H. D. Drew, K. H. Ahn, A. J. Millis, R. Shreekala, R. Ramesh, M. Rajeswari, and T. Venkatesan, Phys. Rev. B **58**, 16093 (1998).

Conference Presentations

Exchange effects on the electronic excitations in the optical spectrum of $LuMnO_3$, J. R. Simpson, A. B. Sushkov, D. B. Romero, H. D. Drew, M. Quijada, J. S. Ahn, H. Ishibashi, S. W. Cheong, and A. J. Millis, American Physical Society March Meeting 2003, Austin, TX.

Optical conductivity of cobalt-doped titanium dioxide, J. R. Simpson, H. D. Drew, S. R. Shinde, Y. Zhao, S. B. Ogale, and T. Venkatesan, American Physical Society March Meeting 2003, Austin, TX.

Electron-phonon interaction effects on the infrared conductivity of $La_{1-x}Ca_xMnO_3$ ($0.2 < x < 0.4$) in the ferromagnetic metallic state, J. R. Simpson, H. D. Drew, and M. Rajeswari, American Physical Society March Meeting 2001, Seattle, WA.

Anisotropic conductivity in $La_{0.7}Sr_{0.3}MnO_3$, J. R. Simpson, H. D. Drew, M. C. Robson, and M. Rajeswari, American Physical Society March Meeting 2000, Minneapolis, MN.

Optical mass in colossal magnetoresistant manganite alloys as a function of carrier concentration, J. R. Simpson, H. D. Drew, V. N. Smolyaninova, R. L. Greene, Amlan Biswas, M. C. Robson, and M. Rajeswari, American Physical Society March Meeting 2000, Minneapolis, MN.

Temperature dependent scattering rate and optical mass enhancement of ferromagnetic metallic manganites, J. R. Simpson, H. D. Drew, V. N. Smolyaninova, R. L. Greene, M. C. Robson, and M. Rajeswari, American Physical Society Centennial Meeting 1999, Atlanta, GA.

Optical conductivity of manganites: Crossover from Jahn-Teller small polaron to coherent transport in the ferromagnetic state, J. R. Simpson, M. Quijada, J. Cerne, R. Shreekala, M. Rajeswari, and H. D. Drew, American Physical Society March Meeting 1998, Los Angeles, CA.

Professional Societies

Member of the American Physical Society
Member of the American Association of Physics Teachers

Academic Awards

University of Maryland

- NSF GK-12 Teaching Fellowship - Fall 2001 to Summer 2003
- University Distinguished Teaching Assistant Award - 1999
- Ralph D. Myers Teaching Award - 1997
- Ralph D. Myers Teaching Award (honorable mention) - 1996

Shippensburg University

- James Eldon Mathematics Award - 1994
- Kappa Mu Epsilon Math Honor Society - 1994
- Phi Kappa Phi Honor Society - 1994
- Foundation Scholarship Award - 1990 to 1994
- Dean's List - 1990 to 1994

Academic Committees

University of Maryland

- Selection Committee for the 2001 Physics Distinguished Alumni Award - Spring 2001
- Committee for Arbitrary and Capricious Grading - Spring 2001 until present

Special Skills

Optics: Michelson Fourier transform infrared spectrometer, grating spectrometer, Spectrograph spectrometer, photo-elastic modulator, charge coupled device camera
Electronics: oscilloscope, lock-in amplifier, spectrum analyzer, signal generator, digital multimeter
Vacuum Systems: helium leak detector, diffusion pump, roughing pump, ion gauge
X-ray radiography: 1.5 MeV van de Graff source, 22 MeV Betatron source
Mechanical: lathe, milling machine, drill press, optical comparator, Instron, vibration table
Chemistry: gas chromatograph, differential scanning calorimeter, viscosity tester

Data Acquisition: LabView, Bomem PCDA, Lotus Macros
Image Analysis: Khoros, IDL, BGrams
Data Analysis: Mathematica, Mathcad
Programming Languages: FORTRAN, Pascal, LISP, ArrayBasic, Basic
Typesetting Languages: LaTeX 2_ε, HTML
CAD: IDEAS, Pro-Engineer, AutoCAD
Spreadsheets: Origin, Excel, Lotus, QuattroPro
Plotting: SigmaPlot, Origin
X-ray simulation: XRSIM
Operating Systems: Windows 3.11, 95, 98, 2000; MSDOS; Linux; Unix; VAX

Personal

Rugby Football - Maryland Exiles and Shippensburg University(treasurer)
- U. S. National 7s championship 2004, 2003, 2001, 1996
- U. S. National 15s championship 2003, 1997
- Rio Grande Select Side and Midwest Local Area Union Champs 1995
- Eastern Pennsylvania Union Collegiate Champs 1994

Private physics tutor - Spring 1999 until present

References

Available upon request.